



**Carlos António  
Delgado Sousa  
Brites**

**Self-Referencing Thermometry in the  
Nanoscale**





**Carlos António  
Delgado Sousa  
Brites**

**Self-Referencing Thermometry in the  
Nanoscale**

”There’s Plenty of Room at the Bottom”

*Richard Feynman, on December 29th 1959 at the  
annual meeting of the American Physical Society*









**Carlos António  
Delgado Sousa  
Brites**

## **Self-Referencing Thermometry in the Nanoscale**

Dissertação apresentada à Universidade de Aveiro para cumprimento dos requisitos necessários à obtenção do grau de Doutor em Física, realizada sob a orientação científica de Luís António Martins Dias Carlos e Vitor Brás Sequeira Amaral, Professores Catedráticos do Departamento de Física da Universidade de Aveiro

Apoio Financeiro da FCT e do FSE no âmbito do III Quadro Comunitário de Apoio.







**o júri / the jury**

presidente / president

**Doutor Aníbal Guimarães da Costa**

Professor Catedrático da Universidade de Aveiro (por delegação do Reitor da Universidade de Aveiro)

vogais / examiners committee

**Doutor Luís António Martins Dias Carlos**

Professor Catedrático da Universidade de Aveiro (orientador)

**Doutor Vitor Brás Sequeira Amaral**

Professor Catedrático da Universidade de Aveiro (orientador)

**Doutor Fernando Palacio Parada**

Profesor de Investigación del CSIC, Facultad de Ciencias, Universidad de Zaragoza

**Doutor Hugh Douglas Burrows**

Professor Catedrático da Faculdade de Ciências e Tecnologia da Universidade de Coimbra

**Doutor João Pedro Estrela Rodrigues Conde**

Professor Catedrático do Instituto Superior Técnico da Universidade Técnica de Lisboa

**Doutor António Manuel Pais Pereira Leite**

Professor Associado da Faculdade de Ciências de Universidade do Porto







## agradecimentos / acknowledgements

I would like to express my gratitude to all those who gave me the possibility to complete this thesis. I want to thank to the Physics Department and in CiCECO of University of Aveiro in general, that gives me all the material conditions to complete this thesis. An acknowledgement is own to Fundação da Ciência e Tecnologia for the financial support (grant SFRH/BD/38472/2007) in the period 2007-2011, and to CiCECO for the financial support in the final part of the thesis (grant PEst-C/CTM/LA0011/2011).

I am deeply indebted to my supervisors Prof. Dr. Luís Carlos and Prof. Dr. Vitor Amaral from the University of Aveiro whose help, stimulating suggestions and encouragement helped me in all the time of research for and writing of this thesis. Also the fruitful collaboration with the Univeristy of Zaragoza ICMA group, especially Prof. Dr. Fernando Palacio and Dr. Angel Milan for all the suggestions and unconditional cooperation. In Aveiro the collaboration of Prof. Dr. Rute André and Prof. Dr. Paulo André was fundamental to produce temperature mappings and discuss some photoluminescent features.

My former colleagues from the Department of Physics/CiCECO and Zaragoza that supported me in my research work. I want to thank them for all their help, support, interest and valuable hints. Especially I am obliged to Patrícia Lima (Aveiro), Carlos Vicente (Aveiro), to Nuno Oliveira e Silva (first in Zaragoza and now in Aveiro), to Rafael Piñol (Zaragoza). I also want to thank Mr Julio Gonçalves, Mr Ivo Mateus and Mr Miguel Rocha for all his assistance on the Physics workshops. The collaboration of Pinturas Ordesa SA (Zaragoza) that donates the resistant UV ink and solvents used for the Solids Sample Holder painting produced in Zaragoza is also acknowledged.

Especially, I would like to give my special thanks to my near family, namely my wife Lisa and my oldest son, Hugo whose patient love and calm (respectively) enabled me to complete this work. Also my youngest son Afonso, whose good pregnant allowed a normal work until the end of the writing of the thesis.







## Palavras-Chave

termometria, nanopartícula, sílica, íon lantânídeo, sensibilidade

## Resumo

Na última década emergiu uma linha de investigação muito activa em termómetros não invasivos e precisos que possam determinar temperatura à escala nanométrica. Esta investigação foi fortemente estimulada pelas numerosas solicitações da nanotecnologia e da biomedicina, por exemplo.

Uma das abordagens mais promissoras propõe o uso de íões trivalentes de lantanídeos que apresenta propriedades fotoluminescentes que dependem da temperatura. Neste trabalho demonstra-se que esta técnica combina as vantagens de ter um limite de detecção de 0.5 graus com sensibilidade até  $4.5 \% \cdot K^{-1}$ .

Este termómetro molecular pode ser processado em filmes finos ou nanopartículas, abrindo os campos de aplicação a diferentes utilizações.

As nanopartículas de sílica produzidas são caracterizadas na presença e na ausência de íões lantanídeos. Sem o metal, as nanopartículas de APTES/TEOS demonstram ser luminescentes sob excitação UV sem necessidade de utilizar qualquer tratamento térmico. O rendimento quântico de emissão depende apenas da proporção dos silanos e pode atingir o valor de  $0.15 \pm 0.02$ . A co-dopagem destas nanopartículas com  $\text{Eu}^{3+}$  e  $\text{Tb}^{3+}$  permite obter sondas com resposta ratiométrica, com a possibilidade de ajustar a gama de temperaturas de operação e a sensibilidade, *via* desenho inteligente da matriz de suporte e dos ligandos de  $\beta$ -dicetona que estão coordenados ao íon metálico.

Quando processados como filmes, este termómetro permite o mapeamento de temperaturas com resolução espacial  $1.8 \mu\text{m}$ .

A racionalização da dependência de temperatura é uma ferramenta útil para desenvolver termómetros que operam em gamas de temperatura específicos (e.g. gama de temperatura fisiológica, 290-340 K) com sensibilidade acima de  $0.5 \% \cdot K^{-1}$ .

A combinação de esforços de um grande número de diversas disciplinas irá previsivelmente permitir o surgimento de termómetros moleculares novos e sofisticados, preenchendo os principais requisitos das nanociências.







## Keywords

thermometry, nanoparticle, silica, lanthanide ion, sensitivity

## Abstract

Non-invasive precise thermometers working at the nanoscale with high spatial resolution, where the conventional methods are ineffective, have emerged over the last decade as a very active field of research. This has been strongly stimulated by the numerous challenging requests arising from nanotechnology and biomedicine.

One of the most promising approaches proposes the use of trivalent lanthanide ions that present photoluminescent properties that are temperature dependent. In this work is demonstrated that the technique possesses both the advantages of self-referencing and limit of detection above 0.5 degree with sensitivity up to  $4.5 \% \cdot K^{-1}$ .

This molecular thermometer can be processed as thin films or nanoparticles, open the field of use to several applications.

The silica nanoparticles produced are characterized in the presence and absence of the lanthanide ions. Without the metal the APTES/TEOS silica nanoparticles prove to be luminescent upon UV excitation without need of the annealing step. The emission quantum yield depends only of the silanes proportion can reach the value of  $0.15 \pm 0.02$ . Co-doping this nanoparticles with  $\text{Eu}^{3+}$  and  $\text{Tb}^{3+}$  the nanoparticles become ratiometric temperature probes with possibility of tailoring the temperature range of operation and the sensitivity, *via* smart design of the host matrix and the  $\beta$ -diketonate ligand that is coordinated to the metal ion.

When processed as film, the thermometer allows temperature mapping with spatial resolution up to  $1.8 \mu\text{m}$ .

The rationalization of the temperature dependent emission provides useful tools to design thermometers working in specific temperature ranges (e.g. physiological temperature range, 290-340 K) with sensitivity above  $0.5 \% \cdot K^{-1}$ .

Combining efforts from a large number different disciplines it is predictable that new and sophisticated molecular thermometers will emerge, fulfilling the major demands of the nanosciences.



## Palabras-Clave

termometría, nanopartículas, sílice, iones lantánidos, sensibilidad

## Resumen

En la última década ha surgido una línea de investigación muy activa en termometría no invasiva y precisa capaz de determinar la temperatura a la nanoescala. Esta investigación ha sido estimulada en gran medida por las numerosas aplicaciones de la nanotecnología y la biomedicina, por ejemplo.

Uno de los enfoques más prometedores propone el uso de iones lantánidos trivalentes que presenta propiedades fotoluminiscentes que son dependientes de la temperatura. Este trabajo demuestra que esta técnica combina las ventajas de tener un límite de detección de 0.5 grados con una sensibilidad de hasta  $4.5\% \cdot K^{-1}$ .

Este termómetro molecular puede ser transformado en películas delgadas o nanopartículas, abriendo el campo de aplicación a diferentes usos.

Las nanopartículas de sílice producidas se caracterizaron en presencia y ausencia de iones lantánidos. Sin el metal nanopartículas APTES o TEOS se emiten bajo la luminiscencia de excitación ultravioleta sin utilizar ningún tratamiento térmico. El rendimiento cuántico de emisión sólo depende de la proporción de silanos y puede alcanzar un valor de  $0.15 \pm 0.02$ . El co-dopaje con estas nanopartículas con  $\text{Eu}^{3+}$  y  $\text{Tb}^{3+}$  permite sondas con respuesta radiométrica, con la posibilidad de ajustar el rango de temperatura de funcionamiento y de la sensibilidad, a través de un diseño inteligente de los ligandos de apoyo de la matriz y  $\beta$ -dicetona que están coordinados con el ión metálico.

En caso de transformación en las películas, este termómetro permite la asignación de la temperatura con una resolución espacial de hasta  $1.8 \mu\text{m}$ .

La racionalización de la dependencia de la temperatura es una herramienta útil para el desarrollo de termómetros que operan en rangos de temperatura específicos (por ejemplo, rango de temperatura fisiológica, 290-340 K) con una sensibilidad más de  $0.5\% \cdot K^{-1}$ .

Los esfuerzos combinados de un gran número de diferentes disciplinas previsiblemente permitirá la aparición de los termómetros moleculares nuevas y sofisticadas, llenando los requisitos principales de las nanociencias.



# Index

<b>Index</b>	<b>i</b>
<b>List of Figures</b>	<b>v</b>
<b>List of Tables</b>	<b>1</b>
<b>1 Introduction</b>	<b>3</b>
1.1 Objectives, Motivation and Thesis Organization . . . . .	4
1.2 Evolution of Thermometry Towards the Nanoscale . . . . .	5
1.2.1 Characterization of Thermometers . . . . .	15
1.3 Trivalent Lanthanide Ions for Thermometry . . . . .	18
1.3.1 General Background on Luminescence . . . . .	18
1.3.2 Trivalent europium/terbium ions luminescent properties . . . . .	23
<b>2 State of the Art in High Spatial Resolution Thermometry</b>	<b>29</b>
2.1 Luminescent Thermometers Review . . . . .	29
2.1.1 Thermometers Based on Organic Dyes . . . . .	31
2.1.2 Thermometers based on Quantum Dots . . . . .	34
2.1.3 Thermometers based on Ln <sup>3+</sup> Phosphors . . . . .	37
2.1.4 Complex Thermometric Systems . . . . .	41
2.2 Non-Luminescent Thermometers Review . . . . .	68
2.2.1 Scanning Thermal Microscopy . . . . .	68
2.2.2 Nanolithography Thermometry . . . . .	71
2.2.3 Carbon Nanotube Thermometry . . . . .	73
2.2.4 Biomolecular-based Thermometry . . . . .	77
2.2.5 Miscellaneous . . . . .	79

<b>3</b>	<b>Materials and Methods</b>	<b>85</b>
3.1	Materials Synthesis . . . . .	86
3.1.1	Sol-Gel Process . . . . .	86
3.1.2	Synthesis of Organic Silica Nanoparticles . . . . .	86
3.1.3	Synthesis of Maghemite Nanoparticles . . . . .	89
3.1.4	Core-Shell Maghemite-Silica Nanoparticles . . . . .	89
3.1.5	Silica Nanoparticles co-doped with $\text{Ln}^{3+}$ complexes . . . . .	91
3.1.6	Di-ureasil Films . . . . .	94
3.2	Experimental Techniques . . . . .	96
3.2.1	Steady State Photoluminescence:Emission and Excitation Spectra .	96
3.2.2	Time-Resolved Spectroscopy . . . . .	98
3.2.3	Other Methods and Techniques . . . . .	101
<b>4</b>	<b>Metal-Free Highly Luminescent Silica Nanoparticles</b>	<b>107</b>
4.1	Metal-Free Silica Nanoparticles in the Literature . . . . .	107
4.2	Metal-Free Si-NPs Characterization . . . . .	109
4.2.1	Morphological Characterization . . . . .	109
4.3	Photophysical Characterization . . . . .	111
4.4	Effect of the Annealing in the Photoluminescence of Si-NPs . . . . .	125
<b>5</b>	<b>Temperature determination using co-doped di-ureasil films</b>	<b>129</b>
5.1	Thermometric Properties of di-ureasil Thin Films co-doped with $\text{Eu}^{3+}/\text{Tb}^{3+}$	130
5.2	Rationalization of the Operation Mechanism of the Thermometer . . . . .	134
5.3	Sensitivity and Temperature Range of Operation . . . . .	136
5.4	Absolute Temperature Determination . . . . .	138
5.5	Incorporation of maghemite NPs in the di-ureasil film . . . . .	139
5.6	Optical Temperature Mapping with Micrometric Resolution . . . . .	140
5.6.1	Spatial Resolution Limit . . . . .	144
<b>6</b>	<b>Nanoparticles for Thermometry Below Room Temperature</b>	<b>153</b>
6.1	Morphological and Spectroscopic Properties of <b>AET</b> samples . . . . .	153
6.2	Rationalization of the Operation Mechanism of the Thermometer . . . . .	159
6.3	Sensitivity and Temperature Range of Operation . . . . .	163

<b>7</b>	<b>Nanoparticles for Thermometry at the Physiological Temperature Range</b>	<b>167</b>
7.1	Strategies to attain the Physiological Temperature Range . . . . .	168
7.2	Morphological Characterization of the Luminescent Molecular Thermometers	169
7.3	Operation Mechanism of <b>PET-1.3</b> . . . . .	172
7.4	Operation Mechanism of <b>AET-1.4a</b> . . . . .	173
7.5	Photophysical Characterization of the Nanothermometers . . . . .	175
7.6	Demonstration of Temperature mapping in Fluids. . . . .	180
7.7	Comparison with Literature Examples . . . . .	183
<b>8</b>	<b>Conclusions and Future Work</b>	<b>187</b>
	<b>Bibliography</b>	<b>193</b>
<b>A</b>	<b>List of Acronyms</b>	<b>223</b>



# List of Figures

1.1	Fahrenheit's Thermoscope . . . . .	6
1.2	Temperature Determination Schemes . . . . .	9
1.3	Near- and Far-Field Thermometric Systems . . . . .	11
1.4	Radiative and non-radiative transitions within a molecule . . . . .	19
1.5	Two Parabola Model . . . . .	22
2.1	Example of QD-based thermometer . . . . .	36
2.2	Example of $\text{Ln}^{3+}$ -based thermometer . . . . .	40
2.3	Polymer-phosphor thermometer structures . . . . .	43
2.4	Example of a complex thermometer using a DNA beacon . . . . .	48
2.5	Example of a intracellular thermometer by [81] . . . . .	53
2.6	Example of a intracellular thermometer by [81] . . . . .	55
2.7	Example of a intracellular thermometer by [179] . . . . .	58
2.8	Luminescent Thermometers Sensitivity . . . . .	64
2.9	Luminescent Ratiometric Thermometers Sensitivity . . . . .	65
2.10	Luminescent Lifetime Based Thermometers Sensitivity . . . . .	66
2.11	Luminescent Thermometers with Spatial Resolution Sensitivity . . . . .	67
2.12	Example of a SThM Thermometer Experimental Setup. . . . .	70
2.13	Example of a SThM Thermometer Temperature Mapping of an Electrode. . . . .	71
2.14	Example of a SThM Thermometer Temperature Mapping of an Human Hair. . . . .	72
2.15	Example of a CNT-based Gallium filled Thermometer. . . . .	74
2.16	Example of a CNT-based Gold-filled Thermometer. . . . .	75
2.17	Example of Biomolecular-based Thermometers. . . . .	78
3.1	Sol-Gel Process . . . . .	87

3.2	Silane Precursors . . . . .	88
3.3	Flux diagram of the Stöber Method . . . . .	88
3.4	Maghemite NPs . . . . .	90
3.5	Comparison of the <b>NPM-2</b> . . . . .	90
3.6	Synthesized core-shell NPs . . . . .	91
3.7	Lanthanide ligand complexes . . . . .	93
3.8	TEM image of <b>AET-1.4a</b> . . . . .	93
3.9	Structure of TESP . . . . .	94
3.10	TEM images of <b>PET-1.3</b> . . . . .	95
3.11	Ureapropyltriethoxysilane hybrid precursor . . . . .	96
3.12	Experimental Layout for Photoluminescence . . . . .	97
3.13	Quantum Yield Equipment . . . . .	102
3.14	DLS experimental setup . . . . .	103
3.15	Electronic Microscopy Facilities . . . . .	105
4.1	Si-NPs Photographs . . . . .	109
4.2	Si-NPs DLS and TEM . . . . .	110
4.3	Si-NPs Room Temperature Emission and Excitation Spectra . . . . .	112
4.4	Si-NPs Room Temperature Emission . . . . .	113
4.5	Si-NPs deconvolution emission spectra fitting procedure. . . . .	115
4.6	Si-NPs photoluminescence comparision. . . . .	117
4.7	Si-NPs time-resolved emission spectra . . . . .	118
4.8	Si-NPs emission decay curves at 10 K . . . . .	119
4.9	Si-NPs emission decay curves at room temperature . . . . .	121
4.10	Si-NPs CIE chromaticity diagram. . . . .	122
4.11	Si-NPs emission quantum yield. . . . .	123
4.12	Si-NPs degradation. . . . .	124
5.1	Emission spectra of <b>UET-1.3</b> in the 10-300 K temperature range . . . . .	131
5.2	Excitation spectra of <b>UET-1.3</b> in the 10-300K temperature range . . . . .	132
5.3	$\Delta$ and integrated areas computed for <b>UET-1.3</b> in the range 10-300 K . . . . .	133
5.4	$\Delta$ parameter for <b>UET-1.3</b> in the 10-300K temperature range. . . . .	134
5.5	$\Delta$ and $I_{Tb}$ temperature cycling . . . . .	135
5.6	Decay Curves and Lifetime of $^5D_0$ and $^5D_4$ for sample <b>UET-1.3</b> . . . . .	137

---

5.7	Sensitivity of <b>UET-1.3</b> . . . . .	138
5.8	Temperature dependence of $\Delta$ at 300-350 K for <b>UET-1.3</b> . . . . .	139
5.9	Temperature dependence of $\Delta$ in 300-350 K for sample <b>UET-1.3-Fe</b> . . . . .	140
5.10	Temperature mapping experimental setup . . . . .	142
5.11	Circuit Temperature Profiles . . . . .	143
5.12	Second Circuit Design . . . . .	144
5.13	Second Circuit Temperature Mapping . . . . .	145
5.14	Temperature Mapping for Different Steps . . . . .	146
5.15	Spatial Resolution on Temperature Mapping . . . . .	147
5.16	Set-up used for thermoreflectance described in [230] . . . . .	148
5.17	Experimental results described in [230] . . . . .	148
5.18	Effect of the fibre inner diameter in the spatial resolution. . . . .	150
6.1	Hydrodynamic sizes of <b>AET</b> samples . . . . .	154
6.2	Comparison of the emission spectra of <b>AET</b> samples. . . . .	156
6.3	Microscopy of <b>AET</b> samples. . . . .	157
6.4	CIE color of <b>AET</b> samples . . . . .	158
6.5	Emission Spectra of <b>AET-1.3</b> . . . . .	159
6.6	$^5D_4$ lifetime of <b>AET-1.3</b> . . . . .	160
6.7	$^5D_0$ lifetime of <b>AET</b> samples serie. . . . .	160
6.8	Integrated intensity for the <b>AET</b> samples . . . . .	162
6.9	Temperature dependence of the emission spectra of <b>AET</b> samples. . . . .	163
6.10	Sensitivity of <b>AET</b> samples . . . . .	164
7.1	Morphological Characterization of <b>PET-1.3</b> and <b>AET-1.4a</b> . . . . .	170
7.2	Optical microscopy images of <b>AET-1.4a</b> . . . . .	171
7.3	Emission spectra of <b>PET-1.3</b> . . . . .	172
7.4	Emission spectra of <b>AET-1.4a</b> . . . . .	173
7.5	Partial energy level diagram of the <b>AET-1.4a</b> system . . . . .	175
7.6	Normalized $\Delta$ and sensitivity of <b>PET-1.3</b> and <b>AET-1.4a</b> . . . . .	176
7.7	Excitation of <b>AET-1.4a</b> sample and the correspondent complex. . . . .	176
7.8	Excitation of <b>PET</b> samples . . . . .	177
7.9	Room-temperature emission spectra of btfa/bpeta samples . . . . .	177
7.10	$^5D_0$ and $^5D_4$ decay curves for <b>PET-1.3</b> and <b>AET-1.4a</b> . . . . .	178

---

7.11 Lifetime of <b>PET-1.3</b> and <b>AET-1.4a</b> . . . . .	180
7.12 Temperature measurement in aqueous suspensions of NPs. . . . .	181
7.13 Calibration curves for <b>PET-1.3</b> and <b>AET-1.4a</b> . . . . .	182
8.1 New results on thermometric materials. . . . .	191

# List of Tables

1.1	High-resolution thermal measurement techniques . . . . .	13
2.1	Figure of merit of luminescent molecular thermometers . . . . .	59
2.2	Non-luminescent thermometers . . . . .	82
4.1	Sizes of Si-NPs in ethanol Suspension . . . . .	111
4.2	Photoluminescence of Si-NPs Gaussian Fits . . . . .	116
4.3	Room-Temperature Si-NPs Lifetimes . . . . .	120
5.1	Summary of <b>UET-1.3</b> thermometric properties . . . . .	137
5.2	Comparison of the results obtained with different optical fibres. . . . .	151
6.1	Summary emission quantum yield values of <b>AET</b> samples. . . . .	156
6.2	Absolute QY of <b>AET</b> samples . . . . .	164
7.1	Elemental analysis of <b>PET-1.3</b> and <b>AET-1.4a</b> . . . . .	171
7.2	Absolute QY of <b>PET-1.3</b> and <b>AET-1.4a</b> . . . . .	179



# Chapter 1

## Introduction

This thesis reports the work developed in the period 2007-2011 in the general subject of accurate temperature measurement at spatial scales below the millimeter range, using optical methods. The problem studied is the use of rare-earth ions to perform temperature measurements at the sub-micrometric scales. The temperature measurement at the nanoscale was recently reviewed [30] and is a challenging and very active topic, with new developments been published regularly.

The use of luminescent probes is common for temperature determination since its photo-physical properties (*e.g.* emission and excitation spectra, emission quantum yield, emission lifetime) are temperature dependent, however the combination of two trivalent lanthanide ions allow ratiometric or self-referencing thermometry with possibility of adjust the temperature range of operation and the sensitivity of the thermometer. The results can be rationalized assuming an energy scheme that involves the excited level of the trivalent lanthanides and the triplet state of the host matrix.

The initial results on this research, published in 2002 [41], demonstrated the temperature dependence of the trivalent lanthanide ions, under UV excitation. A set of experiments were organized in order to validate and interpret these results, using photoluminescence characterization (*e.g.* emission, and excitation spectra, decay curves, among others) and new synthesis to incorporate the lanthanide ions in different host matrixes. The results are transposable to different host matrixes and ligands, allowing the design of luminescent thermometers working in the physiological temperature range (290-330 K). The thermometers were demonstrated be able to map the temperature in electric circuits and fluids with temperature uncertainty of below 0.5 K. The thermometer applications can range from

micro-electronics to biological tissues or catalysis.

The spatial resolution of the temperature determination is higher than the commercial infrared cameras, allowing the temperature discrimination above the absolute uncertainty in a spatial range as low as  $2\mu\text{m}$ .

In the next section are presented the objectives, the motivation and the thesis organization.

## 1.1 Objectives, Motivation and Thesis Organization

Non-invasive precise thermometers working with high spatial resolution down to the nanoscale, where the conventional methods are ineffective, have emerged over the 2010-2012 period as a very active field of research. This has been strongly stimulated by the numerous challenging requests arising from nanotechnology and biomedicine.

The work reported in this thesis focuses on temperature measurement at the sub-micrometric scale, combining magnetic and luminescent features. The concept developed here is the production and characterization of nano-scaled objects that can combine temperature monitoring with other functions, that can play an important role in particular applications (*e.g.* magnetic core). The central objective is to demonstrate that the emission properties of trivalent lanthanide ions can be used for temperature measurement in spatial scales not reached before without compromising the sensitivity. Self-referencing in the temperature determination is advantageous since this property makes the temperature determination insensitive to material inhomogeneities, eventual fluctuation of the excitation or photobleaching. The motivation for this work was a former article published in 2002 [41] that anticipate that organic-inorganic hybrids co-doped with  $\text{Eu}^{3+}$ ,  $\text{Tb}^{3+}$  and  $\text{Tm}^{3+}$  present color and emission properties that can be finely tuned and, most important for this work, are temperature dependent.

This thesis is organized in five main blocks. The first block is formed by the introduction and the chapter 2, where the general frame of the temperature measurement at sub-micrometric scale is given. To set a common basis for the comparison of the enormous variety of thermometers, a definition of sensitivity, limit of detection, spatial resolution are presented. In this section recent examples of luminescent and non-luminescent thermometers working at nanometric scale are reviewed.

The materials and methods chapter presents the experimental methods used to pro-

duce and characterize the materials. The sol-gel process is described since it is the basis of all synthesis performed. The preparation of silica nanoparticles and their doping with lanthanide complexes are presented. Also the synthesis of ureasil films is described. Additionally the experimental techniques used to characterize the luminescent thermometers are detailed, in particular the spectroscopic measurements that allow to perform a photo-physical characterization of the samples.

The third block consists on the chapter 4 and deals with the description of undoped silica nanoparticles with potential applications in bioimaging. This chapter is particularly important because the NPs characterized here are the basis of the molecular thermometers detailed in the following chapters. The emission properties of the silica spheres are presented and discussed, stressing the emission properties independence of the annealing process, in contrast to other reports in the literature.

Chapters 5, 6 and 7 present three strategies to implement molecular thermometers. Chapter 5 presents a luminescent thermometer based on  $\text{Eu}^{3+}$ ,  $\text{Tb}^{3+}$  co-doped ureasil film that can be deposited on the top of an integrated circuit. The temperature spatial scanning profiles obtained from the emission properties are compared with the temperature measurements performed by pyrometers and infra-red cameras. The spatial resolution limit was computed and compared with the state of the art reports on the same subject. Next the thermometer was processed as APTES/TEOS NPs and was characterized producing the sensitivity curve and the temperature range of operation. In the sixth chapter the investigation of the usability of modified co-doped silica NPs as molecular thermometer for liquid mediums is presented. The sensitivity and the calibration curve of nanoparticles in suspension is compared with the same results for the solid samples. The final chapter presents the conclusions and the future work perspectives.

## 1.2 Evolution of Thermometry Towards the Nanoscale

The temperature determination is central for many industrial and biological applications. In fact the world's temperature sensor market earned revenues amounting more than 3 thousand million dollars in 2009 and estimates reach above 5 thousand million dollars in 2015, representing more than 80% of all sensor market nowadays [49]. The accurate temperature determination found many technological solutions since the first thermoscope developed by Gabriel Fahrenheit in the beginning of XVIII century (figure 1.1), nevertheless

the basic concept did not evolve significantly: the temperature is determined indirectly by monitoring a physical property (the thermometric property) that demonstrate to be temperature dependent.

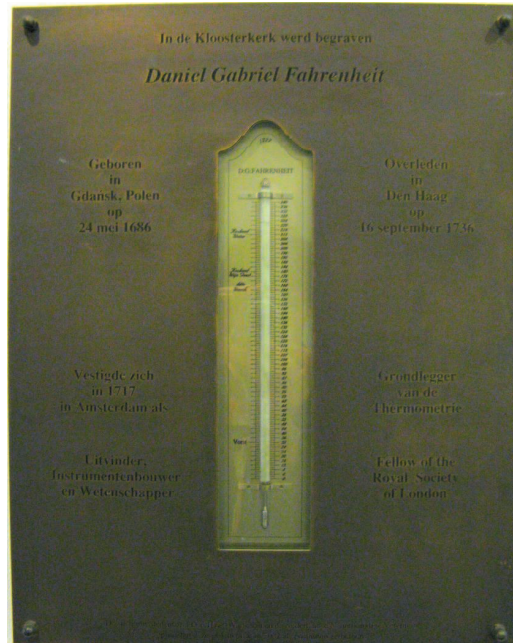


Figure 1.1: Memorial plaque at Fahrenheit’s burial site in *The Hague*, presenting a thermometer in the original temperature scale proposed by the scientist. In the Fahrenheit’s temperature scale, the  $0^{\circ}F$  is ”achieved at the equilibrium temperature of a mixture of ice, water, and ammonium chloride”. To calibrate the device, two additional points were used: ”still water when ice was just forming on the surface” ( $32^{\circ}F$ ) and when the instrument was ”placed under the arm or in the mouth” ( $96^{\circ}F$ ). Fahrenheit was the first scientist to use a scale to quantify the temperature.

The combined effects of thermal information at smaller spatial scales and the unprecedented possibilities opened by nanomaterials and nanotechnologies are paving the development of thermometry in sub-micron scale with high spatial resolution. Indeed, current technological demands in areas such as microelectronics, micro-optics, photonics, microfluidics, and nanomedicine have reached a point that the use of conventional thermometry is not able to make measurements when spatial resolution decreases to the sub-micron scale, as, for example, in intracellular temperature fluctuations [45, 81, 104, 179, 225, 244, 270, 285] and temperature mapping of microcircuits [3, 114, 126, 150, 230] and microfluids [80, 160, 203].

For instance, solid-state thermometers based on the temperature dependence of the

electrical resistance must have a highly accurate and precise design as effects like shot noise and tunnel junctions can be very significant at the nanoscale [218]. Also, the thermometric property must remain stable over time and operating conditions to avoid frequent calibrations. Small changes in synthetic conditions can induce major changes in the thermometric property, thus affecting the reproducibility. Moreover, at the nanoscale many physical properties change, while other new ones arise. Heat transfer and related thermodynamic phenomena, for instance, are drastically altered and materials behave differently than at larger scales. Sensing temperature in an accurate way with sub-micron resolution is therefore critical in order to understand the numerous features of micro and nanoscale electronic and photonic devices, such as thermal transport, heat dissipation, and profiles of heat transfer and thermal reactions [135, 158, 197].

Miniaturization of electronic and optoelectronic devices and circuits and ever faster switching speeds have increased the importance of localized heating problems and, thus, steady-state and transient characterization of temperature distributions is central for performance and reliability analysis [8, 52]. Furthermore, the precise mapping of the temperature of living cells, especially cancer cells that have higher temperature than those of normal tissues due to the increased metabolic activity [81, 179], strongly improves the perception of their pathology and physiology and, in turn, the optimization of premature diagnosis and therapeutic processes (*e.g.* in hyperthermal tumor treatment and photodynamic therapy)[161, 179, 270]. Moreover, the temperature of living cells is modified during every cellular activity, (*e.g.* cell division, gene expression, enzyme reaction and changes in metabolic activity, etc.[285]), thus leading to acute variation of intracellular temperatures from the normal state [244]. There is a high demand for the development of devices capable of accurate temperature determination for such processes as well as to investigate heat production and dissipation arising from most of them [179, 244].

Thermometry at the nanoscale requires, therefore, a new paradigm in the use of both materials and thermometric properties. Moreover, new synthetic techniques are helping to reduce materials limitation for sensing temperature at the nanoscale by either improving qualitatively inherent materials properties, *e.g.*, size dispersion, surface roughness, or by opening entirely new possibilities based on new materials with new properties.

The most popular approaches to nanothermometers have been the miniaturization of the geometrical size of conventional thermometers, although more radical alternatives have been proposed, as, for instance, ex-situ thermometers based on the irreversible temperature-

activated coalescence of silver NPs [132]. Examples of such miniaturization encompass:

- Luminescent thermometers based on temperature-dependent emission intensity and/or lifetime of dye-sensitized polymer dots (Pdots) [254, 272], semiconducting QDs,[270], [102, 139, 157, 162, 272, 242] and  $\text{Ln}^{3+}$ -doped NPs [24, 69, 184, 185, 238];
- Nanoscale infrared (IR) thermometers from metal NPs based on blackbody radiation[42];
- Scanning thermal microscopes based on  $\text{Ln}^{3+}$ -doped NPs [1, 2, 3, 200];
- Nanoscale thermocouples fabricated from point contact junctions [54, 197, 211];
- Liquid- and solid-in-tube nanothermometers fabricated from nanotubes and based on temperature-dependent thermal expansion of liquids (*e.g.* Gallium inside CNTs [75, 75, 73] or Pb-filled ZnO nanotubes [246]);
- Coulomb blockade nanothermometers from nanosized superconductor-insulator-metal tunnel junctions based on the Coulomb blockade of tunneling [209, 233];
- Complex structured nanothermometers from MEMS based on temperature-dependent resonator quality factor[100] or Fermi-level shift [183].

Thermometric systems can be classified as primary or secondary (figure 1.2). The first are characterized by well-established state equations that directly relates measured values to absolute temperature without the need of calibration, while the second must be referred to a well-known temperature for their calibration. Secondary thermometers are sometimes difficult to calibrate at the nanoscale and can only act as sensors, providing temperature changes. Finally, there is a type of temperature sensing actuators (like some paraffins) that only react at a well-defined threshold temperature at which a specific change occurs. Although they can be accurate, these can only be considered as one-temperature thermometers. Therefore, not all the conditions expected for an ideal nanothermometer, namely, stability, accuracy and reproducibility [245], are fulfilled by the systems described in this section and in the next chapter, independent to their validity as temperature sensors and actuators in the nanoscale.

As the size of systems where temperature has to be determined enters into the nanoscale, the question of whether temperature itself can be meaningful at such scale can become

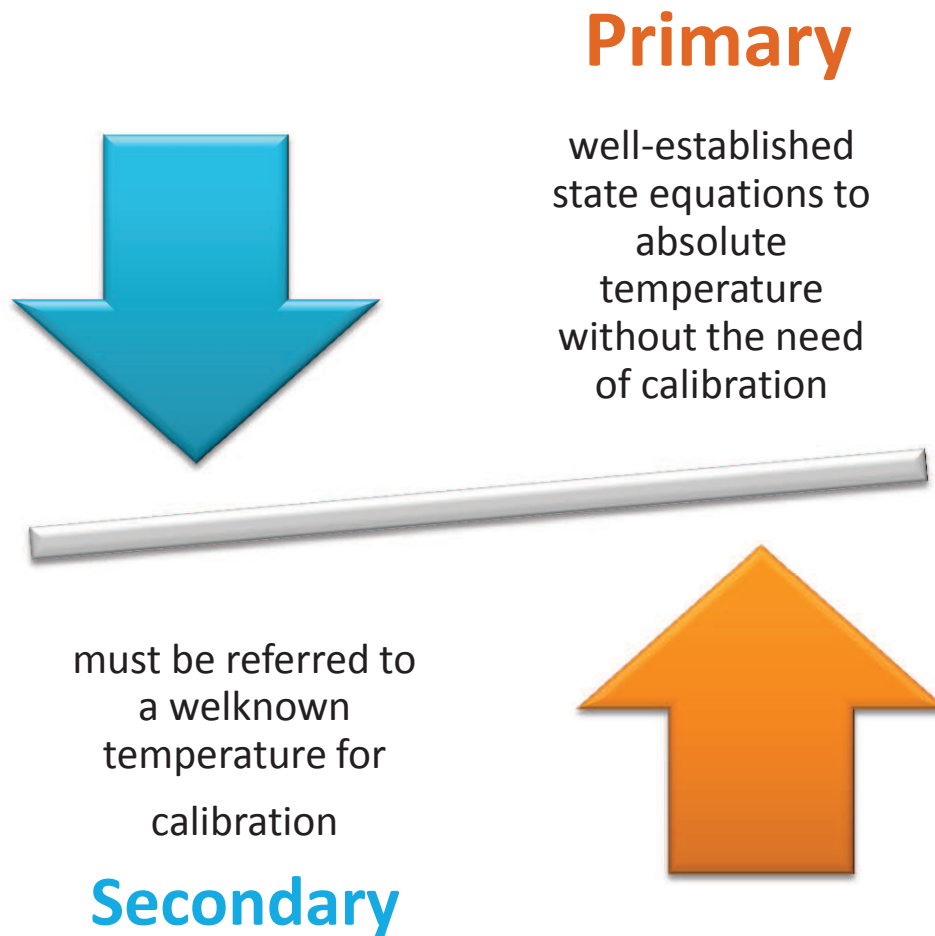


Figure 1.2: Primary thermometric systems have well-established state equations that directly relates measured values to absolute temperature (without the need of calibration), whereas the second must be referred to a well-known temperature for their calibration. The temperature sensing actuators are not classified as thermometric systems.

relevant. The minimal length scales for the existence of temperature have been carefully discussed by Hartmann *et al.* [94, 93].

High-resolution thermometry techniques have been catalogued in many different manners, as, for instance, depending on whether they make use of electrical or optical signals or based on near- or far-field applications. With this very general outline, it is common that the same technique is classified in different ways, for instance scanning thermal microscopy (SThM) can be either categorized as electrical or near-field thermometric method [8, 52]. However, independently of the classification, what really matters is a precise iden-

tification of the advantages and drawbacks of each method, as well as a proper selection accordingly to the required spatial, temporal and temperature resolution. A summary of popular methods for high-resolution thermal measurements, highlighting its advantages and disadvantages is presented in table 1.1.

Another common classification uses the physical contact between the sample and the probe. In the so called contact thermometers, there is an invasive probe material physically connected to the sample where the temperature is measured. The heat transfer to the probe allows to estimate the temperature of the probe using the pre-calibrated thermometric property temperature dependence. This is the method used for all liquid filled systems, such as alcohol and mercury thermometers, using the thermal expansion coefficient. The same property is used on the bimetallic thermometers used widely on industry to measure temperature in furnaces and other high temperature environments. All above examples are obviously not even micrometric scale thermometers. The spatial scale of the micrometer is not reached by the smallest of the contact thermometer, an electrical thermometers, sing as thermometric property the electrical resistance. High integration and easy of fabrication are strong points that explain the proliferation of such kind of probes in small scaled system such as electronic devices. The physical dimensions of electrical thermometers can begin in a few millimeters, excluding the control circuit.

Obvious drawbacks of the contact thermometry results of the nature of the measurement. As the thermal probe is, at best, millimeter sized, the temperature measurement is limited to the probe dimension. The temperature mapping of a sample, the temperature determination in moving objects are examples where it is unpractical with this thermometers: the heat transfer to a probe that is bigger that the sample to sense makes the contact methods inappropriate to measure temperature in scales bellow 1 mm. In this seriation, in order to determine the temperature in spatial scales bellow 1 mm non-contact thermometers should be used (figure 1.2).

Non-contact thermometry includes all the temperature probes that do not establish physical contact with the sample, or the methods for which the access to the probe is made without contact between the probe and the reading system. In fact, the limitations of contact thermometers to work at sub-micron scale referred in table 1.1 lead to the development of non-contact thermometry techniques, such as, IR thermography, thermoreflectance, optical interferometry, Raman spectroscopy, and luminescence. IR thermography is a concept that found numerous industrial applications in several variants of pyrometers



Figure 1.3: Temperature determination methods can be catalogued contact and noncontact methods or in far-field (optical) or near-field (electrical) methods.

or IR cameras. It infers the temperature distribution of a body according to the blackbody radiation spectral distribution of the emitted radiation and knowing the external surface emissivity of the material. Near-field methods opened a possible increase of the spatial resolution by two orders of magnitude [79] and in practice resolutions of about 10 nm can be achieved [79, 70, 231].

Thermoreflectance and optical interferometry use the reflected light that provides information about the local heating state of the device or structure. Thermoreflectance explores the temperature dependence of the reflection coefficient of a material (its refractive index is temperature dependent), resulting in a temperature profile by analysis of the image

produced by reflection with a spatial resolution limited by the optical imaging system [230].

Developments in the period 2000-2010 allowed also micrometer/sub-micrometer spatial resolution (Table 1.1), see, for instance, the reviews by Cahill *et al.*, [34] Christofferson and Shakouri [53] and Christofferson *et al.* [52]. Optical interferometry (in both active and passive modes) provides not only local temperature probing but also accurate measurements of the thermal expansion or deformation of a surface, with spatial and temperature resolutions in passive mode of about 100 nm and 100 nK, respectively [9] (table 1.1). Raman spectroscopy (as well as scanning microscopy) presents a reading velocity and processing that is limited (at least) by the probe movement and by the properties of the material and of the surface. This technique is well suited for large temperature changes, due to the low sensibility, and in spatial terms limited to the laser spot size ( $\sim 0.5\mu m$ ).

Table 1.1: Summary of the advantages, disadvantages and general applications of high-resolution electrical, near- and far-field thermal techniques. The typical spatial ( $\delta x$  ( $\mu m$ )), temporal ( $\delta t$  ( $\mu s$ )) and temperature ( $\delta T$  ( $K$ )) resolutions of each method are also included. The table is adapted from those published by Asheghi and Yang [9] and Christofferson *et al.* [53]

HIGH-RESOLUTION THERMAL MEASUREMENT TECHNIQUES IN MICROMETER-NANOMETER RANGE						
Method	Principle	Typical Resolution			Advantages/Disadvantages	
		$\delta x$ ( $\mu m$ )	$\delta T$ (K)	$\delta t$ ( $\mu s$ )		
Infrared Thermography	Plank blackbody Emission	10	$10^{-1}$	10	<ul style="list-style-type: none"> <li>Well implemented commercial technique</li> <li>Provides temperature image profile of the surface</li> </ul>	<ul style="list-style-type: none"> <li>Detector saturation at high temperatures</li> <li>Difficulties on the precise estimation of the emissivity of the surface materials</li> <li>Spatial resolution for the temperature detection, which is Rayleigh limited (not all "hot bodies" are perfect blackbodies, in the physical meaning of the term)</li> </ul>
Thermoreflectance	Temperature dependence of the reflection	$10^{-1}$	$10^{-2}$	$10^{-1}$	<ul style="list-style-type: none"> <li>High thermal and temporal resolution</li> <li>Quantitative and qualitative measurement.</li> </ul>	<ul style="list-style-type: none"> <li>Requires the calibration of the reflectivity index</li> <li>Spatial resolution limited by the diffraction limit</li> <li>Thermoreflectance coefficient is not available for every material and depends on excitation wavelength and thickness of the optical layer</li> </ul>
Raman	Inelastic scattering of monochromatic light	1	$10^{-1}$	$10^6$	<ul style="list-style-type: none"> <li>No sample preparation needed</li> <li>Works in solids and liquids</li> <li>Small areas (<math>&lt; 1 \mu m</math> diameter) can be probed</li> </ul>	<ul style="list-style-type: none"> <li>Highly time-consuming technique implying image point analysis as slow as <math>0.5 \text{ point} \cdot \text{s}^{-1}</math></li> <li>Low signal and crosstalk with fluorescent molecules</li> </ul>
Micro-thermocouple	Seebeck effect	$10^2$	$10^{-1}$	10	<ul style="list-style-type: none"> <li>Precise temperature calibration</li> <li>Spatial resolution (at one dimension) of 25 nm</li> </ul>	<ul style="list-style-type: none"> <li>The thermometer is separated from the active region of the device limiting, at very short timescales, the access to it</li> <li>Voltage reflections and capacitive coupling limit the timescale for transient thermometry of the device</li> </ul>
Fluorescence Thermography	Temperature dependence of quantum efficiency/ lifetime/intensity	$10^{-1}$	$10^{-2}$	10	<ul style="list-style-type: none"> <li>Diverse experimental techniques to measure temperature</li> <li>High temperature sensitivity</li> <li>Ratiometric algorithms are independent of illumination source</li> </ul>	<ul style="list-style-type: none"> <li>Photobleaching limits the long-term intensity and lifetime determination</li> <li>High-expensive excitation sources and detectors to measure temperature using lifetime-based algorithms</li> </ul>

HIGH-RESOLUTION THERMAL MEASUREMENT TECHNIQUES IN MICROMETER-NANOMETER RANGE (CONT.)						
Method	Principle	Typical Resolution			Advantages/ Disadvantages	
		$\delta x$ ( $\mu\text{m}$ )	$\delta T$ (K)	$\delta t$ ( $\mu\text{s}$ )		
Near-field Scanning Optical Microscopy	Use near field to improve optical resolution	$10^{-2}$	$10^{-1}$	10	<ul style="list-style-type: none"> <li>Spatial resolution below the Rayleigh limit (100 nm)</li> </ul>	<ul style="list-style-type: none"> <li>Depends on the surface characteristics</li> <li>Only access to surface temperature</li> <li>Slow temperature acquisition</li> <li>Vacuum and/or cryogenic temperatures required</li> </ul>
Liquid Crystal Thermography	Crystal phase transitions (change colour)	10	$10^{-1}$	$10^2$	<ul style="list-style-type: none"> <li>Diverse materials available commercially for different temperature ranges</li> <li>Fully integrated with electronic devices</li> </ul>	<ul style="list-style-type: none"> <li>Yields a semi-quantitative temperature map, unless a detailed calibration is performed</li> <li>A layer of the probe must be placed over the sample</li> <li>Not compatible with liquid systems</li> </ul>
Scanning thermal microscopy	AFM with thermocouple or Pt thermistor tip	$10^{-1}$	$10^{-1}$	$10^2$	<ul style="list-style-type: none"> <li>Uses AFM tips to simultaneously measure temperature and determine the surface roughness</li> <li>Sub-micrometric spatial resolution</li> </ul>	<ul style="list-style-type: none"> <li>Slow acquisition times</li> <li>Limited to solid samples</li> <li>Requires fundamental knowledge of tip-sample heat transfer</li> </ul>
Transmission Electron Microscopy	Thermal Expansion	$10^{-2}$	$10^{-1}$	$10^1$	<ul style="list-style-type: none"> <li>High spatial resolution</li> <li>Compatible with different CNTs</li> </ul>	<ul style="list-style-type: none"> <li>Vacuum required</li> <li>Difficult to transpose for practical applications</li> <li>Temperature determination by image analysis</li> </ul>
Optical Interferometry	Thermal expansion or refractive index change	$10^{-1}$	$10^{-4}$	$10^{-1}$	<ul style="list-style-type: none"> <li>Can be integrated in remote detection systems</li> <li>All optical temperature determination</li> </ul>	<ul style="list-style-type: none"> <li>Crossalk with other stimulus as strain/stress and bending</li> <li>Low spatial resolution in the transverse direction</li> </ul>

In the chapter 2 the latest progress of sub-micron high-resolution thermometry (both luminescent and non-luminescent) are reviewed. Luminescent thermometers encompass organic dyes, quantum dots (QDs) and trivalent lanthanide ( $\text{Ln}^{3+}$ ) ions as thermal probes, as well as more complex thermometric systems formed by polymer and organic-inorganic hybrid matrices encapsulating these emitting centers. Emphasis has been put on to ratio-metric examples reporting spatial resolution lower than  $1 \mu\text{m}$ , as, for instance, intracel-lular thermometers based on organic dyes, thermoresponsive polymers, mesoporous silica nanoparticles (NPs), QDs, and  $\text{Ln}^{3+}$ -based up-converting NPs and  $\beta$ -diketonate complexes. To clarify the nomenclature, the next section 1.2.1 will introduce the central concepts for this discussion, such as sensitivity, temperature range of operation, limit of detection and spatial resolution. It follows a general overview on the spectroscopic properties of the lanthanide ions.

### 1.2.1 Characterization of Thermometers

The temperature is a thermodynamical variable that can be determined using any thermometric parameter that responds to temperature variations. To make this discussing general, a generic thermometric parameter  $Q$  is assumed to be temperature dependent. This assumption can be translated by equation 1.1.

$$Q = Q(T) \tag{1.1}$$

The quality of a thermometer can be quantified using its absolute sensitivity, or the absolute change in the thermometric parameter  $Q$  with the temperature. The absolute sensitivity ( $S_a$ ) is defined using the variation of the  $Q$  parameter in respect to the absolute temperature, according equation 1.2.

$$S_a = \frac{\partial Q}{\partial T} \tag{1.2}$$

However the absolute sensitivity is not the most accurate parameter to characterize a thermometer. To make this point clear let us take a numerical example. Let us assume that a thermometer  $A$  presents, at a given temperature  $T$ , a value of the thermometric parameter  $Q_A = 1000 \text{ units}$  and a absolute sensitivity of  $S_a^A = 1 \text{ unit/degree}$ . The physical meaning of this value is the following: when the temperature increases by one unit (from

$T$  to  $T + 1$ ) the thermometric parameter varies of one unit (from 1000 to 1001). Another thermometer  $B$  that presents the same value of absolute sensitivity  $S_a^B = 1$  changes the thermometric parameter of one unit but from  $Q_B = 100$  to 101 *unit*. Using only the absolute sensitivity, both thermometers are similar, nevertheless the thermometer  $B$  presents a relative variation that is 10 times bigger than thermometer  $A$ . This means that the experimental requirement to measure temperature using the thermometer  $B$  is to measure a variation on the thermometric parameter of 1% while for the thermometer  $A$  is 0.1%. In conclusion, the thermometer  $B$  is the most sensitive of the thermometers, demanding a less sensitive detector to measure the same temperature change. This illustrative example makes clear that the accurate parameter to compare different thermometers should take in account not the absolute but the relative variation on the thermometric property  $Q$ . This is accomplished using the relative sensitivity defined in equation 1.3.

$$S_r = \frac{\frac{\partial Q}{\partial T}}{Q} = \frac{\partial \ln(Q)}{\partial T} \quad (1.3)$$

In order to compare the performance of different thermometers, its relative sensitivity was used as a figure of merit. The  $Q$  values were calculated fitting the experimental data graphically reported in literature to polynomial interpolations implemented with MatLab®. A cut-off on the relative sensitivity values is assumed when the absolute temperature resolution  $\delta T$  is below 1 K. This is estimated by  $\delta Q/S_a$ , where  $\delta Q$  is the resolution of  $Q$ , calculated from the standard deviation of the interpolation, and  $S_a$  is the absolute sensitivity.

To make the comparison between references more expedite, the  $S_m$  and  $T_m$  values were computed, representing the maximum value of the relative sensitivity and the temperature at which that value occurs, respectively. In all the examples addressed in the next section the dependence on temperature of the relative sensitivity was computed from published data using equation 1.3.

Using only the value of sensitivity a thermometric system is not fully characterized. In practical terms is often more useful the information about the minimum temperature change that can be detected by a thermometer. This value is called the limit of detection (*LOD*) and is telling about the practical use of a certain thermometer for an application. The *LOD* for a thermometer is dependent on the thermometric system used and on the algorithm used to translate that change into a temperature. Let us return to the numerical

example presented above. If an ideal thermometer presents a value of  $S_r^A = 0.1\% \cdot K^{-1}$  and the detector used only can detect changes of 0.5%. This means that this thermometric system (thermometric material + detector) can detect temperatures higher than 5 K, or in terms of limit of detection, the  $LOD$  is 5K. The numerical estimate for the  $LOD$  is defined using the relative resolution of the detector ( $R_D$ , in percent of the absolute value) and the relative sensitivity ( $S_r$ ) (equation 1.4).

$$LOD = \frac{R_D}{S_r} \quad (1.4)$$

Other information on the thermometers that can be useful is the temperature range of operation. The temperature range of operation ( $\Delta T$ ) defines the temperatures where the relative sensitivity is above a certain criteria. In all the references presented the criterium used is the  $S_r > 0.5\% \cdot K^{-1}$ . The value of  $0.5\% \cdot K^{-1}$  is a reasonable value for common optical detectors, meaning that the sensing system can detect a change of 1/200. For commercial detectors (*e.g.* USB400 from Ocean Optics) the value is ranges from 0.05-0.010% at the wavelength range of the detector.

The concept of spatial resolution gives information on the minimum spatial scale that can be scanned using a certain thermometric setup. It is defined as the minimum distance between two adjacent points that can be detected by a remote sensing system with temperature difference equal to the uncertainty. This quantity is estimated in a temperature profile (the representation of the temperature dependence in unidimensional mapping), using equation 1.5, where  $\delta x$  is the spatial resolution,  $\delta T$  is the temperature uncertainty and  $\partial T/\partial x$  is the slope of the temperature profile.

$$\delta x = \frac{\delta T}{\partial T/\partial x} \quad (1.5)$$

With the concepts defined, it is opportune to review the most relevant contributions on luminescent thermometers that frames the development of the work reported here.

## 1.3 Trivalent Lanthanide Ions for Thermometry

As mentioned before, this thesis intends to demonstrate the use of spectroscopic properties of lanthanide ions as temperature probes. It is central to this discussion to understand the concepts used in the interpretation of the emission properties and the physical background of the observations. With the objective of constitute a general introduction to luminescence, this section presents the fundamentals to interpret the emission and excitation properties of a material and focuses on the particular properties of the trivalent lanthanide ions. Complete and updated reviews can be consulted in the references [37, 122, 220].

### 1.3.1 General Background on Luminescence

Luminescence is a general term which describes any non-thermal processes in which energy is emitted from a material at a different wavelength from that at which it is absorbed. The term broadly includes the commonly-used categories of fluorescence and phosphorescence. Fluorescence occurs where emission ceases almost immediately after withdrawal of the exciting source, whereas in phosphorescence the emission persists for some time after removal of that excitation. The distinction between the so-called types of luminescence is somewhat arbitrary and confusing. Confusion is avoided by using the term luminescence, and specifying the activating energy as a prefix (*e.g.* bioluminescence, cathodoluminescence, photoluminescence, etc.) Photoluminescence requires the absorption of photons with energy  $E = h\nu$  (where  $h$  is the Planck constant and  $\nu$  is the frequency). The interaction mechanisms between the photon and the matter depend on the photon energy. In a simplified picture, when the photon energy of the incident radiation is lower than the energy difference between two electronic states, the photons are not really absorbed and the material is transparent to such radiation energy. For higher photon energy, absorption occurs and the valence electrons will make a transition between two electronic energy levels. The excess of energy will be dissipated through vibrational processes that occur throughout the near infrared (NIR) spectral region. Then, the excited atoms may return to the original level through radiative (with the spontaneous emission of a photon) and nonradiative transitions. Examples of radiative and nonradiative processes will be given considering the typical distribution of electronic levels in a molecule with two electrons.

In the fundamental levels the electrons in the same orbital have opposite spins ( $s_1 = +1/2$  and  $s_2 = -1/2$ ); so that the total spin ( $S = s_1 + s_2$ ) is equal to zero. Thus, the

fundamental state multiplicity ( $M = 2S + 1$ ) is one, and the ground state is designated as singlet (denoted by  $S_0$ ). After optical absorption, the electrons will be excited. If this transition does not involve spin inversion, the excited state is also a singlet ( $S_1$ ), *i.e.* it has the same state multiplicity as the ground level. However, if there is spin inversion, the two electrons have the same spin,  $S = 1$  and  $2S + 1 = 3$ , and the excited state is called a triplet ( $T_1$ ). It should be noted that such absorption involving a triplet state is forbidden by the spin selection rule: allowed transitions must involve the promotion of electrons without a change in their spin ( $\Delta S = 0$ ). The relaxation of the spin selection rule can occur though strong spin-orbit coupling, which is for instance the case of rare earth ions. The figure 1.4 summarizes the typical radiative and nonradiative transitions within a molecule.

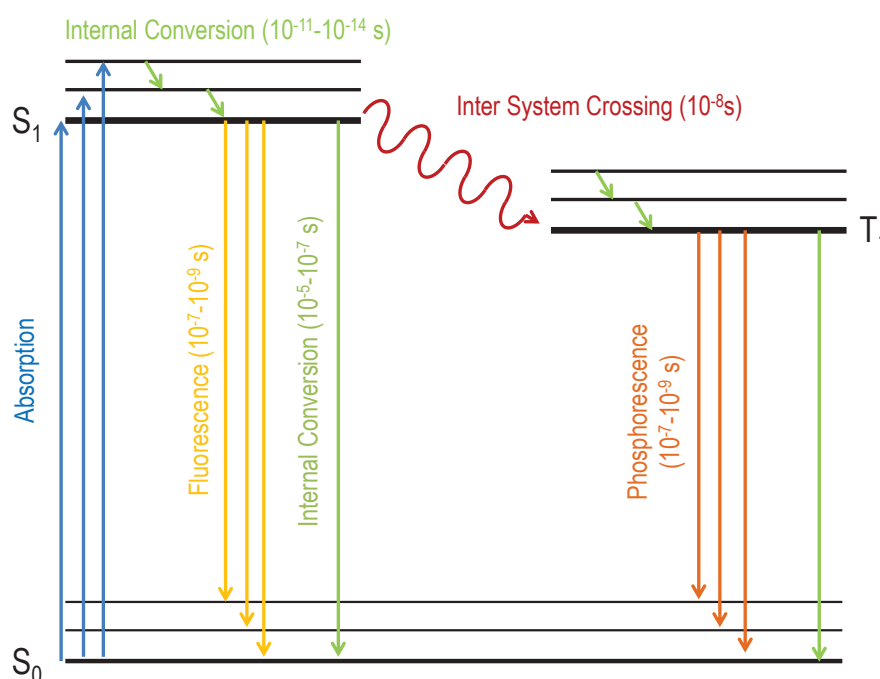


Figure 1.4: Typical radiative and non-radiative transitions within a molecule.

The nonradiative processes can be:

- Internal conversion; an electron close to a ground state vibrational energy level, relaxes to the ground state via transitions between vibrational energy levels giving off the excess energy to other molecules as heat (vibrational energy);
- Intersystem crossing; the electron transition in an upper  $S_1$  excited state to a lower

energy level, such as  $T_1$ .

And the radiative processes can be:

- Fluorescence, *i.e.* emission of a photon from  $S_1$  to the vibrational states of  $S_0$  occurring in a time scale of  $10^{-10}$  to  $10^{-7}$  s;
- Phosphorescence, *i.e.* emission of a photon from  $T_1$  to the vibrational states of  $S_0$ . This process is much slower than fluorescence (higher than  $10^{-5}$  s) because it involves two states of different multiplicity. For very long luminescence time decays (seconds, minutes, even hours), the emission is called glow in the dark. Phosphorescence is red-shifted relatively to fluorescence, because  $T_1$  is excited via inter-system crossing.

Due to the non-radiative transitions the emission will occur at lower energy (longer wavelengths) than that of the absorbed photons. The energetic difference between the maximum of the emission and absorption spectra ascribed to the same electronic transition is known as Stokes shift. If radiative emission occurs, it is very useful to acquire an excitation spectrum. Such measurement can be done by monitoring a certain emission wavelength, under illumination of the material by light of different wavelengths. The resulting spectrum gives us the information of the excitation wavelengths that effectively contribute to the monitored emission. This measurement should not be confused with absorption spectra, although similar results may occur. An absorption spectrum gives information about the spectral range absorbed by the sample, independently of the occurrence (or not) of radiative transitions. An excitation spectrum is a selective measurement that selects the part of the absorption spectrum which contributes to the observation of the monitored emission. Moreover, due to the nonradiative transitions mentioned above, it might be observed a red-shift of the absorption spectrum with respect to the wavelengths of the excitation spectra.

The process of absorbing and emitting light can be understood using a simple rational model of a molecule that can exist in the ground state ( $M$ ) and in excited state ( $M^*$ ). The transition from the ground state to the excited state is promoted by the absorption of a photon of energy  $h\nu_1$  according equation 1.6. The subsequent emission of a photon of frequency  $\nu_2 < \nu_1$  can be assigned to a fluorescent or phosphorescent transition.



In simple experimental terms the fluorescence and the phosphorescence processes can not be distinguished in an emission spectra unless time resolved spectroscopy is used. In steady state acquisition mode the number of photons collected generates the intensity signal usually in counts. Further detail on the time rates of the energy transfer can be predicted using a more complete energy scheme, as that depicted in figure 1.4.

To quantify the efficiency of a luminescent material to convert the excitation energy in emitted photons the emission quantum yield (QY), defined as the ratio between the emitted and absorbed photons is used. In fact the incident photons are not converted in emitted light due backscattering of exciting radiation, conversion of incident energy in other form in the vibrations of the crystal lattice (phonons) and the efficiency of the luminescent center itself. Experimental details on the determination of the emission quantum yield are presented in section 3.2.3.

In an attempt to rationalize the temperature dependence of the photophysical properties, the two-parabola model is widely used. The model uses two parabolas representing the ground state and the excited state, plotted using the configurational coordinate  $r$  (this quantity represents the distance between emitting molecule and its surrounding molecules), as is schematically represented in figure 1.5.

First the excitation is performed when a certain center absorbs the energy that corresponds exactly to the energy difference between the potential energy of the ground energy and the excited energy state that corresponds to a certain vibrational level. The excitation energy is not the same for all centers because the equilibrium distances are not equal for all emitting centers due to the different vibrational states distribution, resulting in a broadening of the absorption band. Once in this state the system will relax to the minimum energy of the excited state degradation energy in the form of heat. This transition results, in general, in a broad absorption transition due to the same phenomena. This broadening is lower when the distance  $\Delta r$  diminishes, (*e.g.* in lanthanide ions) resulting in a very narrow emission band.

When temperature rises, the distance  $\Delta r$  for the equilibrium increases resulting in a different position when the lowest energy of the excited state occupies the position schemed in figure 1.5.

Notice that, in the excited state, the deactivation to the lowest energy level will not happen because the interception of this curve with the energy of the ground state is now in a different position. As result the decay to the ground state is made *via* non-radiative

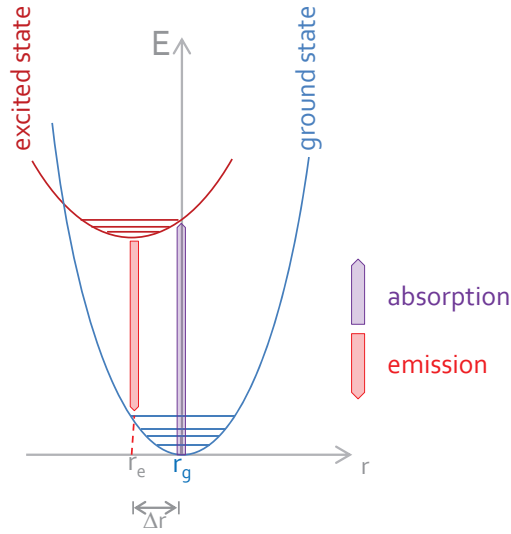


Figure 1.5: Two parabola model for energy absorption and emission from a luminescent center. Two parabolas representing the ground state and the excited state are plotted using the configurational coordinate  $r$ . When the temperature increases the electron occupies the high energy vibrational states until intercept the ground state parabola favoring the non-radiative decay to the ground state.

decay (phonon) and not *via* fluorescence (photon). The material dissipates the energy as heat and the fluorescence signal decreases when the temperature increases. The process is known as thermal quenching. This basic model neglects the existence of centers where nonradiative processes dominate, also called, killer centers.

In fact, not only the emitting centers contribute for nonradiative losses. This is particularly evident for materials that have an excitation center that transfers energy to an emitting center using the lattice. In this case the lattice itself or other centers can act as killing centers activated by temperature. This more realistic model predicts a competition between killing and emitting centers that determines the dependence of the luminescence with temperature. This property can be used as a powerful optical tool to infer the energy levels of luminescent materials and its evolution with temperature.

Representative examples of materials that follow the two parabola model are rare earth ions materials since the offset between centers are very small, especially for  $4f^n$  levels.

The important quantity for the study of these materials is the matching between energy level difference and lattice phonons. If there is a matching between this energy and a certain number of lattice phonons the probability of occur a radiative decay diminishes. If this

energy matching is achieved with a higher number of phonons the thermal quenching is expectable at higher temperatures and the fluorophore presents efficient luminescence.

### 1.3.2 Trivalent europium/terbium ions luminescent properties

The trivalent ions of the lanthanide series ( $\text{Ln}^{3+}$ ) are characterized by a gradual filling of the 4f orbitals, from  $4f^0$  (for  $\text{La}^{3+}$ ) to  $4f^{14}$  (for  $\text{Lu}^{3+}$ ). One of the most interesting features of these ions is their photoluminescence. Several lanthanide ions show luminescence in the visible or near-infrared spectral regions upon irradiation with ultraviolet radiation.

The color of the emitted light depends on the lanthanide ion. For instance,  $\text{Eu}^{3+}$  emits red light,  $\text{Tb}^{3+}$  green light,  $\text{Sm}^{3+}$  orange light, and  $\text{Tm}^{3+}$  blue light. Their emission is due to transitions inside the 4f shell, thus intraconfigurational f–f transitions. Because the partially filled 4f shell is well shielded from its environment by the closed  $5s^2$  and  $5p^6$  shells, the ligands in the first and second coordination sphere perturb the electronic configurations of the trivalent lanthanide ions only to a very limited extent.

This shielding is responsible for the specific properties of lanthanide luminescence, more particularly for the narrowband emission and for the long lifetimes of the excited states.

Although photoluminescence of lanthanide ions can be an efficient process, all  $\text{Ln}^{3+}$  suffer from weak light absorption. Because the molar absorption coefficients  $\epsilon$  of most of the transitions in the absorption spectra of the  $\text{Ln}^{3+}$  are smaller than  $10 \text{ Lmol}^{-1}\text{cm}^{-1}$ , only a very limited amount of radiation is absorbed by direct excitation in the 4f levels. Since the luminescence intensity is not only proportional to the luminescence quantum yield but also to the amount of light absorbed, weak light absorption results in weak luminescence. However, the problem of weak light absorption can be overcome by the so-called antenna effect (or sensitization). Weissman and Lipkin discovered that intense metal-centered luminescence can be observed for lanthanide complexes with organic ligands upon excitation in an absorption band of the organic ligand [257].

#### Lifetime and Intensity Algorithms

The temperature determination by optical means (essentially through luminescence) exploits several methods of examination of the sensitive material. Intensity-based methods are applied when the luminescence of the thermographic phosphors is photo-excited continuously and the resulting intensity is measured in a continuous way. On the other hand,

if the time dependence of the intensity of a particular transition (decay curve) is measured, the thermometric information temperature is inferred through the lifetime of the phosphor emitting level [220, 97]. First the lifetime determination fundamentals are revised.

To model the emission decay curves the general equation 1.6 is rewritten to focus on the process of de-excitation. It can be considered as spontaneous emission of light from an excited state of a material designated as  $M^*$  [194]:



Such emission is a random process, following the first order kinetics traduced in equation :

$$-\frac{d[M^*]}{dt} = k[M^*] \quad (1.8)$$

For a single process, the decay should be characterized by a single exponential curve (equation 1.9) that obeys to a single decay constant  $k$  (other kind of decays are not studied in this thesis). This rate can be expressed in terms of lifetime for the excited state, equal to the reciprocal of the first order decay rate(*ie.*  $\tau = \frac{1}{k}$ ).

$$I = I_0 e^{-kt} \quad (1.9)$$

The decay rate of such process includes the contribution of radiative ( $k_r$ ) and non-radiative ( $k_{nr}$ ) processes to the de-population of the excited state, according

$$k = k_r + k_{nr}$$

. The Mott-Seitz model assumes that only on the non-radiative decay rate ( $k_{nr}$ ) is temperature dependent and the radiative decay rate ( $k_r$ ) is constant with temperature:

$$\tau = \frac{1}{k_r + k_{nr}(T)} = \frac{1}{\tau_0^{-1} + C \exp\left(\frac{-\Delta E}{k_B T}\right)} \quad (1.10)$$

where  $\tau_0$  is the radiative lifetime (at zero absolute temperature) or radiative decay rate ( $k_r$ ),  $C$  is a pre-exponential factor,  $\Delta E$  is the energy gap between the emitting level and the higher excited state, and  $k_B$  is the Boltzmann constant.

Thus, for simple molecules, the excited state lifetime measurement gives useful infor-

---

mation about the energy scheme according the Mott-Seitz model, allowing an estimation of the energy gap between the emitting level and the higher excited state the  $\Delta E$ . For more complex systems the model is not valid anymore, nevertheless the lifetime generally decreases with temperature, allowing it use for temperature determination.

These lifetime-based methods for temperature determination present the critical advantage of virtually be unaffected by light scattering or reflection, by the intensity fluctuation of the excitation light field or inhomogeneous distribution of the phosphor. Lifetimes are measured in the time-domain or frequency-domain modes [220]. In time-domain fluorometry, a square-shaped light pulse excites the fluorophore and the luminescence rises and drops with a typical characteristic that is dependent on the luminescence decay time of the probe. In the frequency-domain approach the luminophore is excited by sinusoidally modulated light and the luminescence follows the excitation frequency with a lifetime-dependent delay. Two luminophore species are sometimes employed, as in the dual-lifetime referencing and dual-lifetime determination approaches. Whereas in the former method, one luminophore species references the lifetime of the other (both species must present similar photobleaching), in the latter one both lifetimes are determined (the lifetimes can be only separated if their ratio is greater than 10)[220].

Lifetime determination, however, may be, in certain conditions laborious and time-consuming, disadvantages that can be easily overcome by intensity-based methods. These algorithms use directly the intensity of one or more transitions to detect temperature. The intensity of each transition is proportional to the total number of atoms (population) in a given excited state at temperature  $T$ , according equation 7.1.

$$I \propto gAh\nu \exp\left(\frac{-E}{k_B T}\right) \quad (1.11)$$

where  $g$  is the degeneracy of the state,  $A$  is the spontaneous emission rate,  $\nu$  is the frequency, and  $E$  is the energy of the level. Frequently two transitions assigned to the same phosphor are used and the ratio between their fluorescent intensities ( $I_1$  and  $I_2$ ) named fluorescence intensity ratio, FIR (or two-color response), taken as a measurement of absolute temperature, since:

$$\frac{I_1}{I_2} = \frac{g_1 A_1 h \nu_1}{g_2 A_2 h \nu_2} \exp\left(\frac{-\Delta E_{12}}{k_B T}\right) \quad (1.12)$$

The main advantage of this FIR numerical technique is the fact that one single emission

---

spectrum contains all the information needed to compute the absolute temperature. The FIR ratio employs a Boltzmann distribution for electrons between adjacent emitting energy levels that is a function of temperature and is manifested as a temperature-dependent intensity ratio between emissions from two distinct lines in the spectrum.

Intensity measurements based on one transition depend crucially on variations of the sensor concentration, small material inhomogeneities (particularly in imaging non-planar surfaces, such as biological tissues) and optoelectronic drifts of the excitation source and detectors, making, thus, inappropriate for precise temperature sensing. Lifetime data and ratiometric (or self-referencing) FIR measurements, in contrast, are not compromised by those disadvantages and, thus, are much more reliable [31, 69, 102, 162, 185, 238, 254, 272]. Nevertheless, real-time temperature mapping through decay time measurements requires more sophisticated equipment, when compared to the faster, easier and cheaper ratiometric luminescence intensity readout. Moreover, for complicated distributions of emitting centers and/or strong interactions between them (for instance energy transfer) lifetime determination may be laborious and time-consuming, as it involves a fit procedure (that could be rather complicated) to the decay curves.

## Summary

This introductory chapter presents the objectives and motivations of this thesis. A general description of the concept of thermometry at the nanoscale is presented and cataloged using different criteria (the extensive review of the literature is presented in the following chapter 2). To make the discussion on the following chapters clear, the concepts of sensitivity, temperature range of operation and limit of detection are presented and their physical meaning discussed.

It follows a general overview on the luminescence basics, focused in the spectroscopic properties of trivalent lanthanide ions. A brief discussion of the luminescent properties that can be used as thermometric properties are presented discussing the main theoretical models that allow their interpretation. In the final part of the chapter intensity- and lifetime based thermometers are presented. For real-time temperature monitoring ratiometric intensity based temperature algorithms are advantageous: an optimal luminescent nanothermometer should produce a ratiometric intensity response to temperature changes. Moreover, ratiometric techniques can be easily implemented typically with a UV excitation

lamp and a handheld spectrometer or even a simple apparatus combining a dichroic filter set to the isobestic point and two photodetector diodes, each set to detect the excitonic or the dopant emission.



# Chapter 2

## State of the Art in High Spatial Resolution Thermometry

This chapter aims to review the latest progress of sub-micron high-resolution thermometry. For the former thermometers the review addresses essentially far-field optical thermometry methods. Although this review chapter does not intend to be comprehensive, illustrative examples of the rich variety of systems designed and developed to sense temperature at the nanoscale, such as luminescent thermometers containing organic dyes, ruthenium complexes, QDs,  $\text{Ln}^{3+}$  ions and temperature-responsive polymers are described. It covers essentially examples reported over the 2005-2012 period and follow two reviews on luminescent nanothermometers published recently based on  $\text{Ln}^{3+}$ -based materials, essentially up-converting NPs [69] and  $\beta$ -diketonate complexes [31]. A more specific review circumscribing the development of modern thermometry in biologic applications and stressing part of the historical path through which thermometry has progressed into contemporary thermodynamics is issued in 2010 [31].

### 2.1 Luminescent Thermometers Review

Amongst non-invasive spectroscopic methods for determining temperature, the thermal dependence of phosphor luminescence - band shape, peak energy and intensity, and excited states lifetimes - is an accurate technique (often referred as thermographic phosphor thermometry). It works remotely with high detection sensitivity and spatial resolution in short acquisition times, even in biological fluids, strong electromagnetic fields and fast-

moving objects [19, 49, 97, 192, 235, 261]. The thermal probes encompass organic dyes, ruthenium complexes, spin crossover NPs, polymers, LDHs, semiconductor QDs, and  $\text{Ln}^{3+}$ -based materials. Apart from these simple systems, in which a single component acts as temperature-responsive emitting center, there are complex systems, in which the changes in the emission intensity and/or lifetime of the emitting state of a particular component are induced by a second one that is the real temperature responsive material. In most of the cases, this temperature sensitive material is a polymer or an organic-inorganic hybrid host. The temperature dependence of the relative sensitivity for non-ratiometric and ratiometric luminescent thermometers is displayed in figures 2.8 and 2.9, whereas 2.10 illustrates that dependence estimated from lifetime or decay time measurements. Examples of the relatively small number of thermometers (luminescent and non-luminescent) that effectively demonstrate temperature sensing or mapping at micron and sub-micron scale are depicted in figure 2.11. Examples of ratiometric (or self-referencing) luminescent thermometers (table 2.1, figure 2.9) include:

- Perylene/N-allyl-N-methylaniline exciplex interconversion [44];
- Monomer-excimer interconversion of 1,3-bis(1-pyrenyl)propane dissolved in the  $[\text{C}_4\text{mpy}][\text{Tf}_2\text{N}]$ , IL [14];
- Aqueous solution of Fluorescein D/Texas-Red A anchored to a DNA chain; [19]
- Platinum octaethyl porphyrin dye [154];
- Pyrene-labeled poly(DEGMA-stat-PyMMA) [189];
- PNIPAM containing 3 HF-AM [46];
- Fullerene  $\text{C}_{70}$  and perylene (internal standard) dispersed in PtBMA [15];
- Semiconducting Pdots embedded RhB [272];
- Thin layer of the epoxy-based negative photoresist SU8 incorporated RhB [114];
- $\text{Zn}_{1-x}\text{Mn}_x\text{Se}/\text{ZnCdSe}$  ( $x > 0.01$ ) core-shell QD structures [102, 162, 239];
- $\text{CdSe}/\text{ZnS}$  and  $\text{CdTe}/\text{ZnS}$  QDs embedded in a sol-gel derived organic-inorganic hybrid [113];

- P(VDC-co-AN), NPs embedded the (tris(benzoylacetonate)mono(phenanthroline))  $\text{Eu}^{3+}$  complex and the BBS organic dye [254];
- $\text{Er}^{3+}$ -based nanocrystals [6, 253];
- $\text{Er}^{3+}/\text{Yb}^{3+}$ [3, 69, 200, 215, 216, 232, 238]and  $\text{Tm}^{3+}/\text{Yb}^{3+}$ -based [61] UCNPs;
- Siloxane hybrid NPs formed by a BTDA-PMMA core covered with a silica outer layer incorporating (in the core) the Eu-DT complex and a OASN reference [185].

### 2.1.1 Thermometers Based on Organic Dyes

Since the organic dyes were patented in 1941 as "temperature indicators", many advances have been made. RhB [193], fluorescein isothiocyanates [87], and cyanine dyes [165] have become very popular in fluorescence imaging or temperature determination in biological context. A large set of organic complexes are commercially available and can be picked up a la carte from an extensive list, attending to the excitation/emission wavelength range required, solubility, facility of vectorization, etc. The design of all kind of sensors is virtually possible, setting up the analyte and defining the experimental conditions to be used. Many examples can be found in the literature describing assemblies with organic dyes for labelling antibodies and antigens [95, 248], or hosting organic dyes in a polymeric matrix [129, 130], for improving their mechanical and chemical stability.

An illustrative example is NPs of Ruphen and PtTFPP embedded in polyacrylonitrile [129, 130]. In order to produce pressure sensitive paints knowledge of the temperature is fundamental. Ruphen allows the measurement of the temperature that is used to calibrate the PtTFPP pressure response. The polyacrylonitrile is employed as a support medium that shields both Ruphen and PtTFPP of oxygen quenching. Ruphen presents a maximum temperature relative sensitivity of  $2.5\% \cdot K^{-1}$  at 320 K [129, 130](table 2.1, figure 2.8).

More complete approaches can be either achieved by means of a ratio of intensities coming from the monomer and excimer/exciple or decay of emission lifetimes. An excimer is an excited dimer whereas an exciple is a combination of two different atoms that exists only in an excited state, *e.g.* excited electron donor-acceptor complex. In order to rationalize the temperature dependence of the emission intensity (or lifetime) a two-state equilibrium model is used. These two states are assigned to conformational changes (or protonation) of one of the emitting species and are responsible due to the temperature

driven change of the fluorescence emission intensity. The existence of an isoemissive point in the emission spectra is strong evidence that corroborates this simple two-state model for temperature dependence. This simple and rational model conjugated with the fact that organic dyes present severe photobleaching and low quantum yields caused a large research interest on the monomer-to-excimer interconversion and monomer-to-excimer emission intensity ratio.

An important example reports the temperature-dependent change of a perylene monomer/excimer, as an organic dye molecular thermometer [44]. The ratiometric variation of the emission intensities of monomer/excimer species was studied using a two-state equilibrium model in the temperature range 290-360 K with  $S_m = 1.3\% \cdot K^{-1}$  at 350 K [44] (table 2.1, figure 2.8). The authors anticipated that the strategy could be easily extended to other aromatic hydrocarbon acceptor/aniline donor systems, such as benzene/aniline or anthracene/aniline, showing two color emission as a function of temperature. Further studies addressing photobleaching, solvent properties and biological compatibility would be desirable.

In contrast to monomer/excimer molecular thermometers, IL-based thermometers [14] are not limited to the boiling point of common organic solvents, instead, they are critically dependent on the thermal stability of the fluorophore itself. The operating temperature range of IL-based thermometers extends that of monomer/excimer molecular thermometers with reduced photobleaching. One of the most relevant examples uses  $[C_4\text{mpy}][Tf_2N]$  as matrix and 3-bis(1-pyrenyl)propane as phosphor, exhibiting an error in temperature lower than 0.35 K and an UV photobleaching of 15% (at 333 K during 24 h, 10 mW). Reversibility and robustness are demonstrated in 303-413 K heating-cooling cycles during 8 h with a maximum of 0.3 K deviation from the operating calibration curve. A maximum temperature relative sensitivity of  $1.4\% \cdot K^{-1}$  at 355 K can be estimated from published data [14] (Table 2.1, figure 2.9). Interestingly enough, some IL gels have been reported to be biocompatible with enzymes, proteins and even living cells [256]. Nevertheless IL-gels presenting a ratiometric temperature response have not been reported yet.

An example of a ratiometric highly sensitive molecular thermometer based on a platinum octaethyl porphyrin was described by Lupton [154]. The intensity ratio uses two transitions of the PtOEP: the first excited triplet level, at 650 nm, and one band, at 540 nm, which origin is not entirely clear. PtOEP is able to monitor temperature changes in the range 290-320 K with a maximum relative sensitivity of  $4.6\% \cdot K^{-1}$  at 305 K, (table 2.1,

figure 2.9). Reportedly, the heating does not contribute to the material cleavage, which is governed by photo-oxidation [154].

A different methodology explores the determination of temperature by monitoring the luminescence change induced by molecular spin crossover. The process involves the switching between two molecular spin states (the so-called HS and LS configurations) in (pseudo)octahedral  $3d^4$ - $3d^7$  transition metal complexes by the action of an external stimulus, *e.g.* temperature, pressure, light irradiation and others [26, 89]. In the case of temperature-induced crossover, the change in the spin state is accompanied by a change in the optical properties of the compound. One of the first examples reported the temperature dependence of the luminescent intensity of a naphthalene fragment covalently linked to a Ni(II) tetraazamacrocyclic complex, cyclam [65]. The intensity of cyclam emission is partially quenched by an energy transfer mechanism whose efficiency decreases with temperature between 300 and 338 K, resulting in a temperature dependent [65] emission with a maximum relative sensitivity of  $3.6\% \cdot K^{-1}$  at 300 K (table 2.1, figure 2.8). More recently, Quintero *et al.* [191] and Salmon *et al.* [202] reported two-component luminescent thermometers also based on the combination of spin-crossover and luminescence in Rh-110 doped ultra-small  $[\text{Fe}(\text{NH}_2\text{Triazole})_3](\text{X})_2$  NPs (where X stands for tosylate or  $\text{NO}_3^-$ ) [191, 202]. The absorption changes of the transition metal complex during the thermal crossover process modulates the Rh-110 luminescence intensity. When deposited on top of nickel nanowires (5 wires, 500 nm wide, 40  $\mu\text{m}$  long, separated by 4  $\mu\text{m}$ ), where temperature changes were induced by resistive heating, spatial resolution at the micrometer scale was estimated [202]. The thermometer operates in the range 305-325 K with  $S_m = 1.9\% \cdot K^{-1}$  at 309 K (table 2.1, figure 2.11).

The temperature mapping on microfluidic devices using dyes as fluorescent thermometers was also considered by Samy *et al.* [203] and, more recently, by Jung *et al.* [114] RhB was incorporated in PDMS and SU8 polymer matrices and the temperature was determined from the optically active thin layer covering the microfluidic device. Samy *et al.* [203] used an intermediate substrate between the fluid and the sensing layer, while Jung *et al.* [114] followed a new approach rendering the intermediate layer unnecessary; both examples shown spatial resolutions in the order of hundreds of microns. The correspondent maximum relative temperature sensitivities are  $S_m = 2.3\% \cdot K^{-1}$ , at 363 K [203] (table 2.1, figure 2.8) and  $S_m = 1.3\% \cdot K^{-1}$  at 338 K [114] (table 2.1, figure 2.9).

A quite different dye-based luminescent molecular thermometer able to map the tem-

perature gradient on a fluid was recently developed by Feng *et al.* [68]. It consisted in a pyrene-containing triarylboron molecule, DPTB, showing temperature-dependant green to blue luminescence with quantum yield greater than 0.64 over the temperature range 223-373 K, that was dissolved in MOE. The temperature can be determined by the blue shift of the broad emission spectra, ascribed to the thermal equilibrium between twisted intramolecular charge transfer and local excited state of the DPTB molecule. The maximum relative temperature sensitivity is  $0.1\% \cdot K^{-1}$  at 373 K (table 2.1, figure 2.10) and the spatial resolution is below 100  $\mu\text{m}$  [68].

Photobleaching is the main limitation of the dye-based thermometers precluding continuous long-term temperature measurement, essential to follow temperature changes at different time scales.

### 2.1.2 Thermometers based on Quantum Dots

Semiconductor QDs have been proposed for small-scale thermometry, since they present temperature dependent photoluminescence (intensity changes or emission peak shifts). Their size-tuneable absorption and emission frequencies, high quantum yield and photostability have made QDs an active field of research and development for imaging, labeling and sensing in many areas. Besides optoelectronics, biology and medicine stand as the most appealing, since bioconjugation of QDs can make them target selective.

Standard colloidal synthesis methods provide nanocrystalline semiconductor particles of various sizes (1-10 nm range), with tuneable emission, from ultraviolet to infra-red, depending on composition. Common materials are Cd-based binary or ternary semiconductors (*e.g.* CdSe, CdS and CdeSeTe). For many purposes, a core-shell structure is preferred, in order to isolate and protect the toxic Cd-based core by a ZnS shell capsule (1-6 monolayer) resulting in an advantageous increase in the photoluminescence yield [163].

In earlier reports,[242] ZnS coated CdS QDs (5 nm size) were shown to present a considerable change (by a factor of 5) in the photoluminescence intensity in the temperature range 100 to 315 K, accompanied by a 20 nm blueshift of the 600 nm-range emission band. Those properties were demonstrated with the QD dispersed in a variety of matrices (*e.g.* poly(lauryl methacrylate) and TiO<sub>2</sub> sol-gel derived films) and were obtained in a broad excitation frequency range. A linear and reversible change in the integrated emission intensity near room temperature with  $S_m = 2.2\% \cdot K^{-1}$  at 313 K [242] (table 2.1, figure

2.8) was achieved as the main thermometric feature of the composites.

The interest of analysing thermal phenomena at small scales fostered studies of single QDs as local thermal sensors. Li *et al.* [139] demonstrated that the time-averaged emission spectra from individual ZnS-coated CdSe QDs, observed through a microscope, is capable of sensing temperature changes with characteristics similar to the ones reported in composite assemblies of QDs. However, the size and shape distribution of QDs leads to differences in the individual characteristics, precluding their use as absolute thermometer, although relative spectra changes are more reliable. With the used technique, a minimum of 1200 QDs (size area with 200-300 nm diameter) were needed to obtain a precision of one degree. The spectral shift ( $0.105 \text{ nm}\cdot\text{K}^{-1}$ ) was reported as the most accurate thermometric property.

To avoid well-known problems associated with the instability and uncertainty of excitation sources or photobleaching and/or photoblinking, the use of dual emission materials is actively being explored. Such dual processes from two excited states in the same QD enable self-calibration of the system and increase the robustness and reliability of intensity-based spectroscopy thermometry allowing ratiometric methods as mentioned above. This was first reported by Vlaskin *et al.* in  $\text{Zn}_{1-x}\text{Mn}_x\text{Se}/\text{ZnCdSe}$  core-shell QD structures [239]. The solubility of such Mn-doped colloidal semiconductors QD in water was recently achieved, enabling their use in biophysical applications [102, 162]. These Mn-doped QD nanocrystals exhibit dual emission processes: the direct excitonic and the  $\text{Mn}^{2+}$  dopant ions emissions, represented schematically in figure 2.1A,B.

The thermally assisted population transfer between the dopant and the excitonic states determines the dynamics of the processes between the levels involved and therefore the intensity ratio of those two emissions. The development of these QD required the compositional tuning of sufficiently large semiconductor gaps, to leave the  $\text{Mn}^{2+}$  levels inside the gap. The use of core-shell structure facilitated the optimization of the properties in a dual step: core doping and energy-gap tuning on the shell. It has been found that the relative intensity of excitonic emission increases with temperature. A discussion of the thermal population mechanisms and its effect on photoluminescence was presented by Beaulac *et al.* [20] and Vlaskin *et al.* [239]. The maximum relative sensitivity values reported near room temperature for these QDs are  $1.3\% \cdot \text{K}^{-1}$  at 318 K [239] (table 2.1, figure 2.8) and detection responds to 0.2 K variations (figure 2.1C-E).

Jorge *et al.* [113] reported the simultaneous temperature and oxygen sensing using

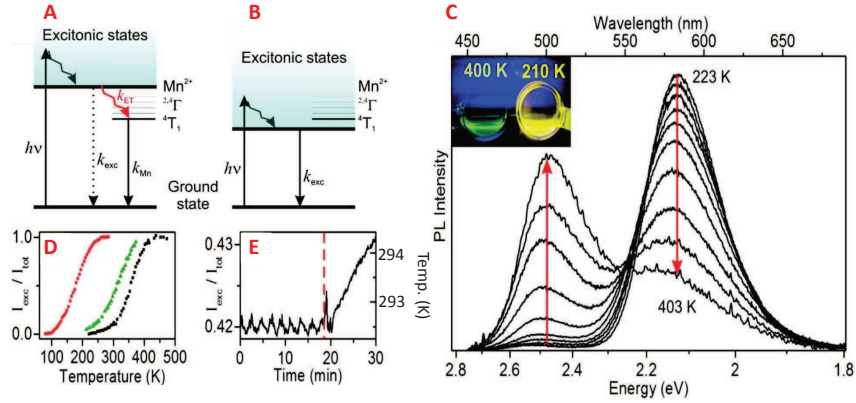


Figure 2.1: Schematic representation of electronic structures related to photoluminescence (PL) in colloidal  $\text{Mn}^{2+}$  QDs, showing the particular cases when  $\text{Mn}^{2+}$  states reside within the (A) and outside (B) of the semiconductor gap. The resulting PL spectra as a function of temperature and correspondent color upon UV excitation are presented in (C). The tunability of the active temperature window is demonstrated by  $I_{\text{exc}}/I_{\text{tot}}$  vs temperature response curves for three different samples (D). PL response to  $\pm 0.2\text{K}$  temperature oscillations (E), and steady warming (dashed line) of  $\text{Mn}^{2+}$  QD. (Adapted from V. A. Vlaskin, N. Janssen, J. van Rijssel, R. Beaulac and D. R. Gamelin, *Nano Lett.*, 2010, 10, 3670-3674) [239].

a sophisticated optical fibre setup. A fibre taper doped with an oxygen sensitive sol-gel derived glass was connected to one arm end of a bifurcated fibre, whereas core-shell CdSe/ZnS and CdTe/ZnS QDs embedded in a sol-gel derived hybrid were placed at the end of the other arm to determine temperature. The temperature behaviour of different samples was tested using an optical fibre bundle to excite and collect the QDs nanocrystals emission (with peak emission wavelengths ranging from 520 to 680 nm). The temperature was determined either by the shift of the peak maximum or the normalized intensity. Using the intensity-based algorithm, the QDs demonstrate ratiometric and linear temperature response (287-317 K) with relative maximum sensitivity of  $0.9\% \cdot \text{K}^{-1}$  at 317 K (table 2.1, figure 2.9).

Several factors still preclude the use of commercially available QDs in nanoscale thermometry, particularly the bluing, the bleaching, and the blinking under continuous illumination [123, 170, 237], and the size distribution of the QDs that leads to a non-homogeneous luminescence individual response. The poor solubility, the agglutination, the instability in different environments, and the toxicity to biological systems can be also other drawbacks.

For example, under acidic ( $pH < 5$ ) or isotonic conditions, QDs aggregate easily and lose luminescence in an intracellular environment and the degradation of QDs has been shown to release toxic heavy metal ions such as Cd [101]. To overcome these disadvantages, the surface of QDs need to be coated with inert materials [171]. Furthermore, the intense activity in the use of QDs for biomedical applications, *e.g.* imaging [237], should pave the way to their use in thermometry. However toxicity and cellular uptake raise problems that still require much research to achieve reproducible and safe methodologies in clinical applications [10, 101].

### 2.1.3 Thermometers based on $\text{Ln}^{3+}$ Phosphors

There are a lot of examples illustrating the temperature dependence of the intensity of the intra-4f transitions and of the lifetime of a particular 4f exciting state, for a comprehensive review of the subject see, for instance, the works on high-temperature thermographic phosphors [97, 192], and temperature-sensitive paints (the  $\text{Ln}^{3+}$  indicator probe is incorporated into a polymer binder and the resulting paint sprayed onto a surface to mapping temperature distribution) [261, 273]. In an interesting and seminal example Wang *et al.* explored the  $\text{Mn}^{2+}$  and  $\text{Eu}^{3+}$  emissions in the range 293 to 423 K using co-doped  $\text{Mn}^{2+}/\text{Eu}^{3+}\text{ZnS}$  NPs [252]. The ratiometric thermometer displays a maximum relative sensitivity of  $1.2\% \cdot \text{K}^{-1}$  at 423 K (table 2.1, figure 2.9). In this chapter, however, emphasis is given on the few examples of  $\text{Ln}^{3+}$ -based thermographic phosphors that effectively illustrate the temperature sensing/mapping at micron and sub-micron scale (Mitsubishi *et al.* reported millimeter resolution in a polymer optode thin film embedded a  $\text{Eu}^{3+}$  tris( $\beta$ -diketonate) complex) [167]:

- A metal stripe covered with a thin film of perdeutero-PMMA heavily doped with a  $\text{Eu}(\text{tta})_3$  complex [126];
- 2D distribution maps using  ${}^5\text{D}_0$  rise time temporal response in  $\text{Y}_2\text{O}_3:\text{Eu}^{3+}$  [120];
- A scanning thermal microscope with  $\text{Er}^{3+}/\text{Yb}^{3+}$  co-doped fluoride glass [200] or  $\text{PbF}_2$  UCNPs [3, 69], glued at the tip extremity.

The intracellular thermometers based on UCNPs and  $\beta$ -diketonate complexes will be deeply discussed in next section. The first report demonstrating high-resolution thermal

imaging with potential application to integrated circuit diagnostics was presented by Kolodner and Tyson using a metal stripe covered with a thin film of perdeutero-PMMA heavily doped with a  $\text{Eu}(\text{tta})_3$  complex (concentration of about 40 wt. %) [126]. Thermal images of the luminescent film were obtained with  $0.7 \mu\text{m}$  spatial resolution and temperature resolution of 0.08 K [126]. Temperature mappings of integrated circuits with better spatial resolutions (up to  $0.35 \mu\text{m}$ ) were more recently reported combining thermorefectance measurements under non coherent UV, visible and NIR illumination [230].

The rise time response of the  ${}^5\text{D}_0$  excited state in  $\text{Y}_2\text{O}_3:\text{Eu}^{3+}$  (3-4% in molar concentration) phosphor was calibrated against the temperature in the range 473-973 K demonstrating 2D rise time thermal imaging over an area of  $500 \text{ mm}^2$  (diameter of the laser beam on the target) [120]. A state-of-the-art high-speed imaging camera (acquisition rate of  $10^6$  frames per second) was used to capture the  $\text{Eu}^{3+}$  temporal response (rise and decay times) that was subsequently post-processed in MatLab® to disclose the thermal map. The uncertainty in the temperature measurements is relatively high, 20% at 673 K, although a decrease of the  $\text{Eu}^{3+}$  activator concentration could significantly lengthens the rise time and then the accuracy of the thermometer. A maximum relative sensitivity of  $2.6\% \cdot \text{K}^{-1}$  at 973 K [120] is computed (table 2.1, figure 2.9), while the spatial resolution was not reported and the temperature determination algorithm is rather complicated, relatively to those of decay time and intensity-based measurements, requiring more sophisticated equipment and post-processing computational analysis[120].

Other example that illustrates the sensing of temperature through a decay time algorithm was reported by Allison *et al.* for YAG:Ce NPs (average size  $\sim 30 \text{ nm}$ )[7]. The decay lifetimes for the NPs varied from 18 to 27 ns (280 to 350 K) with  $S_m = 0.2\% \cdot \text{K}^{-1}$  at 350 K (table 2.1, figure 2.11) and this significant variation, coupled with the high signal strength that was observed, suggested the utilization of YAG:Ce NPs as useful thermographic nanophosphors.

Generally, UCNPs consist of  $\text{Ln}^{3+}$  ions embedded in crystalline host matrices (*e.g.* fluorides, oxides, phosphates or sulphides) [251, 284]. When excited in the UV/Vis range these NPs display down-conversion emission, although they are capable of emitting visible luminescence when excited with NIR light (UC mechanism). The advantage of using  $\text{Ln}^{3+}$ -based UCNPs lies on the fact that weighty and expensive ultrafast lasers are not necessary, since the NPs can be stimulated using low power and commercial NIR lasers (working on the biological window of tissues, 700-1000 nm). Such features makes UCNPs promising

as bioimaging probes with attractive features, such as no auto-fluorescence from biological samples and a large penetration depth, and UCNPs have emerged as novel imaging agents for small animals, including tumour-targeted imaging, lymphatic imaging, vascular imaging and cell tracking [83]. The most studied UCNP-based thermometer uses the  $\text{Yb}^{3+}/\text{Er}^{3+}$  ion pair [2, 3, 69, 215, 216, 232, 238, 250]. The  $\text{Yb}^{3+}$  ions were excited by a 975 nm NIR laser, through an NIR-to-visible UC process in which two low energy photons are "added up" to give one high energy photon [250]. This NIR excitation is very efficient because, at this wavelength, the  $\text{Yb}^{3+}$  ions have a large absorption cross section. Once excited, they transfer their energy to adjacent  $\text{Er}^{3+}$  ions that will glow in the green ( ${}^2\text{H}_{11/2} \rightarrow {}^4\text{I}_{15/2}$  and  ${}^4\text{S}_{3/2} \rightarrow {}^4\text{I}_{15/2}$ ,  $\sim 525$  and  $550$  nm, respectively) and red ( ${}^4\text{F}_{9/2} \rightarrow {}^4\text{I}_{15/2}$ ,  $\sim 660$  nm) spectral regions. These  $\text{Er}^{3+}$  transitions are temperature dependent and their intensities were used to determine the temperature using the ratiometric FIR algorithm. One example reporting temperature-dependent FIR between the green and the red UC  $\text{Er}^{3+}$  emissions was demonstrated by Wang *et al.* in  $\text{ZnO}:\text{Er}^{3+}$  nanocrystals [250]. The intensity boost of the green and the red UC emissions, as the annealing temperature increases, with the concomitant increase of the energy gap between the  ${}^2\text{H}_{11/2}$  and the  ${}^4\text{S}_{3/2}$  levels, are ascribed to the decrease of the non-radiative relaxation and the enhancement of the crystal field effect around the  $\text{Er}^{3+}$  ions, respectively. The relative sensitivity was computed resulting  $S_m = 0.61\% \cdot K^{-1}$  at 273 K [250] (table 2.1, figure 2.9).

The UC mechanism still presents some drawbacks that need further improvements, both in the materials (*e.g.* relative concentration, ratio of the dopants, host material, size control) and in the optical point of view (the quantum yields are low and the maximum relative sensitivity values are around  $\sim 0.5\% \cdot K^{-1}$  at the physiological temperature range, table 2.1). Moreover, resolving temperature with a precision lower than 0.1 K is still to be demonstrated by this approach [69].

The scanning thermal microscope developed by Aigouy and collaborators [3, 2, 200] is able to measure the heating of electrically excited stripes, micro and nanowires, by gluing  $\text{Er}^{3+}/\text{Yb}^{3+}$  co-doped fluoride amorphous glass particles or  $\text{PbF}_2:\text{Er}^{3+}/\text{Yb}^{3+}$  nanocrystals at the end of a sharp atomic force microscope tip (figure 2.2).

By adjusting the electrical current that flows in the structure, the resulting temperature variations modulate the  $\text{Er}^{3+}$  particle emission, giving rise to the thermal contrast. Although the luminescence is affected both by the near-field optical distribution and by temperature variations, this thermal contribution can be treated separately by compar-

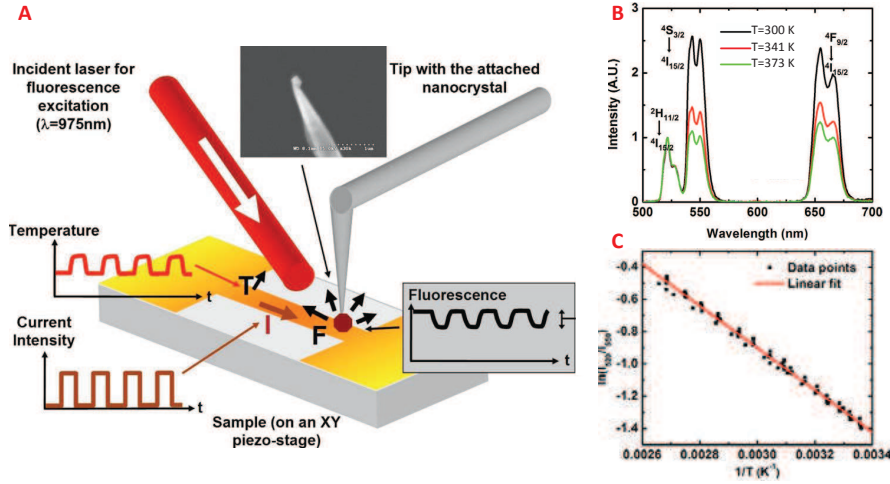


Figure 2.2: Scanning thermal microscope based thermometer developed by Aigouy and collaborators (A) Schematic of the experimental setup used illustrating the excitation laser, the metal strip and the nanocrystals at the end of a sharp AFM tip. The heating of the metal stripe leads to a temperature fluctuation monitored by the fluorescence signal. (B) Example of emission spectra Fluorescence spectra for a fluoride amorphous glass at different temperatures. (C) The evolution of the logarithm of the fluorescence intensity ratio as a function of the inverse temperature is the temperature calibration curve. (Adapted from L. Aigouy, E. Saïdi, L. Lalouat, J. Labéguerie-Eg ea, M. Mortier, P. L ow, C. Bergaud, Journal of Applied Physics, 2009, 106, 074301 and E. Saïdi, B. Samson, L. Aigouy, S. Volz, P. L ow, C. Bergaud, M. Mortier [3, 200].

ing the obtained images with reference ones recorded when the device is not driven by a current. The temperature is determined analyzing the thermal quenching of the  $\text{Er}^{3+}$  emission. Since the fluorescent probe is not in direct contact with the wires surface, the experimental values actually correspond to an average temperature. The results obtained are in good agreement with numerical simulations of the heat dissipation of the micro and nanowires [200].

For the scanning thermal microscope using  $\text{PbF}_2:\text{Er}^{3+}/\text{Yb}^{3+}$  NPs as fluorescence probes  $S_m = 1.0\% \cdot \text{K}^{-1}$  at 345 K [3], (table 2.1, figure 2.9) and the thermometer presents a spatial resolution in the range of the fluorescent particle size ( $< 500\text{nm}$ ). For the SThM with the  $\text{Er}^{3+}/\text{Yb}^{3+}$  co-doped fluoride amorphous glass particles,  $S_m = 1.1\% \cdot \text{K}^{-1}$  at 342 K [200]. Tikhomirov *et al.* [232] and Singh and Rai [215] used an analogous UC mechanism to fabricate optical nanoheaters of fluoride  $\text{Yb}^{3+}/\text{Er}^{3+}$  and  $\text{Gd}_2\text{O}_3:\text{Yb}^{3+}/\text{Er}^{3+}$  co-doped

UCNPs, respectively. The NPs were excited by NIR radiation (diode laser at  $\sim 975$  nm) that is dissipated via phonon relaxation, resulting in a temperature increase, measured by FIR of the  ${}^2\text{H}_{11/2} \rightarrow {}^4\text{I}_{15/2}$  and  ${}^4\text{S}_{3/2} \rightarrow {}^4\text{I}_{15/2}$  transitions until 1173 K. While for fluoride  $\text{Yb}^{3+}/\text{Er}^{3+}$  co-doped NPs the sensitivity is not reported (and cannot be computed due to the absence of data) [232], Singh and Rai estimate  $S_m = 0.21\% \cdot \text{K}^{-1}$  at 600 K (table 2.1, figure 2.9) [215].

These last two examples listed that effectively illustrate the temperature sensing/mapping at micron and sub-micron scale encompass organic-inorganic hybrids and will be discussed in the next section.

## 2.1.4 Complex Thermometric Systems

The use of polymers in luminescence thermometers exploits their extraordinary structural properties. They can play a passive role, simply as a physical support conferring their unique mechanical properties, or they can be an active component in complex thermometric structures thanks to their sensitivity to temperature changes. Actually, the sensing capacity of polymers has been extensively explored, in general (reviews of Hu and Liu [103] and Guo *et al.*[88] are very instructive), and in particular for temperature measurements (see the recent review by Pietsch *et al.*[189]). This is also the case of organic-inorganic hybrids, including LDH materials [105, 268]. Here special focus is given to on the specific characteristics dealing with the nanoscale and on the comparative performances of these thermometers.

### Polymer Based Systems

Polymers have first been used in optical temperature-responsive materials as supporting media to optically-active molecules due to their well-known good processability and mechanical properties [188]. An example is the use of PS and polyacrylonitrile to increase the solubility of  $\text{C}_{70}$ , avoiding simultaneously the luminescence crosstalk with oxygen [11]. Pristine Fullerene  $\text{C}_{70}$  encapsulated in polymer presents delayed fluorescence/prompt fluorescence intensity ratio that is temperature dependent. The thermally activated delayed fluorescence of  $\text{C}_{70}$ -based thermometer was shown to follow temperature changes in a ratio-metric algorithm (perylene was incorporated as an internal standard) in the range 293-363 K [11] with  $S_m = 1.3\% \cdot \text{K}^{-1}$  at 330 K (table 2.1, figure 2.8). Dispersion of  $\text{C}_{70}$  in PtBMA enabled to cover a wider temperature range (293-373 K) [15]. Both delayed fluorescence

lifetime and intensity based thermometers were proposed to measure temperature in the absence of oxygen. The maximum relative sensitivities are  $1.8\% \cdot K^{-1}$  at 330 K, for intensity ratio, and  $2.2\% \cdot K^{-1}$  at 373 K, for delayed fluorescence lifetime [15]. Another example is the use of PVA films to embed thermofluorescent PDA supramolecules and cast the composite on resistance random access memory devices in order to determine imprinted temperature gradients associated to filamentary defects [271]. This is implemented based on the irreversible fluorescence intensity increase of PDAs when temperature increases from room temperature to about 350 K.

The optical principals in complex thermometric systems are similar to those already explained for simple systems, and include temperature induced fluorescence enhancement, quenching or lifetime change, temperature emission shifts, FRET, absorbance enhancement or quenching, absorbance shifts, plasmon resonance, exciton-plasmon interaction, etc.[189]. The temperature sensing mechanism is typically based on a polymer transition from hydrophilic-swollen-globule-state to hydrophobic-collapsed-coil-state [207]. These two processes are interconnected in such a way that the polymer conformation affects the optical emitter environment, such as polarity, microviscosity and donor/acceptor average distances in the case of FRET. Optical emitters representing all the types described in previous sections (organic dyes, QDs and  $\text{Ln}^{3+}$  phosphors) have been used in these polymer structures. An illustration of polymer-phosphor configurations is shown in the scheme of figure 2.3. The simplest system of this kind is that containing a thermo-responsive polymer and an organic dye, which is grafted to the polymer backbone [187] or simply encapsulated.

The most explored polymers are PNIPAM, which has a lower critical solution transition at 305 K, [46, 81, 84, 82, 83, 96, 99, 107, 106, 213, 228, 247, 269, 264] together with others polymers of the same family, such as NNPAM or NIPMAM [82]. Other examples include PEG-based polymers,[47, 82, 136, 135, 136, 266, 265] PMMA [188] and helix-forming polysaccharides (schizophyllan)[214]. In the great majority of these examples, the optically active component is an organic dye and the polymer main role is to change the polarity of the dye surrounding media [81, 84, 189, 15, 107, 83, 214, 269, 82, 264]. Most of these systems are based on changes in the emission intensity and lifetime [84, 83, 214, 247](*e.g.* Gota *et al.* reported a  $S_m$  value of  $10.4\% \cdot K^{-1}$  at 308 K,[83] table 2.1, figure 2.8. Lee *et al.* [136] have reported an interesting example of a thermometer based on a change in intensity (non-ratiometric). The thermometer was designed for biological applications since it is composed of a FDA-approved biocompatible PEG-based copolymer

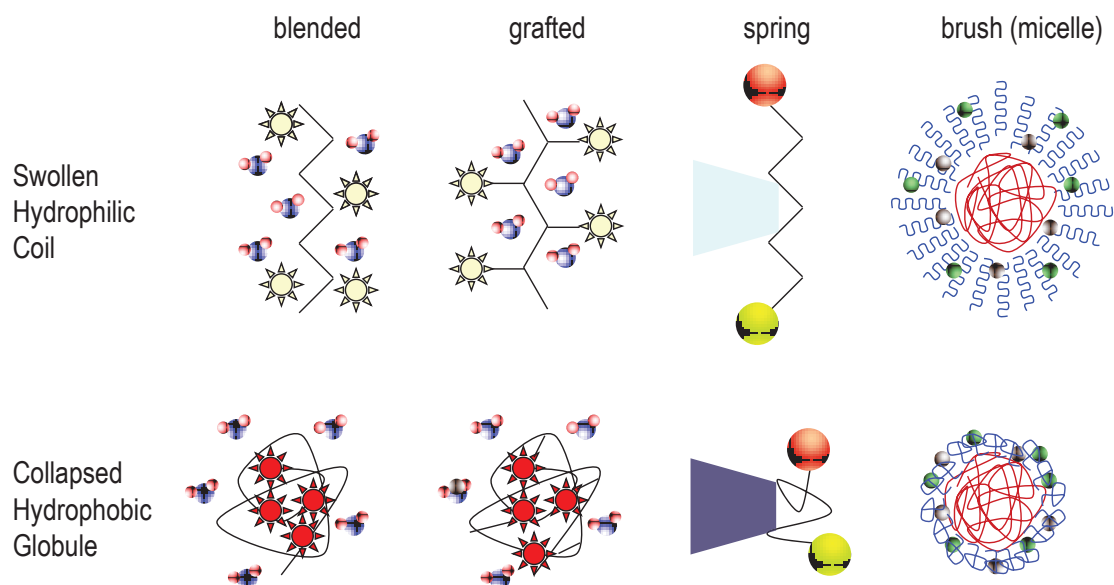


Figure 2.3: Scheme of polymer-phosphor thermometer structures.

and a fluorescent dye emitting in the NIR region allowing intra-tissue sensing in the 274–353 K temperature range. PNIPAM can, for example incorporate hemicyanine (PNIPAM-co-HC [214]), boron-dipyrromethene (PNIPAM-co-BODIPY [247]) or fluorescent modified acrylamide (PNIPAM:FMA [96]).

Another example based on NIR emission designed for biomedical applications is composed of indocyanine green dye encapsulated in a micelle of PEO-PPO copolymer [47]. The micelles volume reduces almost 5-fold when the temperature increases from 290 to 310 K, producing an enhancement of the luminescence emission (non-ratiometric) by about 6 times.

Other thermometers are based on the temperature dependence of an intensity ratio (the ratiometric thermometers listed above), and on the change of the wavelength at which absorption [269, 214] or fluorescence [106] is maximum. The ratiometric thermometer reported by Pietsch *et al.* [189] uses the excimers-to-monomers emission intensity ratio of pyrene. Below the polymer phase transition, pyrene molecules are exposed to the polar environment leading to the formation of excimers, with the corresponding increase of their fluorescence. The ratiometric thermometer reported by Chen and Chen [46] is based on a dual-band dye (3-hydroxyflavone) associated to normal excited state intramolecular charge

transfer and tautomer excited state intramolecular proton transfer. The latter is suppressed in highly polar environment, as that provided by PNIPAM in the low temperature swollen state, leading to a change in the relative normal and tautomer fluorescence intensities. Another approach has been proposed to improve reproducibility problems based on the fluorescence resonance energy transfer between a fluorescent donor, NBD, and an acceptor, RhB [243]. In this case, the donor is also sensitive to pH. This thermometer works between 298 and 318 K with  $S_m = 13.3\% \cdot K^{-1}$  at 313 K (table 2.1). The PNIPAM/porphyrin system reported by Yan *et al.* [269] displays a blue-shift in the absorption maximum upon heating, possibly associated to the change in local polarity. An extended operation range is elegantly achieved by using porphyrins coordinated to different metal ions.

Normally, the operation range is restricted to the phase transition region (typically 300-310 K, in the case of PNIPAM), with some hysteresis being observed. The range can be extended as described in the preceding example by Yan *et al.*[269] using polymers with a upper critical solution transition, such as PMMA [188] or by using other members of the NIPAM monomer family and their copolymers [107]. However, the possible integration of these polymers in an "all-in-one" responsive thermometer is still to be shown. A typical limitation of the thermometers based on polymers is the hysteresis, *i.e.*, differences in the output, for the same temperature value, depending if the temperature increasing or decreasing [82]. This translates to an error in the temperature determination that may extend into a relevant fraction of the operation range. In such conditions the sensitivity depends also on the optical active component as fluorescent dyes whose response is connected to the polarity of the surrounded media, widely used choice. Alternatively, hysteresis can be reduced by using PEG-based methacrylates [46, 265].

Concerning both the hysteresis and limited operation range issues, a significant improvement was presented by Gota *et al.* [82] using a smart combination of polymeric thermometers to cover different temperature ranges with higher sensitivity. Using an ionic component to prevent intermolecular aggregation of N-alkylacrylamide and fluorescent components, it has reported four fluorescent polymeric thermometers that offer good temperature resolution (*e.g.*  $< 0.2K$ ). The temperature dependence was rationalized by a temperature-induced structural change in aqueous solution that generates a large fluorescence enhancement with a small increase in temperature. In fact, this clever phosphor blend results on a fluorescent polymeric thermometer, covering the temperature range 277-340 K, with  $S_m = 12.5\% \cdot K^{-1}$  at 300 K [82] (table 2.1, figure 2.8).

An interesting strategy, followed by Wong *et al.* [262], uses the relaxation time of fluctuations in the fluorescence of a protein (associated to reversible protonation). This depends on pH and temperature and a bifunctional sensor was demonstrated working in the 283-323 K temperature range with  $S_m = 4.1\% \cdot K^{-1}$  (table 2.1, figure 2.8).

Most of the preceding examples are named micro, nano or molecular thermometers, although the name represents only the size of the responsive unit and not the spatial resolution achieved in a temperature measurement. The exceptions are the intercellular thermometers reported by Gota *et al.* [81] and Ye *et al.* [272] (section 2.1.4) and the microfluidics thermometer reported by Graham *et al.* displaying a resolution of  $\sim 50 \mu m$  around 305 K [84]. This latter example is a PNIPAM water-soluble thermometer based on the temperature dependence of the fluorescence lifetime of a benzofurazan copolymer. The temperature was determined using a microscope-coupled CCD camera, by pixel-by-pixel emission intensity decay analysis, resulting in a maximum relative sensitivity of  $S_m = 16.2\% \cdot K^{-1}$  at 307 K [84] (table 2.1, figure 2.11).

The optical limitations of organic dyes, which have already been explained in detail (section 2.1.1), can be overcome by using metal nanoparticles or QDs as the optical emitter component. A convenient choice is gold nanoparticles. In a typical case, such as presented by Mitsuishi *et al.* [167], gold NPs are assembled to PNIPAM copolymers that show folded to extended conformational changes in the 293 to 313 K temperature range inducing a shift in the UV-visible absorption peak of the assembly from 540 nm to 546 nm, corresponding to  $S_m = 0.1\% \cdot K^{-1}$  at 295 K. Another example of a thermometer based on the temperature dependent position of the absorption maximum is that reported by Honda *et al.* [99]. In this case, PNIPAM coats Au NPs and acting as a dielectric with a temperature dependent refractive index that changes the Au surface plasmon peak wavelength. When the optical component is a QD, the polymer transition produces a change on the average inter-QDs that is reflected on the emission properties [134, 135, 138]. For instance, CdTe QDs show increased quantum yields when incorporated into a temperature-sensitive PNIPAM hydrogel and both the fluorescence intensity and the maximum emission wavelengths were sensitive (in a completely reversible way) to external temperature stimuli that induce the typical coil-globule transition of PNIPAM [138].

A further improvement has been the introduction of plasmonic metaresonance sensors [198]. A reversible nanothermometer is built from two different NPs connected by a polymer acting as a molecular spring. This type of complex systems was introduced by Kotov *et al.*

[134]. The underlying optical mechanism involves plasmon resonance and exciton-plasmon interaction. A typical structure consist of Au nanoparticle ( $\sim 20$  nm large) surrounded by CdTe NPs with a smaller size ( $\sim 4$  nm large) linked to the Au surface by a linear polymer (*e.g.* PEG). The variation of the length of the linker polymer in the temperature range of 293-333 K changes the inter-Au/CdTe distance-dependent resonance conditions of the CdTe emission. The relative sensitivity cannot be computed due to the absence of published data [134]. The CdTe-PEG-Au system is, therefore, an intriguing example of a nanoscale superstructure that undergoes a reversible structural change in response to the environmental conditions. The combination of this property with plasmon-exciton interactions, that display a high sensitivity of the optical output on the distance modulations represents the foundation of a new family of sensing and optoelectronic devices [134].

$\text{Ln}^{3+}$  phosphors are also used as optical emitters in complex polymer systems. Most of the examples comprise of  $\text{Ln}^{3+}$   $\beta$ -diketonate complexes as temperature sensors through a thermally driven energy back transfer mechanism between the  $\text{Ln}^{3+}$  emitting level (*e.g.*  $^5\text{D}_0$  and  $^5\text{D}_4$ , for  $\text{Eu}^{3+}$  and  $\text{Tb}^{3+}$ , respectively) and the lowest ligand triplet excited state [121, 235]. Luminescent molecular thermometers based on  $\text{Eu}^{3+}$  tris( $\beta$ -diketonate) coordination compounds were proposed in the past decades involving isolated complexes [121, 220, 235] or complexes embedded into polymers [126, 254, 24, 167, 118, 224] and organic-inorganic hybrid materials (see below) [184, 185]. A serious drawback of  $\text{Ln}^{3+}$   $\beta$ -diketonate complexes relates to their photodecomposition under UV irradiation [37], which decreases luminescence intensity and, thus, makes molecular thermometers based on these complexes not suitable for long-term monitoring. The incorporation of the complexes into polymers [115] and organic-inorganic hybrid hosts [37, 144], however, considerably improves the UV photostability, overcoming, therefore, the main drawback of the use of such complexes as long-term monitoring luminescent thermometers.

One interesting example of polymer-containing  $\text{Eu}^{3+}$  chelates for simultaneous luminescent sensing of temperature and oxygen was reported by Borisov and Wolfbeis using  $\text{Eu}(\text{tta})_3\text{L}$  complexes (L=dipyrazolytriazine derivative) and a palladium porphyrin oxygen indicator embedded into PTBS microbeads [24]. Both indicators of the dual sensor can be excited by a 405 nm LED and their luminescence is easily separated using appropriate filters. Based on the temperature dependence of the  $^5\text{D}_0$  lifetime of the  $\text{Eu}(\text{tta})_3\text{L}$  complex, a luminescent thermometer working in the range 273-333K with  $S_m = 1.1\% \cdot K^{-1}$  at 333 K was demonstrated [24] (table 2.1, figure 2.11). An illustrative example of a ratiometric

polymer-containing  $\text{Eu}^{3+}$  thermometer is the encapsulation of two colour luminescent dyes (tris(benzoylacetonato)mono(phenanthroline) europium(III) and BBS) in gas-impermeable P(VDC-co-AN) NPs [254]. The polymer NPs shows full reversible temperature response enabling rapid colorimetric temperature estimation in the range 273-323K. A photographic readout produces a quantitative two-dimensional thermo-imaging. The relative sensitivity is  $S_m = 7.2\% \cdot K^{-1}$  at 323K (table 2.1, figure 2.9).

Polymer-based thermometers have some drawbacks, as hysteretic phase transitions, already mentioned, and a possible non-uniform response across the polymer-bead in the case where the optical response depends on the local chemical environment. The multi-optical response of the system to temperature, pH, oxygen content and saline conditions may constitute a drawback since the temperature response may be hindered by the change in other parameters but it is also an opportunity to design multi-responsive logic devices [234, 187]. Polymer-based thermometers have the advantage of having higher sensitivities if only a narrow range (typically around room temperature) is requested. Also, these polymers can be designed as biocompatible beads, which is of fundamental importance for in-vivo applications.

A special case of complex thermometric systems based on polymer conformation transitions is the one using DNA that will be presented in section 2.5 due to their implication in biological systems. The unique  $\pi$ -stack structure of double-helical DNA can be used to develop novel DNA-based nanodevices, as the electronic properties depend strongly on the orientation of the  $\pi$ -stacking [109, 110, 223]. Thus, transitions between double-stranded DNA structure from B- to Z-DNA conformations can be induced by changes in temperature. Differences in the electronic properties of each  $\pi$ -stacking and in the charge transfer process from a fluorescent probe, like, for instance, 2-aminopurine, result in marked changes in emission that can be readily monitored. Based on these results, Tashiro and Sugiyama have proposed a molecular nanothermometer and shown that fluorescence intensity correlates reproducibly with temperature in the range between 275 and 305 K [229].

Barilero *et al.* [19] proposed a different approach using organic dyes as unimolecular fluorescent temperature probes for dual-emission-wavelength measurements in aqueous solutions. The basic concept relies on a non-thermal chemical reaction (either a conformational transition or a protonation) inducing a modification of the dye emission spectra as the temperature changes. A sophisticated temperature sensing method using a DNA molecular beacon that spontaneously exchanges its configuration from a closed state (dis-

playing a stem and a loop) to an open form was recently proposed [19] 2.4. The optical signal comes from the labeling of the beacon extremities by a pair of fluorophores engaged in FRET conferring appropriate photophysical properties for a ratiometric analysis. The authors describe a Fluorescein/Texas-Red donor/acceptor pair thermometer for the temperature interval 278-318 K with  $S_m = 4.5\% \cdot K^{-1}$  at 295 K (table 2.1, figure 2.9).

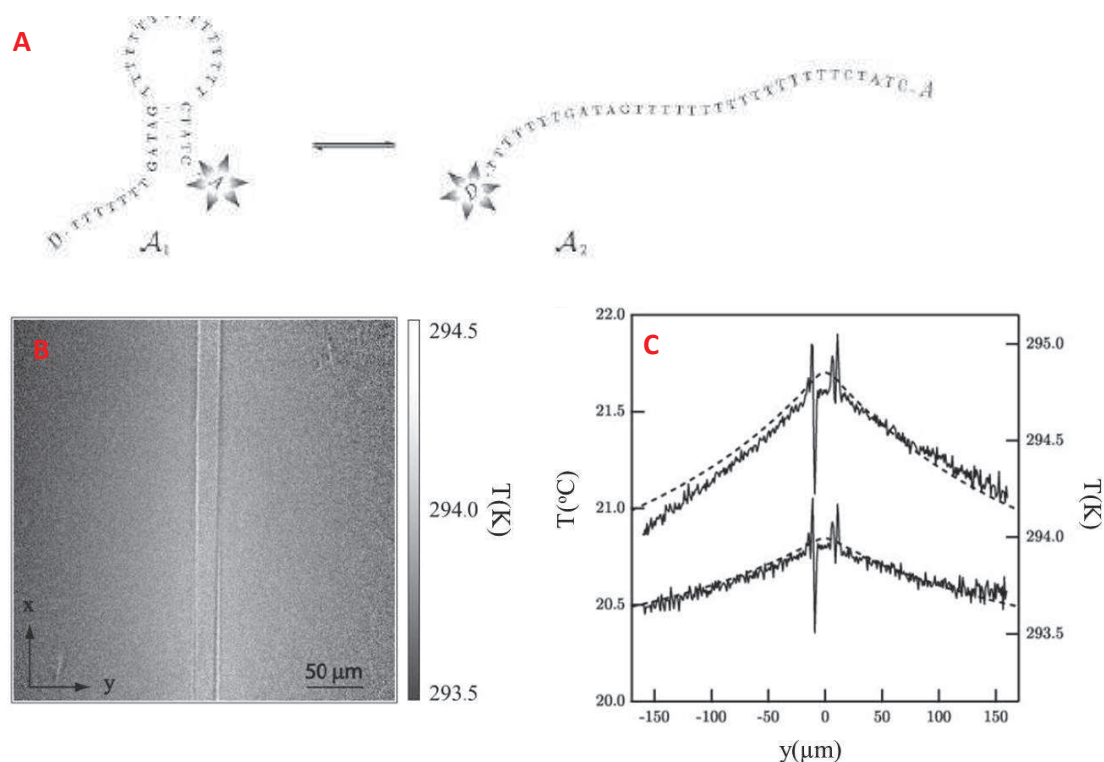


Figure 2.4: (A) The molecular beacon platform: in the closed state (A1), stable at the lowest temperatures, the two fluorophores engaged in energy transfer (i.e., the Fluorescein D and Texas- Red A) are in close proximity. Hence, upon exciting the donor, one essentially collects fluorescence emission from the acceptor. In contrast, at the largest temperatures the open state (A2) is favored, the two fluorophores are distant, and the donor excitation essentially results in the donor; (B) normalized ratiometric image (x,y) from which the temperature field can be retrieved using the temperature calibration curve emission. (C) FEM simulations (dashed line) and experimental (solid line) temperature profiles along the y-axis for two different values for the current ( $i=2.83\text{mA}$  on top and  $2.00\text{ mA}$  at bottom). (Adapted from T. Barilero, T. Le Saux, C. Gosse and L. Jullien, *Anal. Chem.*, 2009, 81, 7988-8000) [19].

Using  $130\ \mu\text{m}$  thick microfluidic chamber locally heated by a thin film resistor, tem-

perature measurements were illustrated by ratiometric fluorescence imaging, exciting at 480 nm and monitoring the ratio of the intensities at 535 and 620 nm. Microfluidics minimizes undesired photobleaching and the experimental conditions were setup in order to avoid crosstalk with pH and ionic strength changes in the fluid induced by temperature changes. The temperature profiles were compared with simulated results showing a concordance of 0.15 K within the experimental error of the reference thermocouple used [19]. The approach might have limitations to measure temperature in biological tissues or even in moving fluids.

### **Organic-Inorganic Hybrids Based Systems**

The synergy of the intrinsic characteristics of organic-inorganic hosts with the luminescence features of emitting centers (*e.g.* organic dyes, QDs and  $\text{Ln}^{3+}$  ions) offer excellent prospects for designing new luminescent organic-inorganic hybrids with enhanced desired characteristics, therefore opening exciting new directions in materials science and related technologies, with noteworthy results in the ecofriendly integration, miniaturization, and multifunctionalization of devices [37, 38, 67, 133, 205, 204].

Progresses in nano and biotechnology crave the miniaturization of luminescent thermometers down to the micro and nanoscale regimes with high spatial resolution; the intracellular temperature mapping is, for instance, an example. Organic-inorganic hybrids embedded organic dyes, QDs or  $\text{Ln}^{3+}$  ions - particularly processed in the form of NPs - have emerged as an interesting class of materials to develop new micro and nanothermometers, mostly due to:

- Flexibility, relative facile chemistry, and highly controlled purity, since they are synthesized from pure precursors;
- Low processing temperature, a key factor for devices miniaturization and for reduction of the processing cost;
- Encapsulation of large amounts of emitting centers, isolated from each other and protected by the organic-inorganic host, enabling the control of nonradiative decay pathways;
- Amelioration of the thermal and optical stability and mechanical properties, relative to those of the isolated emitting centers, overcoming, therefore, some of the main

drawbacks of the use of isolate dyes, QDs and  $\text{Ln}^{3+}$  chelates as long-term monitoring luminescent thermometers.

Non-ratiometric [81, 227] and ratiometric [185, 254] thermometers acting at the sub-micron scale were fabricated using  $\text{Ln}^{3+}$ -based organic-inorganic hybrids. There are few examples reported between 2009 and 2012 of thermometers encompassing mixtures of organic dyes with  $\text{Ln}^{3+}$   $\beta$ -diketonate complexes embedded into siloxane matrices [185, 184]. These examples, as mentioned above, are among the few ones involving  $\text{Ln}^{3+}$  ions that effectively illustrate the temperature sensing/mapping at micron and sub-micron scale).

Peng *et al.* [184] reported the incorporation of the Eu-DT complex into siloxane hybrid NPs (formed by a BTD-PMMA hybrid matrix with a silica outer layer). The NPs display strong temperature dependence, in both luminescence intensity and  $^5\text{D}_0$  lifetime, over the physiological range. In fact, the intensity of the  $^5\text{D}_0 \rightarrow ^7\text{F}_2$  transition decreases by  $3.07\% \cdot \text{K}^{-1}$  on increasing temperature from 298 to 318 K, corresponding to  $S_m = 6.8\% \cdot \text{K}^{-1}$  at 323 K (table 2.1, figure 2.8). The temperature resolution is 0.3 K, assuming a precision of 1% in emission intensity. The  $^5\text{D}_0$  lifetime drops rapidly with the increase of temperature in that range displaying a maximum relative sensitivity of  $S_m = 3.2\% \cdot \text{K}^{-1}$  at 320 K [184] (table 2.1, figure 2.10). Another example of a non-ratiometric thermometer was presented by Tan and Wang [227] involving a dual luminophore probe based on a mixture of several  $\text{Eu}^{3+}$  and  $\text{Tb}^{3+}$  complexes ( $\text{Eu}(\text{dbm})_3 \cdot 2\text{H}_2\text{O}$ ,  $\text{Eu}(\text{acac})_3 \cdot 2\text{H}_2\text{O}$ ,  $\text{Tb}(\text{acac})_3 \cdot 2\text{H}_2\text{O}$  and  $\text{Tb}(\text{ca})$ ). The hydrogels (based on the octyltriethoxysilane matrix) are able to measure the temperature in the range 283-323 K with  $S_m = 2.1\% \cdot \text{K}^{-1}$  at 320 K [227] (table 2.1, figure 2.8).

Ratiometric thermometers were demonstrated by Peng *et al.* [185] using siloxane hybrid NPs formed by a BTD-PMMA core (incorporating the Eu-DT complex and a OASN reference) covered with a silica outer layer ( $S_m = 7.2\% \cdot \text{K}^{-1}$  at 323K, table 2.1, 2.9)[185].

Layer double hydroxides (LDHs) are another class of organic-inorganic hybrids also used in complex thermometric systems. LDH layers promote temperature changes in alignment, packing and or conformational constrains of an optically responsive part, which is sensitive to those changes [268, 105]. While Itho *et al.* [105] use changes in intensity to monitor the temperature, Yan *et al.* [268] use the ratio between two fluorescence intensities. Nevertheless, in both examples, rather than a thermometer the material is presented as an on/off sensor working between 293 and 373 K.

## Intracellular Thermometers

Temperature biological sensors are an integral part of cell membranes and their role is essential for the cell survival. The understanding of how these biological sensors process thermal information and how thermal processes develop at cellular level is of utmost importance in cell physiology. Apart from biological and structural approaches based on the conformation changes of DNA, RNA, proteins and lipids and their catalytic influence on subsequent biological processes [5, 125] there has been strong interest in the direct measuring and mapping of intracellular temperature [45, 179, 244]. Temperature influences both the cell equilibrium constants and its biochemical reaction kinetics governing, for instance, the creation and maintenance of concentration gradients, the metabolism and a large variety of other cellular activities [225, 81, 270]. Moreover, the cellular pathogenesis of diseases (*e.g.* cancer) is characterized by extraordinary heat production (pathological cells are warmer than normal ones because of their enhanced metabolic activity, as mentioned in the introduction) [81, 272, 272, 117], and temperature fluctuations of a few degrees are significant, for instance, in biomedical and cancer diagnosis and during hypothermia therapy or surgery [14]. Direct observation of intracellular temperature distribution and of its time evolution open new possibilities for understanding endogenous energy management in the cell, whether by performing work or by producing heat (thermogenesis), and how heat is released and to determine exogenous heat impact (thermal shocks) [152]. Furthermore, the direct observation of inhomogeneous intracellular temperature progression raises interesting new possibilities, including further innovations in nanomaterials for sensing local responses, as well as the concept of subcellular temperature gradient for signalling and regulation in cells [270]. Intracellular temperature mapping will result in a better understanding of cellular events and the establishment of novel diagnoses and therapies. This section describes developments oriented to measured temperature inside the cell.

Looking ahead to cellular temperature measurements, the introduction of fluorescent probes (NBD and LAURDAN) within the cells membrane was reported by Chapman *et al.* [45] A considerable temperature-dependent Stokes shift was reported, as the membranes undergo a gel-to-liquid-crystalline phase transition. LAURDANs micro environmental sensitivity permits a good temperature resolution (0.1-1.0 K) on a short dynamic range determined by the bilayer properties of the membrane. On the other hand, NBD is responsible for rapid, heat-induced electronic changes resulting in good sensitivity on fluorescence life-

time, which can provide temperature resolution of 2 K and  $S_m = 1.5\% \cdot K^{-1}$  at 340 K [45] (table 2.1, figure 2.10).

The work of Zohar *et al.* [285] was a pioneering example on thermal imaging of metabolic heat signals in single cells. Combining diffraction-limited spatial (30 nm) and sampling-rate-limited time resolution and using the temperature dependent luminescence intensity of the  $\text{Eu}(\text{tta})_3 \cdot 3 \text{H}_2\text{O}$  complex, intracellular heat waves generated by ligand-receptor interactions in single Chinese hamster ovary cells were imaged [285]. A decade later, Susuki *et al.* reported a technique for detection and measurement of the temperature changes in a single HeLa cervical cancer cell using a devised microthermometer comprising a glass micropipette filled with the same thermosensitive  $\text{Eu}(\text{tta})_3 \cdot 3 \text{H}_2\text{O}$  complex [225]. The micrometer size of the tip of this pipette enable to measure the local temperature with 0.1 K precision and micrometer spatial resolution (upon 365 nm excitation) [225]. The heat production in a single HeLa cell occurred with some time delay after the ionomycin-induced  $\text{Ca}^{2+}$  influx from the extracellular space. The time delay inversely depended on extracellular  $[\text{Ca}^{2+}]$  and the increase in temperature was suppressed when  $\text{Ca}^{2+}$ -ATPases were blocked by thapsigargin.

These observations strongly suggest that the enzymatic activity of  $\text{Ca}^{2+}$ -ATPases in endoplasmic reticulum leads to the heat production [225]. More recently, Gota *et al.* [81], reported the first polymer-based intracellular thermometer, where cell-to-cell resolution ( $\sim 10 \mu\text{m}$ ) was achieved. The system is composed of the thermoresponsive PNIPAM combined with the water-sensitive fluorophore, DBD-AA. It was designed to be biocompatible, to avoid cell-induced fluorescence quench and intra-cell precipitation, and to be pH insensitive. A practical use of this thermometer was verified by measuring cell-by-cell temperature increase after exposing them to an external chemical stimuli which causes heat production [81]. The internalised thermometer works in the 300-306 K range with a temperature resolution of  $\sim 0.3$ - $0.5$  degree and  $S_m = 9.4\% \cdot K^{-1}$  at 304 K (table 2.1, figure 2.8); outside the cell  $S_m$  is larger,  $12.7\% \cdot K^{-1}$  at 308 K (table 2.1, figure 2.8). The thermometer could not reveal, however, intracellular temperature distribution, as the relative large size ( $> 62$  nm in hydrodynamic diameter) and low hydrophilicity of the fluorescent nanogel hindered its spreading throughout the cell.

McCabe *et al.* [161] reported the first demonstration of a biomolecular intracellular thermometer through temperature-sensitive mutants of lacI controlling LacZ expression which is sensitive to the intracellular heat content of *Escherichia coli* in near-real time

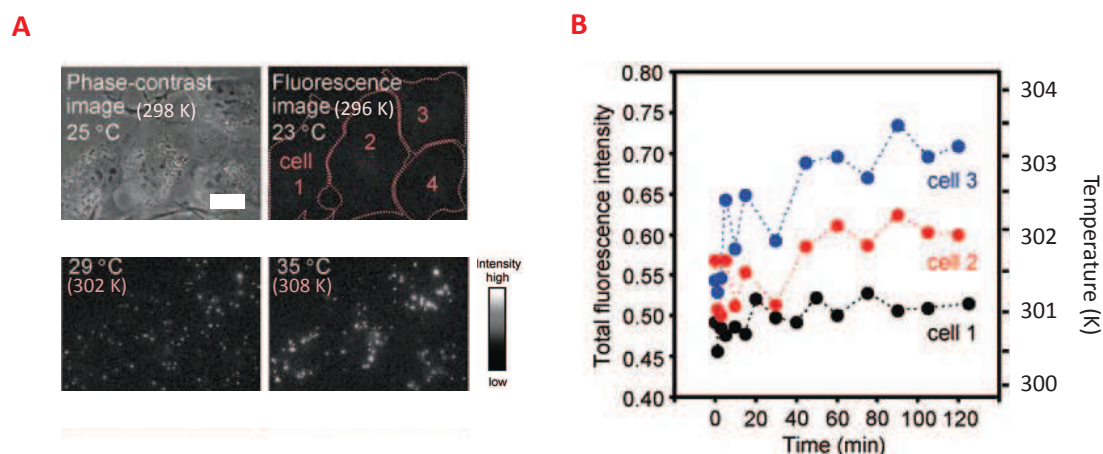


Figure 2.5: (A) Phase contrast and fluorescence images of living COS7n cells (scale bar corresponds to  $20\mu\text{m}$ ); (B) Temperature evolution of three different cells after the addition of camptothecin. (Adapted from C. Gota, K. Okabe, T. Funatsu, Y. Harada and S. Uchiyama, *J. Am. Chem. Soc.*, 2009, 131, 2766-2767) [81].

[161]. *lacI* is a DNA-binding protein which inhibits the expression of genes coding for proteins involved in the metabolism of lactose in bacteria. Calibrated fluorometric (and colorimetric) measurements showed that both whole *E. coli* cells and lysates expressed significant repeatable changes in  $\beta$ -galactosidase activity in the physiologically relevant temperature functional range (298 to 318 K) with at least 0.7 degree sensitivity (between 308 and 318 K),  $S_m = 19.6\% \cdot K^{-1}$  at 318 K, (table 2.1, figure 2.8). This model system suggests that changes in cellular heat content can be detected independently of the medium in which cells are kept, a feature of particular importance when the medium is heterogeneous or nonaqueous, or otherwise has a low heat transfer capacity [161].

The use of mesoporous materials as vehicles for the storage and controlled release of entrapped specific chemicals includes examples which respond to temperature changes as external stimuli [71, 208]. Based on this possibility, Aznar *et al.* [12] have developed a temperature sensor that can be internalised in a cell. The sensor consists of a mesoporous silica NPs loaded with *Safranin O* and functionalised with paraffin, as capping molecule that can melt at a defined temperature. The paraffin forms a hydrophobic layer that can block the pores and inhibit guest release at temperature below the paraffin melting point. Above this temperature the paraffin melts uncapping the pores. The NPs was endocited by HeLa cells and the stain was released above 312 K, the specific melting temperature of

the paraffin used in the experiments. As paraffins have a well-defined melting point, varying the paraffin type permits to develop temperature sensors at correspondingly different temperatures.

Intracellular thermal measurements are one of the great challenges for the application of photoluminescent QDs, which would complement their present use in chemically selective imaging [163]. In the period 2009-2012 the general thermal sensitivity properties of QDs (*e.g.* streptavidin-coated CdSe/ZnS core/shell QDs, QD655) have been used to measure intracellular temperatures in a single living cell (upon external chemical and physical stimuli) [104, 113, 157, 270]. For instance, the photoluminescence spectral shifts from endocytosed QD655 QDs were used to map intracellular heat generation in NIH/3T3 cells following  $\text{Ca}^{2+}$  stress and cold shock, showing that individual cells (like drosophila embryos, for instance) may use transient thermal gradients for signalling [270].

The imaging of living tissues up to a high depth requires NIR excitation in the biological window through multiphoton processes. The technique of two-photon fluorescent microscopy has been recently developed using femtosecond lasers and it has been shown that QDs present a large NIR two-photon excitation cross-section. Maestro *et al.* [157, 155, 156] demonstrated the potential use of CdSe and CdTe QDs as thermal mapping probes, as the emission peak and intensity depend on the environment temperature and can be imaged by means of high-resolution two-photon fluorescence microscope. The authors performed studies with QDs in phosphate buffered saline solutions and in HeLa cervical cancer cells. The NIR two-photon excitation leads to a temperature sensitivity of the QDs emission and intensity changes much higher than those achieved under visible one-photon excitation. Reported relative maximum sensitivity is  $0.310 - 1\% \cdot K^{-1}$  at 330 K (table 2.1, figure 2.8), for 2 nm sized QD, emitting near 525 nm at room temperature, when excited with a 900 nm laser.

Another very interesting example has been reported by Huang *et al.* involving local heating of superparamagnetic streptavidin-coated  $\text{MnFe}_2\text{O}_4$  NPs conjugated with DyLight549 to convert a rf magnetic signal into cell stimuli [104]. The NPs were targeted to specific proteins on the plasma membrane of HEK 293 cells and heated by a rf magnetic field (40 MHz, 8.4 G) between 303 and 319 K. The temperature profile was studied through the temperature dependence of the fluorescence intensity of DyLight549 (exclusively localized on the plasma membrane of the expressing cells) and Golgi-targeted GFP (co-expressed within the cell) as nanoscale thermometers. After applying the rf magnetic

field, the local temperature increased at the plasma membrane with the corresponding decrease in the DyLight549 fluorescence intensity ( $S_m = 1.5\% \cdot K^{-1}$  at 305 K, table 2.1, figure 2.8), while the Golgi-targeted GFP fluorescence intensity remained essentially unchanged, clearly demonstrating that the heat is generated locally at the plasma membrane without cytoplasmic heating [104] (figure 2.6). The rf magnetic field-induced NPs heating is sufficient to trigger the opening of TRPV1 ion channels within seconds, as established by measuring the calcium influx into HEK 293 cells. The potential of this approach to study neuronal signalling was demonstrated triggering behavioural responses in *C. elegans* worms.

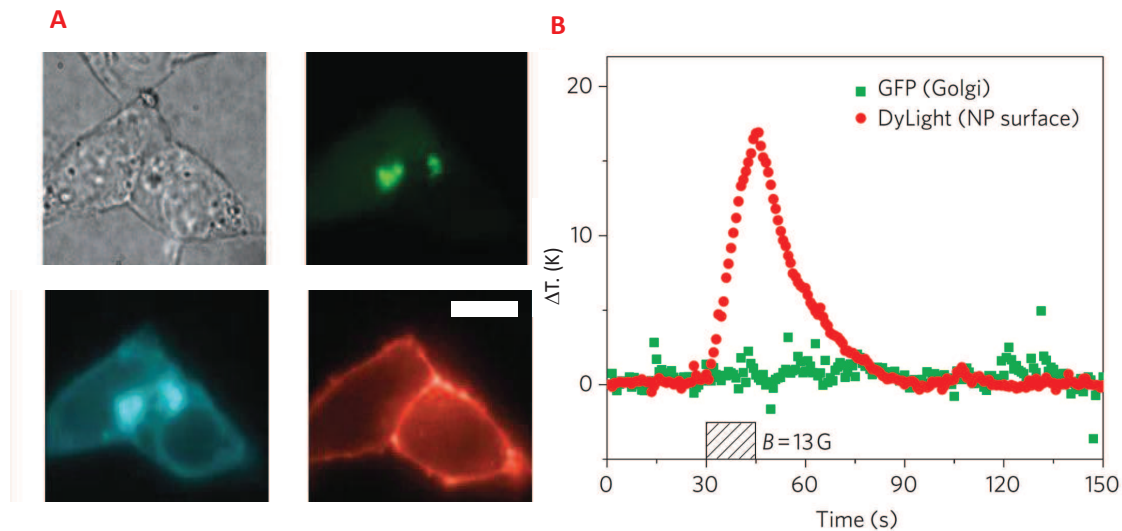


Figure 2.6: (A) Differential interference contrast (DIC) image displaying cells green fluorescence image indicating the Golgi localized GFP cyan fluorescence marking the membrane protein AP-CFP-TM red fluorescence of the DyLight549 on the NPs, which are exclusively localized on the plasma membrane of the AP-CFP-TM expressing cells. The scale bar corresponds to  $20 \mu m$ . (B) The application of the 13G RF magnetic field (hatched box), leads to the local temperature increase at the plasma membrane (red, measured by DyLight549 fluorescence). In the same time period, the temperature remained constant at the Golgi apparatus (green, measured by of Golgi-targeted GFP). (Adapted from H. Huang, S. Delikanli, H. Zeng, D. M. Ferkey and A. Pralle, *Nat. Nanotechnol.*, 2010, 5, 602-606) [104].

The cellular thermometers discussed so far are non-ratiometric and rely on measuring changes in the luminescence signal at a single wavelength. Highly efficient and reliable cel-

lular measurements require, however, luminescent temperature sensors that besides being nontoxic and having a bright optical signal to prevail over the background cell autofluorescence should also display ratiometric (or self-referencing) readout. Vetrone *et al.* [238], Fischer *et al.* [69] and Ye *et al.* [272] showed a major step forward towards the development of ratiometric cellular thermometers.

Vetrone *et al.* devised a nanothermometer based on the temperature-sensitive UC green emission of NaYF<sub>4</sub>:ErYb NPs [238]. The UCNPs are excited through low power and inexpensive NIR lasers with wavelengths in the optical penetration window of cells and tissues. The internalization of the NPs by HeLa cervical cancer cells exploits the thermal sensitivity of the ratiometric intensity ratio between the Er<sup>3+</sup> <sup>2</sup>H<sub>11/2</sub> → <sup>4</sup>I<sub>15/2</sub> (green emission) and <sup>4</sup>S<sub>3/2</sub> → <sup>4</sup>I<sub>15/2</sub> (yellow-green emission) transitions to create a nanothermometer capable of measuring the internal temperature of a living cancer cell, from 298 K to its thermally induced death at 318 K [238]. The cells were placed in a confocal fluorescence microscope and excited at 920 nm so that the UC Er<sup>3+</sup> fluorescence permitted the measurement of the inner HeLa cell temperature with  $S_m = 1.0\% \cdot K^{-1}$  at 298 K (table 2.1, figure 2.11). Temperature-dependent confocal fluorescence microscopy images of HEK 293 cells transfected with similar NaYF<sub>4</sub>:ErYb NPs with sub-micrometer resolution were obtained by Fischer *et al.* [69] based on the ratiometric sensing of the green and red (<sup>4</sup>F<sub>9/2</sub> → <sup>4</sup>I<sub>15/2</sub>) Er<sup>3+</sup> lines. The NPs are able to detect (without using an exterior reference) the cellular changes occurring between 298 and 318 K, as a result of the external heating. However, the thermometer sensitivity is not reported and no data is published to estimate it. These NPs are one of the few examples reported so far of cellular thermometers based on Ln<sup>3+</sup> ions, the other three examples involves the Eu(tta)<sub>3</sub> · 3H<sub>2</sub>O complex [225, 275, 285]. Two-photon excited NIR-to-visible UCNPs (NaYF<sub>4</sub>:Yb<sup>3+</sup>/Ln<sup>3+</sup>, Ln=Er, Ho, Tm, and CaF<sub>2</sub>:Yb<sup>3+</sup>/Ln<sup>3+</sup>, Ln=Er, Tm) were also used for high-contrast intracellular fluorescence images of HeLa cells [79, 52] and *in vivo* whole body nude mouse [276]. A cost-effective 915 nm laser is employed as a new promising excitation approach for better NIR-to-NIR UC photoluminescence *in vitro* or *in vivo* imaging providing drastically less heating of the biological specimen and larger imaging depth, due to quite low water absorption [276]. Tissue penetration depths in the biological window as large as 2 mm were also demonstrated using the CaF<sub>2</sub>:Tm<sup>3+</sup>/Yb<sup>3+</sup> UCNPs (due to the Tm<sup>3+</sup> NIR emission at 800 nm), which are more than 4 times those achievable based on the visible emissions of the particles with Er<sup>3+</sup> [61]. Furthermore, as the Tm<sup>3+</sup> <sup>3</sup>H<sub>4</sub> → <sup>3</sup>H<sub>6</sub> transition is sensitive

to temperature changes, the authors also demonstrated the ability of  $\text{CaF}_2:\text{Tm}^{3+}/\text{Yb}^{3+}$  UCNPs as nanothermometers [61] (table 2.1, figure 2.11).

Pdots formed by RhB attached to amphiphilic amino-terminated PS blended with semi-conducting polymers (Pdot-RhB NPs) showed ratiometric temperature sensing under 450 nm excitation that matches well the physiologically relevant temperature range [272]. After internalization into live HeLa cells (via endocytosis) the Pdot-RhB NPs (size-tuned between 20 and 160 nm) can measure intracellular temperatures in a live-cell confocal fluorescence imaging mode with  $S_m = 2.6\% \cdot K^{-1}$  at 343 K (table 2.1, figure 2.11). The average cell temperatures reported are in very good agreement with those measured with conventional thermocouples [272].

Although rare, there are also some reports on non-luminescent cellular thermometers [173, 240, 244]. Wang *et al.* have designed a thermocouple device for detecting intracellular temperature accurately [244]. The thermocouple consists of a sandwich structure formed by a tungsten substrate, an insulating layer made of polyurethane and a platinum tip. Calibration experiments using different Pt thicknesses showed that a 100 nm one matched almost perfectly the temperature-voltage curves produced by standard thermocouples of macro scale. The device showed a temperature resolution better than 0.1 degree and a time response of  $\sim 400$  ns. Insertion of the thermocouple in a single U251 cell allowed the observation of intracellular temperature fluctuations induced by the addition of camptothecin, a DNA *topoisomerase I* inhibitor that can promote tumour cell death. Other examples of the use of non-luminescent temperature sensors in biological systems with subcellular resolution include complex RNA structures that change their conformation in response to temperature [173] and MWCNTs filled with cuprous iodide, which displays strong temperature-dependent NMR characteristics [240]. In addition, an AFM cantilever with a heating resistor above a sharp silicon tip of 5-10 nm has been used to investigate heat conductance on biological materials with nanometric spatial resolution [90].

Very recently Okabe *et al.*, claimed the development of the first effective intracellular temperature mapping. It is based on the temperature-dependent fluorescence lifetime of a novel polymeric thermometer using time-correlated single photon counting coupled with fluorescence lifetime imaging microscopy [179]. The polymer chains encompass thermosensitive, hydrophilic and fluorescent units and can effectively diffuse throughout the cells. With a spatial resolution at the diffraction limited level (200 nm) and  $S_m = 4.4\% \cdot K^{-1}$  at 311 K (table 2.1, figure 2.8) - at 307 K for  $S_m$  calculated based on the lifetime (table 2.1,

figure 2.9) the intracellular temperature mapping reported indicates that: i) the nucleus and centrosome of a COS7 cell displayed a significantly higher temperature than the cytoplasm and ii) the temperature gap between the nucleus and the cytoplasm depends on the cell cycle (figure 2.7). The heat production from mitochondria was also observed as a nearby local temperature increase [179].

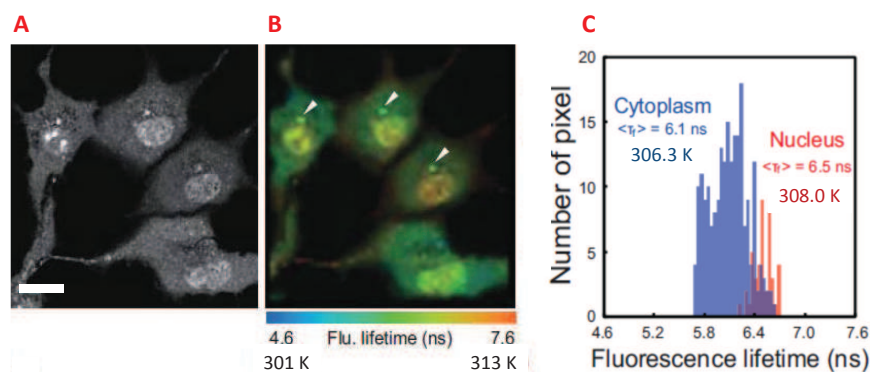


Figure 2.7: Temperature mapping in living COS7 cells. Confocal fluorescence image (A) and fluorescence lifetime image (B) of a fluorescent polymer internalized in the COS7 cells, demonstrating higher temperature in the nucleus than in the cytoplasm of the cell. (C) Histograms of the fluorescence lifetime (and correspondent temperature) in the nucleus and in the cytoplasm in a representative cell (the leftmost cell in A) demonstrating a mean temperature gradient of 1.9 K. The room temperature was maintained constant at 293 K during the measurement. The scale bar corresponds to 20  $\mu\text{m}$ . (Adapted from K. Okabe, N. Inada, C. Gota, Y. Harada, T. Funatsu, S. Uchiyama, Nature Comms., 2011, in press) [179].

## Figure of merit of luminescent molecular thermometers

Table 2.1: Figure of merit of luminescent molecular thermometers displaying the maximum relative sensitivity values ( $S_m, \% \cdot K^{-1}$ ), the temperature range of operation ( $\Delta T, K$ ), the temperature at which  $S_m$  is maximum ( $T_m, K$ ) and the thermometric property associated to each example. Self-referencing (or ratiometric) examples are highlighted and, when reported, the spatial resolution is indicated.

ORGANIC DYES					
Phosphor	Refs.	$S_m$	$\Delta T (T_m)$	Thermometric Property	Observations
Ru–phen complex	[129,130]	2.5	280–325 (320)	Emission lifetime	Oxygen sensor reported
Perylene and <i>N</i> -allyl- <i>N</i> -methylaniline in PS	[44]	1.3	327–357 (350)	Monomer–to–exciplex interconversion	Ratiometric
1,3-bis(1-pyrenyl)propane in [C <sub>4</sub> mpy][Tf <sub>2</sub> N]	[14]	1.4	303–413 (355)	Monomer/excimer emission intensity ratio	Ratiometric
Fluorescein D/Texas–Red A in DNA	[19]	4.5	278–318 (295)	FRET	DNA molecular beacon labelled with acceptor/donor pair; simultaneous oxygen sensor; ratiometric
PtOEP	[154]	4.6	290–320 (305)	Emission intensity ratio	Ratiometric
Naphthalene fragment linked to a Ni(II) cyclam	[65]	3.6	300–370 (300)	Emission intensity	Non–ratiometric
RhB in PDMS	[203]	2.3	293–373 (363)	Emission intensity	Non–ratiometric, temperature mapping
RhB in SU8	[114]	1.3	293–353 (338)	Emission intensity ratio	Reference intensity corresponds to the room temperature measurement; ratiometric; temperature mapping
DPTB dissolved in MOE	[68]	0.1	323–373 (373)	Maximum emission wavelength	Non–ratiometric, spatial resolution of 40 $\mu$ m
Fe(NH <sub>2</sub> Trz) <sub>3</sub> (tos) <sub>2</sub>	[202]	1.9	305–325 (309)	Emission intensity	Non–ratiometric, spatial resolution at the micrometer range
NBD/Laurdan	[45]	1.5	300–340 (340)	Emission lifetime	Intracellular thermometer

POLYMERS AND LAYERED DOUBLE HYDROXIDES					
Phosphor	Ref.	$S_m$	$\Delta T (T_m)$	Thermometric Property	Observations
Pristine Fullerene and C <sub>70</sub> in PS NPs	[11]	1.3	293–363 (330)	Emission intensity	Non-ratiometric
C <sub>70</sub> in PtBMA	[15]	2.2	293–363 (363)	Emission lifetime	Only demonstrated in the absence of oxygen; perylene as internal standard for intensity ratio; ratiometric
		1.8	293–363 (330)	C <sub>70</sub> /perylene emission intensity ratio	
PNIPAM:DBDAA	[81]	12.7	298–313 (308)	Emission intensity	Non-ratiometric (in a KCl buffer).
		9.4	298–313 (304)	Emission intensity	Non-ratiometric; intracellular thermometer; spatial resolution of 10 $\mu\text{m}$
PNIPAM-co-HC	[213]	18.9	288–313 (308)	Emission intensity	Non-ratiometric
PNIPAM-co-BODIPY	[247]	11.5	288–308 (302)	Emission intensity	Non-ratiometric
PNIPAM containing 3HF-AM	[46]	6.7	293–325 (314)	Emission intensity ratio	pH insensitive; ratiometric
Pyrene-labelled poly(DEGMA-stat-PyMMA)	[189]	3.5	278–303 (294)	Emission intensity ratio	Ratiometric
Magnetite NPs with NIPAM:FMA	[96]	16.7	298–318 (314)	Emission intensity	Non-ratiometric
NNPAM/NIPAM/NIPMAM	[82]	12.5	275–340 (300)	Emission intensity	Non-ratiometric

POLYMERS AND LAYERED DOUBLE HYDROXIDES (CONT.)

Phosphor	Ref.	$S_m$	$\Delta T (T_m)$	Thermometric Property	Observations
GFP	[262]	4.1	283–323 (322)	Relaxation time	Maximum sensitivity at pH=6
GFP	[62]	0.5	293–333 (333)	Polarization Anisotropy	Ratiometric intracellular thermometer, spatial resolution ~300 nm
PNIPAM	[83]	10.4	293–318 (308)	Emission lifetime	Average fluorescence lifetime computed from two lifetimes
NIPAM labelled with benzofurazan	[84]	16.2	295–310 (307)	Emission lifetime	Describes the fluorescence lifetime imaging microscopy; spatial resolution ~50 $\mu\text{m}$
Pdot–RhB NPs	[272]	2.6	313–343 (343)	Polymer/RhB emission intensity ratio	Intracellular thermometer; ratiometric
MnFe <sub>2</sub> O <sub>4</sub> NPs coated with streptavidin–DyLight549	[104]	1.5	300–315 (305)	Emission intensity	Cellular membrane temperature measurement; non–ratiometric
RhB and NBD	[243]	13.3	298–318 (313)	FRET	Non–ratiometric, intracellular thermometer
PNIPAM–coated Au NPs	[167]	0.1	290–310 (295)	Wavelength of maximum emission	Non–ratiometric
Fluorescent Polymer	[179]	4.4	293–323 (311)	Emission lifetime	Intracellular thermometer, spatial resolution of 200 nm
Mutant of <i>lacI</i> ( <i>Its265</i> )	[161]	19.6	308–318 (318)	Emission intensity	Non–ratiometric

## QUANTUM DOTS

Phosphor	Ref.	$S_m$	$\Delta T (T_m)$	Thermometric Property	Observations
(CdSe)ZnS QDs	[242]	2.2	278–313 (313)	Emission intensity	Non-ratiometric
Zn <sub>0.99</sub> Mn <sub>0.01</sub> Se/ZnCdSe NPs	[239]	1.0	173–273 (185)	Excitonic intensity ratio	ZnMnSe/ZnCdSe diameters are 4.5/1.0nm; ratiometric
		1.3	293–373 (318)		ZnMnSe/ZnCdSe diameters are 4.0/0.6nm; ratiometric
		0.9	293–373 (383)		ZnMnSe/ZnCdSe diameters are 3.7/0.4nm; ratiometric
CdSe and CdTe QD solutions	[155,157]	$0.3 \times 10^{-1}$	315–330 (330)	Wavelength of maximum emission	QDs incorporated in HeLa cells, excited using a 900 nm laser; non-ratiometric
CdSe/ZnS and CdTe/ZnS	[113]	0.9	287–320 (320)	Emission intensity ratio	Simultaneous oxygen sensing using a bifurcated fibre; ratiometric

LN<sup>3+</sup> PHOSPHORS

Phosphor	Ref.	$S_m$	$\Delta T (T_m)$	Thermometric Property	Observations
YAG:Ce NPs	[7]	0.2	315–350 (350)	Emission lifetime	Non-ratiometric
Y <sub>2</sub> O <sub>3</sub> :Eu <sup>3+</sup>	[120]	2.6	473–973 (973)	Rise time	Non-ratiometric; relatively high uncertainty
ZnO:Er <sup>3+</sup> NPs	[253]	0.6	273–473 (273)	Emission intensity	Ratiometric
PbF <sub>2</sub> :Er <sup>3+</sup> /Yb <sup>3+</sup> NPs	[1,2]	1.0	315–415 (345)	<sup>2</sup> H <sub>11/2</sub> → <sup>4</sup> I <sub>15/2</sub> / <sup>4</sup> S <sub>3/2</sub> → <sup>4</sup> I <sub>15/2</sub> intensity ratio	Ratiometric, spatial resolution below 500 nm
Er <sup>3+</sup> /Yb <sup>3+</sup> co-doped fluoride amorphous glass particle	[200]	1.1	335–375 (342)	<sup>2</sup> H <sub>11/2</sub> → <sup>4</sup> I <sub>15/2</sub> / <sup>4</sup> S <sub>3/2</sub> → <sup>4</sup> I <sub>15/2</sub> intensity ratio	Ratiometric, spatial resolution below 500 nm
Gd <sub>2</sub> O <sub>3</sub> :Yb <sup>3+</sup> /Er <sup>3+</sup> UCNPs	[216]	0.2	295–1000 (600)	<sup>2</sup> H <sub>11/2</sub> → <sup>4</sup> I <sub>15/2</sub> / <sup>4</sup> S <sub>3/2</sub> → <sup>4</sup> I <sub>15/2</sub> intensity ratio	Ratiometric
NaYF <sub>4</sub> :Er <sup>3+</sup> /Yb <sup>3+</sup> UCNPs	[238]	1.0	298–318 (298)	<sup>2</sup> H <sub>11/2</sub> → <sup>4</sup> I <sub>15/2</sub> / <sup>4</sup> S <sub>3/2</sub> → <sup>4</sup> I <sub>15/2</sub> intensity ratio	Ratiometric intracellular thermometer
Er <sup>3+</sup> /Yb <sup>3+</sup> and Tm <sup>3+</sup> /Yb <sup>3+</sup> UCNPs	[61]	2.3	293–318 (318)	<sup>2</sup> H <sub>11/2</sub> → <sup>4</sup> I <sub>15/2</sub> / <sup>4</sup> S <sub>3/2</sub> → <sup>4</sup> I <sub>15/2</sub> intensity ratio	Ratiometric
		0.2	293–318 (315)	Intensity ratio between two sub-Stark energy levels of the Tm <sup>3+</sup> <sup>3</sup> H <sub>4</sub> excited state	

## ORGANIC-INORGANIC HYBRID NPs

Phosphor	Ref.	$S_m$	$\Delta T$ ( $T_m$ )	Thermometric Property	Observations
Eu(tta) <sub>3</sub> •3H <sub>2</sub> O embedded into PMMA	[126]	4.4	293–333 (330)	Emission intensity	Non-ratiometric intracellular thermometer, uncertainty of 0.3 K
Eu(tta) <sub>3</sub> L complexes embedded into PTBS microbeads	[24]	1.1	275–340 (333)	Emission lifetime	Using poly(vinyl methylketone) as support polymer
P(VDC-co-AN) NPs co-doped with an Eu <sup>3+</sup> complex and BBS	[254]	7.2	273–323 (323)	<sup>5</sup> D <sub>0</sub> → <sup>7</sup> F <sub>2</sub> /BBS intensity ratio	Two dimensional thermo-imaging; ratiometric
Eu-DT embedded into BTB/PMMA NPs	[184]	6.8	283–323 (323)	<sup>5</sup> D <sub>0</sub> → <sup>7</sup> F <sub>2</sub> intensity	Non-ratiometric
		3.2	283–323 (320)	<sup>5</sup> D <sub>0</sub> lifetime	
Eu-DT and OASN in silica NPs	[185]	7.2	283–323 (323)	<sup>5</sup> D <sub>0</sub> → <sup>7</sup> F <sub>2</sub> /OSAN intensity ratio	Ratiometric
Eu <sup>3+</sup> and Tb <sup>3+</sup> embedded into PAA/OTES hydrogels	[227]	1.7	283–323 (310)	<sup>5</sup> D <sub>0</sub> → <sup>7</sup> F <sub>2</sub> intensity	Non-ratiometric
		2.1	283–323 (320)	<sup>5</sup> D <sub>4</sub> → <sup>7</sup> F <sub>5</sub> intensity	

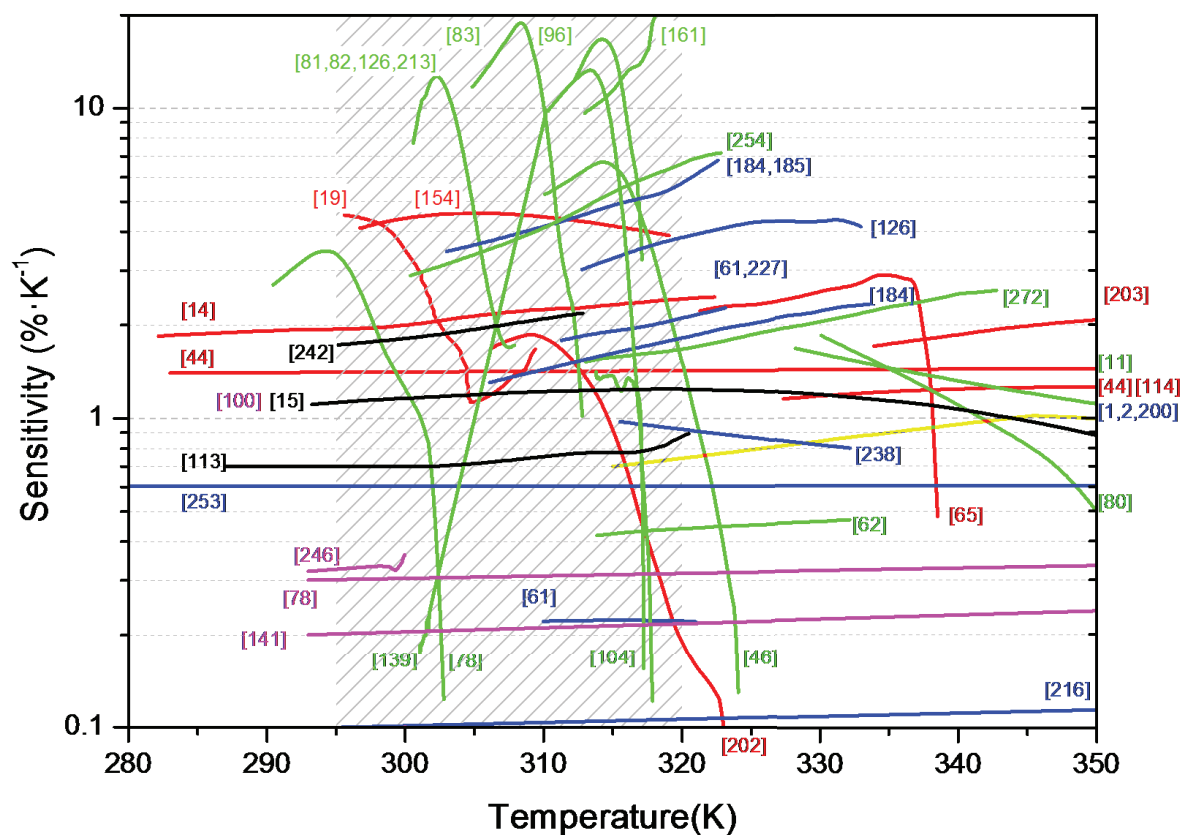


Figure 2.8: Temperature dependence of the maximum relative sensitivity value  $S_m$  for the series of thermometers reported in tables 2.1 and 2.2. The dye-, polymer-, QDs- and Ln<sup>3+</sup>-based luminescent thermometers are displayed in red, green, black and blue, respectively. The non-luminescent thermometers are shown in magenta. The physiological temperature range area is shadowed. For an intelligible reading of the figure superimposed curves were removed, presenting the one with the largest  $S_m$ . The numbers presented are correspondent to the references.

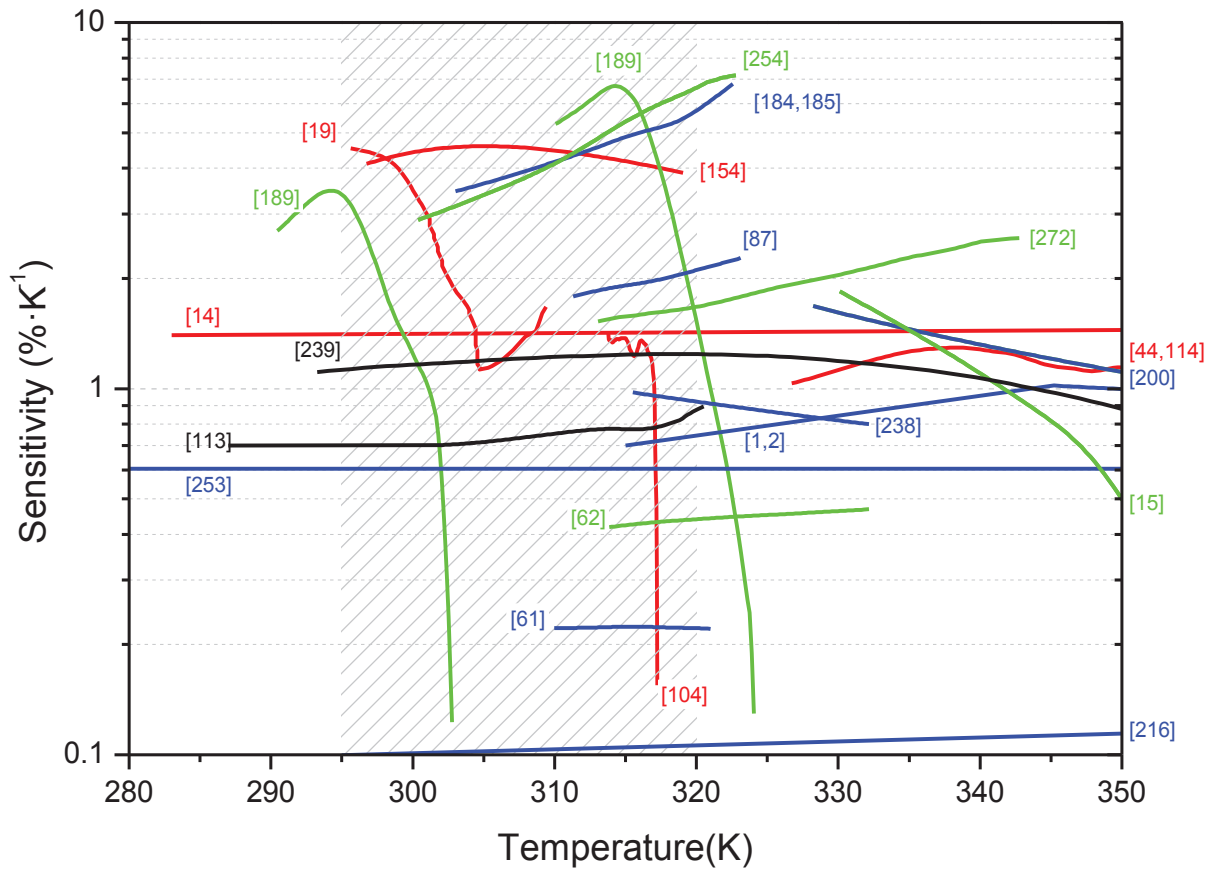


Figure 2.9: Temperature dependence of the relative sensitivity values for the series of luminescent ratiometric thermometers reported in table 2.1. The dye-, polymer-, QDs- and Ln<sup>3+</sup>-based thermometers are displayed in red, green, black and blue, respectively. The physiological temperature range area is shadowed. For an intelligible reading of the figure superimposed curves were removed, presenting the one with the largest  $S_m$ .

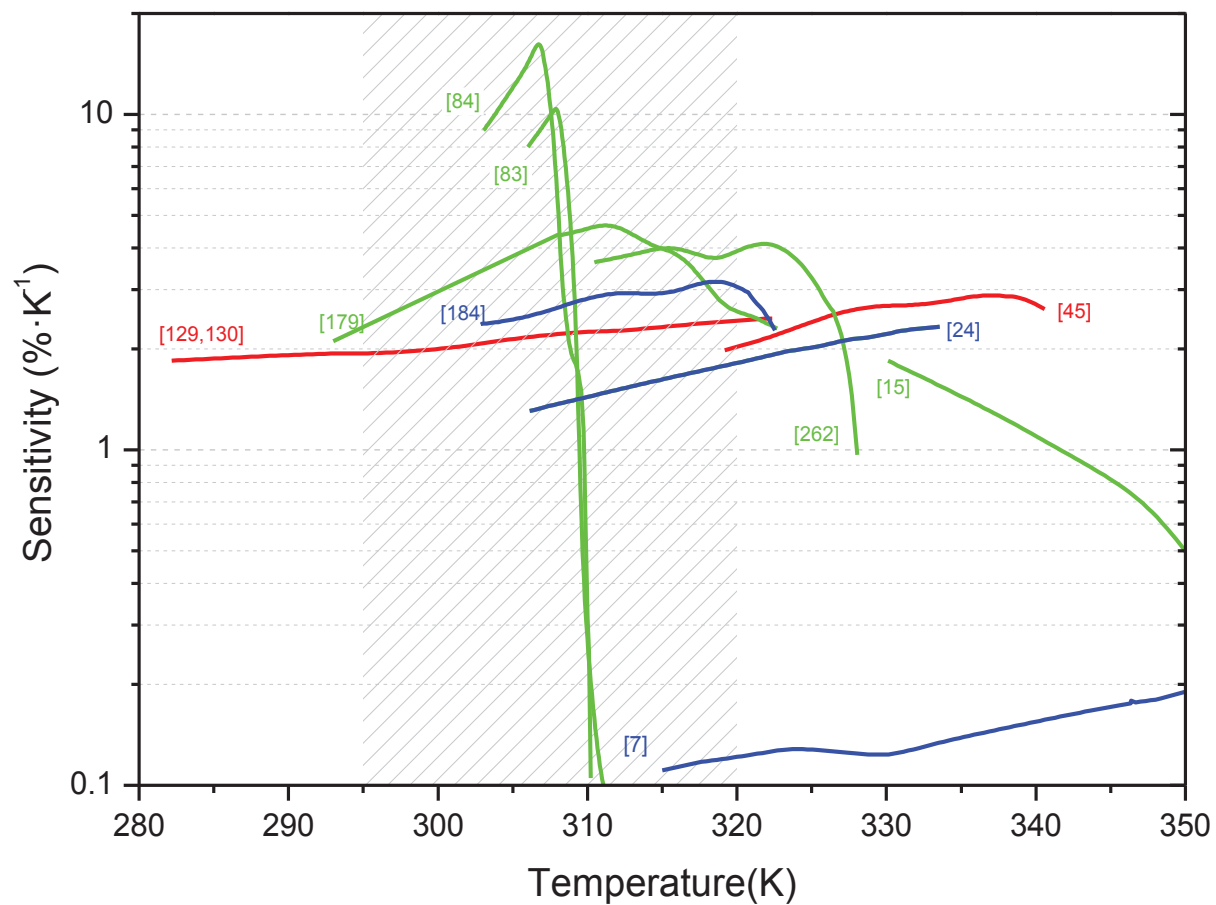


Figure 2.10: Temperature dependence of the relative sensitivity values estimated from lifetime or rise time measurements of the examples reported in table 2.1

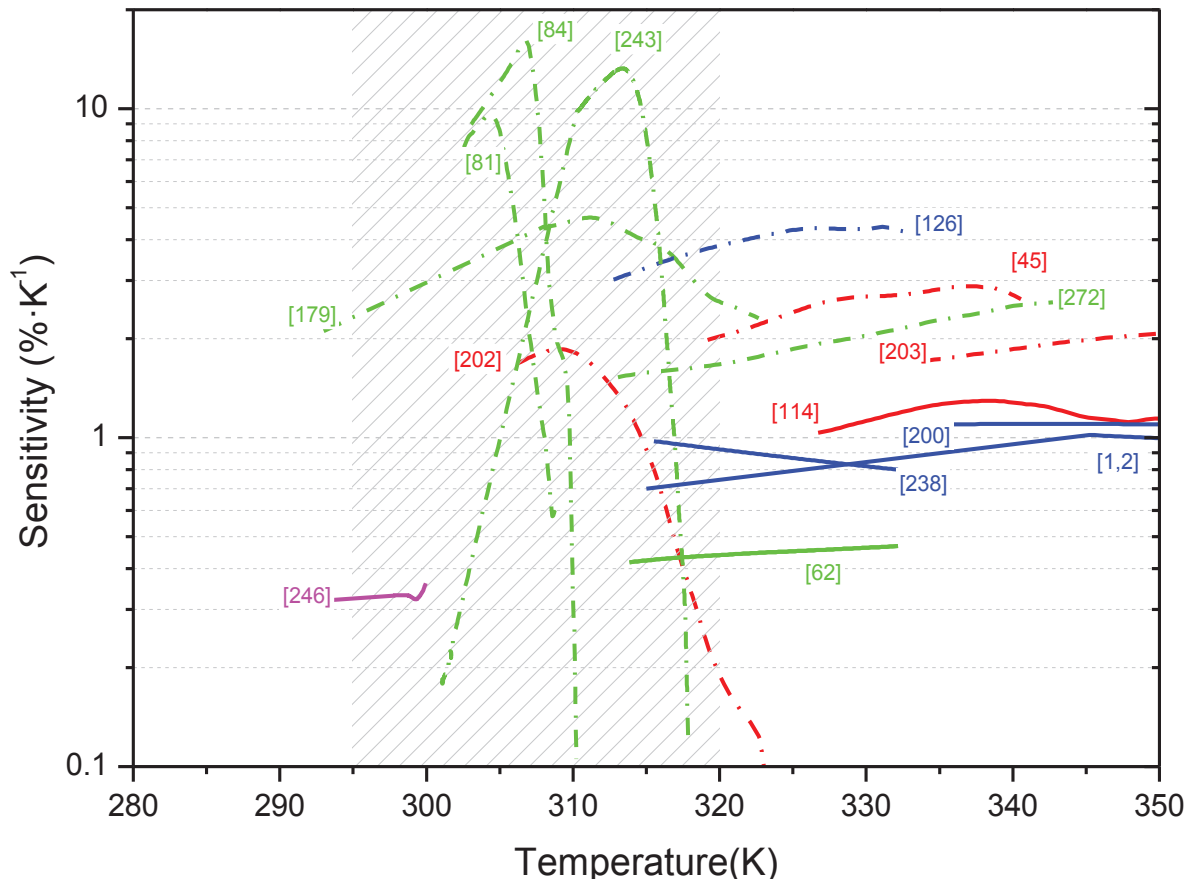


Figure 2.11: Temperature dependence of the relative sensitivity values for the series of thermometers reported in tables 2.1 and 2.2 that display spatial resolution on the micron and submicron scale (the non-ratiometric luminescent thermometers are marked as dotted lines). The physiological temperature range area is shadowed.

## 2.2 Non-Luminescent Thermometers Review

This section will cover a large variety of thermometric systems of nano-size and molecular dimensions, in which thermometric property is not directly related to luminescence. Some of them cannot be considered thermometers or even sensors in a strict sense, as they only respond to a given temperature threshold. Driving forces for the development of this kind of thermometry have been endless demands in nanolithography and microelectronics, developments in the use of nanotubes, whether carbon or metal oxides, in addition to the many application possibilities offered by these systems as well as strong clinical needs to monitor temperature at cellular level and to map temperature distributions in tissues with high spatial resolution.

### 2.2.1 Scanning Thermal Microscopy

Soon after the invention of the STM [22] the interest in measuring temperatures with very high spatial resolution became an obvious step forward. The technique, known as SThM, was developed in 1986 by Williams and Wickramasinghe employing a STM probe with a thermocouple junction of  $\sim 100$  nm fabricated at the probe tip [260]. Monitoring the two metals that constitute the thermocouple performs the temperature measurement. Temperature differences as small as 1 mK between the thermocouple junctions could be detected. The main purpose, however, of this first SThM was not for mapping the temperature distribution on a surface but to provide a mean for material-independent profiling of surfaces. Combined STM/SThM devices, where a thermal sensor is used as a tunnelling source and as a temperature detector, have also been used [92, 222]. The use of such instruments is limited to conducting surfaces.

A wider variety of samples can be imaged using the AFM for SThM, as the specimens do not need to be conductors. Two main types of scanning probes have been developed. The first one is a thermocouple junction situated at the extremity of the tip as described in the previous paragraph for the STM-based devices [166, 159]. The second probe is a resistive wire bent at its extremity to form a sharp tip. The sample temperature is determined by measuring the variation of the electrical resistance of the wire [92, 137, 195]. Resistive tips were initially used in dc mode, the measurements being relevant only for low thermal conductivity materials. However, quantitative thermal conductivity measurements can be performed with uncertainty several orders of magnitude smaller using the tip in

the ac mode. Contrary to dc data, the dependence of *ac* measurements on the ambient temperature is negligible. One example is the so-called  $3\text{-}\omega$  method based on that under ac heating and given the linear dependence of the probe electrical resistance to temperature, the third harmonic of the tip voltage is also linear to the temperature [137]. A schematic description of the experimental setup is depicted in figure 2.12. A large number of SThM probes have been developed, either as individually crafted cantilevers and sensors [91, 131, 153, 159, 169, 190], 186, or as batch fabricated thermocouples [59, 166, 212, 280]. Cretin *et al.* give an updated description of the working principles of various near-field microscopes, recent developments and the kind of information that can be obtained [55]. A number of developments based on new cantilevers and new AFM-based temperature measuring techniques have been stated in since 2007 [1, 2, 17, 57, 64, 124, 199, 259, 258, 274, 281, 279]. Sadat *et al.* [197] have reported a thermometric AFM- based technique which does not require integrated temperature sensors in AFM probes.

The technique allows direct mapping of topography and temperature fields of metal surfaces with  $\sim 0.01$  degree temperature resolution and  $< 100\text{nm}$  spatial resolution. It uses point contact junctions that consist of the measurement of the thermoelectric voltage of a platinum-gold point contact that is a function of the local temperature. The authors prepared a Si AFM cantilever with a tip radius of  $\sim 20$  nm, depositing a double Ti/Pt (5/40 nm) layer on both sides of the cantilever. On a gold surface a temperature distribution was scanned using the AFM tip in soft contact ( $\sim 10$  nN). The Ti/Pt-coated AFM cantilever (estimated to have a contact diameter of  $\sim 10$  nm) was anchored to a thermal reservoir at room temperature and produces a well-defined and reproducible electrical conductance that depends only on the local temperature of the point contact. Figure 2.13 shows a topographical image of the test device with a varying area of cross section, the temperature distribution along a measuring line and a three-dimensional representation of the temperature field in a section of the test device. The technique is intrinsically limited to metals and is not applicable to biological systems [137].

Instead, cantilever-based AFM has been specifically designed to investigate heat conductivity in biological materials [90]. The AFM cantilevers were a modification of those developed in the millipede project [22]. It was made entirely of silicon and to improve the resolution of heat-conductivity measurements a resistor for Joule heating was placed above a sharp silicon tip etched to a tip radius of 5-10 nm. Thermal conductivity in proteoliposomes, human hair and collagen samples was measured with a spatial resolution of  $\sim 10$

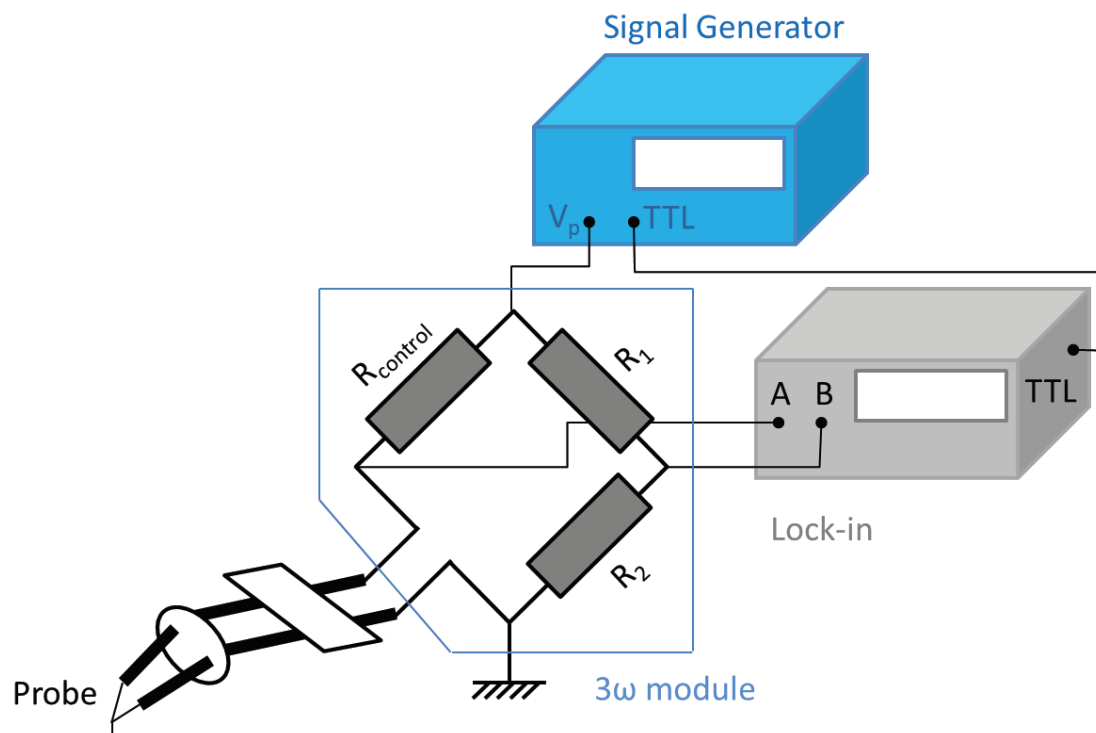


Figure 2.12: Schematic view of an AFM/SThM device based on ac heating of the resistive probe and monitoring ac current. Temperature at the tip is related to the third harmonic of the voltage (Adapted from S. Lefevre and S. Volz Rev. Sci. Instrum., 2005, 76, 033701) [137].

nm and thermal resolution of 50 nW, as depicted in figure 2.14.

Optical techniques, particularly luminescent ones, can be very useful to measure temperatures and to map temperature distribution on a surface as described in detail in previous sections. The combination of AFM and a luminescent probe allows overcoming the so called Rayleigh diffraction limit which fixes the minimum dimensions of a focusing spot to about half size of the wavelength used. The use of this technique, known as NSOM, for thermometric purposes has been reviewed by Cahill *et al.* [34] and Christofferson *et al.* [53].

An interesting technique based on the tunnelling of the free electron gas has been demonstrated by Pavlov [183]. The relative shift in the Fermi levels between two metallic electrodes, *e.g.* a copper substrate coated with copper oxide and a STM platinum tip in the demonstrator, should correlate with absolute temperature according to the Fermi-

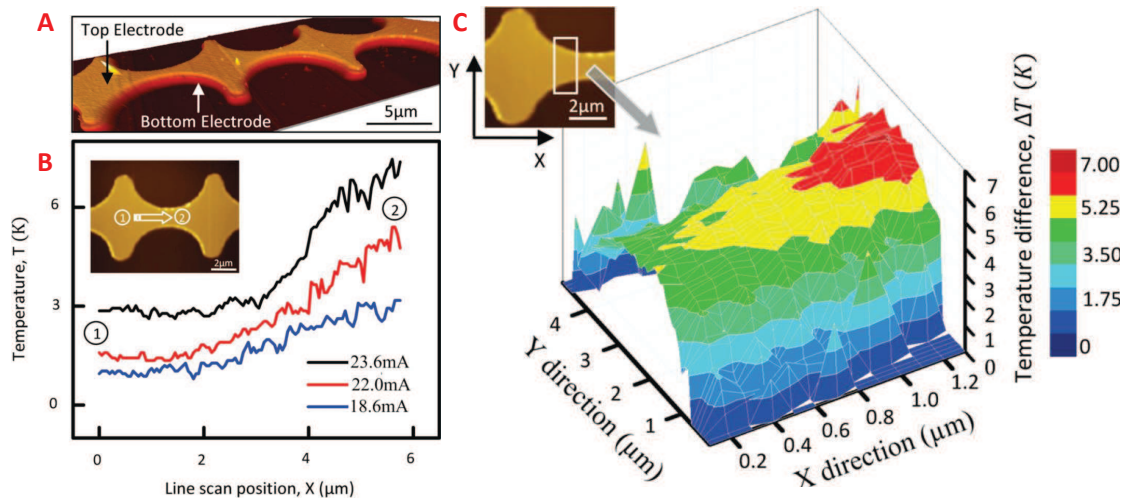


Figure 2.13: (A) Topographical image of a test device with varying cross section. The device features a bottom electrode (100 nm thick) that is electrically isolated from the top electrode (30 nm thick) by a 10 nm thick  $\text{Al}_2\text{O}_3$  layer. An electric current injected into the bottom electrode leads to temperature gradients in both electrodes. (B) The temperature distribution along a line from point 1 to 2 (shown in inset) is measured with 50 nm spatial resolution for three different bottom electrode heating currents. (C) Three-dimensional representation of the temperature field in a section of the test device indicated in the inset. (Adapted from S. Sadat, A. Tan, Y. J. Chua and P. Reddy, *Nano Lett.*, 2010, 10, 2613-2617) [197]

Dirac equation. Measuring the tunnelling current at zero voltage between the tip and the substrate, Pavlov has shown that the Fermi-level shift provides a measure of the substrate from room temperature up to 1250 K, with  $S_m = 0.5\% \cdot K^{-1}$  at 500 K (table 2.2) and nanometer spatial resolution ( $\sim 20$  nm) [183]. The temperature measuring technique is limited to metallic substrates and tips.

## 2.2.2 Nanolithography Thermometry

A number of temperature sensors and thermocouples fabricated using vapour deposition or lithography techniques and suitable for the temperature observation at the nanoscale have been described. As an example, a focused  $\text{Ga}^+$  beam has been used to deposit a Pt nano-strip by decomposition of an organometallic precursor like  $(\text{CH}_3)_3\text{Pt}$  on a tungsten nano-strip previously deposited on an electrical insulator substrate by decomposition

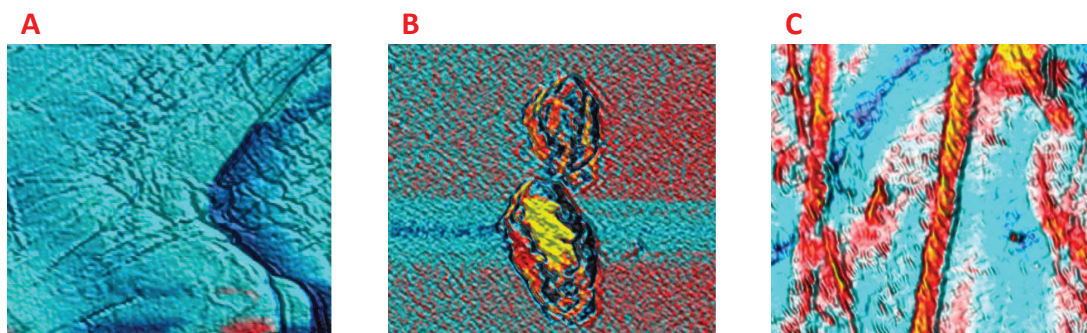


Figure 2.14: (A)  $2.2\mu\text{m}$  scan on a human hair that was bleached and pre-treated with strong detergents. The colour texture corresponds to variations in the heat flux of about  $100\text{ nW}$  from dark blue to violet, with decreasing heat conductance towards violet. (B)  $2.2\mu\text{m}$  scan of a vesicle preparation with reconstituted membrane proteins prepared on a silica wafer surface with highly resolved differences in thermal conductivity within the vesicles. (C)  $8.8\mu\text{m}$  scan of a preparation of collagen fibres on a glass substrate with a color texture corresponding to a high thermal conductance for dark blue and lower thermal conductance from red to yellow. (Adapted from W. Haeberle, M. Pantea, and J. K. H. Hoerber, *Ultramicroscopy*, 2006, 106, 678-686) [90].

of  $\text{W}(\text{CO})_6$  molecules [50]. The resulting  $\text{Pt}(\text{Ga})/\text{W}(\text{Ga})$  nanoscale junction has a temperature coefficient of approximately  $5.4\text{ mV/degree}$ , a value more than 100 times larger than conventional *K-type* thermocouples. Another temperature sensor consists in a parallel array of nanoscale thermocouples formed by two p- and n-type nanowire electrodes deposited in a substrate. The number of electrodes can be very large, those resulting in an array of thermocouples connected to each other in parallel banks of series-connected thermocouples [180]. Unfortunately, no data regarding temperature sensitivity is provided and so comparison with other nanosensors is difficult. Nanolithography techniques have also been used to deposit metal strips and thermocouples in AFM tips, some of which have been described in the previous section [90, 166, 283]. Microfabricated metallic structures have also been used to develop temperature sensors and thermometers [25, 153, 211, 278]. Chu *et al.* [54] have developed thin-film gold/nickel thermocouples with junction areas as small as  $100\text{ nm}^2$  on silicon and  $500\text{ nm}^2$  on quartz to measure temperature rises in transient resist heating processes at the microsecond scale. Irradiation by a  $15\text{ keV}$ ,  $150\text{ nA}$  electron beam of  $1.7\text{ }\mu\text{m}$  radius for  $100\text{ }\mu\text{s}$  yielded an increase of temperature at the resist bottom surface of approximately  $62\text{ K}$  on quartz substrates and of  $18\text{ K}$  on silicon

substrates. An example of the design of a sub-micrometer thermometer by miniaturizing microscopic traditional thermometers was presented by Shapira *et al.* [211]. The rationale was to miniaturize a Au-Ni thermocouple and to measure its thermovoltage. The thermometer presents  $S_m = 0.4\% \cdot K^{-1}$  at 300 K (table 2.2) with a temporal resolution of 12  $\mu s$  (to detect a decrease in the measured signal of 5% of its initial value) and a spatial resolution of  $\sim 5\mu m$ .

### 2.2.3 Carbon Nanotube Thermometry

The use of a CNT as a thermometer was first suggested by Gao and Bando [73] by measuring the thermal expansion of liquid gallium inside a CNT. The thermometer resembles a common mercury thermometer in the nanosize. As the authors observed, thermal expansion coefficient of Ga varies linearly and reproducibly in the temperature range between 323 and 773 K with values close to those corresponding to macroscopic volumes. Thermodynamic analysis shows that the surface tension in a one-dimensional nanoscale liquid Ga column inside a CNT affects the column inner pressure, the effect increasing as the column diameter decreases. The analysis provides a quantitative explanation of why a 75 nm diameter column of liquid Ga has the same expansion coefficient as that of Ga in a macroscopic state in the temperature range of 323 to 773 K [74]. In a first experiment, a CNT was filled with Ga and placed in a Gatan holder equipped with a twin heating system inside a scanning electron microscope. The meniscus of the gallium column was rising and falling as the temperature was increased and reduced in the range 323-773 K (figure 2.15). In later experiments it was shown that Ga remains liquid inside the encapsulating CNT at temperatures as low as 203 or 193 K, depending on the Ga phase formed during solidification [151]. These are temperatures significantly lower than solidification temperature of bulk Ga (237.6 K) and extend the operative range of this kind of thermometers to as low as 204 K. Similar CNT thermometers were also developed using In as low melting metal filling, operated in the temperature range between 443 K and 650 K [74], and with Ge [267].

The possibility to use the thermometer outside the microscope chamber in a standard air environment was later reported based on the observation that the surface of a gallium column inside a one-side open CNT oxidizes at high temperature in the presence of oxygen with partial pressure  $\sim 6.66 \times 10^{-5}$  Pa. Consequently, the meniscus leaves a tiny mark

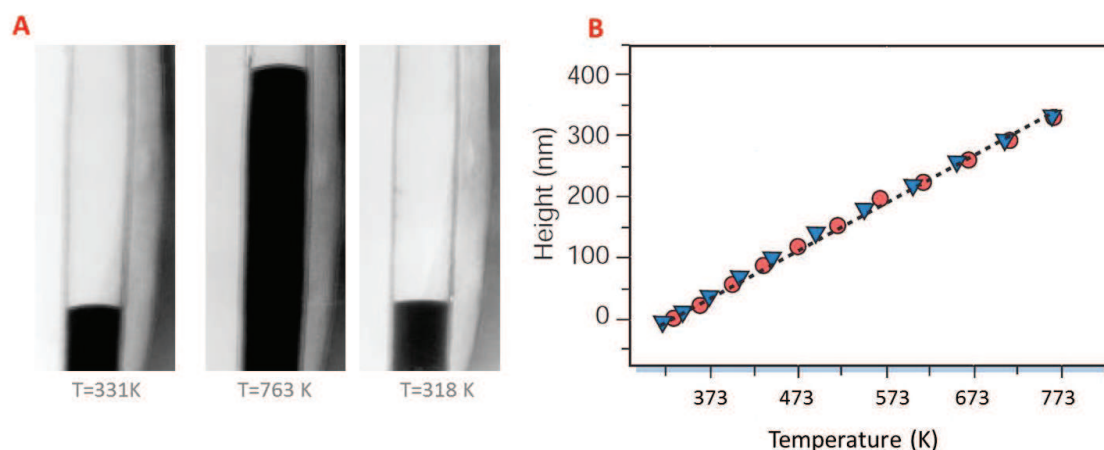


Figure 2.15: Expansion of gallium inside a CNT. With temperature increase the level of the gallium meniscus increases (A). The height of the gallium meniscus plotted against temperature, measured in steps of  $30 - 50^\circ\text{C}$  in the range  $50 - 500^\circ\text{C}$  produces a calibration curve for temperature determination (B); the average (dotted line) mimics the measurements obtained during heating (red circles) and cooling (blue triangles) stages. (Adapted from Y. H. Gao and Y. Bando, *Nature*, 2002, 415, 599-599) [73].

around the CNT wall corresponding to the Ga oxide layer which is clearly observed by TEM [75, 151]. The temperature accuracy is estimated within 5-10%.

CNTs have, however, a limited stability at high temperature in air, suffering fast degradation above 873 K [4, 77]. Consequently, other nanothermometers based on the same idea of nanotubes filled with metals of low-melting point have been developed. The same group of Y. Bando has developed Ga-filled single-crystalline MgO nanotubes which can serve as nanothermometers over a wider temperature range than CNTs [142]. A MgO nanotube was filled with two fragments of Ga, one at each end of the nanotube, and the nanotube sealed. The distance between the tips of each Ga fragment was taken as the thermometric variable and found to have a linear dependence with the temperature in the range between 303-967 K [142] which was also reversible, *e.g.*, the distance decreased as the temperature was increased and vice versa. The working range depends of the total length of the Ga segments and of the distance between their respective tips and in principle its limits are given by the high stability of the single-crystalline MgO nanotube with a melting point of 3073 K and the wide temperature range of 303-2478 K for the Ga in liquid state [143]. Such wide temperature range together with the low vapour pressure of liquid Ga make these type of thermometers quite promising to measure high temperatures with nanospatial res-

olution. This will be particularly so if the use of microscopies, whether TEM or AFM, for the thermometer calibration and reading out of the temperature can be overcome.

Indium has also been used as filling metal of low melting point in single crystalline  $\text{In}_2\text{O}_3$  nanotubes [140] and in silica ones [141]. The as-prepared silica nanotubes consist of an array of nanotubes that can easily be dispersed into individual nanothermometers by an ultrasonic vibration process. The thermal expansion of the liquid In has a linear dependence with the temperature in the range around 425 K, the melting point temperature of In, and 773 K, the highest temperature in the experiments. Although it is not reported, the thermometer maximum sensitivity can be estimated from the linear dependence of the column expansion with the temperature as  $0.4\% \cdot K^{-1}$  at 530 K (table 2.2). Gallium oxide nanotubes,  $\beta - \text{Ga}_2\text{O}_3$ , filled with an Au(Si) alloy have also been used to develop nanothermometers for high temperature measurements [78], as shown in figure 2.16.

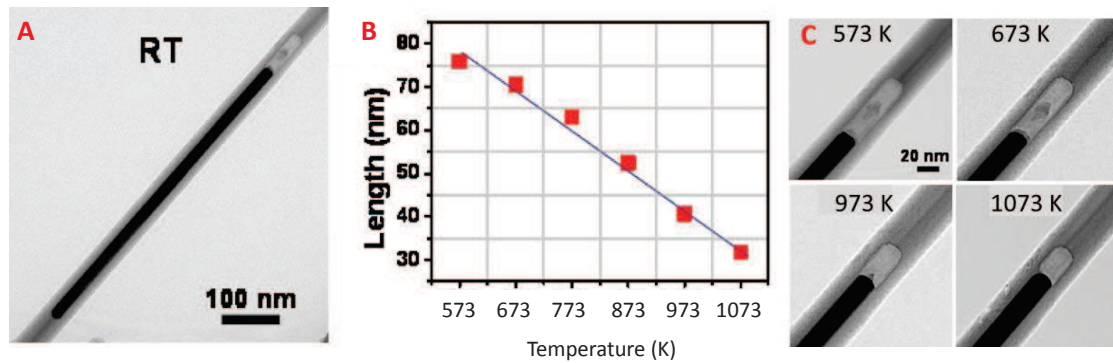


Figure 2.16: (A) TEM image of a  $\text{Ga}_2\text{O}_3$  nanotube before heating. (B) Distance of the Au filling to the top of the cavity during heating as a function of temperature. (C) TEM images of an Au-filled  $\text{Ga}_2\text{O}_3$  nanotube during heating at different temperatures. (Adapted from N. W. Gong, M. Y. Lu, C. Y. Wang, Y. Chen and L. J. Chen, Appl. Phys. Lett., 2008, 92, 073101-1-3) [78].

The Au(Si) filling alloy, where  $\sim 6\%$  is Si, has a rather large coefficient of thermal expansion of  $1.5 \times 10^{-4} K^{-1}$ , ten times larger than that of bulk Au and more than twice that of Ga. The coefficient of thermal expansion of the  $\beta - \text{Ga}_2\text{O}_3$  nanotube is more than two orders of magnitude smaller, so the influence of the expansion of the nanotube on the filling alloy can be neglected. The filling starts to be fluid-like at  $\sim 623$  K and it becomes fluid at  $\sim 673$  K, however, the Au(Si) shows linear expansion already at 573 K and all the way up to 1173 K, where  $\text{Ga}_2\text{O}_3$  becomes unstable. The reported safe range for temperature

measurements is 573-1073 K. The maximum relative sensitivity is  $0.3\% \cdot K^{-1}$  at 940 K (table 2.2). Nanotube-based thermometers have been further developed to include a solid filling instead of liquid-like or liquid ones. Such is the case of the Pb filled ZnO nanotube with a working temperature region between 293 to 573 K and a maximum relative sensitivity of  $1.1\% \cdot K^{-1}$  at 573 K (table 2.2) [246]. The solid filling makes the structural integrity of the outer shell much less demanding than in the case of the liquid-filled thermometers. The drawback of this thermometric design is the high temperature limitation due to some leaking of Pb as it starts melting at above 573 K. The use of single crystalline nanotubes stable at higher temperatures could extend the applicability of Pb as filling material in nanotube thermometry to a second region with Pb in liquid state.

Dorozhkin *et al.* observed that electrical conductivity through an empty CNT is diffusive with a resistance per unit of length of  $10 \text{ k}\Omega \cdot \text{mm}^{-1}$ , whereas a Ga-filled CNT shows metallic behaviour with a low resistance per unit of length of  $100 \text{ k}\Omega \cdot \text{mm}^{-1}$ , two orders of magnitude smaller [63]. Based on this observation, these authors developed an electrically controlled temperature sensor that can also act as a switch, using electrical conductivity as the thermometric property. The thermometer can work in a wide temperature range from 353 up to 773 K. However, the thermometer calibration and resistivity reading must be measured using an AFM, thus rendering its use as rather complicated. Bichoutskaia *et al.* [21] have proposed an electromechanical nanothermometer based on the conductivity changes induced by the thermal interaction and relative motion of the components of double-walled CNT. The nanothermometer can be calibrated as a thermocouple. In thin films of MWCNTs the turn-on field and emission current at a fixed applied electric field are temperature independent above 373 K, the higher the temperature the larger the emission current [21]. Consequently, a film of  $\sim 7$  nm can form a simple thermometer in the temperature range 373 to 600 K under vacuum. The sensitivity of the thermometer can be modified by the applied electric field and by the area of the MWCNTs.

When the number of charge carriers, *e.g.* electrons, moving across a potential barrier is sufficiently small, the uncertainties due to independent random events become significant. This effect, known as shot noise, *e.g.*, each electron that tunnels through the barrier can be considered as a discrete "shot", is independent of frequency up to several hundred GHz. When shot noise is measured in combination with Johnson noise, Spietz *et al.* [219, 218] showed recently that shot noise can be exploited to achieve accurate temperature measurements from the mK range to many hundreds of Kelvin. More recently, Sayer *et al.*

[206] have reported on a CNT thermometer that operates on these principles. The thermal resistance of SWCNT is determined from Johnson and shot electrical noise measurements of the SWCNT in a porous anodic alumina template. As the magnitude of the shot noise does not follow the expected curve for an isothermal device due to significant self-heating of the CNT device, measurements are fitted to self-heating shot noise model that assumes constant device resistance. The resulting thermal resistance of the SWCNT device is found to be  $(1.5 \pm 0.1) \times 10^8 K \cdot W^{-1}$ .

## 2.2.4 Biomolecular-based Thermometry

Among the many techniques developed to determine temperature at the nanoscale, the use of temperature-dependent molecules and biological components is probably one of the most fascinating ones. Some of these techniques, like those based on the thermo-conformation changes of DNA, RNA, proteins and lipids and their catalytic influence on subsequent biological processes [5, 125] or on differences on the electronic properties of fluorescent probes associated to temperature-dependent structural or conformational changes [45, 81], have been used to sense temperature inside cells and have been described above. This section describes thermometry developments based on biological entities, like DNA, mRNA and others.

Living cells are able to sense harmful temperatures changes and induce either heat-shock or cold-shock proteins. The sensing of temperature is made by proteins, nucleic acids and mRNAs that either act as true thermometers, responding directly to temperature changes by modifying their conformation structure, or indirectly undergoing complex reactions [172]. In particular, Narberhaus *et al.* [173, 128, 51] and Shah and Gilchrist [210] have described that certain mRNAs respond to temperature changes by three-dimensional conformational changes. RNA thermometers are located in some specific areas of the RNA structure, particularly in the 5'-end untranslated region that shields the ribosome-binding sites at physiological temperatures. With the onset of heat shock, destabilisation of the RNA starts and favours the release of the ribosome-binding sites and translation initiation. In the case of a temperature downshift, on the other hand, cell growth comes to an almost complete stop, bulk gene expression is drastically reduced and cold-shock proteins are expressed. Some of these mRNA proteins undergo a structural rearrangement to a conformation thermodynamically more stable at low temperature and less susceptible

to degradation [76, 86, 125, 255]. The conformational change of RNA thermometers can be followed by NMR and UV spectroscopy. While naturally occurring thermometers are complex systems, considerably simpler RNA thermometers that can be used to induce or repress gene expression by a simple temperature shift have been developed [176, 175, 241], as depicted in figure 2.17.

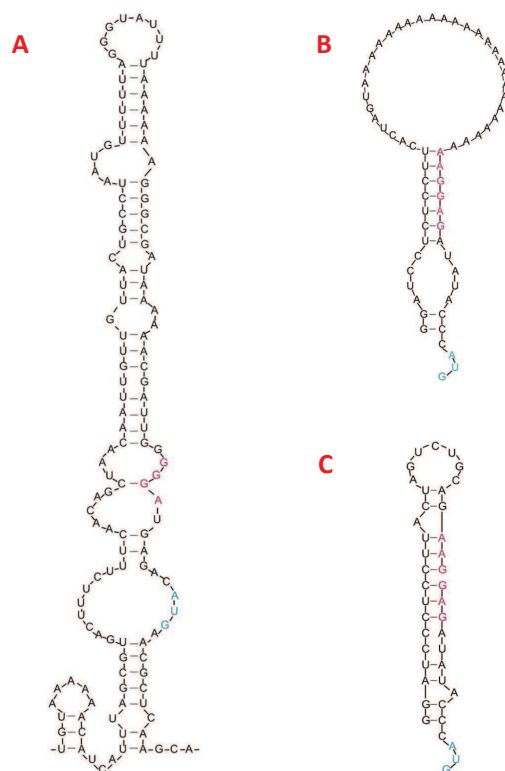


Figure 2.17: Examples of a natural and two synthetic RNA thermometers. (A) Proposed RNA secondary structure of the 5' UTR (untranslated region) from the *prfA* gene of the pathogenic bacterium *Listeria monocytogenes*, which functions as an RNA thermometer; (B) Secondary structure of the synthetic RNA thermometer U6; (C) Structure of the synthetic RNA thermometer U9. (Adapted from J. Neupert and R. Bock, *Nature Protoc.* 4, 2009, 1262-1273). [175].

The thermometers, which are fully operational *in vivo* as translational regulators at physiological temperatures, are built from a single small RNA stem-loop structure containing the ribosome binding site. The thermometers were optimized to work at 310 K, however, following the same principles, it should be possible to design a thermometer optimized to work at any temperature by selecting different loop sizes [175]. The mimicking

of natural thermometry for the development of recording temperature devices have been proposed by Höfner and Zerbetto [98]. The principal components of their temperature sensor are short RNA sequences forming individual helical hairpins and each having a characteristic transition temperature to a different conformation structure. The detection system is based on the subsequent hybridization to specific RNA sequences and the analysis is carried out with the help of a statistical mechanical package specifically designed to study conformation changes in RNA. A list of eight RNA sequences operational in the range from 263 to 333 K at intervals of 10 degrees is proposed. The device, still waiting for experimental validation, could be the basis of a new *ex-situ* thermometric technology of interest for the quality control of perishable products.

### 2.2.5 Miscellaneous

In this section, a few families and scattered examples of micro and nanoscale thermometry that do not fit in the families outlined in the preceding sections are gathered. Coulomb blockade thermometers exploit the differential resistance of tunnel junctions as thermometric parameter at cryogenic temperatures. The advanced design gathers superconductor-insulator-normal metal tunnel junction embedded in a rf resonant circuit with nanometric dimensions (typically hundreds of nanometers)[168, 209, 233]. While conductance at zero bias voltage is suppressed, the conductance at non-zero broaden as temperature increases, resulting in a peak with a fwhm being proportional to the number of junctions and to  $k_B T$ . Moreover the high temperature limit is determined by the electric characteristics of the junction, which allows the tailoring of the thermometer using an appropriate configuration. Coulomb blockade thermometers sensitivity decreases when temperature increases, resulting in hypothetical infinite maximum relative sensitivity at the limit of  $T \rightarrow 0K$ . For temperatures of the order of tens of Kelvin a monotonical decrease of  $S_m$  towards 1 is expected. This tendency is exactly what has been reported by Schmidt *et al.* [209] presenting meaningless maximum relative sensitivity  $S_m > 100\% \cdot K^{-1}$ , for  $T < 0.9K$  [209]. In line with these results Tilke *et al.* [233] reported  $S_m = 5.4\% \cdot K^{-1}$  at 27 K, using n-doped silicon nanowires (table 2.2).

An interesting microthermometer was proposed by Hopcroft *et al.* [100]. The motivation for this thermometer was the need for high accurate temperature determination in high performance resonators in order to account for the temperature dependence of the

resonate frequency. The proposed solution was to use the resonator itself, by an indirect measure of the temperature dependence of its quality factor. The thermometer works between 295 and 370 K with  $S_m = 1.2\% \cdot K^{-1}$  at 320 K (table 2.2). A completely different approach of nanothermometry based on one-use ex situ thermometers, which can record the temperature they were exposed to and be read later when the event is over, was suggested by Lan *et al.* [132] and by Wang and Huang [249] based on the irreversible temperature-activated growth of NPs. The nanothermometer proposed by Lan *et al.* [132] works by measuring the diameter and areal density of silver NPs deposited on a carbon supporting film coated a TEM copper-grid. The spatial resolution achieved between 570-1000 K,  $\sim 16$  nm, is controlled by the distance between neighbouring nanospheres, related to the nanosphere size and areal density [132]. The maximum relative sensitivity is  $0.4\% \cdot K^{-1}$  at 800 K (table 2.2). The thermometer proposed by Wang and Huang [249] is also based on the growth of NPs exposed to a thermal event (characterized by a given temperature and time). In this case, size is indirectly determined by changes in the Raman scattering of semiconductor NPs due to boundary effects that induce asymmetric broadening and a shift in Raman peaks. Two sets of NPs exposed to the same thermal history are used in order to determine both the maximum temperature and duration of the thermal event. This concept was demonstrated using anatase and rutile  $TiO_2$  NPs, works between 673-973 K and 5-60 s. Brintlinger *et al.* [29] have reported a method for mapping temperature at the nanoscale using a transmission electron microscope and the melting point of metal islands. The germanium metal islands are deposited on the reverse side of a commercial silicon nitride membrane whereas local temperature gradients are produced by Joule heating in a thin wire in the front side of the membrane. As the solid-liquid transition in the islands induces contrast changes, the absolute temperature (above or below the melting temperature) can be mapped over the whole field of view with spatial resolution of the order of 100 nm. The technique is applicable to a variety of materials with spatial resolution that can be scaled down to lengths approaching characteristic scattering distances of thermal carriers of  $\sim 10$ -100 nm. Another example consists in a miniaturized device based on the Seebeck effect [119]. The nanoscale thermocouple is composed of Cu and Cu-Ni joined tips with a diameter of  $\sim 50$  nm, having an expected Seebeck coefficient of  $39.45 \mu V \cdot K^{-1}$ , corresponding to a minimum detectable temperature change of 28 K with the used device. The joined tips can be then manipulated in a TEM in order to sense local temperature that changes due to the electron beam and due to an electric current passing

through a MWCNT. The thermometer was also used to study the relationship between melting/deformation and the local temperature increase on a metallic filler.

Table 2.2: Figure of merit of non-luminescent molecular thermometers including the thermometric property associated to each example. When reported, the spatial resolution is indicated.

NON-LUMINESCENT THERMOMETERS

Description	Ref.	$S_m$	$\Delta T$ ( $T_m$ )	Thermometric Property	Observations
$\beta$ -Ga <sub>2</sub> O <sub>3</sub> , filled with an Au(Si) alloy	[78]	0.3	573–1073 (940)	Thermal expansion	For temperatures above 1073K the Ga <sub>2</sub> O <sub>3</sub> becomes unstable
Pb filled ZnO nanotubes	[246]	1.1	293–573 (573)	Thermal expansion	Expansion thermometer working in the solid state
In filled silica nanotubes	[141]	0.4	293–773 (530)	Thermal expansion	Working in high temperature ranges
Silicon micromechanical resonators	[100]	1.2	295–370 (320)	Resonator quality factor (Q)	Temperature resolution of better than 2mK in a 1 Hz bandwidth.
Tunnelling current	[183]	0.5	300–1300 (500)	Fermi-level shift	Demonstrated in a MEMS device
<i>n</i> -doped Si nanowires	[233]	5.4	15–30 (27)	Peak width of the conductance dip	Coulomb blockade behaviour at temperatures up to 20 K
Ag NPs	[132]	0.4	600–1000 (800)	NP diameter	Maximum spatial resolution of 16 nm
		0.2	600–1000 (790)	NPs areal density	
Au–Ni nanowires	[211]	0.4	295–300 (300)	Thermovoltage	Spatial resolution $\sim 1 \mu\text{m}$ and temporal resolution of 12 $\mu\text{s}$

## Summary

The diversity of luminescent and non-luminescent thermometers operating at the sub-micron scale described in this chapter clearly point out the emergent interest of nanothermometry in numerous fields, such as electronic and optoelectronic machines and devices, micro- and nanofluidic systems, living cells and tissues, nanostructures, and in many other conceivable applications, such as thermally-induced drug release and wherever exothermal chemical or enzymatic reactions occur at sub-micron scale. Nanothermometry has indeed experienced a continuous and unprecedented growth over the period 2005-2012 following, in most examples, the technological trends of sub-micron miniaturization and it is foreseen that this trend will continue for the next coming years. Innovation in the rational design of new thermometric systems in the nanoscale will undoubtedly lead to qualitatively new progresses in nanothermometry, with consequences in nanotechnology that cannot be yet foreseen. However, despite actual promising progresses, the research can be considered as in its early stages and more basic knowledge is still needed before nanothermometer prototypes become a commercial reality. a range of  $\sim 10K$ , meaning that they are not wide-range thermometers but on/off temperature sensors. Setting a reasonable limit of  $0.5\% \cdot K^{-1}$  as a quality threshold (meaning that the relative variation of the thermometric parameter is 0.5% per degree of temperature change), the wide variety of thermometers available is evident (tables 2.1 and 2.2); however, this number drastically decreases if self-referencing is required, as shown in figure 2.9 for the luminescent thermometers. The lifetime-based methodology to sense temperature is intrinsically limited by the long acquisition times required to collect reliable data, as mentioned above, and does not present improved relative sensitivity values, when compared to those of the intensity-based ratiometric thermometers (figure 2.9). The major obstacle for progress has been the unavailability of a single molecular thermometer with the following requirements (that should be simultaneously satisfied):

- High temperature resolution ( $< 0.5$  degree);
- Ratiometric temperature output;
- High spatial resolution ( $< 3\mu m$ );
- Functional independency of changes in pH, ionic strength and surrounding biomacromolecules;

- Concentration-independent output.

A new generation of nanothermometers intend to exploit the synergetic integration of different functionalities in a nanometric platform, for instance assembling together heater and thermometer elements in the same NPs (*e.g.* a Fe-based magnetic core or an Au rod covered with luminescent centers).

# Chapter 3

## Materials and Methods

In this chapter, the methods and techniques used in the synthesis of the materials and their characterization are described.

A general introduction to the sol-gel process including a discussion on acid versus basic catalytic systems is presented in materials synthesis section. A special attention is given to Stöber method for the production of silica spheres.

The experimental approach used in the development of the different materials used in this work is described in detail. The techniques section presents the characterization techniques used to study the properties of the prepared materials. A particular emphasis is given to photoluminescence measurements, detailing the equipment, and the different measurement modes used, as well as the information that is possible to extract from each of them. Also, the structural characterization of the materials by electronic microscopy and dynamic light scattering is presented.

## 3.1 Materials Synthesis

### 3.1.1 Sol-Gel Process

The sol-gel (SG) process is an organic polycondensation reaction in which metal alkoxide molecules form polymeric structures by hydrolysis of some or all the substituents, resulting in mono-, bi-, or tri-dimensional crosslinked networks. A high control of the purity and composition of the final materials can be achieved by using simple small molecules as precursors. The use of a solvent based chemistry makes this method very attractive because of the simplicity of the experimental setup [122].

The basic reaction mechanism is discussed, taking silicon-based sol-gel process as a model system. Silicon-based sol-gel allows an easy incorporation of organic groups by means of organically modified silanes. This feature makes sol-gel a very popular process for the formation of hybrid materials. In general terms, polycondensation reaction can be catalyzed by an acid or a base (reaction schemes depicted in 3.1), obtaining materials with different final properties. Initially, the silane precursor is hydrolyzed resulting in a hydroxyl substituted silane. Then, the condensation occurs in two steps. In the first one (fast step) an intermediate species is formed that later condensates forming a siloxane Si–O–Si bond.

The main advantage of the Sol-Gel method lies on the flexibility of the synthesis processes. A tuning of the properties of the synthesized material can be achieved just by changing the solvent, or the acid (or base) used in the procedure, even maintaining the same silanes. The numerous variations are then multiplied by the large variety of silanes available. In fact, as NPs for biolabeling is concerned, most of methods are based on small silane molecules such as tetraethyl orthosilicate (TEOS) and 3-aminopropyl triethoxysilane (APTES)(structural formulas in figure 3.2), due to their simplicity, and the capability of the silica surface for biological vectorization and functionalization. Therefore, these have also been the main precursors used in this work.

### 3.1.2 Synthesis of Organic Silica Nanoparticles

In a typical synthesis procedure, 20 mL of 2-isopropoxyethanol (IPE, Aldrich, 99%) and 2 mL of concentrated ammonia solution (Panreac, 25wt%) were mixed under magnetic stirring during 5 min, and then, 0.2 mL of TEOS (Aldrich, 99.99%) and 0.4 mL of APTES (Aldrich, 98%) were injected into the solution at once. The mixture was aged during two

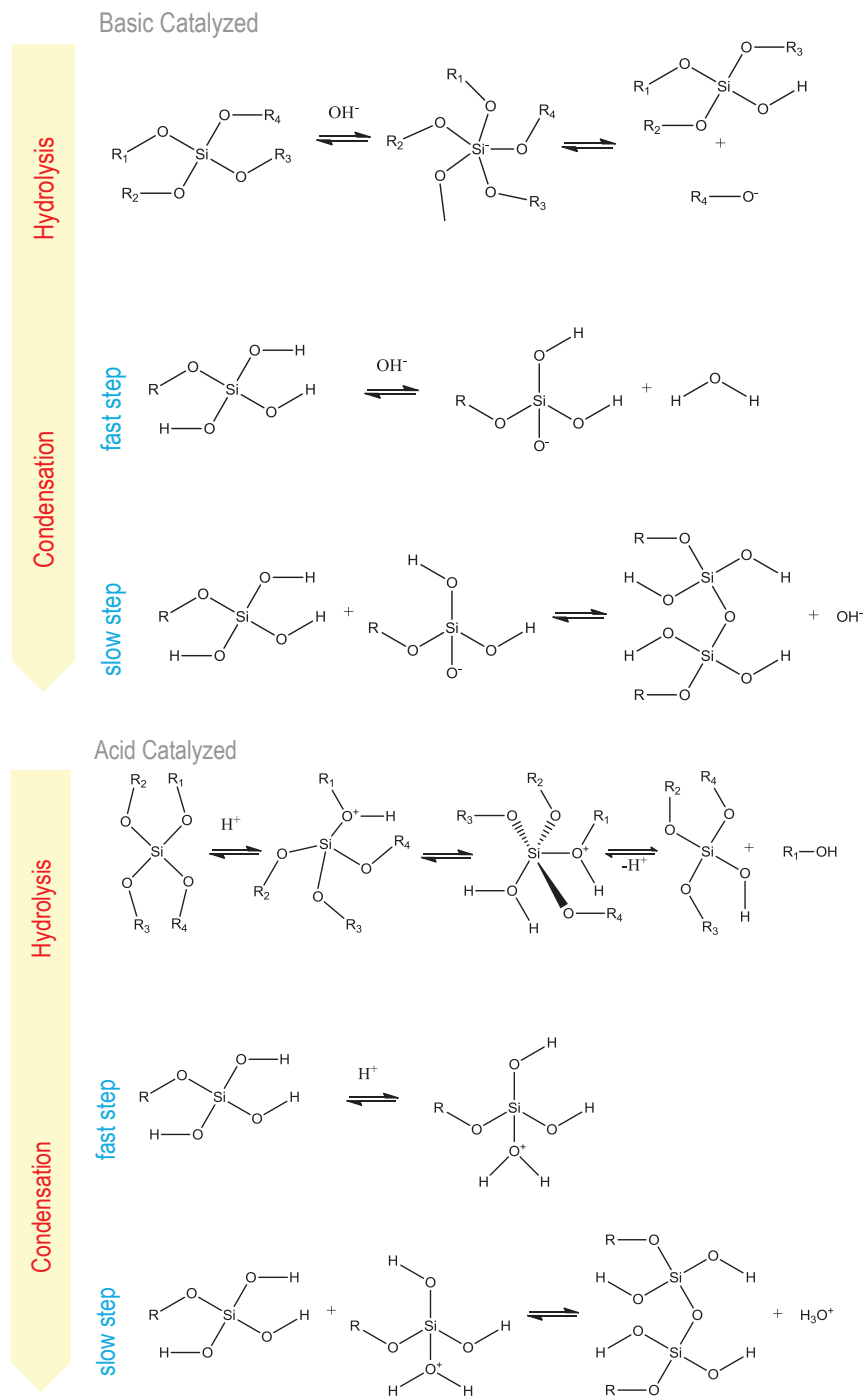


Figure 3.1: Base-(top) and acid-(bottom)catalyzed sol-gel process scheme, depicting hydrolysis and condensation reactions.

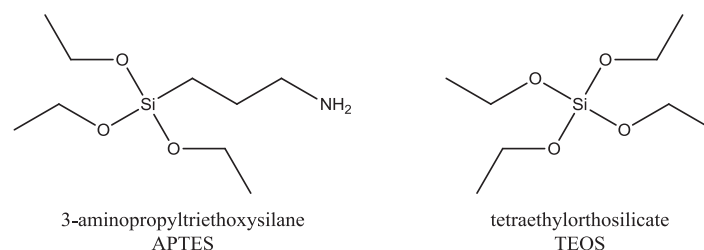


Figure 3.2: APTES and TEOS structural formula.

hours at room temperature ( $\sim 300\text{K}$ ) and dried under vacuum at 318 K during 10 hours to obtain white yellowish powders (figure 3.3). The ratio of APTES to TEOS was varied while keeping the net volume of silica precursor constant (0.6 mL, nom. 2.6 mmol). Three different samples were prepared, named **AT-1.2**, **AT-1.1** and **AT-2.1** (APTES:TEOS volume ratios of 1:2, 1:1 and 2:1 and mol % APTES of 33, 49 and 65%, respectively). All reagents were used as received without further purification.

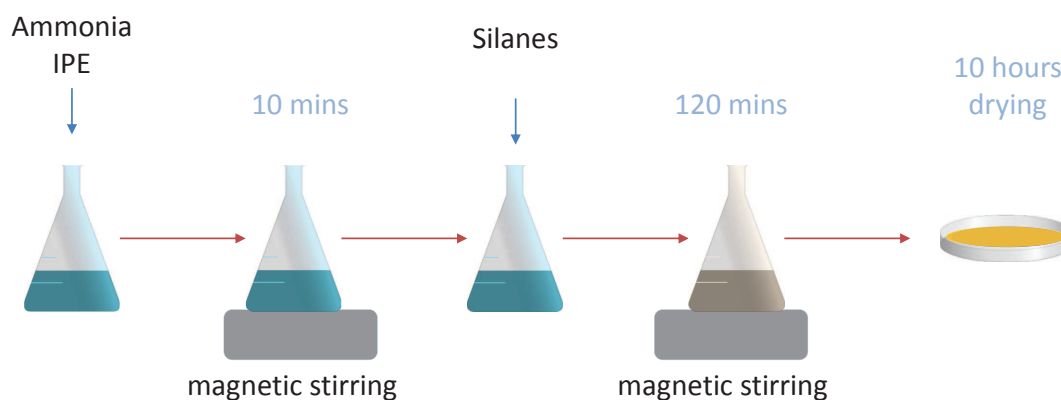


Figure 3.3: Flux diagram of a typical Silica NPs synthesis by Stober Method.

Further optimization of the synthesis recipe, namely through a fine-tuning of the APTES/TEOS volume ratio and its influence on the morphological, structural, and photoluminescence features of the particles lied beyond the scope of this work.

### 3.1.3 Synthesis of Maghemite Nanoparticles

Iron oxide nanoparticles were prepared by basic hydrolysis of  $\text{FeCl}_2/\text{FeCl}_3$  aqueous solutions following the procedure described by Kang *et al.* [116]. All reagents were used as received without further purification. An aqueous solution (25.0 mL) containing  $\text{FeCl}_2 \cdot 4 \text{H}_2\text{O}$  (3.137 g, 24.749 mM, Aldrich),  $\text{FeCl}_3$  (5.200 g, 32.058 mM, Aldrich) and HCl conc. (0.85 mL, 10.285 mM, Aldrich) were added dropwise to a 1.5 M NaOH (Aldrich) solution (250 mL) under continuous stirring. The solution was kept under stirring during 30 minutes, and the precipitate was separated by magnetic decantation. The precipitate was washed twice by redispersion in water and centrifugation, and it was finally redispersed in 0.01 M HCl (300 mL). The resulting suspension remained stable after one year, without showing visible aggregation or deposit (see figure 3.4). The concentration of the solution is 2 mg/mL. This magnetic NP suspension was labeled as **NPM-1**.

Another preparation of maghemite nanoparticles with higher size use also iron oxide nanoparticles. It was prepared by basic hydrolysis of  $\text{FeBr}_2/\text{FeBr}_3$  aqueous solutions according to the following procedure: an aqueous solution (25 mL) containing  $\text{FeBr}_2$  (6.914 g, 32.058 mM, Aldrich),  $\text{FeBr}_3$  (9.475 g, 32.058 mM, Aldrich), were added dropwise to a 1.5 M NaOH (Aldrich) solution (250 mL) under stirring at 368K. The solution was kept under stirring for 30 min, and then cool down to room temperature. The precipitate was separated by magnetic decantation and then was washed twice by redispersion in water and centrifugation. After this, it was redispersed in 0.01M HCl (500 mL). Finally it was separated by centrifugation and then redispersed in water. The average size determined by TEM is  $11.8 \pm 2.3$  nm. The second set of magnetic NPs was labeled as **NPM-2**.

The values obtained using TEM images ( $11.7 \pm 2.3$  nm) are slightly lower than the ones obtained by DLS ( $14.3 \pm 3.4$  nm) because the last measures the hydrodynamic size of the **NPM-2**.

### 3.1.4 Core-Shell Maghemite-Silica Nanoparticles

The core-shell NPs were prepared using a procedure similar to that described in section 3.1.2, but adding in the beginning 0.5 mL of maghemite suspension (1 mg/mL) of prepared before (section 3.1.3). The APTES:TEOS proportion of APTES:TEOS 2:1 was used since it presented the highest quantum yield (see chapter 4). All reagents were used as received without further purification. In a typical synthesis, the silica coating of the  $\gamma - \text{Fe}_2\text{O}_3$



Figure 3.4: Maghemite NPs aqueous suspension (2.0 mg/mL) produced by the method described by Kang *et al.*[116]

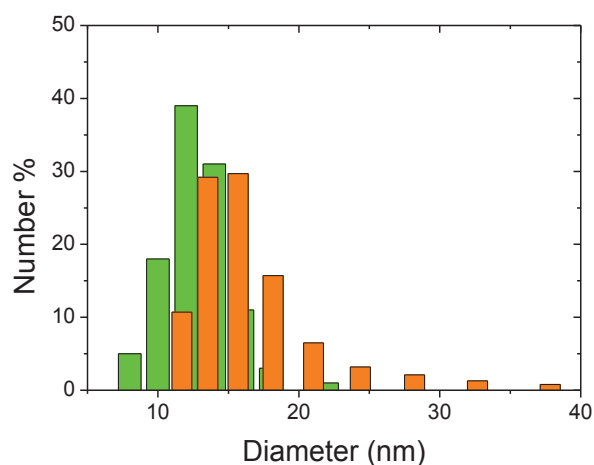


Figure 3.5: Comparison of the **NPM-2** size distribution estimated using TEM images (green) and DLS (orange) measurements.

nanoparticles **NPM-1** was carried out using the modified Stöber method.  $\gamma - Fe_2O_3$  ferrofluid (0.5 mL, 1.0 mg) was added to a mixture of 20.0 mL of IPE and 2.0 mL of ammonia. After 30 minutes of continuous magnetic stirring 0.2 mL of TEOS and 0.4 mL of APTES were injected into the solution at once. The mixture was aged during two hours maintaining a regular stirring at room temperature and then dried under vacuum at 318 K during 10 hours to obtain pale yellow powders (figure 3.6). The resulting powder was labeled as **MAT-1**. The **MAT-1** NPs demonstrated to be well dispersed in water

producing stable suspensions after sonication.

The silica coating of the  $\gamma - Fe_2O_3$  **NPM-2** NPs was carried out using also the modified Stöber method. The **NPM-3** ferrofluid (0.5 mL) was added to a solution of isopropanol (20 mL, Aldrich, 99%) and ammonia (2 mL, Panreac, 25wt%). This solution was stirred for 30 min and TEOS (0.2 mL, Aldrich, 99.99%) and (APTES) (0.4 mL, Aldrich, 98%) were added. The mixture was aged during two hours at room temperature and dried under vacuum to obtain brown powders, named as **MAT-2**.

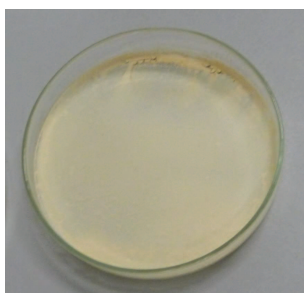


Figure 3.6: Resulting silica recovered maghemite NPs (**MAT-1,2**) using modified by Stöber Method

### 3.1.5 Silica Nanoparticles co-doped with $Ln^{3+}$ complexes

#### Ligands complexes synthesis.

Here is described the synthesis of  $Eu(btfa)_3(MeOH)(bpeta)$ ,  $Tb(btfa)_3(MeOH)(bpeta)$ ,  $Eu(acac)_3 \cdot 3H_2O$  and  $Tb(acac)_3 \cdot 3H_2O$  complexes.

The starting chemicals were europium or terbium chloride hexahydrate ( $EuCl_3 \cdot 6H_2O$  or  $TbCl_3 \cdot 6H_2O$ , Aldrich), 4,4,4-trifluoro-1-phenyl-1,3-butanedione (btfaH, Aldrich), 1,2-bis(4pyridyl) ethane (bpeta, Aldrich), methanol (MeOH, Merck). The  $Ln(btfa)_3 \cdot 2H_2O$  ( $Ln=Eu, Tb$ ) complexes were prepared following the procedure reported in reference [60]. A MeOH solution of bpeta (0.037 g, 0.2 mmol) was slowly added to a methanol solution of  $Eu(btfa)_3 \cdot 2H_2O$  (0.166 g, 0.2 mmol). The reaction mixture was stirred for 24 h at room temperature. The same method has been adopted for the synthesis of the  $Tb^{3+}$  complex, using the corresponding stoichiometric ratio. The complexes obtained,  $Eu(btfa)_3(MeOH)(bpeta)$ , and  $Tb(btfa)_3(MeOH)(bpeta)$ , were filtrated, washed and dried

under vacuum. The metal ( $\text{Eu}^{3+}$  or  $\text{Tb}^{3+}$ ) first coordination sphere is formed by three btfa ligands, one bpeta unity and one MeOH molecule (figure 3.7).

The  $\text{Eu}(\text{acac})_3 \cdot 3\text{H}_2\text{O}$  complex was prepared by an addition an EtOH solution of acacH (0.310 mL, 0.3 mmol) to an EtOH solution of  $\text{EuCl}_3 \cdot 6\text{H}_2\text{O}$  (0.357 g, 0.1 mmol) followed by the addition of an aqueous ammonium solution until the pH reaches 6.5. The reaction mixture was stirred for 24 h at room temperature. The same method has been adopted for the synthesis of the  $\text{Tb}^{3+}$  complex, using the corresponding stoichiometric ratio.

**Elemental Analysis.** Elemental analysis for C, H and N were performed with a CHNS-932 elemental analyser with standard combustion conditions and handling of the samples at air. The results are in good agreement with the proposed formula of  $\text{Eu}(\text{btfa})_3(\text{MeOH})(\text{bpeta})$  and  $\text{Tb}(\text{btfa})_3(\text{MeOH})(\text{bpeta})$ . Anal. Calcd. (%) for  $\text{EuC}_{43}\text{H}_{34}\text{F}_9\text{N}_2\text{O}_7$ : C, 50.90; H, 3.35; N, 2.76; found; C, 50.41; H, 3.47; N, 2.71. Anal. Calcd. (%) for  $\text{TbC}_{43}\text{H}_{34}\text{F}_9\text{N}_2\text{O}_7$ : C, 50.56; H, 3.33; N, 2.74; found: C, 50.16; H, 3.32; N, 2.85.

The synthetic method adopted for the preparation of the complexes and the data from the elemental analysis and FI-IR spectroscopy indicate that the  $\text{Ln}^{3+}$  first coordination sphere encompasses three btfa anionic ligands, one bpeta group and one methanol molecule (coordinated via the hydroxyl group) or first coordination sphere encompasses three acac anionic ligands and three water molecules (figure 3.7). [145].

## AET samples

The  $\text{Ln}^{3+}$ -containing  $\gamma\text{-Fe}_2\text{O}_3@TEOS/APTES$  nanoparticles ( $\text{Ln}=\text{Eu}$ ,  $\text{Tb}$  or  $\text{Eu/Tb}$ ), named as **AEu**, **ATb** and **AET**, respectively, were prepared following the procedure described above by addition  $\text{Ln}(\text{btfa})_3(\text{MetOH})(\text{bpeta})$  solution (1 mL, 6.0 g/L) to the reaction medium prior to the addition of the alkoxysilane precursors. The proportions in volume where performed maintaining a total volume of 1.0 mL of  $\text{Ln}(\text{btfa})_3(\text{MetOH})(\text{bpeta})$  solution. The NPs synthesized are similar to **MAT-1**, except that are co-doped with the trivalent lanthanide ions. The prepared samples include several  $\text{Eu}^{3+} : \text{Tb}^{3+}$  proportions. Samples labeled as **AET-2.1**, **AET-1.1**, **AET-1.2** and **AET-1.10** correspond to the  $\text{Eu}^{3+}$  to  $\text{Tb}^{3+}$  mass proportions of 2:1, 1:1, 1:2 and 1:10, respectively.

All the above procedure was followed in the preparation of acac doped samples, except that the  $\text{Eu}(\text{acac})_3 \cdot 3\text{H}_2\text{O}$  and  $\text{Tb}(\text{acac})_3 \cdot 3\text{H}_2\text{O}$  complexes replace the  $\text{Eu}(\text{btfa})_3(\text{MetOH})(\text{bpeta})$  and  $\text{Tb}(\text{btfa})_3(\text{MetOH})(\text{bpeta})$  complexes (figure 3.7). The NPs synthesized are similar to

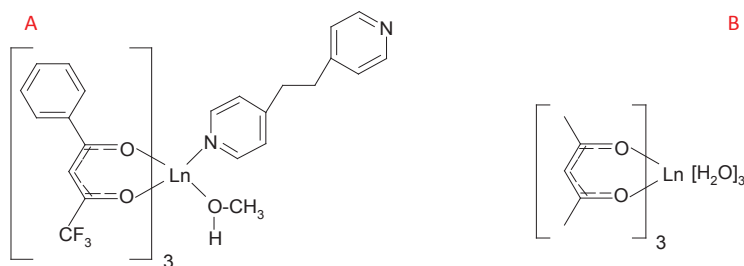


Figure 3.7: Chemical structure of (A)  $\text{Ln}(\text{btfa})_3(\text{MeOH})(\text{bpeta})$  and (B)  $\text{Ln}(\text{acac})_3 \cdot 3 \text{H}_2\text{O}$  (Ln=Eu and Tb)

**MAT-2**, except that are co-doped with the trivalent lanthanide ions. The proportion prepared was 1:2 and the sample was labeled as **AET-1.4a**.

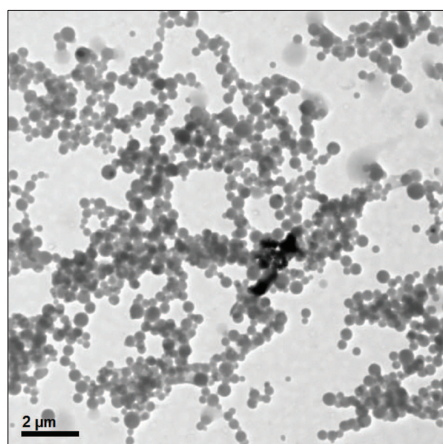


Figure 3.8: TEM image of **AET-1.4a**: general view of the sample showing the spherical silica beads.

## PET sample

The silica coating of the **MAT-2** NPs was carried out using an acid catalysed silica co-condensation of TEOS and N-(triethoxysilylpropyl) – O – Polyethylene Oxide Urethane (TESP, figure 3.9). In a typical procedure, 1.0 mL of **MAT-2** was added to 20 mL of isopropoxiethanol. The pH of the solution was lowered by addition of 2.0 mL of HCl 1M, and 0.2 mL of TEOS was added and the solution was stirred during 90 min. Then, 0.20 g of TESP was added at once and after stirring for 150 min, the suspension was placed in a petri plate and evaporated at 318 K overnight. The resulting powder sample was labelled as **TPT**.

The  $\text{Eu}^{3+}/\text{Tb}^{3+}$  co-doped NPs, named as **PET-1.3**, were produced using an Eu:Tb ratio of approximately 1:3 adding the  $\text{Ln}(\text{btfa})_3(\text{MetOH})(\text{bpeta})$  (Ln=Eu and Tb) solutions (1 mL, 6.0 mg/mL) to the reaction medium prior to the addition of the alkoxy silane precursors.

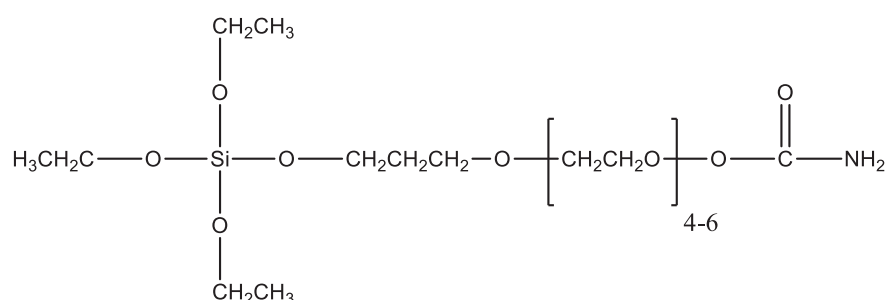


Figure 3.9: Chemical structure of N-(triethoxysilylpropyl) – O – Polyethylene Oxide Urethane (TESP)

### 3.1.6 Di-ureasil Films

#### UET samples

The synthesis of the di-ureasil organic/inorganic hybrids was realized as described in [58].

The first step of the synthesis involves the reaction, in tetrahydrofuran (THF, Riedel de Höen), of the isocyanate group of the alkoxy silane precursor 3-isocyanatopropyl triethoxysilane (ICPTES, Fluka), with the terminal amine groups of the doubly functional  $\alpha,\omega$ -

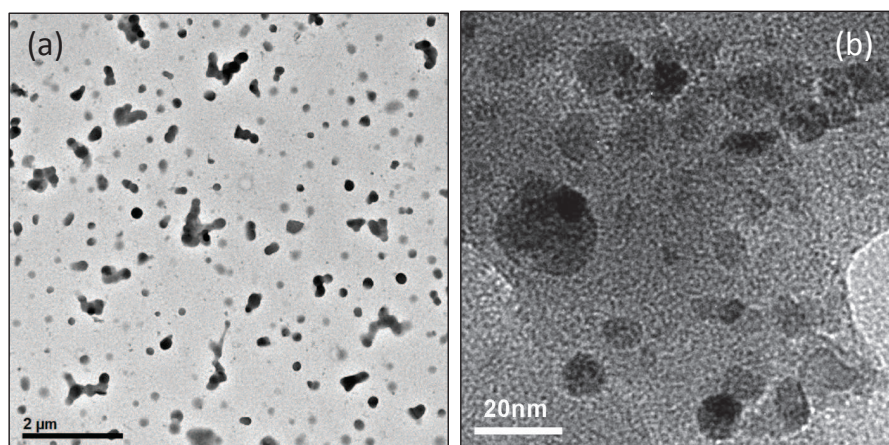


Figure 3.10: TEM images of **PET-1.3**. (a) General view of the sample showing the spherical silica beads. (b) Detail of encapsulated iron oxide.

diaminepoly (oxyethylene-co-oxypropylene) (Jeffamine ED-600®, Fluka) to form ureapropytriethoxysilane, a urea cross-linked organic-inorganic hybrid precursor (figure 3.11).

In the second step, the lanthanide complexes of europium and terbium were incorporated as ethanolic solutions together with water and HCl for promoting the hydrolysis of the alkoxy silane precursor. The hydrolysis and condensation reaction result in a cross-linking of the organic chains by O–Si–O bridges, thus forming an organic-inorganic network. All reagents were used as received without further purification. In a typical synthesis, a solution of Jeffamine ED-600® (1.0 mL, 1.75 mmol) in dried THF (5.0 mL) was mixed with ICPTES (0.91 mL, 3.5 mmol) (molar ratio Jeffamine ED-600® to ICPTES 1:2) and kept under stirring at room temperature for 24 h. In the second step, the complexes  $[\text{Ln}(\text{btfa})_3(\text{MetOH})(\text{bpeta})]$  (Ln=Eu, Tb) were dissolved in EtOH (0.82 mL, 14.04 mmol) and mixed with HCl 0.5 M (0.04 mL) and H<sub>2</sub>O (0.051 mL) (molar ratios are 1:3 and 1:4 for 1:2 and ICPTES:EtOH, respectively). This solution was mixed with the hybrid precursor solution prepared in the first step under stirring at room temperature. The Eu:Tb complex mass proportion is 1:3, corresponding to 5 mg or 0.00480 mmol of Eu<sup>3+</sup> complex for 15 mg, 0.00144 mmol of Tb<sup>3+</sup> complex. Gelation occurred within 20 min yielding colorless transparent monoliths or films. The resulting material was labeled as **UET-1.3**.

The same synthetic strategy can be used incorporating maghemite NPs in the formed film. In the last step the maghemite suspension was added (0.5 mL of 2 mg/ml suspension), resulting in a pale orange transparent monolith or film, labeled as **UET-1.3-Fe**.

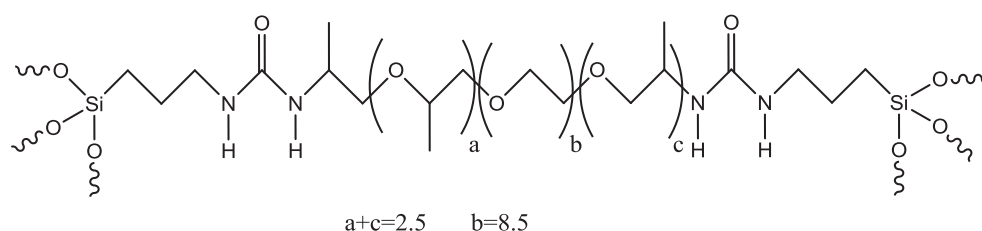


Figure 3.11: Ureapropyltriethoxysilane hybrid precursor

## 3.2 Experimental Techniques

### 3.2.1 Steady State Photoluminescence: Emission and Excitation Spectra

The emission and excitation spectra constitute the basic spectroscopic analysis of a material. The measurement of the excitation and the emission spectra requires a monochromator to select a narrow wavelength interval of an excitation source and another monochromator to select a narrow wavelength interval of the emitted spectra. Typically both requirements are fulfilled by an experimental layout including mirrors and diffraction gratings, using, for example, a Czerny–Turner configuration. In steady state mode, the emission or excitation signal is collected during the interval of time that includes all the decay of the intensity.

An emission spectrum is acquired by exciting the sample with an absorbed wavelength, usually the maximum intensity absorption (or excitation) peak, and the emission monochromator scans the luminescence within a wavelength interval.

An excitation spectrum is measured by setting the emission monochromator fixed in a given emission wavelength (for instant the one corresponding to the maximum of the emission spectrum). The excitation monochromator is then scanned in a given wavelength interval and the luminescence intensity corresponding to the monitored emission wavelength is measured.

In the DF–UA/CiCECO facilities the emission spectra were recorded on a Fluorolog3 2-Triax, Horiba Scientific, with a modular double grating excitation spectrometer and a TRIAX 320 single-emission monochromator coupled to a R928 Hamamatsu photomultiplier, using the front face acquisition mode (see experimental layout in figure 3.12). The

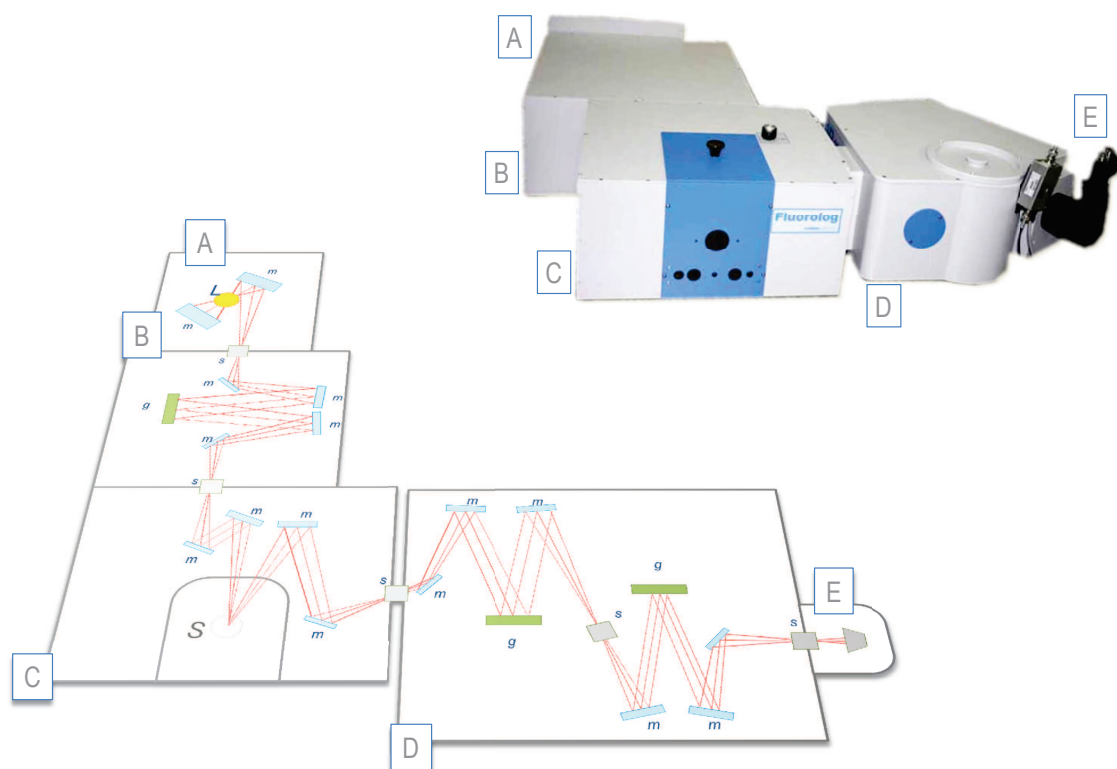


Figure 3.12: Experimental Layout for Photoluminescence measurements. The black letters are the source compartment (A), a single-grating excitation monochromator (B), sample chamber with a helium cryostat (C) a double-grating emission monochromator (D) and the detector (E) and the color letters mark the grating (g), mirror (m), lamp (L), slit (s) and sample chamber (S)

excitation source was a 450W Xe arc lamp. The emission spectra were corrected for detection and optical spectral response of the spectrofluorimeter, and the excitation spectra were corrected for the spectral distribution of the lamp intensity using a photodiode reference detector.

The low temperature PL measurements were performed using a He closed-cycle cryostat and the temperature was increased using a Lakeshore 330 auto-tuning temperature controller with a resistance heater.

### 3.2.2 Time-Resolved Spectroscopy

The requiring processes beyond fluorescence and phosphorescence take place in distinct time scales the measurement of the emission properties for different time domains. The photoluminescence time-resolved mode enables the evaluation of the time-scale in which the processes behind the emission occur (dynamical evaluation). Moreover, it is a powerful technique to permit the unequivocally establishment of different emission and excitation components with distinct time scales.

In simple terms, the time-resolved spectroscopy (TRS) study the dynamic processes in materials by spectroscopic techniques. The technique involves the use of a pulsed excitation source and requires that the spectral detection takes place after a certain time interval subsequent to the excitation pulse. If the time scale of the decay is in the order of the  $10^{-6} - 10^{-3} s$  a pulsed Xe-Hg lamp is used as a light source. The equipment is a HR460 Jobin Yvon-Spex spectrometer coupled to a R928 Hamamatsu photomultiplier. A pulsed Xe-Hg lamp is used as a pulsed excitation source. All the spectra are corrected for the response of the detector. The same information can be extracted to the  $10^{-9} - 10^{-6} s$  time scale using the NanoLED as a light source. The emission decay curves in the nanosecond time scale were recorded on a spectrofluorometer (Fluorolog TCSPC, Horiba Scientific) coupled to a TBX- 04 photomultiplier tube module (950 V), 200 ns time-to-amplitude converter.

The exciting sources available are two Horiba-Jobin-Yvon pulsed diodes (NanoLED-390, peak at 390 nm, 1.2 ns pulse duration, 1 MHz repetition rate, and 150 ns synchronization delay and NanoLED-330, peak at 330 nm, 1.2 ns pulse duration, 1 MHz repetition rate, and 150 ns synchronization delay). The experimental excitation pulse was measured using a LUDOX scattering solution in water.

The standard measurement modes on the laboratory equipment allows to measure, among other, emission spectra for a constant delay or the decay of an emission in the time domain.

#### Time Resolved Emission Spectra

Time resolved spectroscopy includes also the analysis of the emission spectra recorded for different time intervals since the pulse of excitation until the measurement. The technique is a powerful tool to evaluate the change in the emission in the time domain. If the

experimental emission spectra, measured for different time delays were compared, it is easy to evaluate the temporal evolution of an emission profile, evaluating the eventual different time scales of the transitions that are part of the emission spectra.

The equipment sends a pulse of light and for a given delay the intensity at a certain wavelength is recorded. If the delay is fixed and the wavelength varies in a defined range, the emission spectra is recorded for the delay selected.

Experimental strategies to measure such information include pulsed light sources (as mercury lamps) and NanoLEDs. In the first approach the light source is pulsed and, after the defined time delay, the intensity is recorded point by point over the spectral range previously defined. Time constraints to the apparatus user may also become significant in using this method, especially if a good spectral resolution of a decay is required on top of good time resolution. In practical terms, it is usual to record more than one scan to improve the signal-to-noise ratio (SNR) of the emission spectra.

In the second strategy the photons are analyzed by a single channel analyzer that is sensitive only to photons following in a certain time window. The experimental setup allows to make cumulative measurements for a preset time (run time preset, RTP mode) or until the intensity reach a preset value (intensity preset, IP mode). The intensity time evolution for each wavelength is registered, allowing the reconstruction of the emission spectra for each time delay. In fact the analysis of the decay curves recorded at selected wavelengths carries important spectroscopic information and a section dedicated the decay curves analysis is given below.

### **Decay Curves and Mott-Seitz Model Fitting**

The basic experimental output of TRES is a decay curve, that corresponds to the temporal evolution of the intensity at the selected wavelength. The experimental setup allows to define the excitation and the emission wavelengths. The temporal parameters include the initial delay, the time interval between acquisitions and the total time interval to scan.

The decay curve is rationalized according the energy diagram of the transitions monitored on the measurement, (see section 1.3.2 for details). In the simplest case the decay curve obeys to a single exponential decay curve. The MatLab ® program was used to produce a script to evaluate the decay lifetime from the decay curve data. The numerical strategy follows some fundamental steps. First the intensity was normalized to the interval

0-1 and the semi-logarithmic plot taken to evaluate the fit to a single exponential decay. A single exponential fit to the function using the equation 3.1 produces sets of values ( $I_0$ ,  $t_0$ ,  $\tau$ ), thus allowing the computing of the decay lifetime( $\tau$ ). Using a Non-linear Least Squares Algorithm the interactive Levenberg-Marquardt method was implemented. The robust linear least-squares fitting method used corresponds to the bi-square weights method. The fits goodness was evaluated using the 95% confidence intervals.

$$I = I_0 \exp\left(-\frac{t - t_0}{\tau}\right) \quad (3.1)$$

The general equation that models the intensity decrease with time is 3.1. For faster and reliable fit the curve expression is modified, taking the logarithm on the natural basis of each therm. If the emission decay is actually in agreement with a single exponential decay, the curve will be fitted to a straight line with reasonable concordance. Nevertheless due to the limit of detection of the intensity there is a baseline that corresponds to the noise level of the detector. The evaluation of the baseline is due taking the average of these values there is a constant line representing the noise level of the measurement. The region of interest to perform the fit, in order to estimate the decay lifetime  $\tau$ , corresponds to the time span between the initial time and the interception of the two straight lines defined above.

This procedure was implemented to analyze the emission decay curves in the temperature range of interest for each sample. The lifetimes for each temperature can be computed and their temperature dependence analyzed. In a typical measurement, the experimental data shows a S-shaped curve in good agreement with the predictions of the Mott-Seitz model.

This model assumes that there is a competition between radiative and non-radiative decay paths for the electronic excited state. The radiative path is assumed to be temperature independent, meaning that the radiative de-excitation takes place with a constant probability  $p_R$  and the non-radiative or thermal path probability (defined as the inverse of the lifetime) temperature dependence is described by a Boltzman factor  $p_{NR} \propto \exp(\Delta E = B/k_B T)$ , and the total lifetime is given by the equation 3.2, where  $\Delta E$  is the energy difference between electronic excited state and the host level that that promotes non-radiative de-excitation of the emitting center.

$$\tau = \frac{1}{p_R + p_{NR}} = \frac{1}{\tau_{rad}^{-1} + k \exp(-\Delta E/(K_B T))} \quad (3.2)$$

Manipulating the equation 3.2 it is possible to establish a practical expression (equation 3.3) that can be easily handled by MatLab ® fitting functions. The experimental data fitting to this equation, permits to compute the characteristic energy difference  $\Delta E$  using the numerical  $D$  parameter using the relation  $\Delta E = D/k_B$ . The numerical fitting is implemented using a Non-linear Least Squares Algorithm the interactive Levenberg-Marquardt method. The robust linear least-squares fitting method used corresponds to the bi-square weights method. The fits goodness was evaluated and the confidence intervals used to estimate the errors is 95%.

$$\tau = \frac{A}{B + C \exp(-D/T)} \quad (3.3)$$

The  $\Delta E$  value computed numerically gives information about the energy level structure of the materials. Cross-check of the  $\Delta E$  with the established energy diagram can be an important tool to evaluate possible non-radiative decay paths on each sample.

In practical terms the total characterization of the non-radiative decay paths can be a time consuming measurement. Moreover the number of decays recorded, multiplied by the temperatures of interest can provide tens of decays per sample to analyze. The huge amount of experimental data recorded for each sample encouraged the implementation of a set of MatLab ® scripts to speed up the data reduction needed to perform the analysis of experimental data.

### 3.2.3 Other Methods and Techniques

#### Absolute Quantum Yield

The absolute quantum yield was computed using phosphor standard powders, regarding equation 3.4.  $\phi$  represents the experimental quantum yield,  $A$  and  $A_{std}$  is the emission integrated intensity of the sample and of the standard, respectively;  $r$  and  $r_{std}$  represents the reflectivity of the sample and of the standard, respectively. Finally  $\phi_{std}$  is the standard absolute quantum yield [263].

$$\phi = \frac{A}{A_{std}} \frac{(1 - r_{std})}{1 - r} \phi_{std} \quad (3.4)$$

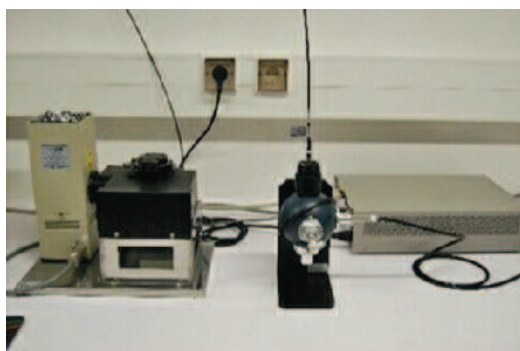


Figure 3.13: Quantum Yield Experimental Setup

The absolute emission quantum yields were measured using a quantum yield measurement system C9920-02 from Hamamatsu with a 150 W Xenon lamp coupled to a monochromator for wavelength discrimination, an integrating sphere as sample chamber and a multichannel analyzer for signal detection. Three measurements were made for each essay and the average is reported. The method is accurate within 10%.

### Dynamic Light Scattering

Dynamic light scattering (DLS) is a powerful technique to characterize materials at the nanoscale. As the name suggests, it consists in the analysis of the scattered light originated from a sample. In fact the technique is widely used to determine the size distribution profile of small particles in solution. The process of measurement consist on the evaluation of the Brownian motion, on the determination of the diffusion rate in order to evaluate the particle size as the hydrodynamic diameter or the Stokes diameter ( $d_H$ ).

In fact the hydrodynamic diameter is always larger than the particle diameter because the equivalent hard sphere that diffuses at the same rate as the molecule includes the hydration and shape effects, and is correlated to the diffusion of the particles within the solvent.

The light scattering gives a time-dependent fluctuation in the scattering intensity due to the Brownian motion of the molecules in solution. The information on the size of the particles is obtained by the autocorrelation function.

The hydrodynamic diameter ( $d_H$ ) is computed using the Stokes-Einstein equation 3.5, using the Boltzmann constant ( $k_B$ ) and the absolute temperature ( $T$ ). The properties of



Figure 3.14: DLS Marvern equipment (Zetasizer - Nano ZS90) in the UniZar/ICMA laboratory.

the solution are taken in account in the viscosity  $\eta$  and the diffusion coefficient of the particles in the solvent ( $D$ ).

$$d_H = \frac{k_B T}{3\pi\eta D} \quad (3.5)$$

This technique is dependent on the ionic strength of the solvent due to the electrical double layer around the particles and on the interaction of the solvent the particles, the surface structure or functionalization.

The DLS measurements were performed on the UniZar/ICMA equipment. The apparatus is a Zeta-Sizer Nano-ZS90 from Marvern. The preparation of the suspension is done by dissolving a about 1 mg of sample into 1 mL of solvent (usually water). The sample was sonicated before the measurement to promote the complete dispersion on the solvent.

The suspension was transferred to a plastic cuvette that is placed inside the Zeta-Sizer. The equipment stabilized the temperature for one minute and begins the measuring of the size distribution. The output can be extracted from the equipment using the software interface into the form of number of particles, intensity, volume, etc. The most used form is the number of particles distribution.

Very commonly the size distribution histogram presents a gaussian or a set of gaussian

profiles. In these cases, it is possible to use a gaussian fit to the histogram of experimental sizes to estimate the mean value and the standard deviation of sizes.

All size distributions reported in the following chapters corresponds to three consecutive agreeing measurements, to ensure that the reported values characterize the samples in an accurate way.

## Electronic Microscopy

An electron microscope is a scientific instrument that analyses a beam of electrons to examine objects on with high spatial resolution . In an optical microscope, the wavelength of light limits the maximum magnification that is possible to a scale of the order of the wavelength used,  $\sim 1\mu m$ . As electrons have can have smaller wavelengths, it is possible to achieve a higher magnification, improving the spatial resolution typically 1000 times when compared with an optical microscope.

In basic terms, an electron microscopy is based on the same basic principles of light microscopy but uses electrons instead of photons to interact with the sample. The advantage of use electrons is in the use of wavelengths in the order of tens of the picometer ( $10^{-12}m$ ) allowing spatial resolution in the same order of magnitude. The electron microscopes use electromagnetic and/or electrostatic lenses (composed by solenoids) to control the path of electrons.

The device can produce electrons with different wavelengths (depending on the accelerating voltage used) that allows different sample characterization. While the in Transmission Electron Microscope (TEM),the electrons in the primary beam that are transmitted through the sample are analyzed, in the the Scanning Electron Microscope (SEM) produces images by detecting secondary electrons which are emitted from the surface due to excitation by the primary electron beam.

The chemical characterization of a sample is possible using energy dispersive spectroscopy (EDS), an analytical technique used in concert with SEM and TEM. This tool is very useful for material characterization since it can perform qualitative and semi-quantitative microanalysis on a specimen allowing a mapping of the elements.

In practical terms scanning electron micrographs where obtained in CiCECO/RMNEUA microscopy facilities, using a Hitachi SU-70 FEG-SEM and the chemical composition (and elemental maps) was determined on a Bruker AXS Quantax 400 energy dispersive Xray spectrometry system (EDS). The samples for observation where prepared using the double



Figure 3.15: Ultra-high Resolution Analytical Scanning Electron Microscope HR-FEG-SEM Hitachi SU-70 of the CiCECO/RNME-UA (a) and Unizar/ICMA TEM JEOL-2000 FXII (b), respectively used for the electronic micrographs acquisition.

coated conductive carbon tape. It requires no drying time, holds the sample firmly to the surface, and can be used as a ground strap from the sample surface to sample holder. All samples were coated with carbon prior to observation.

Transmission electron microscopy (TEM) observations were carried out in a transmission electron microscope JEOL-2000 FXII (photographs in figure 3.15 - UniZar/ICMA). The sample preparation involves the dispersion of the powders in a solvent (water or ethanol) in amounts of approximately 1mg/mL with the help of a sonicator. After a second sonication (10 mins) the TEM grid is impregnated with the sample by dip-coating or by adding a drop and drying. The samples were always deposited on copper TEM grids.

## Summary

This chapter lists the experimental procedures and techniques used in this thesis. In the following chapters the reader is submitted to this section that intends to have a detailed description of all the synthesis routes and characterization techniques. The synthesis of the nanoparticles and films follows the sol-gel route presented here briefly. The photophysical characterization of the samples encompasses the steady-state emission and excitation spectra, emission quantum yield and time resolved spectroscopy. The numerical algorithms to perform data analysis (implemented in MatLab®) are briefly described. The morphological

characterization uses electronic microscopy and dynamic light scattering.

## Chapter 4

# Metal-Free Highly Luminescent Silica Nanoparticles

Stable, cost-effective, brightly luminescent and metal-free organosilica NPs (Si-NPs) were prepared using the Stöber method without any thermal treatment above 318 K. The white-light photoluminescence results from a convolution of the emission originated in the  $\text{NH}_2$  groups of the organosilane and oxygen defects in the silica network. The time-resolved emission spectra are red shifted, relatively to those acquired in steady-state regime, pointing out that the NPs emission is governed by donor-acceptor (D-A) recombination mechanisms. Moreover, the increase of the corresponding lifetime values with the monitored wavelength further supports that the emission is governed by a recombination mechanism typical of D-A pair attributed to an exceptionally broad inhomogeneous distribution (fwhm  $\sim 100$  nm) of the emitting centers peculiar to silica-based NPs. These NPs exhibit the highest emission quantum yield value ( $0.15 \pm 0.02$ ) reported so far for organosilica biolabels without activator metals. Moreover, the emission spectra and the quantum yield values are quite stable over time showing no significant aging effects after exposure to the ambient environment for more than 1 year stressing the potential of these NPs as metal-free biolabels.

### 4.1 Metal-Free Silica Nanoparticles in the Literature

Light-emitting silica-based micro and nanoparticles (Si-NPs) have provided a remarkable interest in the past decade due to their intriguing emission features and potential

applications in photonics (*e.g.* photonic crystals [18], synthetic opals [171], and highly emissive broadband phosphors for solid-state lighting) [85, 177], biology and biomedicine (*e.g.* chemical sensing [111], single oxygen generation for photodynamic therapy [72], bio-analytical assays [250] and medical diagnostics and therapy) [186]. In bioimaging and biosensing, silica based NPs are skilled to obtain sensitive data in a non-invasive manner, promising a breakthrough in early-stage cancer diagnosis, stem cell tracking, drug delivery, pathogen detection and gene delivery [43, 201, 226, 112, 35, 37, 149, 27].

The Si-NPs are typically produced by embedding different emission centers, such as organic fluorophores [112, 35], QDs [43, 201], or  $\text{Ln}^{3+}$  [37, 149], into the silica skeleton. Whereas the photobleaching is the main limitation of the dye-based NPs precluding continuous long-term use, the incorporation of QDs and  $\text{Ln}^{3+}$  ions into silica usually involves multiple processing steps requiring the use of expensive and/or environmentally toxic luminophores. Therefore, luminescent silica-based NPs (and/or organogels) which do not require doping with metal activator ions are an interesting alternative to those traditional doped materials, especially in terms of environmental suitability and low manufacturing cost. Illustrative and intriguing examples are the sol-gel derived luminescent organosilica NPs proposed by Schmedake *et al.* [108, 217] Wang *et al.* [250], Kong *et al.* [127], Zhanbotin *et al.* [277], and Enrichi *et al.* [66]. Monodisperse and submicrometer organosilica NPs (variable sizes ranging from 50 and 550 nm) were synthesized from the co-condensation of tetraethoxysilane (TEOS) and several organosilanes (*e.g.* 3-aminopropyltriethoxysilane, APTES [108, 127, 217, 250, 277], 3-aminopropyltrimethoxysilane, phenyltriethoxysilane, 1,4-bisnaphthyltrimethoxysilane, 1-naphthyltrimethoxysilane, and 1,4 - bis (triethoxysilyl) benzene) [250] under basic (via a modified Stöber route [221] or a water/oil microemulsion) [16] and acid [66] conditions. The TEOS:organosilane molar ratio was varied accordingly to the organosilane used. For NPs incorporating APTES (those exhibiting higher emission quantum yields) the molar percentage of APTES ranged from 0 to 80% [66, 108, 127, 217, 250, 277]. When these NPs were calcinated at temperatures between 473 and 973 K, they not only exhibited a tunable blue-greenish photoluminescence upon UV excitation [66, 108, 127, 217, 250, 277] but also gave rise to a strong phosphorescence afterglow (lifetime values in water between  $0.1 \times 10^{-3}$  and  $3.3 \times 10^{-3}$  s, for APTES concentrations of 25 and 50%) [250]. The emission quantum yield depends on the synthesis and processing conditions and on the relative amount of APTES. A quantum yield as high as 0.12 was reported by Schmedake *et al.* [27, 149] for low-doped APTES spheres calcined

at 473 K, whereas Wang *et al.* [127, 250] listed values between 0.01 and 0.09.

## 4.2 Metal-Free Si-NPs Characterization

In this chapter is reported the tuneable photoluminescence (steady state and time-resolved emissions) and the emission quantum yields of non-calcined organosilica NPs prepared through a modified Stöber procedure mixing TEOS with APTES.

Three different samples were prepared following the procedure described in detail in section 3.1.2, named **AT-1.2**, **AT-1.1** and **AT-2.1** (APTES:TEOS volume ratios of 1:2, 1:1 and 2:1 and mol % APTES of 33, 49 and 65%, respectively). These values are similar to those already reported for analogous organosilica NPs [66, 108, 127, 217, 250, 277]. Figure 4.1 shows the photographs of aqueous suspension (concentration of 2.5 mg/mL) of **AT-1.2**, **AT-1.1** and **AT-2.1** (from left to right) Si-NPs under daylight (left) and irradiated by a 365 nm UV lamp (right). Further optimization of the synthesis recipe, namely through a fine-tuning of the APTES/TEOS volume ratio and its influence on the morphological, structural, and photoluminescence features of the particles lies beyond the scope of this work.

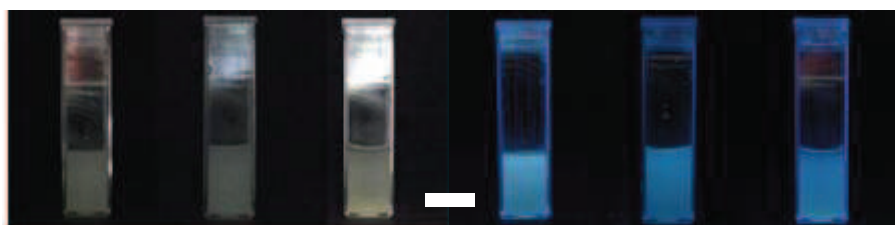


Figure 4.1: Photographs of aqueous suspension (concentration of 2.5 mg/mL) of **AT-1.2**, **AT-1.1** and **AT-2.1** (from left to right) NPs under daylight (left) and irradiated by a 365 nm UV lamp (right). The scale bar corresponds to  $1 \times 10^{-2}$  m.

### 4.2.1 Morphological Characterization

The distribution of hydrodynamic diameters of particles in aqueous suspensions of **AT-1.2**, **AT-1.1** and **AT-2.1** samples was examined by DLS and presented in figure 4.2A. Although the measurements were disturbed by particle luminescence, the presence of a

single peak in all the cases points out a good dispersibility in water, a monomodal size distribution, and the absence of particle aggregation.

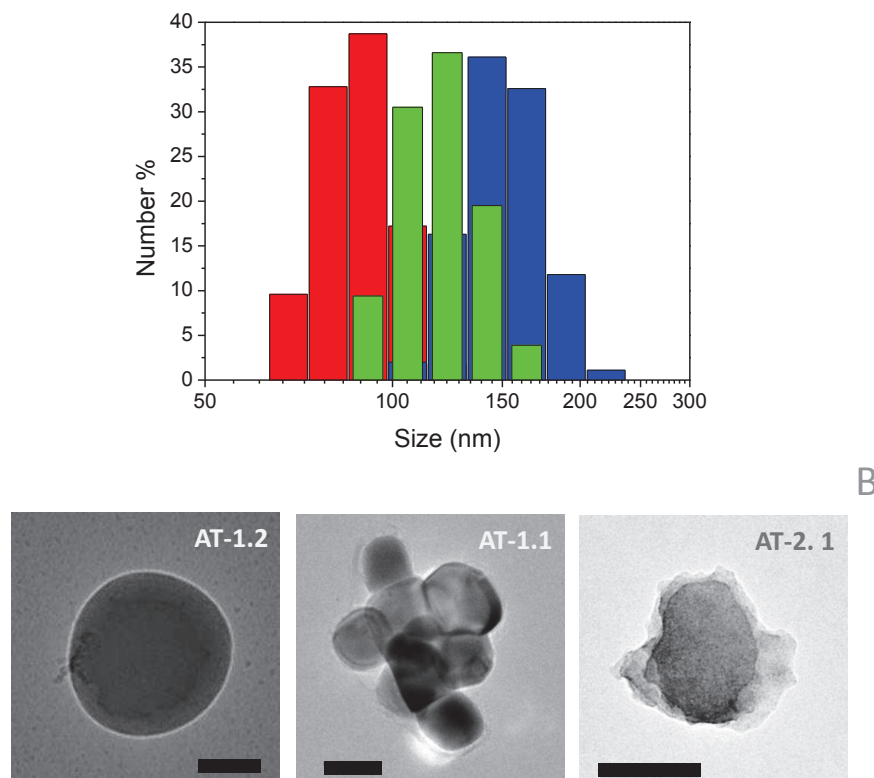


Figure 4.2: (A) DLS size distribution of the Si-NPs water suspensions. The blue, green and red bars correspond to **AT-1.2**, **AT-1.1** and **AT-2.1**, respectively. (B) TEM images of **AT-1.2**, **AT-1.1** and **AT-2.1** NPs in water suspensions. All the scale bars correspond to 100 nm.

The obtained average hydrodynamic diameters and relative standard deviations (in parenthesis) were 141 (15%), 120 (15%) and 88 (14%) nm, respectively, for water suspensions. NPs average size and the corresponding standard deviation obtained in ethanol suspensions were similar (table 4.2.1), although DLS shows bimodal size distribution, probably due to aggregation effects.

The TEM images from water suspensions of the Si-NPs (figure 4.2B) show spheres with an average size and a relative standard deviation (in parenthesis) of 100 (25%), 105 (16%) and 169 (20%) nm, for **AT-1.2**, **AT-1.1** and **AT-2.1** NPs, respectively. Similar measurements using ethanolic suspensions are presented in table 4.2.1, presenting a different trend, due to the interaction between the Si-NPs and the solvent.

Table 4.1: Si-NPs average size and relative standard deviation (in parenthesis) obtained by DLS measurements and TEM images of ethanol suspensions.

	<b>AT-1.2</b>	<b>AT-1.1</b>	<b>AT-2.1</b>
DLS	92 (14%)	142 (15%)	122* (10%)
TEM	18/242** (43%/37%)	112 (32%)	235 (18%)

\* DLS size distribution of **AT-2.1** shows a small peak for high sizes (representing less than 10% in number, with mean diameter of 531 nm and 27% relative standard deviation) that could be attributed to an incomplete dispersion of the sample.

\*\* The two peaks observed corresponds approximately the same number of particles.

Usually the particles show a dense core surrounded by a layer of a lighter material that may correspond to silica and propylamine-silica respectively. Varying the APTES concentration has noticeable effects on the structural properties of the spheres, in good agreement with that reported before for analogous organosilica NPs [108, 217, 250]. Particle size appears to be inversely related to the APTES concentration and the TEM images (figure 4.2B) suggest that surface roughness also increased with that concentration. As it should be expected, TEM sizes are smaller than DLS sizes for **AT-1.2** and **AT-1.1** samples due to the hydration layer around the particles in dispersion. For the **AT-2.1**, however, DLS average size is smaller than TEM average size. This discrepancy in the diameter values is due to a stronger effect of **AT-2.1** luminescence in DLS measurements as that sample is by far the most efficient emitter of the three (see next section for details).

### 4.3 Photophysical Characterization

Figure 4.3 shows the room temperature emission (A and B, excited at 385 nm) and excitation (C and D, monitored at 500 nm) spectra of **AT-1.2** (blue), **AT-1.1** (green) and **AT-2.1** (red) Si-NPs acquired before (A and C) and after (B and D) the annealing at 873 K. After annealing, it is evident the increase of the relative intensity of the high-energy excitation band at  $\sim 2.88eV$  (430 nm) in **AT-1.2** and **AT-1.1** and  $\sim 3.10eV$  (400 nm) in **AT-2.1**. The emission spectra of the Si-NPs (Figures 4.3 and 4.4) are formed of a broad band (full width at half maximum, fwhm,  $\sim 0.8eV$  whose energy and number of

components depends on the excitation wavelength. In particular, for excitation wavelengths between 315 and 365 nm the emission spectra unequivocally display a main component in the blue spectral region,  $\sim 2.58 - 2.48\text{eV}$  (480-500 nm), resembling that observed for APTES-containing Si-NPs [108] and amine-functionalized hybrids [112], and a low-relative intensity band at higher energies  $\sim 2.95\text{eV}$  (420 nm), marked with an arrow in figure 4.4 ascribed to the presence of TEOS, as detailed below. Increasing the excitation wavelength (365-405 nm) only the low-energy component associated with the presence of APTES subsists (figure 4.4). For the entire selected excitation wavelength range (315-405 nm), no significant emission differences are detected between the **AT-1.2**, **AT-1.1** and **AT-2.1** Si-NPs (figure 4.3A,B and figure 4.4).

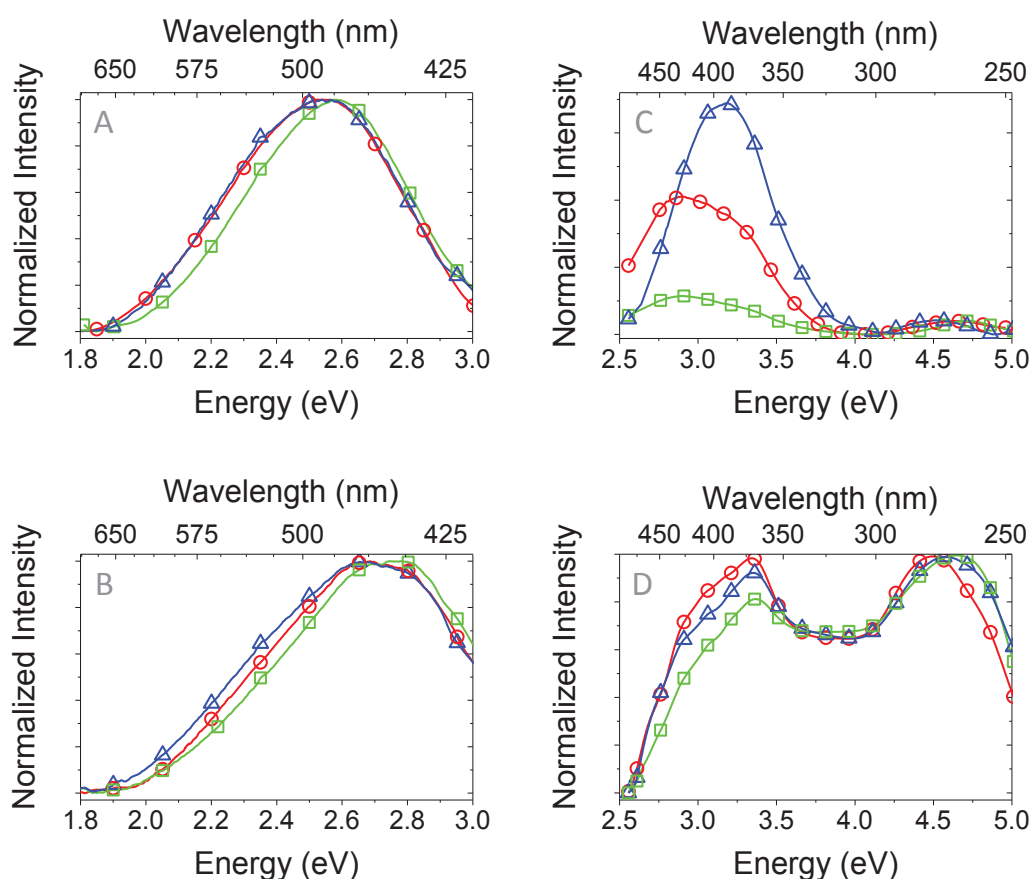


Figure 4.3: Room temperature emission (A and B, excited at 385 nm) and excitation (C and D, monitored at 500 nm) spectra of **AT-1.2** (blue), **AT-1.1** (green) and **AT-2.1** NPs acquired before (A and C) and after (B and D) the annealing at 873 K.

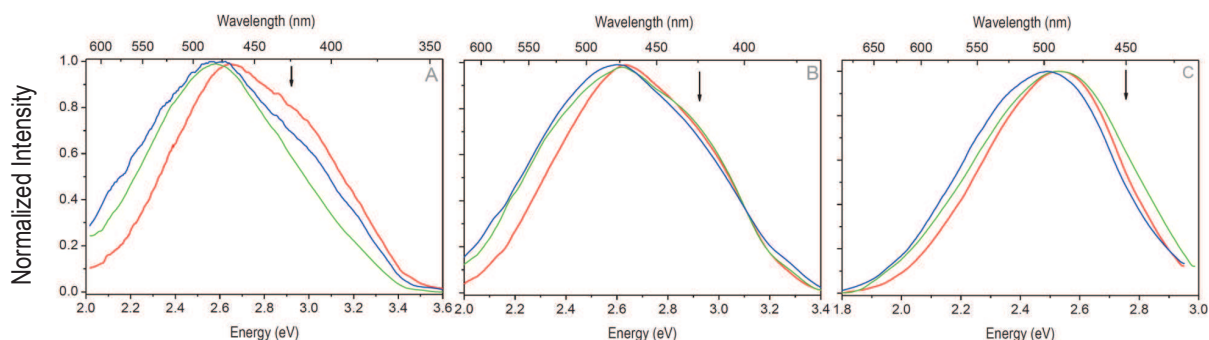
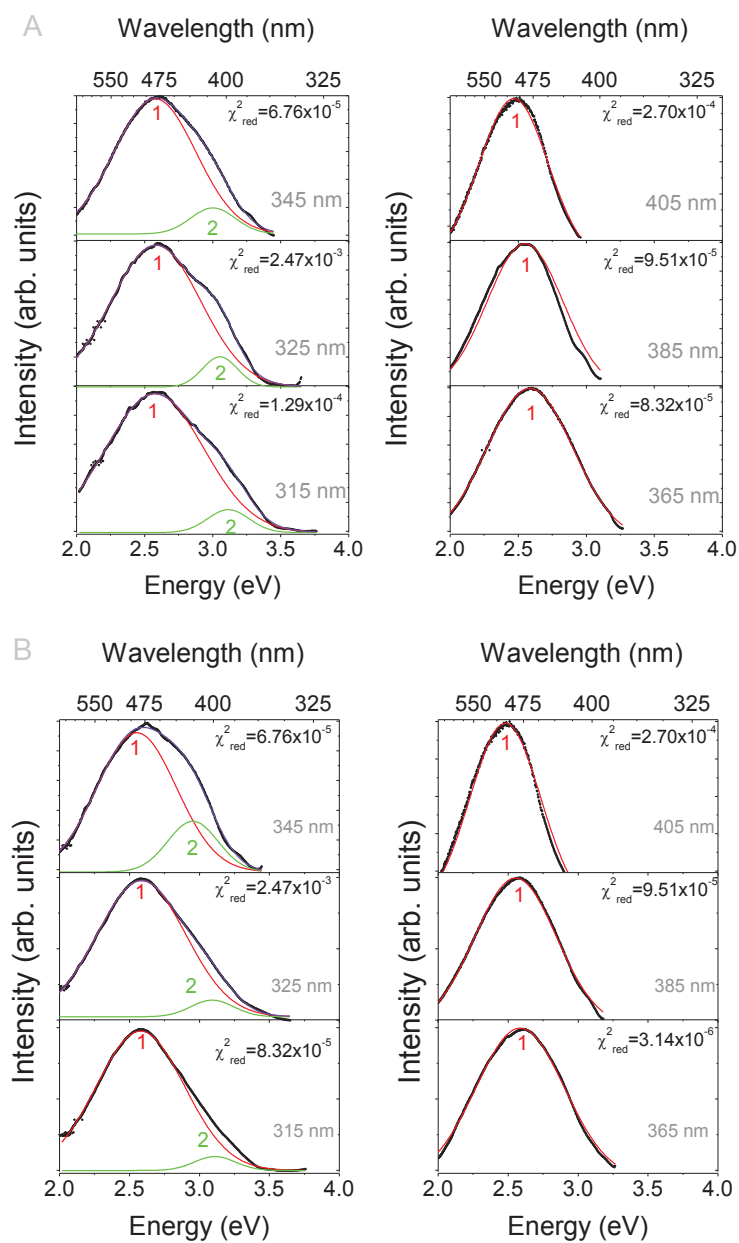


Figure 4.4: Room temperature emission spectra of **AT-1.2** (blue), **AT-1.1** (green) and **AT-2.1** (red) NPs, excited at (A) 315, (B) 345 and (C) 405 nm, respectively.

In an attempt to gain full insight into the emission features, energy and fwhm of the APTES- and TEOS-related components a deconvolution fitting procedure was performed following a previously detailed method (see [36] for a detailed description). Figure 4.5 shows the curve fitting results for **AT-1.2**, **AT-1.1** and **AT-2.1**. All the values for the fitting parameters (energy peak position, fwhm and intensity) are summarized in table 4.3. The emission energy of the APTES-related component is almost independent of the selected APTES:TEOS ratio varying from 2.530 to 2.650 eV. These values are very close to those previously reported for APTES/TEOS-containing NPs [108] (figure 4.6), reinforcing that, for APTES concentration values above 33 %, the emission energy is almost independent of the APTES/TEOS ratio. The TEOS-related component varies between 2.953 and 3.115 eV (table 4.3), as the excitation wavelength decreases from 345 to 315 nm.



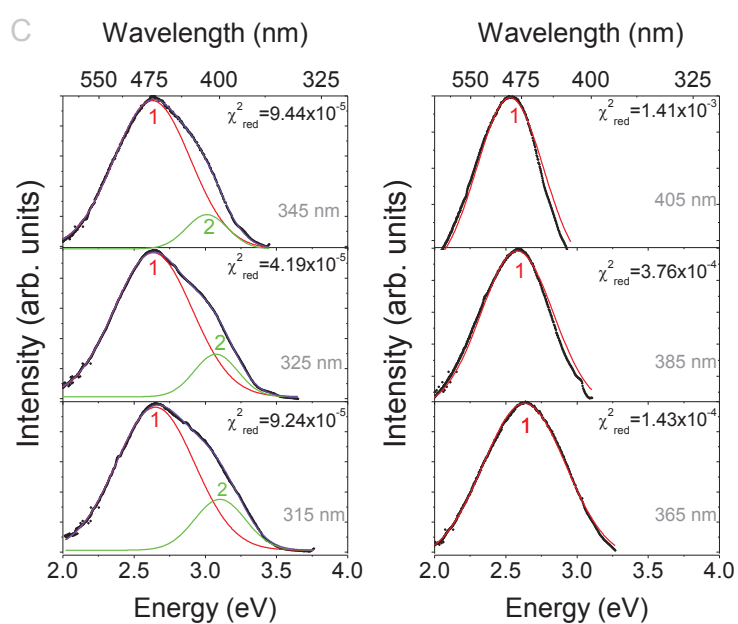


Figure 4.5: Deconvolution fitting procedure of the emission spectra of (A) **AT-1.2**, (B) **AT-1.1** and (C) **AT-2.1** Si-NPs excited at the different wavelengths indicated. The numbers (1) and (2) assign the APTES- and TEOS-based components, respectively.

Table 4.2: Summary of the deconvolution fitting procedure on the emission curves of **AT-2.1**, **AT-1.1** and **AT-1.2**. The higher and the low energy bands correspond to the TEOS- and APTES-related emissions, respectively. The adjusted curves are presented in figure 4.5.

		$\lambda_{exc}(\text{nm})$					
<b>AT-2.1</b>		315	325	345	365	385	405
$E_{MAX}$ (eV)		$2.650 \pm 0.002$	$2.634 \pm 0.001$	$2.629 \pm 0.002$	$2.603 \pm 0.004$	$2.581 \pm 0.035$	$2.530 \pm 0.001$
$fwhm$ (eV)		$0.552 \pm 0.002$	$0.550 \pm 0.001$	$0.536 \pm 0.003$	$0.581 \pm 0.001$	$0.507 \pm 0.002$	$0.467 \pm 0.002$
$Area$		$0.657 \pm 0.004$	$0.659 \pm 0.002$	$0.662 \pm 0.005$	$0.758 \pm 0.003$	$0.626 \pm 0.003$	$0.578 \pm 0.003$
$E_{MAX}$ (eV)		$3.103 \pm 0.002$	$3.075 \pm 0.001$	$3.012 \pm 0.002$			
$fwhm$ (eV)		$0.356 \pm 0.003$	$0.304 \pm 0.002$	$0.291 \pm 0.005$			
$Area$		$0.151 \pm 0.004$	$0.108 \pm 0.002$	$0.083 \pm 0.004$			

		$\lambda_{exc}(\text{nm})$					
<b>AT-1.1</b>		315	325	345	365	385	405
$E_{MAX}$ (eV)		$2.578 \pm 0.001$	$2.571 \pm 0.001$	$2.552 \pm 0.004$	$2.554 \pm 0.001$	$2.554 \pm 0.002$	$2.540 \pm 0.003$
$fwhm$ (eV)		$0.630 \pm 0.002$	$0.633 \pm 0.002$	$0.569 \pm 0.005$	$0.625 \pm 0.002$	$0.583 \pm 0.002$	$0.543 \pm 0.002$
$Area$		$0.770 \pm 0.003$	$0.756 \pm 0.003$	$0.669 \pm 0.010$	$0.830 \pm 0.004$	$0.761 \pm 0.003$	$0.676 \pm 0.004$
$E_{MAX}$ (eV)		$3.111 \pm 0.004$	$3.092 \pm 0.003$	$2.953 \pm 0.003$			
$fwhm$ (eV)		$0.293 \pm 0.008$	$0.306 \pm 0.007$	$0.359 \pm 0.005$			
$Area$		$0.036 \pm 0.002$	$0.045 \pm 0.002$	$0.154 \pm 0.008$			

		$\lambda_{exc}(\text{nm})$					
<b>AT-1.2</b>		315	325	345	365	385	405
$E_{MAX}$ (eV)		$2.585 \pm 0.001$	$2.583 \pm 0.001$	$2.586 \pm 0.002$	$2.576 \pm 0.001$	$2.561 \pm 0.001$	$2.543 \pm 0.005$
$fwhm$ (eV)		$0.720 \pm 0.003$	$0.659 \pm 0.002$	$0.602 \pm 0.003$	$0.632 \pm 0.001$	$0.559 \pm 0.002$	$0.504 \pm 0.002$
$Area$		$0.865 \pm 0.005$	$0.807 \pm 0.004$	$0.731 \pm 0.005$	$0.837 \pm 0.002$	$0.719 \pm 0.004$	$0.640 \pm 0.003$
$E_{MAX}$ (eV)		$3.115 \pm 0.003$	$3.053 \pm 0.001$	$3.002 \pm 0.003$			
$fwhm$ (eV)		$0.305 \pm 0.007$	$0.257 \pm 0.004$	$0.327 \pm 0.005$			
$Area$		$0.060 \pm 0.003$	$0.067 \pm 0.002$	$0.077 \pm 0.003$			

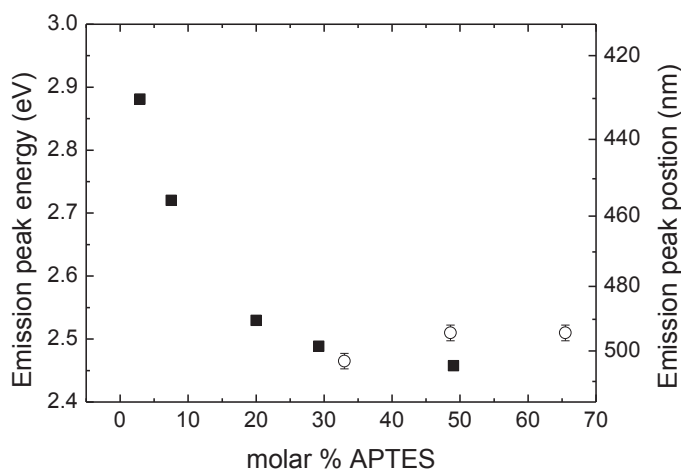


Figure 4.6: Emission peak energy (and corresponding wavelength) of the APTES-related component of **AT-1.2**, **AT-1.1** and **AT-2.1** Si-NPs (open circles) as a function of APTES molar concentration. The emission peak energy (and wavelength) of the samples prepared by Jakob & Schmedake [108] (squares) is also displayed.

The emission dependence on the excitation wavelength, already observed for silica NPs [127, 248] and amine-functionalized organic-inorganic hybrids [28, 39, 40, 85, 177], provides strong evidence of disordered-related processes generally associated with transitions occurring within localized states in noncrystalline structures [39]. This dependence was previously modeled as radiative recombinations involving thermal relaxation within localized states, in the framework of the extended multiple trapping approach [196]. The excitation spectra of the **AT-1.2**, **AT-1.1** and **AT-2.1** Si-NPs are very similar, as found for the emission spectra (Figures 4.3C,D). The spectra monitored at the emission wavelength corresponding to the intensity maximum comprise a main broad band (fwhm of  $\sim 0.9\text{eV}$ ) peaking at  $\sim 3.10\text{eV}$  (400 nm), for **AT-1.2** and **AT-1.1**, and  $\sim 2.88\text{eV}$  (430 nm), for **AT-2.1**, and a low-relative intensity component at  $\sim 4.60\text{eV}$  (270 nm). These two components were previously assigned to the presence of APTES and TEOS, respectively [36, 177]. The high relative contribution of the TEOS-related component for the **AT-1.2** NPs, with respect to the low TEOS-content ones (**AT-1.1** and **AT-2.1**), reinforces the previous attribution.

Time-resolved spectroscopy furnishes unequivocal arguments pointing out the selective contribution of the APTES and TEOS to the overall emission features of the Si-NPs. Figure 4A illustrates for **AT-1.2** the 10 K time-resolved emission spectra excited at 350 nm

and acquired at distinct starting delay (SD) values. For SD between  $0.05$  and  $20.00 \times 10^{-3}$  s, the TEOS- and the APTES-related bands, centered at  $\sim 2.76$  and  $2.44$  eV (450 and 508 nm), respectively, are clearly discerned (the arrow in figure 4.7 assigns the TEOS-based component). At higher SD values ( $SD > 20.00 \times 10^{-3}$  s) only the long-lived APTES-related band is detected.

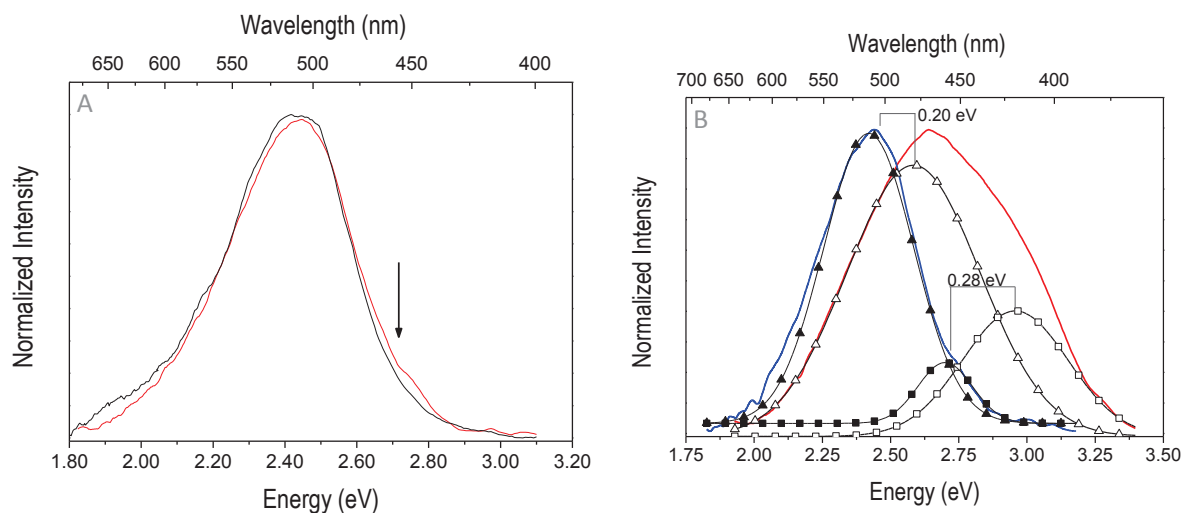


Figure 4.7: (A) Time-resolved emission spectra of **AT-1.2** NPs ( $SD = 0.05 \times 10^{-3}$ ,  $5.00 \times 10^{-3}$  and  $20.0 \times 10^{-3}$  s, blue, red and black lines, respectively). (B) Emission spectra of the same sample acquired in time-resolved ( $SD = 0.05 \times 10^{-3}$  s, blue line) and in steady state (red line) modes. The APTES- (triangles) and TEOS (squares)-based components resulting from the fitting of the steady-state (open symbols) and time-resolved (solid symbols) spectra are also shown. The numbers assign the energy shift between the emission maximum intensity of the steady-state and time-resolved emission spectra. All the spectra were acquired at 10 K and excited at 350 nm.

The decay curves monitored at those maximum intensity bands of figure 4.7 are well fitted with single exponential functions yielding to lifetime values of  $(50.4 \pm 1.9) \times 10^{-3}$  s and  $(5.2 \pm 0.9) \times 10^{-3}$  s, for the APTES and TEOS-related emissions, respectively (figure 4.8).

Independently of the selected excitation wavelength, the time-resolved emission spectra are shifted towards the red, relatively to the corresponding steady-state emission spectra (figure 4.8). This later observation is a solid indication that the emission is governed by a recombination mechanism typical of D-A pairs, mediated by some localized centers [48, 282]. For longer SD times a red shift in the emission spectra is expected because distant

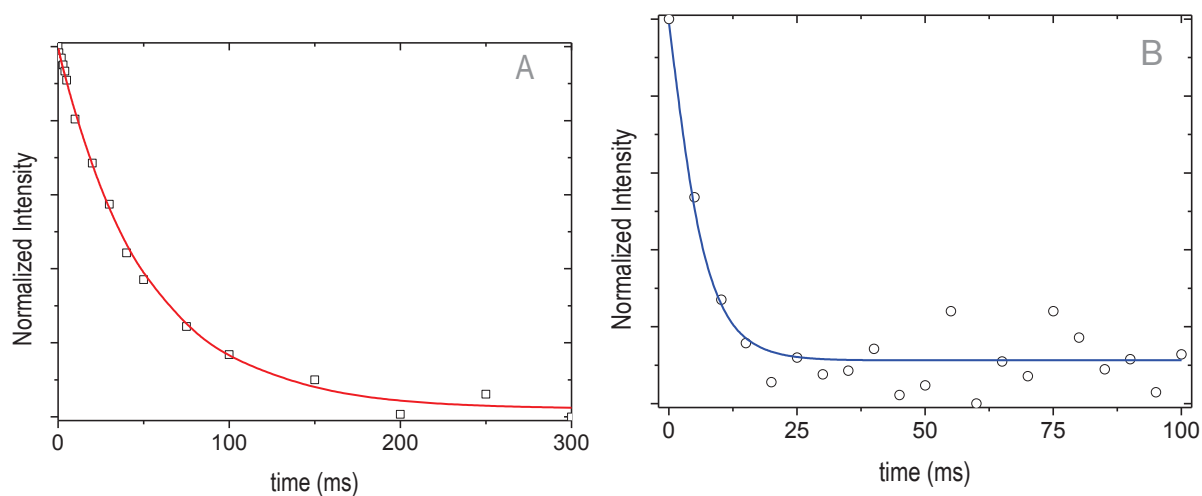


Figure 4.8: Decay curves of **AT-1.2** (10 K) monitored at (A) 500 nm (APTES-related component, squares, excitation wavelength of 360 nm) and at (B) 455 nm (TEOS-related component, circles, excitation wavelength of 350 nm). The solid lines represent the best fit of experimental data to a single exponential decay, where  $I_0$  is the intensity at  $t = t_0 = 0.05 \times 10^{-3} s$ .

pairs have a smaller recombination probability. The respective energy levels therefore have larger lifetimes, a situation that is favored with increasing delay time. As a consequence, the recombination takes place at lower energies (the lifetime measured at longer wavelengths is always longer than that measured at lower ones indicating a significant Coulomb interaction between donors and acceptors) [39, 48, 282]. For **AT-1.2**, the energy shift between the energy of the maximum intensity of the emission spectra acquired in steady-state and time-resolved modes for the APTES- and TEOS-related emissions is 0.20 and 0.28 eV, (figure 4.8B) corresponding to 7.0 and 8.5% respectively.

The room-temperature emission decay curves (figure 4.9) reveals a non-exponential behavior, being well described by a bi-exponential function in good agreement with the presence of two emission components, under an excitation wavelength of 330 nm. The corresponding lifetime values are listed in table 4.3. Accordingly to the values measured at 10 K, it can be tentatively assign the high and low values to the APTES- and TEOS-related excited states, respectively. The increase of both lifetime values with the monitored wavelength supports that the emission is governed by a recombination mechanism typical of D-A pairs [48, 282]. Moreover, these features were recently attributed to an exceptionally broad inhomogeneous distribution of the emitting centers peculiar to silica-based NPs [236].

Table 4.3: Lifetimes of the TEOS- ( $\tau_{TEOS}$ ) and APTES-related ( $\tau_{APTES}$ ) components of **AT-1.2**, **AT-1.1** and **AT-2.1**. The decay curves, excited at 330 nm, were measured monitoring different wavelengths ( $\lambda$ ) along of the broad emission band at room temperature (figure 4.9). The  $r^2$  parameter illustrates the quality of the fit.

	$\lambda(nm)$	$\tau_{TEOS}$	$\tau_{APTES}$	$r^2$
<b>AT-1.2</b>	360	$3.8 \pm 0.2$	$9.9 \pm 0.5$	0.995
	405	$5.6 \pm 0.1$	$15.2 \pm 0.3$	0.998
	550	$6.2 \pm 0.2$	$15.7 \pm 0.9$	0.994
<b>AT-1.1</b>	360	$4.5 \pm 0.1$	$11.5 \pm 0.5$	0.998
	430	$5.0 \pm 0.1$	$12.7 \pm 0.4$	0.999
	550	$5.9 \pm 0.3$	$12.9 \pm 0.6$	0.998
<b>AT-2.1</b>	360	$5.0 \pm 0.2$	$12.8 \pm 1.2$	0.994
	450	$5.5 \pm 0.2$	$13.6 \pm 2.4$	0.987
	550	$6.2 \pm 0.6$	$13.7 \pm 0.6$	0.998

D-A pair type recombination mechanisms has been used to explain the emission features of amine/amide-functionalized organosilica materials [39, 40, 196] and other amorphous semiconductors, such as amorphous and hydrogenated-Si [196]. More recent reports on D-A related emission include N-Al doped 6H-SiC for LED applications [181], CdGeAs<sub>2</sub> single crystals [13], and ZnO [164]. The room-temperature quantum yield and the temperature dependence of the lifetimes of the excited states (ranging from  $10^{-3}$  s, at 10 K, to  $10^{-9}$  s, at room temperature) can be explained only by assuming that the radiative component values of APTES- and TEOS-related emissions at room temperature are much higher than the corresponding ones measured from the lifetimes at low temperature ( $20 - 190s^{-1}$ ). A similar strong dependence is reported for sol-gel derived amine- and amide-functionalized hybrids [178].

The emission features of all the Si-NPs were further quantified through the measurements of the Commission Internationale d'Eclairage (CIE) (x,y) color coordinates (2° standard observer) and the absolute emission quantum yield. For a selected excitation wavelength (365 nm) the CIE (x,y) color coordinates are (0.21,0.30), for **AT-1.2** and **AT-2.1**, and (0.18,0.25), for *AT-1.1*, lying within the blue/green and greenish/blue regions of the chromaticity diagram, respectively (figure 4.10). These results point out that the APTES molar percentage can be used to control the emission color within the green and blue regions.

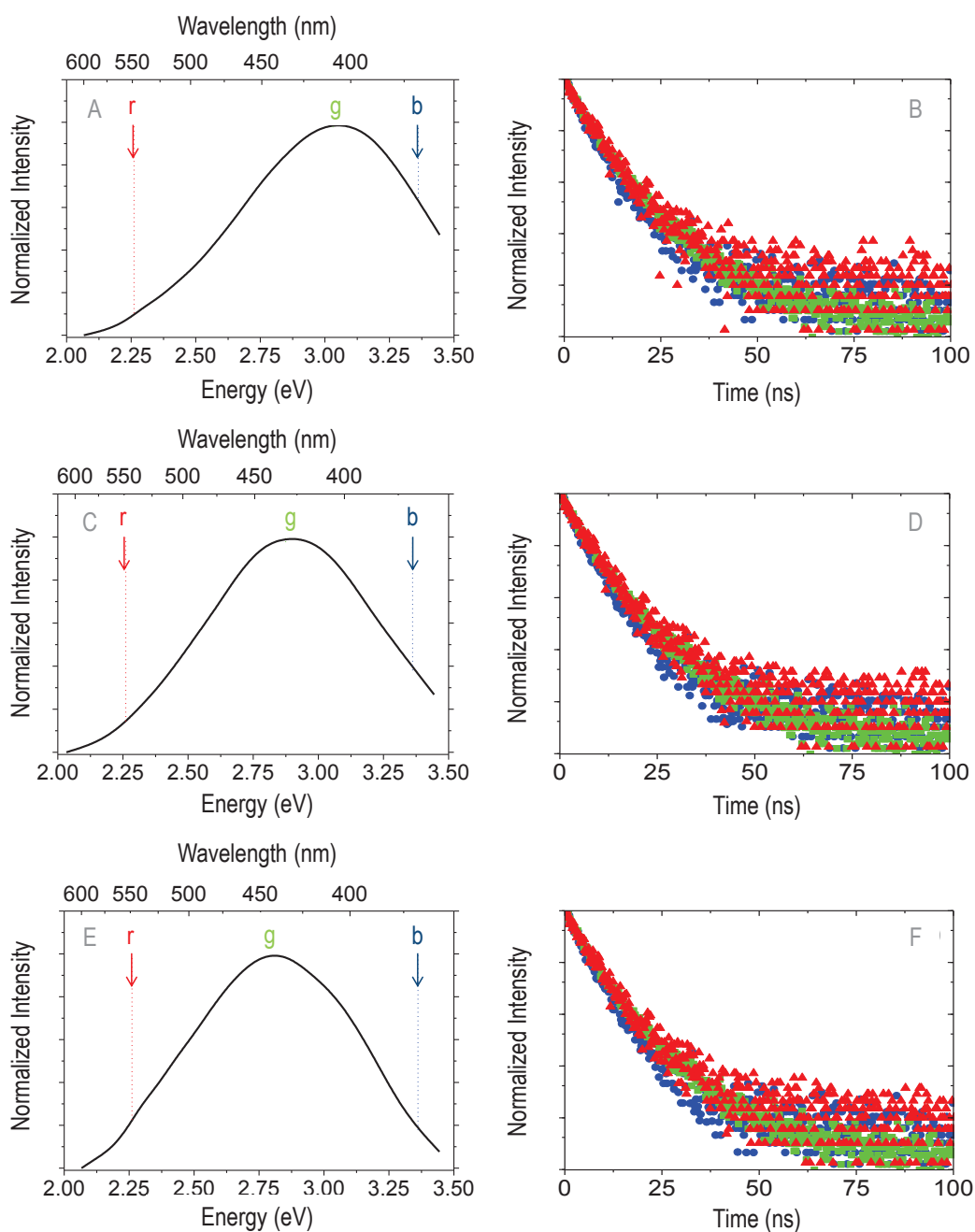


Figure 4.9: Time-resolved emission spectrum (A,C,E) and emission decay curves (B,D,F) at 300 K of **AT-1.2** (A,B), **AT-1.1** (C,D) and **AT-1.2** (E,F) NPs, excitation wavelength of 330 nm. The decay curves were monitored along of the broad energy emission band, before (blue), on (green) and after (blue) the emission maximum. The SD and time window used are  $6 \times 10^{-9}$  and  $170 \times 10^{-9}$  s, respectively.

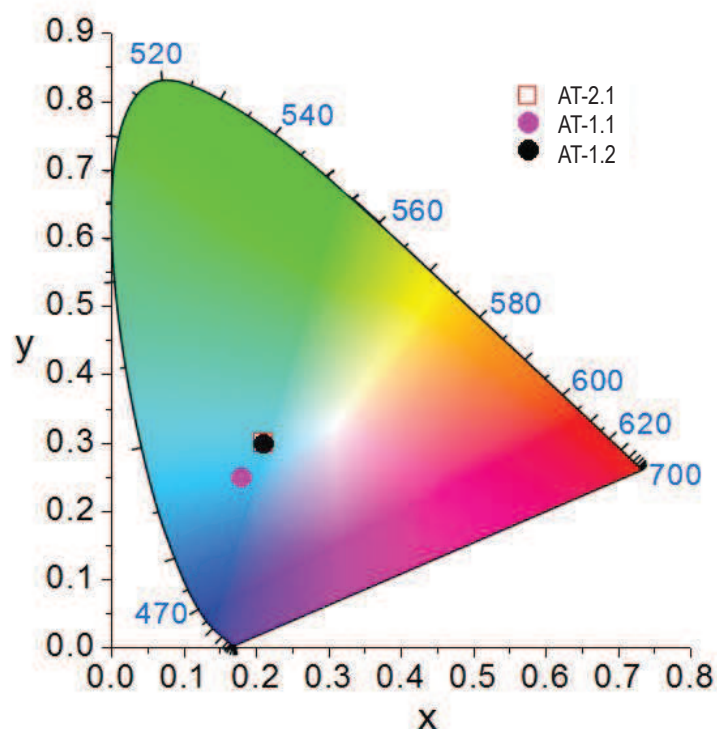


Figure 4.10: CIE chromaticity diagram showing the (x,y) emission color coordinates of the NPs excited at 365 nm.

The absolute emission quantum yield values vary from sample to sample depending on the APTES molar percentage and excitation wavelength. A maximum value of  $0.15 \pm 0.02$  was measured for **AT-2.1** in 350-375 nm excitation wavelength range (figure 4.11). The **AT-1.2** and **AT-1.1** Si-NPs present emission quantum yield values three times lower, similarly to the results previously reported for calcined samples with similar APTES molar percentage [108]. It should be noted that the maximum quantum yield values were attained under selective excitation conditions for the APTES emission reinforcing the principal role of the APTES in the emission features, when compared with that of TEOS. Under lower excitation wavelengths (300-350 nm), there is a significant decrease in the quantum yield values (figure 4.11) revealing a non-efficient TEOS-to-APTES energy transfer. Moreover, the decrease in the molar percentage of APTES (from 66 % in **AT-2.1** to 49/33 % in **AT-1.1** and **AT-1.2**) reinforces that TEOS acts as emission quencher, as it was also suggested by the above mentioned decrease in the lifetime value of the APTES component in the **AT-1.2** with respect to that of **AT-2.1**.

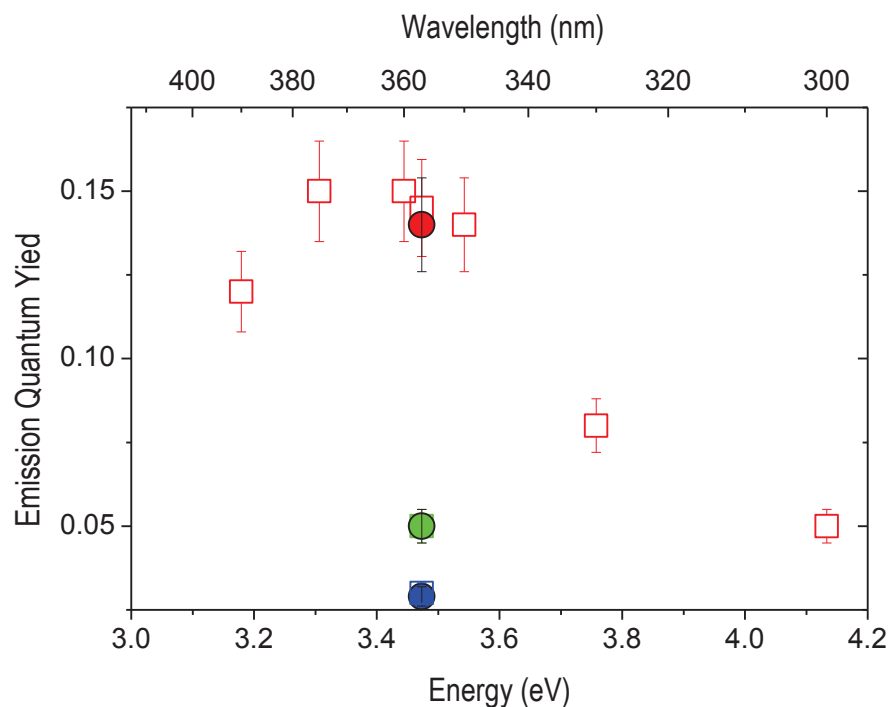


Figure 4.11: Absolute emission quantum yield of **AT-1.2** (blue), **AT-1.1** (green) and **AT-2.1** (red) NPs in the 300-390 nm excitation wavelength range, before (circles) and after (triangles) the annealing at 873 K.

The photoluminescence emission from the Si-NPs is stable over time showing no aging effects after exposure to the ambient environment for more than 1 year (figure 4.12A). This same conclusion was reported by Wang *et al.* [250] for calcined APTES/TEOS NPs exposed to the ambient environment for 6 months. The emission photostability under UV excitation was illustrated for **AT-1.2** by continuous illumination during 5 hours (figure 4.12B). The intensity of the maximum of emission decreases 46% essentially in the first hour of irradiation remaining stable after that period. The absolute emission quantum yield for **AT-1.2** was also monitored within the time interval of more than 1 year, decreasing to  $0.11 \pm 0.01$ .

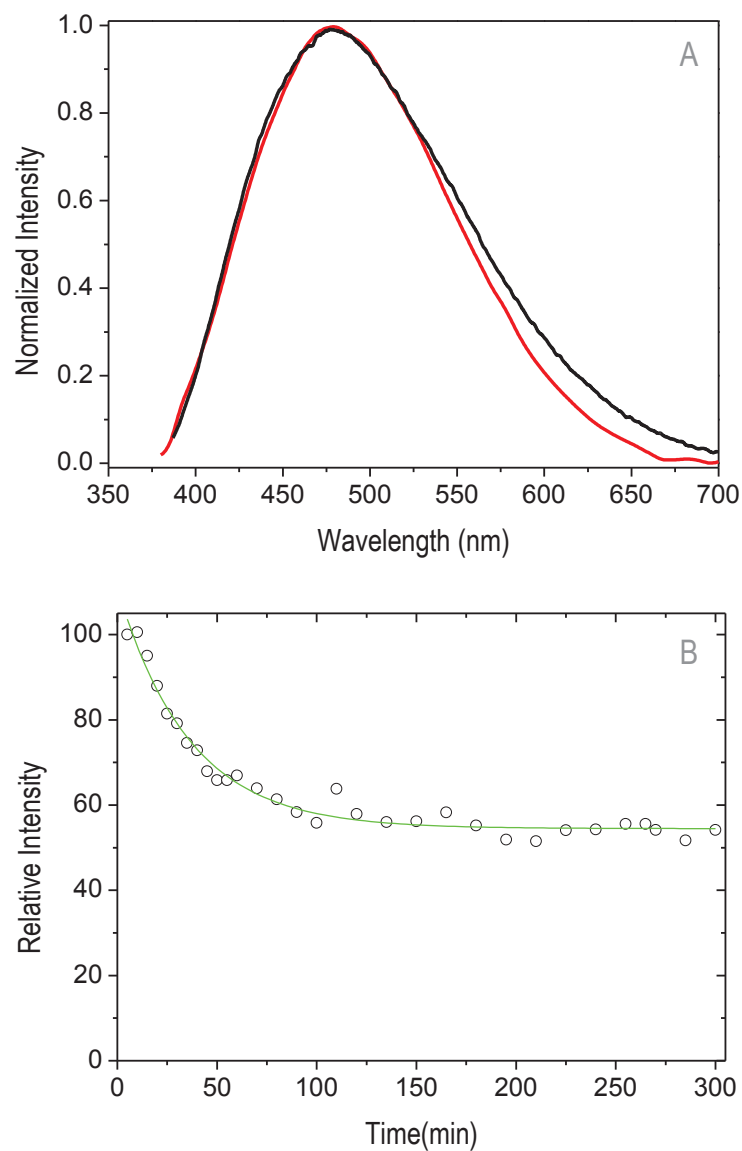


Figure 4.12: (A) Room temperature emission spectra of **AT-2.1** NPs excited at 360 nm. The red and black lines correspond to acquisitions with a time interval of one year, demonstrating the high stability of these NPs. The same behavior is observed for all the other samples. (B) Room temperature photostability under continuous UV irradiation (360 nm) of **AT-2.1** NPs.

## 4.4 Effect of the Annealing in the Photoluminescence of Si-NPs

In order to evaluate the effect of the annealing on the emission quantum yield values and in the emission/excitation spectra the Si-NPs were calcined at 873 K during 4 h (figures 4.11 and 4.3B,D, respectively). This work reports, for the first time, that both the emission spectral features (energy and fwhm) and the quantum yield values do not change with the calcination temperature in the 303-873 K interval (figures 4.11 and 4.3). Although the number of components, energy and fwhm of the excitation spectra monitored within the broad band emission is also almost independent of the calcination temperature (figures 4.3A,B) it is observed a decrease in the relative intensity of the APTES-related component (high-wavelength side of the excitation spectra) relatively to that of the TEOS-associated component (figures 4.3C,D). Increasing the calcination temperature up to 1073 K no emission is discerned (not shown), as already observed by Wang *et al.* [250] for analogous Si-NPs.

Wang *et al.* [250] reported that the increase of the calcination temperature above 873 K leads to a significant decrease in the N and H content (from 2.54% and 2.85% to 0.21% and 0.86%, respectively). Higher temperatures (*e.g.* 1073 K) led to more loss of C, H, and N until a percentage close to zero was reached. The dependence of the H and N weight percentages on the calcination temperature is related with the diminution of the relative contribution of the APTES-related component, with respect to that of TEOS-based one, as clearly illustrated in the excitation spectra of figures 4.3C,D. This rationalization fully agree with the constancy of the emission quantum yields with increasing calcination temperature up to 873 K (figure 4.11) because:

- The APTES-related emission is more efficient than that of the TEOS-contribution;
- The emission quantum yield establishes a ratio between the number of emitted and absorbed photons which is kept constant as the main excitation path for the APTES-related component involves direct excitation (since the TEOS-to-APTES energy transfer is not efficient, as discussed above).

Furthermore, at calcination temperatures around 1073 K the concentration of N and H atoms is reduced to negligible values and, as mentioned above, no emission could be dis-

cerned reinforcing the interpretation for the nature of the Si-NPs emission proposed in this work.

This explanation differs from that known in the literature to interpret the origin of the emission of APTES/TEOS NPs after calcination. In fact, the emission properties of calcined APTES/TEOS NPs prepared under basic conditions were previously ascribed to the introduction of carbon and/or oxygen defects in the silica network resulting from calcination of the aminopropyl groups [108, 253]. This suggestion was based on the former work of Green *et al.* [85] in hybrid materials made from the reaction of APTES (or tetramethoxysilane) and TEOS with a variety of organic carboxylic acids. The creation of a carbon substitutional silicon defect needs, however, a heating process at temperatures above 523 K at least, as explicitly mentioned by Green *et al.* [85]. Moreover, likewise to water-soluble hybrids generated from the reaction of APTES with a variety of organic carboxylic acids [85], the organosilica NPs do not require any heating above room temperature to be luminescent (as demonstrated here). Therefore, the results presented point out that carbon defects cannot account for the observed white-light emission and the luminescent species must be related to the presence of the  $\text{NH}_2$  groups of the APTES layer and to oxygen-related defects in the silica skeleton, probably  $\bullet\text{O}-\text{O}-\text{Si} \equiv (\text{CO}_2)$  oxygen-related defects, as detected by electron paramagnetic resonance in di-ureasil hybrids [39].

## Summary

Stable, cost-effective, brightly luminescent and metal-free APTES/TEOS NPs (molar percentage of APTES between 33 and 66%) were prepared using the Stöber method without any thermal treatment above 318 K. Contrarily to what has been already reported, was demonstrated that there is no need to perform any time- and energy-consuming high-temperature annealing treatment for preparing quite efficient metal-free tunable luminescent organosilica NPs exhibiting quantum yield of  $0.15 \pm 0.02$ , between 350 and 375 nm, the highest value reported so far for Si-NPs without activator metals. Moreover, calcination generally induces irreversible agglomeration, making consequently difficult the NPs dispersion in solvents.

Furthermore, a thermal annealing up to 873 K does not change at all the emission spectra and the quantum yield of the particles. The nature of the NPs light-emission features is rationalized through time-resolved spectroscopy pointing out that the emission

is governed by D-A recombination mechanisms mediated by the  $\text{NH}_2$  groups of APTES and  $\bullet\text{O}-\text{O}-\text{Si} \equiv (\text{CO}_2)$  oxygen-related defects in the silica network (maximum lifetime values of, respectively,  $(50.4 \pm 9.2) \times 10^{-3}$  and  $(5.2 \pm 0.9) \times 10^{-3}$  s, at 10 K, and  $(15.7 \pm 0.9) \times 10^{-9}$  and  $(6.2 \pm 0.2) \times 10^{-9}$  s, at 300 K). The emission spectra and the emission quantum yield of the Si-NPs are stable over time showing no aging effects after exposure to the ambient environment for more than 1 year. Synthesis routes based on the Stöber method without any requirement of performing subsequent time and energy-consuming calcination process can be therefore used as general approaches to fabricate a wide array of metal-free silica-based NPs with high potential for biolabeling.



# Chapter 5

## Temperature determination using co-doped di-ureasil films

Temperature sensing using optical methods is, by its nature, a non-contact approach that allows the absolute temperature measurements interrogating photons coming from an optical probe.

In general terms, sensing systems are optically active layers where are incorporated probes that respond to the stimuli that needs to be quantified. In the temperature determination context, there are some examples reported, including simultaneous temperature and pressure/oxygen monitoring [23, 24]. The experimental scheme is quite simple, because it is based on the direct measurement of the temperature by analysis of the emitted radiation features (or color), when the surface is illuminated by an UV radiation [23, 24].

From the different numerical methods used for temperature measurements, (discussed previously in the section 1.3.2) the most profitable is the FIR. This simple analysis defines the first generation of optical temperature sensors, based on the physical principle of Boltzmann temperature distributions of the excited states of a lumiphore specie, using a pair of lanthanide ions (the widely reported examples are  $\text{Er}^{3+}$  and  $\text{Yb}^{3+}$ [1, 2, 3, 199, 200]). The authors suggest that the technique can be applied to nano-crystals to sense temperature in the sub-micrometric spatial scale.

For lanthanide salts, the sensing physical mechanism involves only the population of  $4f^n$  levels fluctuation with temperature [1, 3], resulting in small sensitivities for narrow ( $\sim 20K$ ) temperature ranges. It is important to notice that the temperature determination is performed in the assumption that both transitions are in thermal equilibrium and are

depopulated by a Boltzmann factor proportional to the energy difference between the excited states.

In this chapter is presented a second generation of optical temperature sensors using the monitoring of two emissions of two different lanthanides, implemented using optically active films.

First, the thermometric properties of co-doped di-ureasil thin films are presented and the physical principles that governs the temperature determination are discussed. Second, the temperature calibration of the material is presented and it's relative sensitivity is estimated from the spectroscopic data. Here special focus will be given to the data reduction that lead to temperature determination. In the discussed example the thermometer processed as a film is used as a thermometer. A proof of concept for using a integrated circuit mapping is presented and the spatial resolution limit of the thermometer is discussed.

## 5.1 Thermometric Properties of di-ureasil Thin Films co-doped with $\text{Eu}^{3+}/\text{Tb}^{3+}$

The incorporation of lanthanide ions in polymeric or di-ureasil hybrid matrixes for temperature determination was suggested for the first time in 2002 [41]. This exciting result motivated a new set of experiments to rationalize the temperature dependence of the  $\text{Eu}^{3+}, \text{Tb}^{3+}$  co-doped hybrid films.

The films were produced as described in detail in section 3.1.6 using a  $\text{Eu}^{3+}:\text{Tb}^{3+}$  proportion of 1:3, and labeled as **UET-1.3**. The emission and excitation spectra in steady state mode where acquired in the temperature range 10-300 K (figures 5.1 and 5.2).

The emission spectra presents a typical sharp band profile, characteristic of  $\text{Eu}^{3+}$  and  $\text{Tb}^{3+}$  lanthanide ions. The most intense transitions are observed at the wavelength range 475-710 nm (identified in the figure 5.1) are ascribed to  $\text{Eu}^{3+}$  and  $\text{Tb}^{3+}$  transitions.

The excitation spectra is also temperature dependent (figure 5.2) and presents a typical band profile assigned to excitation via host-matrix. The excitation spectra demonstrates that the material is excitable using conventional handheld UV lamps centered at 365 nm. Also the emission quantum yield is as high as  $0.16 \pm 0.02$  meaning in practical terms that it is possible to use commercial sensors to detect the emission of the material.

The transitions ascribed to  $\text{Eu}^{3+}$  and  $\text{Tb}^{3+}$  present different temperature dependences

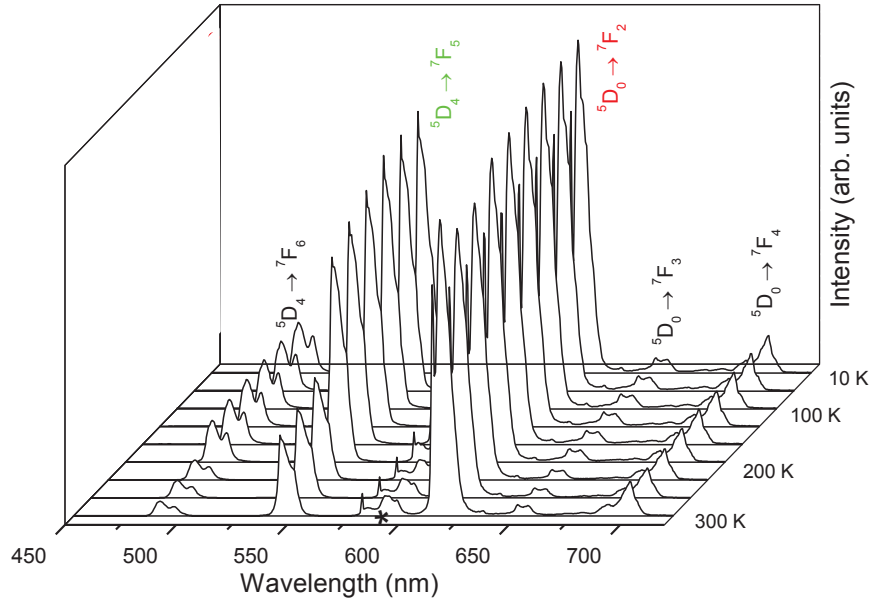


Figure 5.1: Emission spectra of **UET-1.3** in the 10-300K temperature range. The emission spectra exhibits  $\text{Eu}^{3+}$  transitions  ${}^5D_0 \rightarrow {}^7F_J$  ( $J=1,4$ ) and the  $\text{Tb}^{3+}$  transitions  ${}^5D_4 \rightarrow {}^7F_J$  ( $J=5,6$ ). The asterisk marks the region where there are overlapped the transitions  ${}^5D_4 \rightarrow {}^7F_4$  and  ${}^5D_0 \rightarrow {}^7F_0$ . The excitation wavelength is 358 nm for all spectra.

depending on the temperature range. The discussion will be focused in the sensitive  $\text{Eu}^{3+}$  transition  ${}^5D_0 \rightarrow {}^7F_2$  ( $\sim 612$  nm), marked in red) and  $\text{Tb}^{3+}$  transition  ${}^5D_4 \rightarrow {}^7F_5$  at ( $\sim 545$  nm, marked in green), because these transitions are known as specially sensitive to the local environment of the lanthanide ion [146].

Of major interest for thermometry, the emission spectra of the sample (figure 5.1) is temperature dependent, meaning that different transitions present different intensity variations with temperature. This is observable also on excitation spectra (figure 5.2) of the sample.

The integrated intensities of emissions assigned to the transitions of  $\text{Eu}^{3+}$  ( ${}^5D_0 \rightarrow {}^7F_2$  at ( $\sim 612$  nm)) and  $\text{Tb}^{3+}$  ( ${}^5D_4 \rightarrow {}^7F_5$  at ( $\sim 545$  nm)) were computed using the equations 5.2 and 5.1 and labeled as  $I_{Eu}$  and  $I_{Tb}$ , respectively.

$$I_{Tb} = \int_{540}^{550} I(\lambda) d\lambda \simeq \sum_{\lambda=540nm}^{\lambda=550nm} I(\lambda) \Delta\lambda \quad (5.1)$$

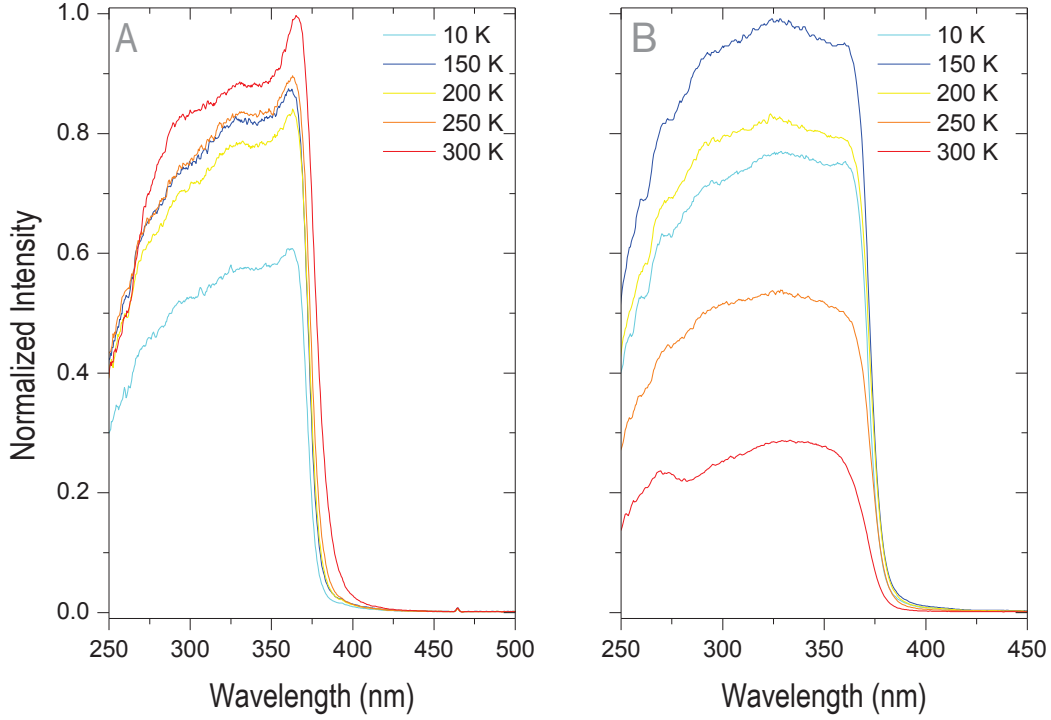


Figure 5.2: Excitation spectra of **UET-1.3** in the 10-300K temperature range. The excitation spectra was obtained monitoring the wavelengths 614 nm (A) and 545 nm (B).

$$I_{Eu} = \int_{610}^{620} I(\lambda) d\lambda \simeq \sum_{\lambda=610nm}^{\lambda=620nm} I(\lambda) \Delta\lambda \quad (5.2)$$

In a simple analysis of figure 5.3-A it is possible to observe that  $I_{Eu}$  intensity is constant for all the temperature range. The transition  $I_{Tb}$  is constant for  $T < 150K$  and decreases for temperatures  $T > 150K$ .

An experimental thermometric parameter  $\Delta$  was defined using the integrated intensities, according equation 5.3.

$$\Delta = I_{Eu}^2 - I_{Tb}^2 \quad (5.3)$$

The parameter  $\Delta$  satisfies the criteria of repeatability and physical meaning. First, the superimposition of the  $\Delta$  parameter computed for different heating cycles demonstrate to be similar, within the experimental error of the measurements (figure 5.4). This means that  $\Delta$  can accurately be used as a thermometric parameter for temperature determination.

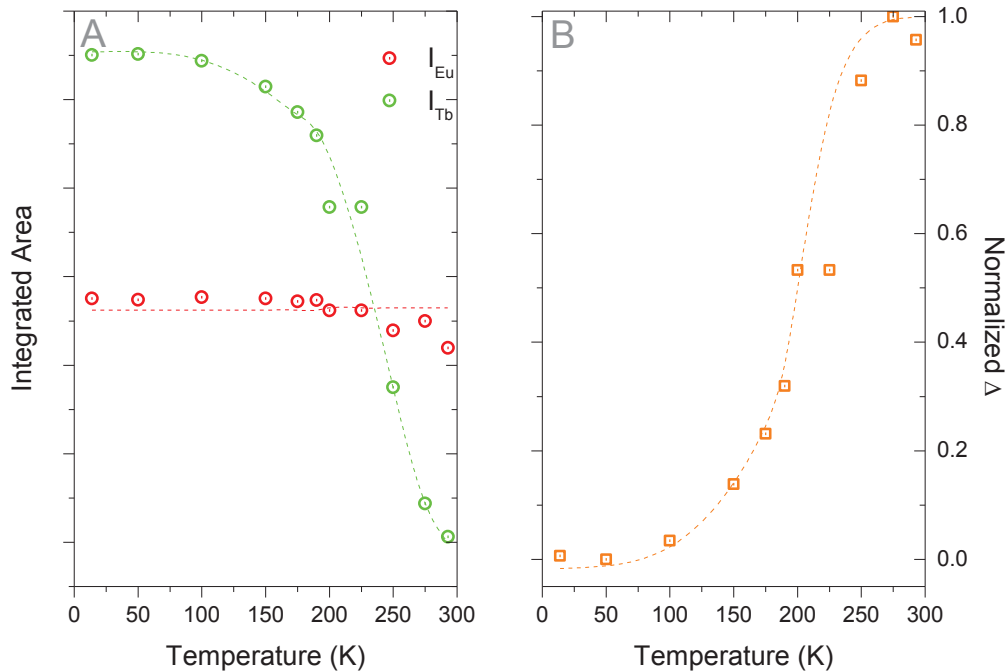


Figure 5.3: A - Integrated areas computed using the emission spectra of **UET-1.3** at the temperature range 10-300 K. The excitation wavelength is 358 nm. B -  $\Delta$  parameter computed from the integrated areas. All dashed lines are guides for the eyes.

Another advantage of using  $\Delta$  is that it is independent of the signal fluctuations of the excitation source or reflectivity of the sample itself. So, the measurement of temperature can be performed using an inner reference of the thermometer itself: one transition references the other and an absolute temperature measurement is achievable. Second, the  $\Delta$  parameter has a direct physical meaning, as it reflects the difference in the population of the excited state of both lanthanide ions.

The dependence of the  $\Delta$  parameter with temperature in the 10-300 K range allows to identify the temperature of 150 K as the limit between the low and the high sensitivity temperature range.

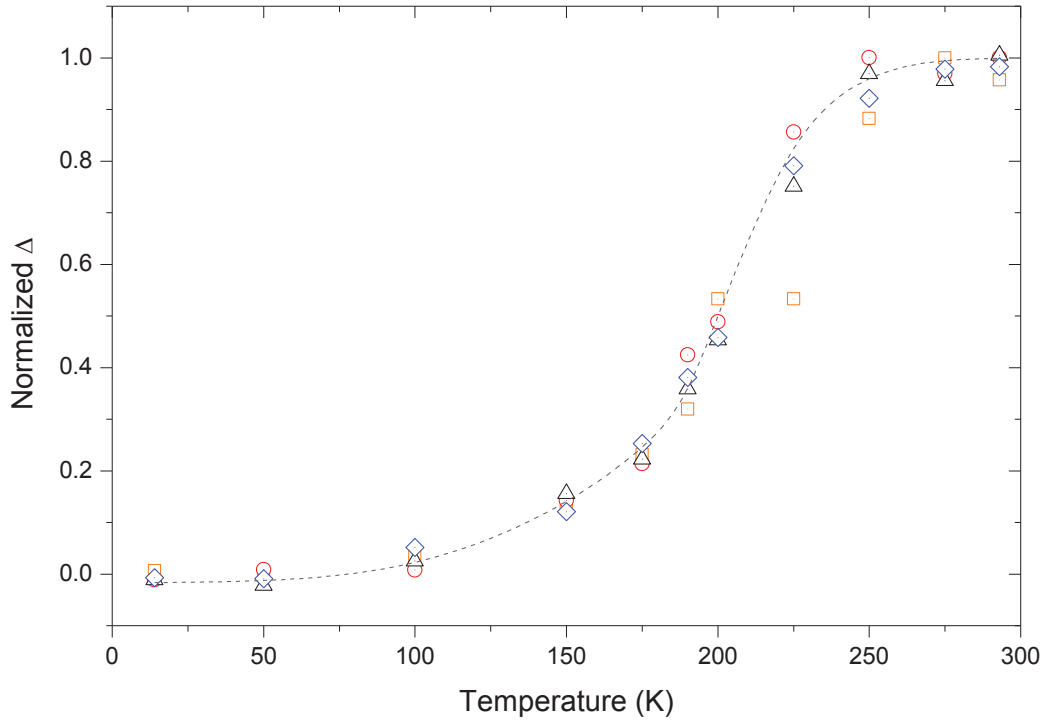


Figure 5.4: Temperature dependence of the  $\Delta$  parameter (open symbols) in the 10-300K temperature range, computed from the emission spectra of the **UET-1.3** sample. The interrupted line is a guide for the eyes.

## 5.2 Rationalization of the Operation Mechanism of the Thermometer

First it is important to rationalize the different temperature dependence of  $\text{Eu}^{3+}$  ( ${}^5\text{D}_0 \rightarrow {}^7\text{F}_2$ ) and  $\text{Tb}^{3+}$  ( ${}^5\text{D}_4 \rightarrow {}^7\text{F}_5$ ) transitions in the temperature range 10-300 K because the temperature determination is based in the emission spectra of the lanthanide co-doped di-ureasil film. In the experimental point of view, the plot  $\Delta = f(T)$  constitutes the calibration curve that is clearly a function of the dependence of the emission spectra of both lanthanide transitions with the temperature.

In theory, both  $\Delta$  parameter and terbium integrated emission ( $I_{Tb}$ ) could be used as thermometric parameter, nevertheless, the use of the first presents advantages of self-referencing and insensitivity to eventual photobleaching, that reduces and local inhomogeneities modifies the readed emission not because the temperature is changing but be-

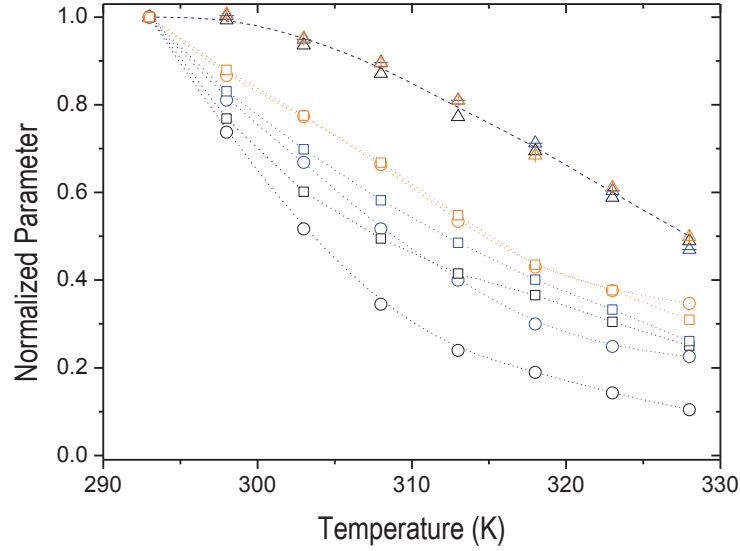


Figure 5.5: Temperature dependence of the normalized parameters  $\Delta$  (open triangles) and  $I_{Tb}$  (open circles) in the temperature range 290-330 K for several cycles, showing that the  $I_{Tb}$  is not suitable to use as thermometric parameter. Also  $I_{Eu}$  (open squares) is presented for comparison. In contrast the superimposition of the  $\Delta$  parameter in several cycles demonstrate that this parameter can be used as thermometric parameter. All interrupted lines are guides for the eyes.

cause the material is in degradation. In practical terms, the superimposition of the both parameters computed for a cycled temperature change, demonstrate that only  $\Delta$  is reproducible on several cycles (figure 5.5).

The constant intensity of  ${}^5D_0 \rightarrow {}^7F_2$  transition means that the excited state  ${}^5D_0$  is not significantly depopulated in the considered temperature range. In contrast, the variation of the  ${}^5D_4 \rightarrow {}^7F_5$  intensity, means that for temperatures above 150 K there is an active non radiative decay path for the terbium ascribed transition, probably via host matrix.

These two observations are in good agreement with the following assumptions:

- $\text{Eu}^{3+}$  and  $\text{Tb}^{3+}$  do not direct or indirectly transfer energy, *i.e.* the both lanthanides interact with the matrix individually;
- The emission properties (and so the calibration curve) can be rationalized using a simple two level scheme that involves the excited state of the lanthanide and the state of the matrix responsible for the non-radiative energy dissipation.

These are precisely the assumptions of the Mott-Seitz model, so it is not strange that the observed temperature dependence of the  $\Delta$  parameter is S-shaped and can be fitted to a sigmoid function, of general equation 5.4.

$$y = y_0 + \frac{A}{B + Ce^{-D \times T}} \quad (5.4)$$

The fact of a sigmoid function can be used to interpolate experimental data constitute an advantage since it is simple to implement computational routines to fit experimental data and the first derivative of the  $\Delta$  parameter (or sensitivity), will be a bell-shaped curve.

The temperature range of operation of the thermometer was established defining a quality criteria of change of the thermometric parameter  $\Delta$ , according the detection limit of the equipment used. This, in practical terms is equivalent to argue that for values below a certain limit of detection of the equipment temperature (emission) changes are not measurable by the experimental setup. In section 5.3 sensitivity and temperature range of operation of the thermometer is computed.

If the assumptions presented in this section are correct, the most sensitive thermometer's range of operation is located in room temperature due to the energy difference  $\Delta E$  between the  ${}^5D_4$  terbium excited state and the host level  $H$ . This information can be estimated, according the Mott-Seitz model for excited state lifetime temperature dependence. The decay curves obtained by monitoring a transition from  ${}^5D_4$   $Tb^{3+}$  excited state and from  ${}^5D_0$   $Eu^{3+}$  excited state produce dissimilar results. The lifetime of  ${}^5D_0$  is constant with temperature while the lifetime of  ${}^5D_4$  decays when temperature increases (figure 5.6).

The  ${}^5D_4$  lifetime temperature dependence is in good agreement with the behavior predicted by the Mott-Seitz model. The fit of the lifetime computed from decay curves produce a characteristic energy value of  $\Delta E = 2111 \pm 57 cm^{-1}$  with correlation coefficient of  $r^2 = 0.982$ . In line with the energy transfer model, the host matrix depopulated the excited state of the  $Tb^{3+}$  in a non radiative path that explains the decrease of  ${}^5D_4 \rightarrow {}^7F_5$  intensity when the temperature increases.

### 5.3 Sensitivity and Temperature Range of Operation

The analysis of the emission spectra of the **UET-1.3** film produces a calibration curve on the temperature range 10-300K presented in the figure 5.8.

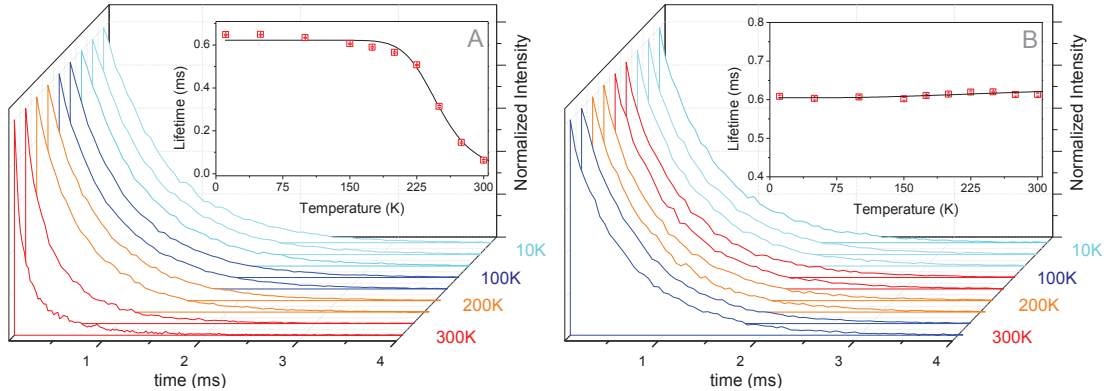


Figure 5.6: Decay Curves and Lifetime of  ${}^5D_0$  (A) and  ${}^5D_4$  (B) for sample **UET-1.3** in the temperature range 10-300 K. The excitation wavelength is 358 nm.

Table 5.1: Summary of **UET-1.3** thermometric properties: temperature range of operation ( $\Delta T$ ) at which  $S_r > 0.5\% \cdot K^{-1}$ , maximum relative sensitivity ( $S_m$ ) and the correspondent temperature ( $T_m$ )

Sample	$\Delta T(K)$	$S_m(\% \cdot K^{-1})$	$T_m(K)$
<b>UET-1.3</b>	135-323	1.9	271

The computing of the relative sensitivity (using equation 1.3) it is possible to generate the curve shown in figure 5.7. The shadowed area corresponds to the temperatures where the sensitivity is above  $0.5\% \cdot K^{-1}$ , a reasonable sensitivity value for commercial detectors (see discussion in section 1.2.1). The maximum sensitivity computed for **UET-1.3** is  $1.9\% \cdot K^{-1}$  at 271 K.

The cross analysis to the calibration and sensitivities curves allows to extrapolate from data in figures 5.4 a region of operation for this thermometer of 135-323 K within the criteria  $S_r > 0.5\% \cdot K^{-1}$ , and define the temperature range of operation regions where practical calibration curves can be generated by fit of experimental data to simple functions as polynomials, for example.

As pointed out by [41], this material indeed demonstrate a high potential as thermometer, and combined with good processability as films, is adequate for temperature mapping of surfaces. For summary purposes, relevant data where compiled in table 5.3.

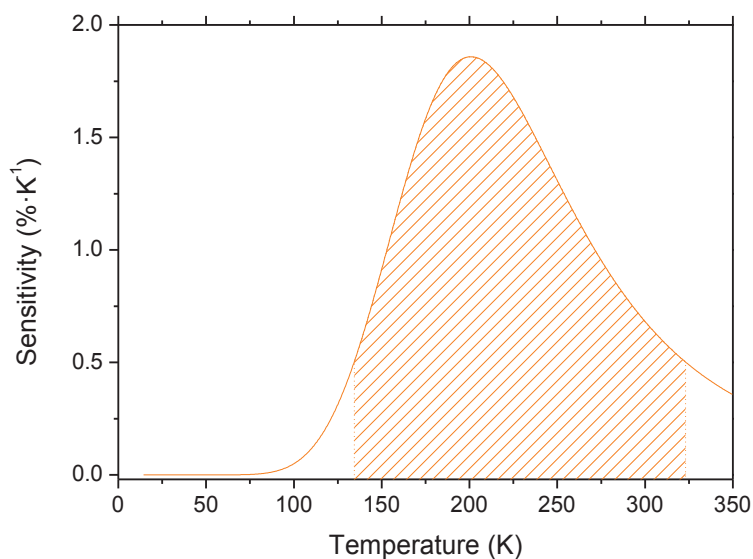


Figure 5.7: Relative sensitivity of **UET-1.3** sample. The shadowed area corresponds to the temperature range for which the relative sensitivity is above  $0.5\% \cdot K^{-1}$  and defines the temperature range of operation between 135-323K.

## 5.4 Absolute Temperature Determination

Following the definition of the temperature range of operation, the calibration curve was generated, cycling the temperature in the range 300 - 350 K in 10 K steps, when temperature was increased (figure 5.8-A).

The sample was placed on a controllable heating (He closed-cycle cryostat with a Lakeshore 330 auto-tuning temperature controller with a resistance heater, see chapter 3). The emission spectra recorded for each temperature, using a delay time of 5 minutes after the temperature is reached by the temperature controller setup. This procedure intends to guarantee that the temperature is stable in each step of the calibration curve acquisition.

A local calibration curve was generated (figure 5.8-B) using a second degree polynomial fit to convert the relative  $\Delta$  parameter ( $\Delta/\Delta_0$ ) to the absolute temperature, using this material, with excitation wavelength 357 nm ( $\Delta_0$  corresponds to the  $\Delta$  parameter computed for room temperature). The correlation coefficient is as high as  $r^2 = 0.992$  showing the good adequacy of the second order polynomial to experimental data, in this temperature range.

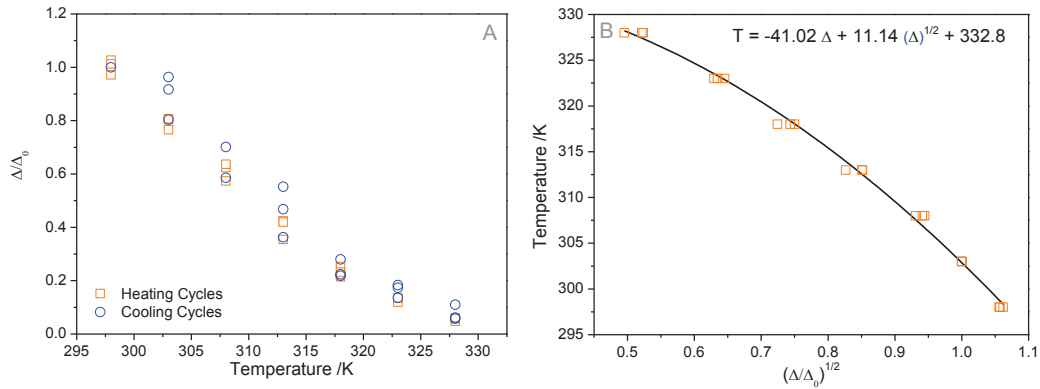


Figure 5.8: **A**- $\Delta$  parameter computed on temperature cycling **B**-Temperature dependence of the  $\Delta$  parameter in the 300-350 K temperature range. The solid line corresponds to the best fit of experimental data to a second order polynomial, presented in the graph and constitutes the calibration curve.

## 5.5 Incorporation of maghemite NPs in the di-ureasil film

The **UET-1.3** film can be synthesized incorporating the maghemite NPs, as described in detail in section 3.1.6. The resulting film, named **UET-1.3-Fe** where successfully used to recover an integrated circuit and to produce a monolith for further photophysical characterization.

The steady-state photoluminescence was recorded in the temperature range 300-330K and the correspondent values of the  $\Delta$  parameter computed using the same strategy described in the previous section. The results are depicted in figure 5.9.

The comparison of the sensitivity curve with the previous one for the **UET-1.3** sample shows only slight differences, indicating that the incorporation of the maghemite NPs does not change significantly the energy scheme proposed before for the **UET-1.3** sample.

This result demonstrate that the incorporation of a magnetic responsive material is fully compatible with the temperature sensitive host matrix, without major changes in the calibration curve generated for the **UET-1.3** and **UET-1.3-Fe** samples (figure 5.9).

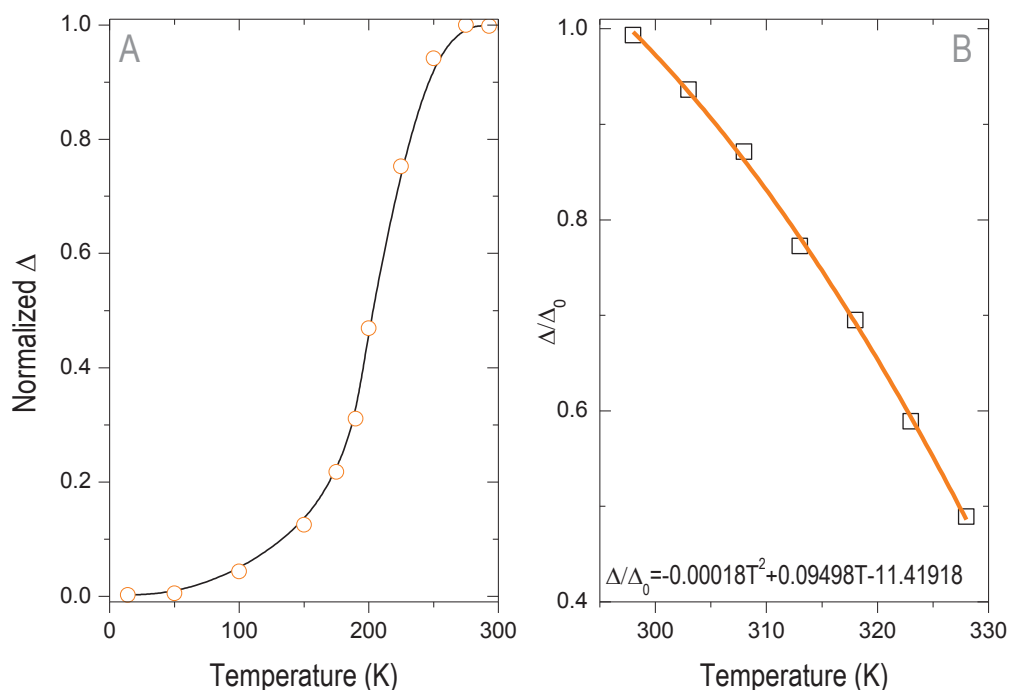


Figure 5.9: Calibration data of **UET-1.3-Fe** sample. **A**- $\Delta$  parameter computed on temperature cycling **B**-Temperature dependence of the  $\Delta$  parameter in the 300-350 K temperature range. The solid line corresponds to the best fit of experimental data to a second order polynomial, presented in the graph and constitutes the calibration curve.

## 5.6 Optical Temperature Mapping with Micrometric Resolution

A demonstration of the spatial resolution distribution of the **UET-1.3** thermometer (processed as film) was realized mapping the temperature of an integrated circuit covered with an optical layer.

The integrated circuit was specially designed to be used for the temperature determination. The basic concept is to produce a predictable and non-trivial temperature profile. The facilities of DFUA workshop allowed to produce integrated circuits of copper tracks on a commercial polymeric substrate. An integrated circuit was designed in order to produce a temperature distribution profile with large temperature gradients. The predicted temperature profile was computed using the heat dissipation and neglecting the thermal

conductivity of the plate, using a MatLab® routine implemented for this effect. The temperature profile prediction and the temperature obtained using the emission spectra are presented in the figure 5.11.

Over the integrated circuit was brushed a thin layer of the temperature sensitive material (**UET-1.3**) using a conventional paint brush. The layer was evaporated in the oven at 318 K during 12 hours.

The experimental setup (figure 5.10) was mounted using a commercial USB detector (Ocean Optics 4000) and an optical fibre bundle (Ocean Optics, QP450-1-XSR) to excite the material and collect the emitted radiation. The optical fiber bundle is composed of one central  $450\mu m$  diameter fiber surrounded by six identical fibers. The lateral fibres were used to take the excitation light to the sample and the central fibre to collect the emission originated in the **UET-1.3** film. The distance between the fibre bundle end and the film is compatible with an field of view of the inner fibre of 1 mm diameter, according to the manufacturer reported numerical aperture ( $0.22 \pm 0.02$ ). A collimating lens was used to maximize the excitation signal. Mounting the fibre bundle on a translation stage it is possible to cover the surface of the circuit moving it under the fibre end, in a line-by-line scanning.

The emission was then gathered for two different directions, identified in the figure 5.10 by A and B. Direction A produce a complex temperature profile while direction B produces a high temperature gradients. The circuit was mounted on a translation stage that was controlled manually by a linear positioner screw. The resolution is  $2\mu m$  and the step used is  $450\mu m$

For comparison purposes, the temperature was measured using a commercial IR thermal camera (FLIR-50). At focal distance, the IR camera produces a thermal image of the integrated circuit with with pixel-to-pixel distance correspondent to  $\sim 250 - 350\mu m$ . The exported temperature map can be converted in pixel to distance using the dimensions of the integrated circuit.

The comparison between the two temperature mappings is illustrated in figure 5.11 showing a better spatial resolution for the **UET-1.3** thermometer, despite the of the optical fibre inner area represents about 2.5 the camera pixel size.

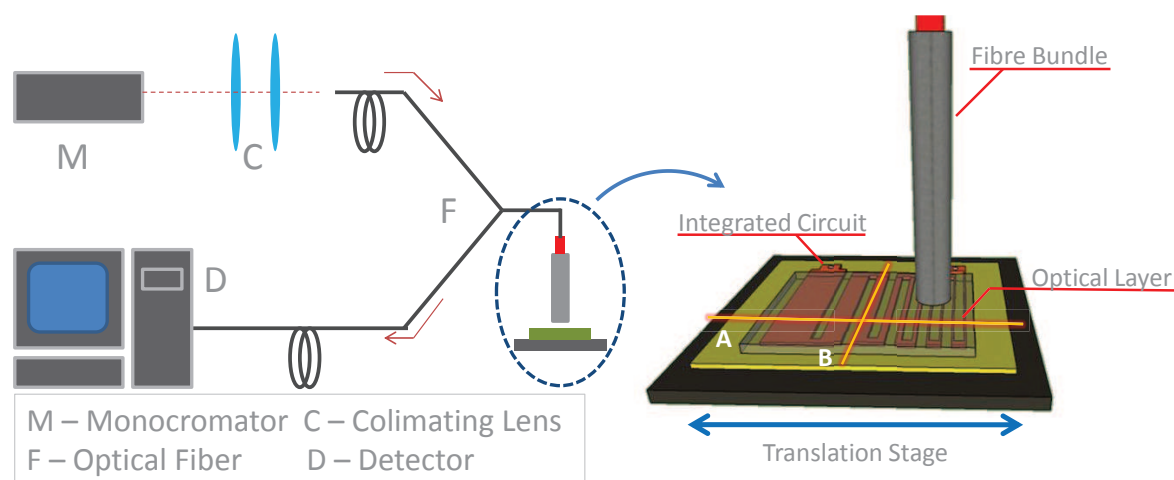


Figure 5.10: Experimental setup used for temperature mapping of a integrated circuit recovered with a film of **UET-1.3**.

An *a priori* analysis of the experimental system points out to the fibre field of view as the lower limit of resolution of the sensing system. This statement motivates the first set of temperature mappings using a step correspondent to the optical fibre inner diameter ( $450\mu m$ ). However, experimental results, presented in figure 5.11 point out to a much higher spatial resolution because this step was able to follow small temperature changes in a most accurate form, when compared to the pixel size.

Results presented in figure 5.11 show that the temperature profile measured using the emission spectra is in close agreement with the temperature profile produced from the IR camera, but with higher spatial resolution. The thermometer demonstrates to measure absolute temperatures in regions with high temperature gradients (line B in figure 5.11), as well as in regions presenting complex temperature distributions (line A in figure 5.11).

The spatial resolution achieved was estimated by the minimal distance resolved by the thermometer, when the temperature changes above the temperature uncertainty ( $0.5K$  in this case, the noise level of the detector estimated by the temperature fluctuation in regions where the temperature is expected to be constant). The obtained value of  $35\mu m$  depends not of the optical fiber inner diameter because for steps smaller than the fibre core diameter the system can detect gradients in temperature.

A detailed analysis of the origin of the detected photons makes clear that the fibre collects information in a field of view that is averaged in the emission spectra that is finally

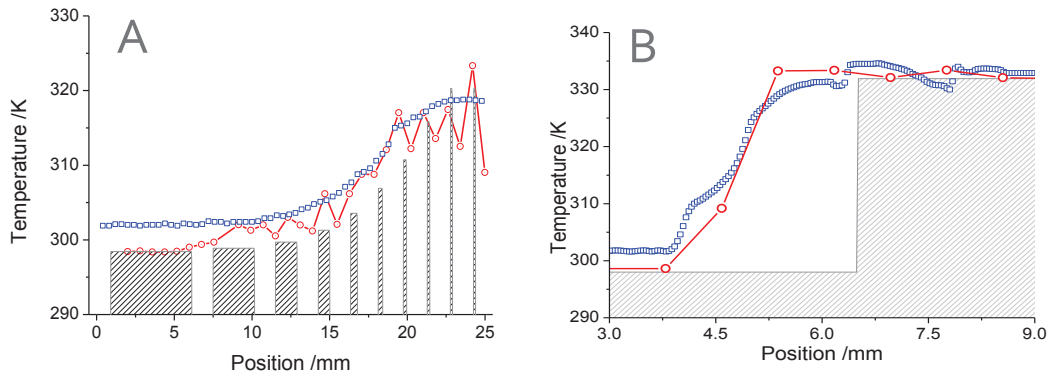


Figure 5.11: Comparison between temperature profiles obtained by IR camera (blue open squares) and temperature determination using the calibration curve for **UET-1.3** (red open circles). The solid line represents the temperature profile prediction (neglecting the thermal conductivity of the plate).

converted to temperature using the calibration curve of the material. The spatial resolution is quite below the resolution limit due to the temperature determination is based on the spectral information, that can change drastically on few micrometers (*e.g.* line B of figure 5.11). All these results motivated a new series of experiments trying to evaluate the spatial resolution limit of the sensing system, described in the next section.



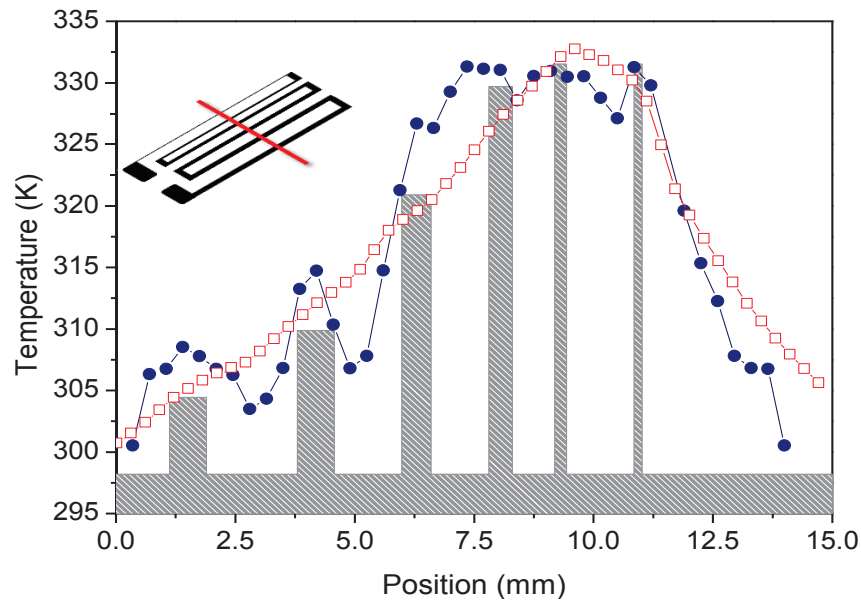


Figure 5.13: Temperature mapping using the second circuit. The open squares represents the IR camera temperature profile and the solid circles the temperature profile reconstructed using the emission spectra by the calibration curve. The step used in the fibre bundle is  $325\mu m$

experimental setup was planned to determine the value of the minimum distance where temperature can be determined by the thermometer out of the temperature uncertainty.

This mapping illustrate that IR camera the temperature algorithm makes a significant averaging integrating the information of several pixels. This is evident from the IR camera temperature mapping of an integrated circuit as the camera cannot distinguish the temperature between two adjacent tracks (separated by  $\sim 1.6mm$ ). Additionally, the temperature starts to decrease at 9.5 mm, before the position of the last track, that presents the highest temperature (narrowest the track highest the temperature). This indicate that at 9.5 mm the temperature algorithm takes into account points located away from the next adjacent track at 11 mm which should be at a lower temperature. These results point out that the IR camera integrates temperature over, at least, 1.6 mm, corresponding to an effective field of view of 5-7 pixels (according to the manufacturer the field of view of each pixel ranges between  $250-350\mu m$ ).

The third circuit design uses once more narrower tracks that produce a new temperature profile. The results of the temperature mapping on the third circuit are presented in

figure 5.14. The temperature profile was computed using the previous MatLab® routine. The new setup includes a motorized positioner (MFA-CC Miniature Linear Stage, from Newport®) controlled by LabView® software that allows line-by-line scanning of the integrated circuit, with resolution of  $0.5\mu m$ . The circuit was replicated in order to minimize eventual fabrication defects since the design was in the limit of resolution of the fabrication process. The circuit recovery followed the previously described procedure.

In parallel, a small portion of **UET-1.3** was processed as monolith in order to generate a new calibration curve for comparison with the ones obtained in the previous synthesis.

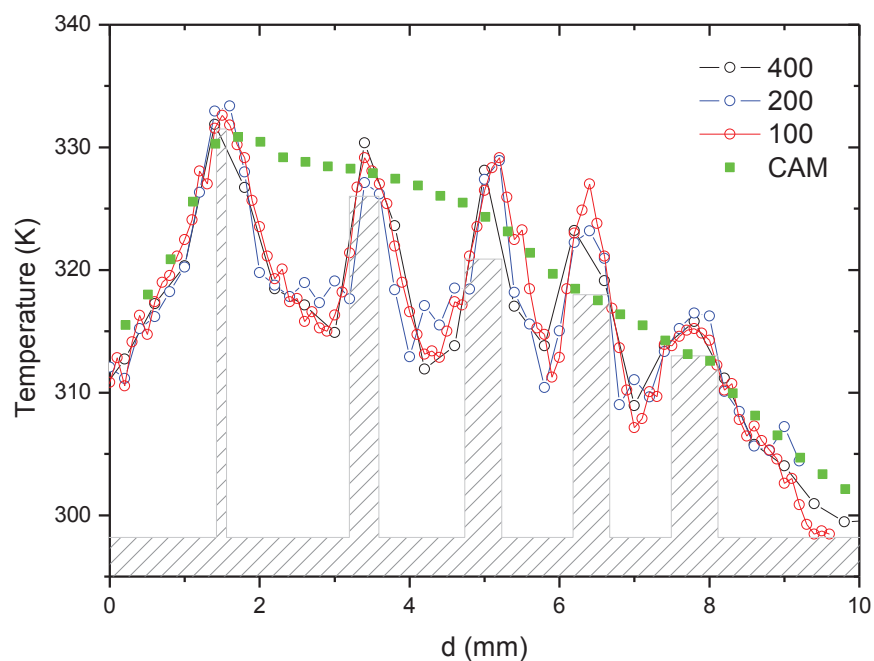


Figure 5.14: Temperature mapping using the third circuit and different scanning steps.

### Fibre Diameter and Scanning Step Effect

The emission originated on the **UET-1.3** optical layer was measured scanning the circuit with steps of 400, 200, and  $1000\mu m$ . The corresponding temperature profiles were computed using the calibration curve. The calibration points obtained using the new monolith produces again the same calibration curve within the experimental error. All the temperature profiles were compiled on the figure 5.14 and the respective values of spatial resolution depicted in figure 5.15

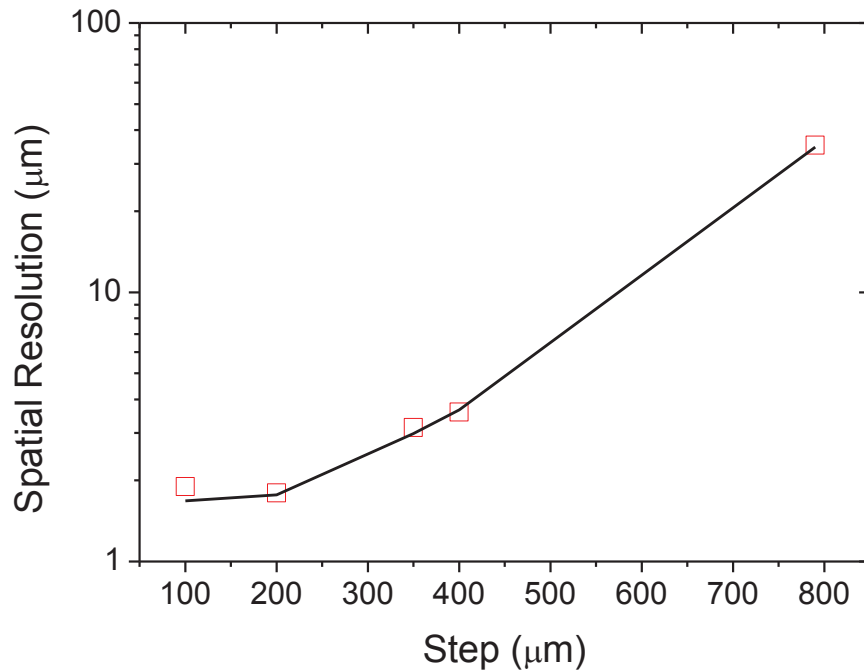


Figure 5.15: Spatial resolution obtained in the temperature mapping of a temperature step of 90 degrees. The plot represents the spatial resolution on temperature mapping (in units of distance to originate a temperature uncertainty of 0.5 K) using different scanning steps (horizontal axis).

Using the  $450\mu\text{m}$  collecting fibre, and when the scanning step decreases the spatial resolution tends to the limit value of  $\sim 1.7\mu\text{m}$  for values of the scanning step below  $200\mu\text{m}$ , considering the temperature uncertainty ( $0.5\text{K}$ ) of the thermal system.

The spatial resolution limit, indeed does not mean that the optical fibre plus optical layer system can resolve two temperatures that are  $1.7\mu\text{m}$  distant, because this value is far below the minimum step that produces a variation in the spatial resolution limit, correspondent to  $\sim 200\mu\text{m}$ . The spatial resolution should be interpreted as a spatial limit of detection of the same equipment and the value of  $\sim 200\mu\text{m}$  represents the minimum step in order to improve the spatial resolution.

It is important to compare the spatial resolution limit computed for this system with the previously reported for temperature mappings. Indeed there are not many examples of references reporting such measurement in a quantitative way. The exception is a report of Tessier *et al.*, [230] (experimental setup in figure 5.16).

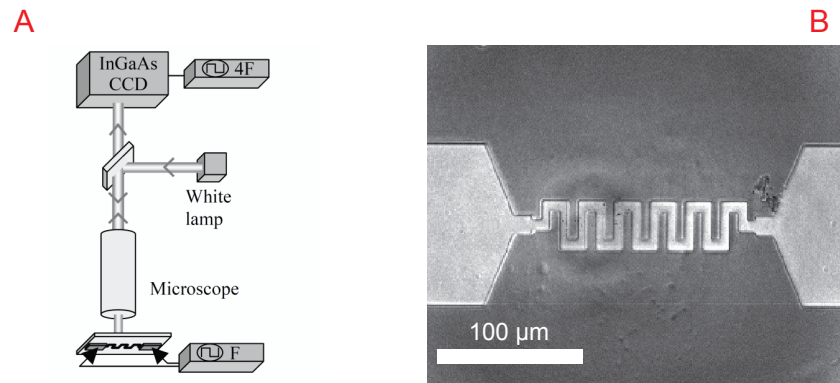


Figure 5.16: Set-up used for thermoreflectance described in the reference [230] for imaging through the substrate with an InGaAs CCD camera (A). The device is powered at a frequency  $F$  with contact needles on its active lower side. (B) Thermal image of a gold resistor dissipating 609 mW, obtained through the  $500\mu\text{m}$  silicon substrate with a  $\times 50$ ,  $\text{NA}=0.6$ , objective. The spatial resolution measured along the dotted line is  $1.7\mu\text{m}$ , which is in the order of the diffraction limit of the radiation. In silicon near the resistor the temperature step corresponds to 27 K.

The author reports a temperature mapping using a thermoreflectance-based algorithms operating at  $536 \pm 13\text{nm}$  in order to obtain temperature images. The calibration curve uses the relative variation of the reflectance  $\Delta R/R$  with the temperature, finding a linear relation with slope  $(3 \pm 0.5) \times 10^{-5}$  per degree [230]. The 2D temperature mapping reported was imported to MatLab ® and the temperature profile presented in figure 5.17.

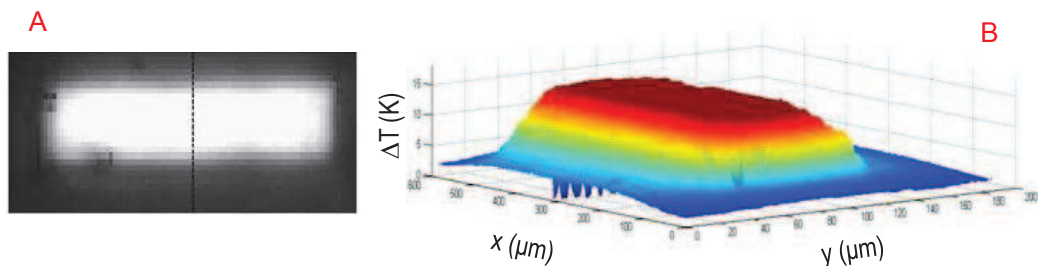


Figure 5.17: Temperature mapping described in reference [230]. The temperature profile (B) is perfectly continuous, unlike what is observed under visible illumination, when several materials are seen under the encapsulation (A)

The spatial resolution reported is  $\sim 1.7\mu\text{m}$ , and limited by the diffraction limit that depends on the wavelength used. This value in good agreement with that obtained for the  $450\mu\text{m}$ -core fibre diameter.

Analyzing the experimental setup used to record the temperature profile, it becomes clear that the signal collected (emission spectra) is dependent on the fibre inner diameter (determining the fibre field of view), that, by it turn defines the spatial resolution of the system. A logical conclusion is that decreasing the collecting fibre diameter the spatial resolution decreases and the signal collected degrades.

Using the same experimental setup (except the collecting fibre) it was verified that only a fibre with inner diameter of  $200\mu\text{m}$  was able to collect enough signal for temperature reconstruction. For the fibres with inner diameter of  $105\mu\text{m}$  and  $50\mu\text{m}$  the emission of the lanthanides lie in the noise level of the USB-4000 detector, making the temperature mapping impossible to perform.

The spatial resolution was estimated scanning a temperature step of 90 K with the  $200\mu\text{m}$  fibre. The results are presented in figure 5.18.

The results presented in figure 5.18 demonstrate that the fibre inner diameter is determinant in the spatial resolution achieved by the thermometric system. Regarding the  $200\mu\text{m}$  core fibre, steps above  $100\mu\text{m}$  produce spatial resolution values that increase monotonically until the value of  $2.5\mu\text{m}$  for a scanning step of  $400\mu\text{m}$ . For values bellow  $100\mu\text{m}$  the spatial resolution is independent of the scanning step and gives a constant value of  $1.4\mu\text{m}$ . Interestingly enough, the spatial resolution achieved by a narrower fibre is always better, for the same scanning step. The only disadvantage in using smaller fibres lies on the signal-to-noise-ratio (SNR).

More important, the limit scanning step is about half of the fibre inner diameter, independently of the fibre used. The limit in the spatial resolution value always decrease with the fibre inner diameter.

The results can be rationalized if the the following assumptions are used:

- The spatial resolution is defined by the fibre field of view (area probed at each position) and decreases with the fibre area;
- The lower spatial resolution is achieved when the scanning step is lower than the radius of the collecting fibre, because the field of view of the fibre does not change significantly when the fibre moves;

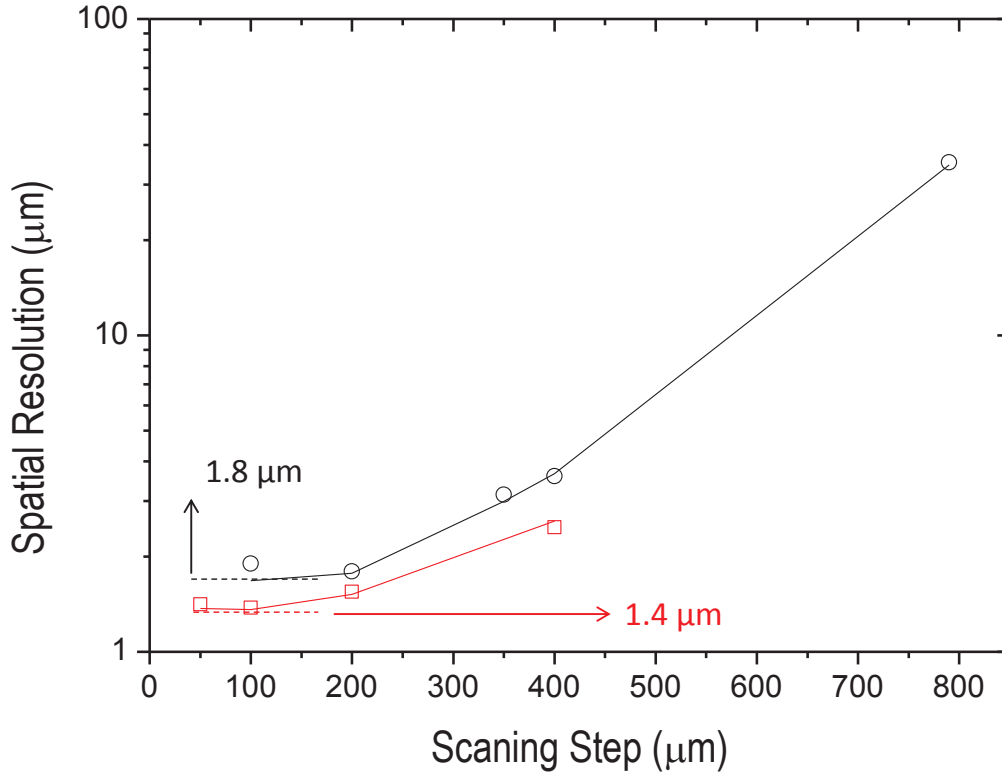


Figure 5.18: Spatial resolution obtained in the temperature mapping of a temperature step of 90 K. Spatial resolution on temperature mapping (in units of distance to originate a temperature uncertainty of 0.5 K) using different scanning steps (horizontal axis) for the 450  $\mu\text{m}$  (squares) and 200  $\mu\text{m}$  (circles) diameter fibre.

- The spatial resolution decreases until a limit defined only by the relation between the change in the fibre field of view and the temperature uncertainty  $\Delta T$  (assumed constant in all experiments  $\Delta T = 0.5\text{K}$ );

The last point is key to understand the experimental results. Let us take a numerical example using the actual values of the fibres diameter. The spatial resolution limit and the area illuminated by each fibre are gathered in table 5.6.1. Notice that the ratio of areas is approximately 4 four times the spatial resolution limit ( $5.12 = 4 \times 1.58$ ), meaning that an empirical relation between the ratio of areas and spatial resolution will be  $\delta x_A / \delta x_B = 4 \times A_A / A_B$ .

The empirical law establishes that when the fibre field of view decreases the area integrated by the detector decreases and the temperature is the mean temperature value

Table 5.2: Comparison of the results obtained with different optical fibres. The spatial resolution limit ( $\delta x$ ) and the area of the field of view of the fibre ( $A$ ) are presented for comparison purposes.

Fibre	Core Diameter ( $\mu m$ )	$\delta x$ ( $\mu m$ )	$A$ ( $mm^2$ )
A	450	1.8	0.159
B	200	1.4	0.031
Ratio (A/B)	2.25	1.28	5.12

averaged over the area. This result doesn't take in account the signal degradation that precludes the detection in the limit Fibre Core Diameter  $\rightarrow 0$  and anticipate that using narrower fibres and more sensitive detectors should be possible to improve the resolution limit using co-doped films and acquiring the emission spectra with an optical fibre.

## Summary

In this chapter the temperature 1-D mapping using **UET-1.3** was presented. The material is a versatile di-ureasil hybrid host incorporating  $Eu^{3+}$  and  $Tb^{3+}$  lanthanides that demonstrates to be processable as film or as bulk material. Its emission properties are temperature dependent and allow the absolute temperature determination applying an experimental parameter  $\Delta$  defined using the integrated intensities of both lanthanides. The  $\Delta$  dependence on temperature doesn't present significant hysteresis in the temperature ranges 10-300K or 300-330K. Moreover, repeating the procedure of film/ bulk material production the calibration curve remains unchangeable within the experimental error. The sensitivity of the material is above  $0.5\% \cdot K^{-1}$  between 200 and 330 K reaching the maximum value of  $2.0\% \cdot K^{-1}$  at 280K.

The processability of the material as film combined with the possibility of measure temperature motivated a proof of concept of temperature mapping using integrated circuits recovered with an optical layer of **UET-1.3**. The experimental technique is versatile because it allows the recovery of the circuit both by direct brush or more accurate techniques (in the thickness control point of view) such as spin coating or printing. The material properties allow good adhesion in common surfaces like conventional imprinted circuits and silicon wafers. The experimental setup uses an optical fibre bundle for excitation and

emission collect that determines limit the spatial resolution of the thermometric system. The higher spatial resolution was achieved for steps lower than half of the fibre inner diameter and corresponds to a value of  $1.7\mu m$  (fibre of  $450\mu m$  inner diameter) or (fibre of  $200\mu m$  inner diameter) distance to originate the temperature uncertainly ( $0.5K$ ).

The most significant results presented in this chapter were reported in [33, 32].

# Chapter 6

## Nanoparticles for Thermometry Below Room Temperature

The exceptional temperature dependent emission properties of lanthanide co-doped di-ureasil films encouraged the development of silica nanoparticles carrying the same thermometric valence than the monoliths or films. The starting point were silica nanoparticles prepared by modified Stöber method, as described in section 3.1.2.

In this chapter it is reported the development and characterization of organic modified silica nanoparticles co-doped with  $\text{Eu}^{3+}$  and  $\text{Tb}^{3+}$  for temperature measurement at sub-micrometric spatial scale. First the photoluminescence characterization of the sample set is detailed and the excitation and emission spectra are discussed, keeping in mind the temperature monitoring. It follows the rationalization of the experimental results, upgrading the three levels energy model used for **UET-1.3** thermometers. Next the sensitivity and temperature range of operation is computed for the different samples of the set. Finally the possibilities of temperature monitoring at sub-micrometric scale are addressed.

### 6.1 Morphological and Spectroscopic Properties of AET samples

Following the experimental route defined in section 3.1.2, a set of samples were prepared using several  $\text{Eu}^{3+} : \text{Tb}^{3+}$  proportions. Samples labeled as **AET-2.1**, **AET-1.1**, **AET-1.2** and **AET-1.10** corresponds to the  $\text{Eu}^{3+}$  to  $\text{Tb}^{3+}$  mass proportions of 2:1, 1:1,

1:2 and 1:10, respectively.

The multifunctional nanoparticles are dispersible in water, presenting a bimodal hydrodynamic size distribution centered at 120 and 390 nm as seen in DLS measurements (figure 6.1). All samples of the **AET** set present similar size distribution of hydrodynamic sizes.

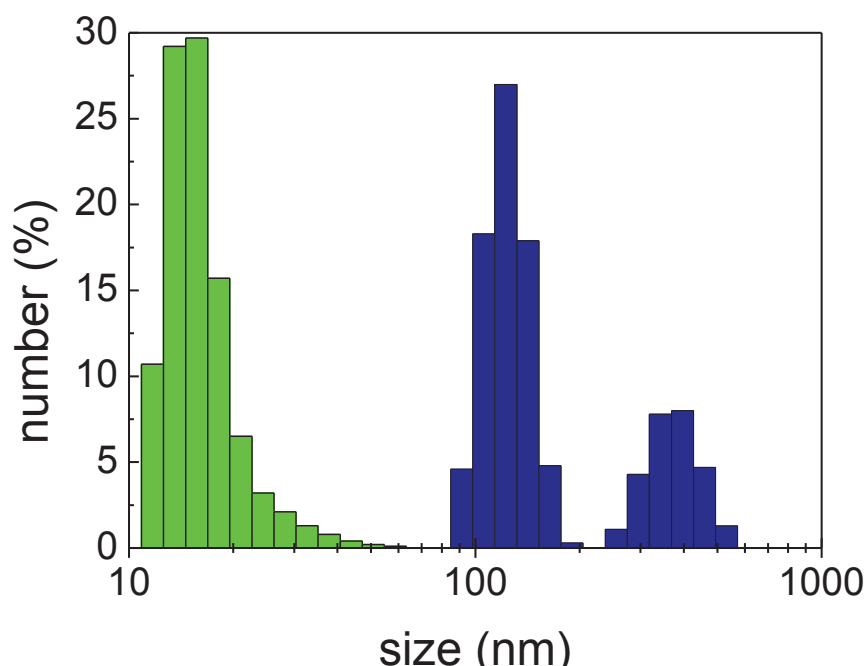


Figure 6.1: Hydrodynamic Sizes measured by DLS of **AET-1.2** silica NPs (blue bars at right) and maghemite core (green bars at left). The bimodal distribution for **AET-1.2** is probably due to aggregation during the dispersion process.

DLS measurements are consistent with SEM and TEM images 6.3. In the TEM images (example in figure 6.3C), the **AET** samples show regions with high and low contrast assigned to  $\gamma - Fe_2O_3/Eu^{3+}/Tb^{3+}$  cores and to the siliceous matrix, respectively. In SEM images (example in figure 6.3 B) it is evident the aggregation of the **AET** samples that occur during evaporation of the dispersions on the sample holder. The EDS mappings show  $Eu^{3+}$  and  $Tb^{3+}$  distributions with contours and shapes similar to those of the nanoparticles, indicating that most of the nanoparticles contain both lanthanide complexes.

The samples present red emission at room temperature when are illuminated with UV radiation. In optical microscopy observations, the **AET** samples present red spots at room temperature (figure 6.3 D) with sizes of the order of  $5\mu m$ , with each spot corresponding

to the emission either of a NP or a NP cluster, since both sizes rely below the diffraction limit of the optical setup.

Comparison of the emission features of the  $\text{Eu}^{3+}$  complex isolated with those of **AEu** (doped only with the  $\text{Eu}^{3+}$  complex) and **AET-1.3** shows that the energy, the full width at half maximum (fwhm) and the relative intensities of the  ${}^5\text{D}_0 \rightarrow {}^7\text{F}_{0-4}$  transitions are strongly altered, indicating an effective interaction between the  $\text{Eu}^{3+}$  ions and the TEOS/APTES layer (figure 6.2). To quantify further the differences in the emission features between the nanocomposites and the  $\text{Eu}^{3+}$  complex, the fwhm and the energy of the  ${}^5\text{D}_0 \rightarrow {}^7\text{F}_0$  transition were estimated by deconvoluting the emission spectra at  $T=14$  K, assuming a single Gaussian function, resulting in the outcome that, whereas the energy of the  ${}^5\text{D}_0 \rightarrow {}^7\text{F}_0$  transition for **AEu** ( $17276.3 \pm 0.5\text{cm}^{-1}$ ) is blue shifted in comparison with the energy estimated for  $\text{Eu}^{3+}$  complex isolated ( $17266.7 \pm 0.2\text{cm}^{-1}$ ), the energy of **AET-1.3** is red-shifted ( $17259.9 \pm 0.5\text{cm}^{-1}$ ); the corresponding fwhm values are similar and around  $25 - 30\text{cm}^{-1}$ . As reported for similar organic/inorganic hybrids incorporating analogous  $\beta$ -diketonate complexes [148, 144], all experimental data point out to that the embedding of the complexes within the  $\gamma - \text{Fe}_2\text{O}_3@$ TEOS/APTES nanoparticles induces the replacement of the labile MeOH molecule in the  $\text{Eu}^{3+}$ -first coordination sphere, thus anchoring the complexes at the particle surface (via the silanol groups or the nitrogen atoms of APTES).

This is supported by the increase in the  ${}^5\text{D}_0$  lifetime of  $0.443 \pm 0.002\text{ms}$  for  $\text{Eu}^{3+}$  complex isolated, of  $0.589 \pm 0.030\text{ms}$  for **AEu** and of  $0.530 \pm 0.003\text{ms}$  for **AET-1.3**, after the complexes embedding into the nanoparticles (figure 6.6). This increase (already reported elsewhere [148, 144]) is in good agreement with the replacement of the MeOH molecule by silanol groups or nitrogen atoms of APTES. Further, the interaction between the  $\text{Eu}^{3+}$  ions and the particle surface is inferred by the calculus of the  ${}^5\text{D}_0$  quantum efficiency,  $\eta = k_r / (k_r + k_{nr})$ , based on the empirical radiative ( $k_r$ ) and non-radiative ( $k_{nr}$ ) transition rates [37]. The value obtained for **AEu** (0.72) is higher than that for the  $\text{Eu}^{3+}$  complex isolated (0.49), illustrating the aforementioned replacement of the MeOH molecule with the concomitant decrease of  $k_{nr}$  (from  $1.146\text{ms}^{-1}$  for the  $\text{Eu}^{3+}$  complex isolated to  $0.468\text{ms}^{-1}$  for **AEu**). The corresponding maximum absolute emission quantum yields ( $0.32 \pm 0.03$  and  $0.10 \pm 0.01$ , for the  $\text{Eu}^{3+}$  complex isolated and **AEu**, respectively) are listed in table 6.1.

The red color is a clear evidence of the dominance of the  $\text{Eu}^{3+}$  emission at room-

---

Table 6.1: Maximum room temperature absolute emission quantum yield values of the  $\text{Eu}^{3+}$  complex isolated (365.0 nm), **AEu** (357.0 nm), **AET** (357.0 nm), obtained for the excitation wavelength reported in parenthesis

Sample	$\text{Eu}^{3+}$	<b>AEu</b>	<b>AET-1.1</b>	<b>AET-1.2</b>	<b>AET-1.3</b>
Quantum Yield	$0.10 \pm 0.01$	$0.27 \pm 0.03$	$0.37 \pm 0.04$	$0.20 \pm 0.02$	$0.24 \pm 0.02$

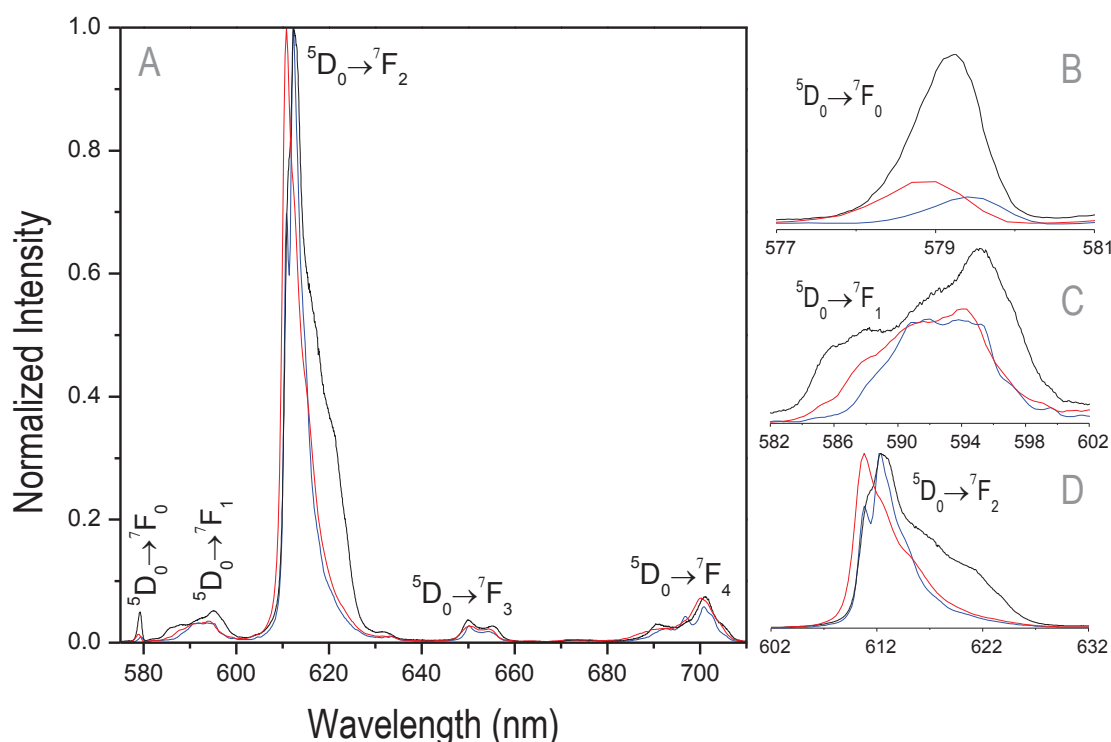


Figure 6.2: (A) Room-temperature emission spectra of  $\text{Eu}^{3+}$  complex isolated (black line), excited at 376.0 nm, **AEu** (red line) and **AET-1.3** (blue line), both spectra excited at 357.0 nm. (B), (C) and (D) A magnification of the  ${}^5\text{D}_0 \rightarrow {}^7\text{F}_{0-2}$  transitions. The presence of a single  ${}^5\text{D}_0 \rightarrow {}^7\text{F}_0$  ( $\text{Eu}^{3+}$ ) line, the local field splitting of the  $\text{F}_{1,2}$  levels in three and five Stark components, respectively, and the high relative intensity of the  ${}^5\text{D}_0 \rightarrow {}^7\text{F}_2$  transition indicate that the  $\text{Eu}^{3+}$  ions occupy a single low-symmetry local environment (without an inversion centre). This is unequivocally supported by the  ${}^5\text{D}_0$  and  ${}^5\text{D}_4$  decay curves which are well modeled by single exponential functions.

temperature. The same experiment at lower temperature produce a similar image with orange spots (figure 6.3 E), demonstrating that the emission actual color is a direct measurement of the absolute temperature. This is the first evidence that the **AET** luminescent

molecular thermometer coupled with an optical microscope can constitute a thermometer with micrometer spatial resolution.

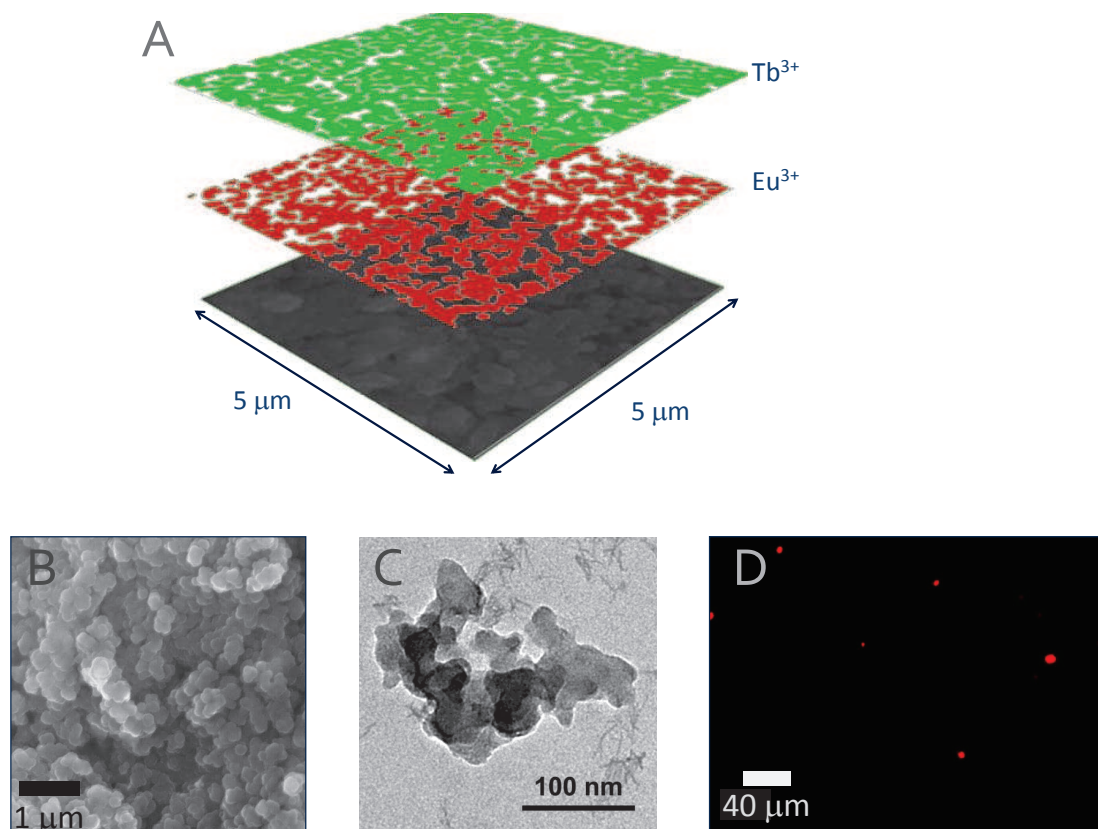


Figure 6.3: Microscopy of **AET** samples: TEM (C), SEM (B) (with the correspondent EDS mapping of the elements Eu and Tb (A)) and Fluorescence Microscopy images at room temperature (D) and at 125K (E)

This temperature dependence is appropriately illustrated by the calculus of the *Commission Internationale d'Éclairage* (CIE) (x,y) color coordinates (figure 6.4) strongly depends on the relative proportion of the  $\text{Eu}^{3+}$  and  $\text{Tb}^{3+}$  complexes anchored at the surface of the nanoparticles (Figs. 6.4 B,C). Therefore, the ability to fine-tune the nanocomposites emission from the green area towards the red region of the spectrum as a function of the temperature is readily managed by changing the relative proportion of embedded complexes.

As the emitted color is temperature dependent, the emission spectra varies with the temperature range 10-300 K for all the samples in the set. An illustrative example is the

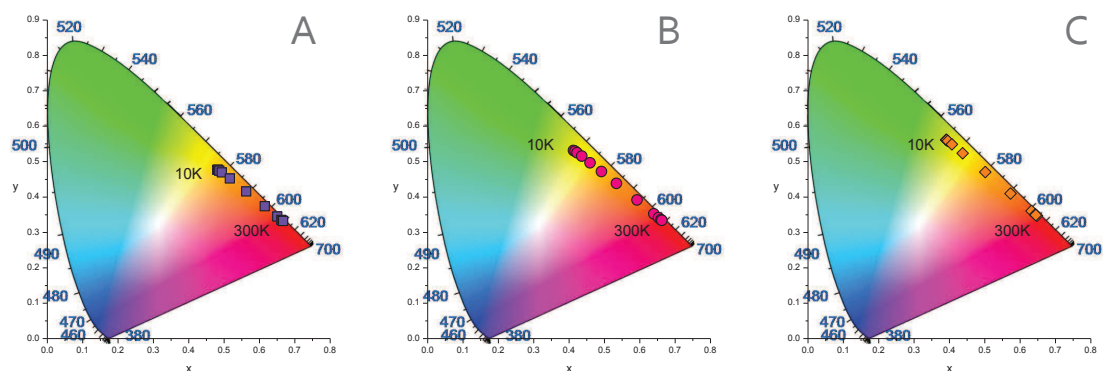


Figure 6.4: Emission color by CIE of **AET-1.1** (A), **AET-1.3** (A) and **AET-2.1** (A) for the temperature range 10-300K. The excitation wavelength is 358 nm for all samples.

**AET-1.3** emission spectra illustrated in figure 6.5. Both transitions assigned to  $\text{Eu}^{3+}$  and  $\text{Tb}^{3+}$  are present in the emission spectra and demonstrate to be temperature dependent. Whereas the intensity of the green  $\text{Tb}^{3+}$  luminescence strongly decreases as the temperature increases, the intensity of the red  $\text{Eu}^{3+}$  lines starts to increase at precisely the same temperature at which the  $\text{Tb}^{3+}$  emission starts to decrease (this behavior is observed in high  $\text{Eu}^{3+}$  concentrated samples **AET-1.1**, **AET-1.2** and **AET-1.3**). For low  $\text{Eu}^{3+}$  concentrated **AET-1.10** the red  $\text{Eu}^{3+}$  emission remains approximately constant when  $\text{Tb}^{3+}$  emission starts to decrease.

The analysis of the lifetime of the excited state of both lanthanide ions gives important information about the energy scheme that governs the temperature dependence of the emission of the **AET** samples. The temperature dependence of the  ${}^5D_0$  and  ${}^5D_4$  lifetimes were computed from the decay curves for all samples. The decay curves are well modeled by single exponential functions. The numerical fitting was implemented in MatLab® using a Non-linear Least Squares Algorithm the interactive Levenberg-Marquardt method, according to the procedure described in section 3.2.2.

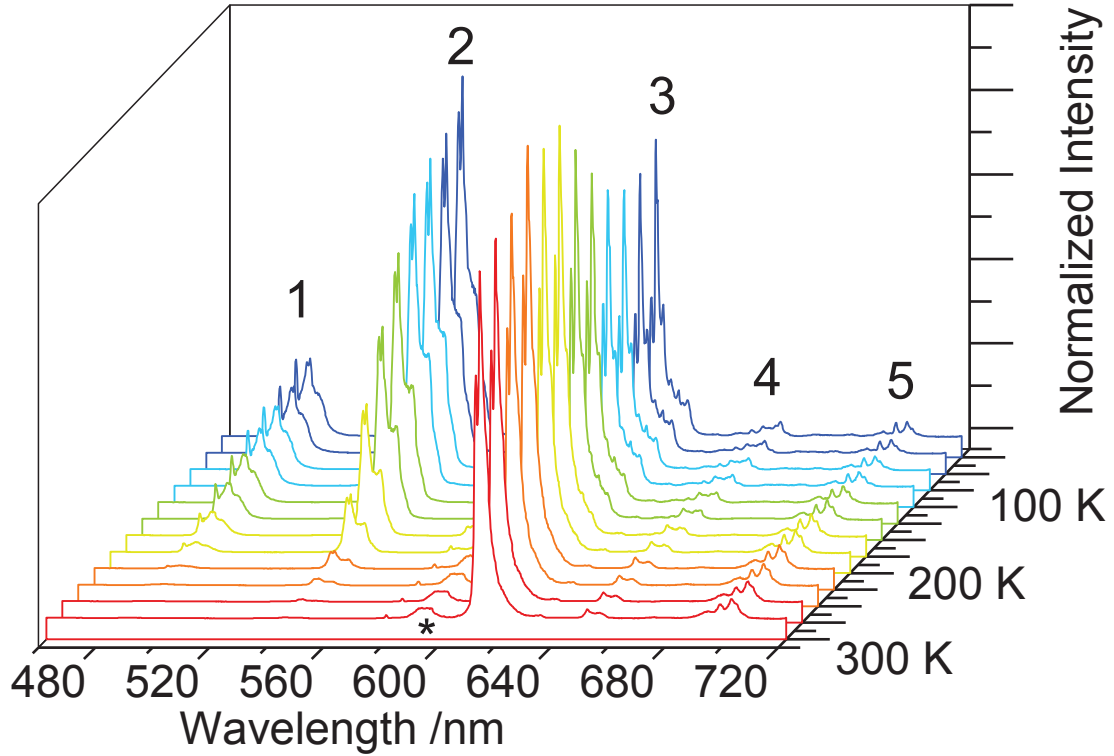


Figure 6.5: Steady state emission spectra of **AET-1.3** in the temperature range 10-300 K. The excitation wavelength is 358 nm.

## 6.2 Rationalization of the Operation Mechanism of the Thermometer

The rationalization of the operation mechanism of the thermometer follows the same basic model used before to interpret the **UET-1.3** temperature dependence. As observed previously for the **UET-1.3** sample, the lifetime of the  $\text{Eu}^{3+}({}^5\text{D}_0)$  and  $\text{Tb}^{3+}({}^5\text{D}_4)$  excited states present dissimilar behaviors in the temperature range 10-300K. The computed results are similar for all samples, so, for simplicity of analysis, let the discussion be centered in the lifetime dependence of sample **AET-1.3** depicted in figures 6.7 and 6.6. Whereas the  ${}^5\text{D}_0$  lifetime remains approximately constant ( $0.53 - 0.75 \times 10^{-3}\text{s}$ ) the  ${}^5\text{D}_4$  lifetime decreases approximately one order of magnitude [182]. This result exclude direct  $\text{Tb}^{3+}$ -to- $\text{Eu}^{3+}$  energy transfer within the lanthanide ions.

The non-radiative de-excitation of the  $\text{Tb}^{3+}({}^5\text{D}_4)$  level ( $20590 \pm 5\text{cm}^{-1}$ ) may be ap-

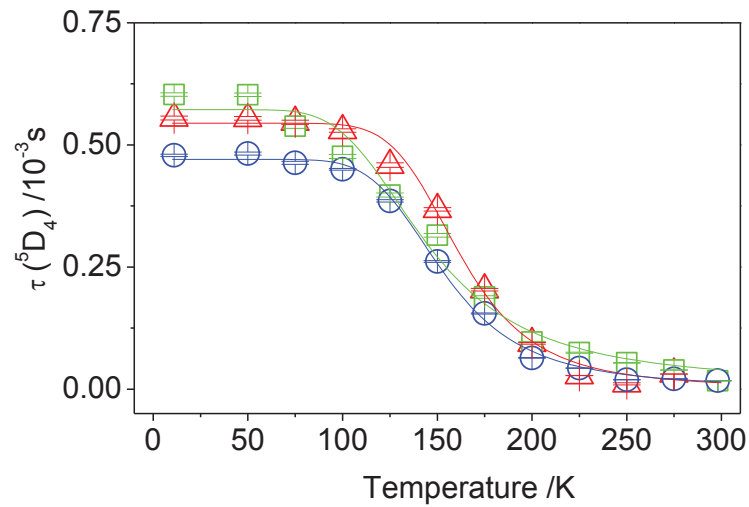


Figure 6.6:  ${}^5D_4$  lifetime of **AET** samples for the temperature range 10-300K. The excitation wavelength is 358 nm and the monitored wavelength is 545 nm ( ${}^5D_4$ ). The red triangles, green squares and blue circles correspond to **AET-1.1**, **AET-1.2** and **AET-1.3** respectively.

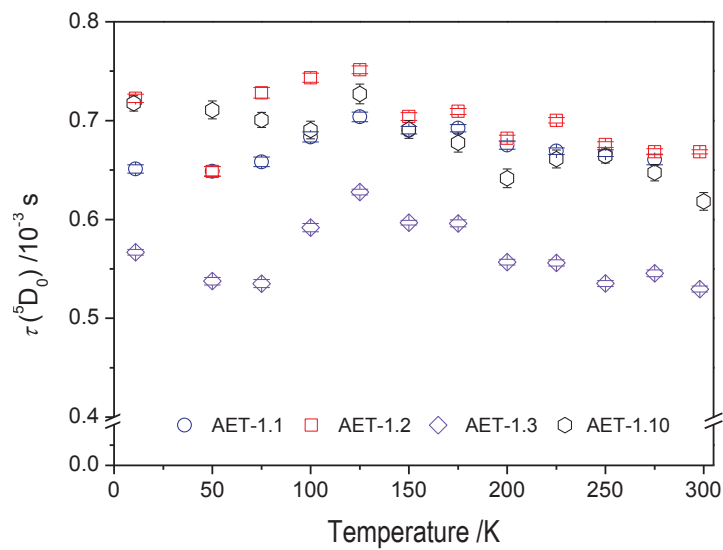


Figure 6.7: Temperature dependence of the  ${}^5D_0$  lifetime (14-300 K) of **AET-1.1**, **AET-1.2**, **AET-1.3** and **AET-1.10**. The decay curves are monitored at 700.5 nm and excited at 357.0 nm. The error bars are the product of the root mean square error of the single exponential fit by the mean value of the characteristic time computed at each temperature.

proximately described by the Mott-Seitz model, using the same arguments used before for the **UET-1.3** sample. The activation energies obtained for **AET-1.1**, **AET-1.2** and **AET-1.3** are  $615 \pm 19$ ,  $521 \pm 18$  and  $687 \pm 14 \text{cm}^{-1}$ , respectively. These values for energy fall in the region where the energy level of the host TEOS/APTES layer was previously reported [108, 250]. In the next section these experimental results are rationalized using the previous host-lanthanide energy scheme.

In the integrated intensity the results do not follow the decay observed in the decay lifetimes with the temperature increase, in contrast with **UET-1.3** sample, where the intensity of  ${}^5\text{D}_0 \rightarrow {}^7\text{F}_2$  transition is constant in this temperature range. This means that the excited state  ${}^5\text{D}_0$  is not significantly depopulated in the considered temperature range. Also the variation of the  ${}^5\text{D}_4 \rightarrow {}^7\text{F}_5$  intensity with temperature reinforces that an active non radiative decay path is activated by temperature.

In the **AET** samples both  $\text{Tb}^{3+}$  and  $\text{Eu}^{3+}$  transitions are temperature dependent. This behavior can be understood considering the presence of a thermally activated non-radiative mechanism associated to the emitting centers of the TEOS/APTES layer. Those energy is centered at  $22500 \pm 1500 \text{cm}^{-1}$ , in accord with the one previously reported for amino-propylsilica nanospheres annealed at 673K [108, 250].

The rationalization of the temperature dependence now demands a more refined model in order to explain the temperature dependence of the  $\text{Eu}^{3+}$  emission. Assuming a concerted two-step process involving only the Boltzmann energy factor  $\Delta E$ , first the excited triplet state of the host layer with energy above that of the  ${}^5\text{D}_4$  emitting state is populated through thermally-driven  ${}^5\text{D}_4$ -to-host energy transfer (diminishing, therefore, the  ${}^5\text{D}_4 \rightarrow {}^7\text{F}_5$  intensity and finally triplet level transfers a fraction of this absorbed energy to the  ${}^5\text{D}_0$  state (directly and/or via the  $\text{Eu}^{3+}$  ligands). The second step explains the increase of the  $\text{Eu}^{3+}$  integrated emission observed in the samples **AET-1.1**, **AET-1.2** and **AET-1.3**.

Experimental results bear out the above interpretation. For diluted  $\text{Eu}^{3+}$  nanoparticles, the probability of the host-to- $\text{Eu}^{3+}$  energy transfer mechanism should be strongly reduced, because the larger average  $\text{Eu}^{3+}$  to  $\text{Tb}^{3+}$  distance makes a direct energy transfer less probable to occur. Then the  ${}^5\text{D}_0 \rightarrow {}^7\text{F}_2$  intensity should be practically temperature independent as observed in the emission spectra of **AET-1.10** (integrated areas in figure 6.8 and emission spectra in figure 6.2).

The decrease in the  ${}^5\text{D}_0 \rightarrow {}^7\text{F}_2$  intensity discerned above 250-275 K range (most

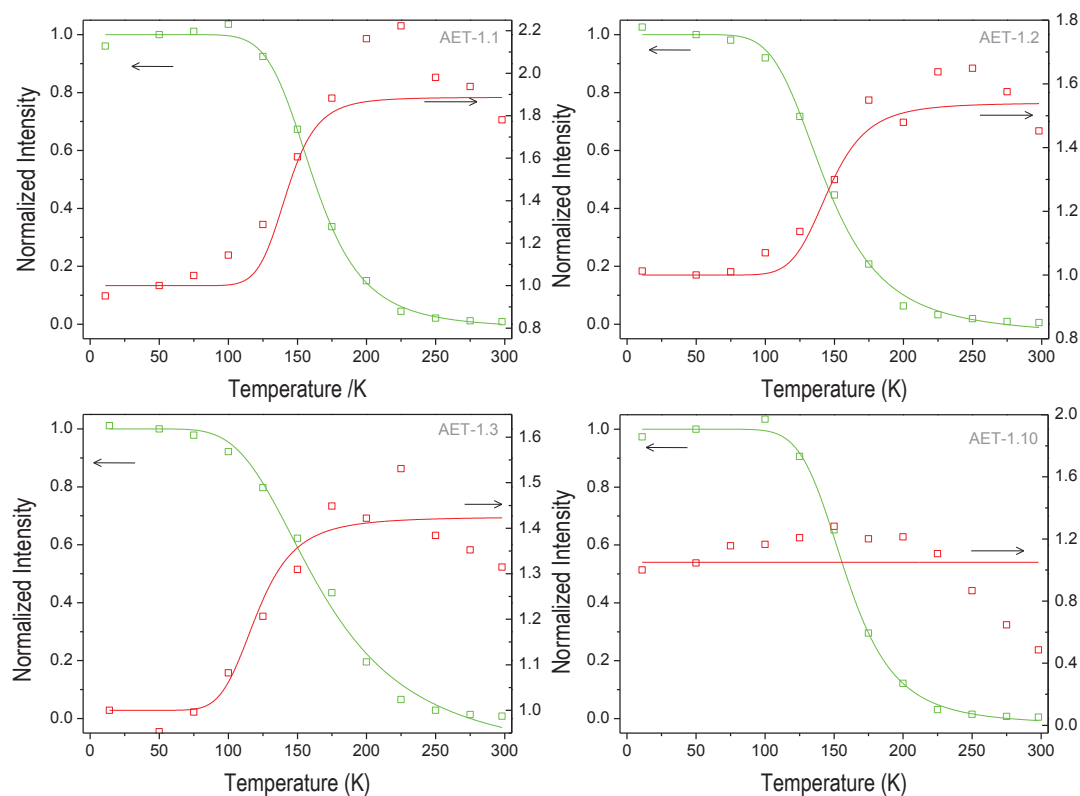


Figure 6.8: Integrated intensity of the  ${}^5D_0 \rightarrow {}^7F_2$  (605-635 nm, red squares) and  ${}^5D_4 \rightarrow {}^7F_5$  (535-560 nm, green squares) transitions as a function of temperature for **AET-1.1**, **AET-1.2**, **AET-1.3** and **AET-1.10** (excitation at 357 nm). The green lines represent the best fit to the experimental data using the Mott-Seitz expression (equation 3.2) (correlation coefficients  $r^2 > 0.989$ ) and the red lines are just guides for the eyes.

evident for **AET-1.10**) should be probably associated with a  $\text{Eu}^{3+}$ -to-host back transfer mechanism. According to the selection rules of the multipolar and exchange mechanisms that govern these energy transfer processes [146] and to the energy levels scheme of these nanoparticles, the  ${}^5D_2$  level (located at  $21505 \pm 5\text{cm}^{-1}$ ) is a good candidate to be involved in this thermally-activated back-transfer process (mediated through the multipolar mechanism).

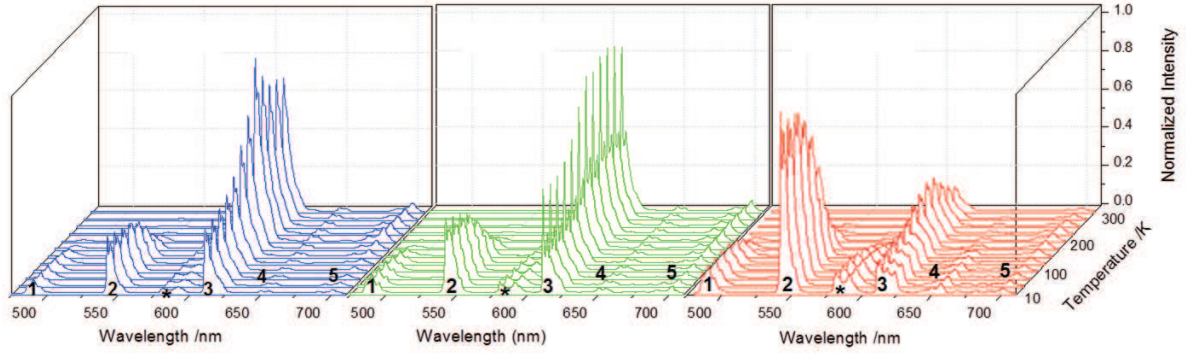


Figure 6.9: Temperature dependence (14-300 K) of the emission spectra of **AET-1.1**, **AET-1.2** and **AET-1.10**, (from left to right) excited at 357.0 nm. The sharp lines assigned to 1, 2, 3, 4 and 5 correspond to the  ${}^5D_4 \rightarrow {}^7F_{6,5}$  ( $Tb^{3+}$ ) and  ${}^5D_0 \rightarrow {}^7F_{2-4}$  ( $Eu^{3+}$ ) transitions, respectively. In the area marked with an asterisk there is a superposition between the emission of  $Eu^{3+}$  ( ${}^5D_0 \rightarrow {}^7F_{0,1}$ ) and  $Tb^{3+}$  ( ${}^5D_4 \rightarrow {}^7F_4$ ).

### 6.3 Sensitivity and Temperature Range of Operation

The absolute temperature measurement is computing defining an experimental parameter ( $\Delta = I_{Eu}^2 - I_{Tb}^2$ ), related to the integrated areas  $I_{Tb}$  and  $I_{Eu}$  of the temperature-dependent  ${}^5D_4 \rightarrow {}^7F_5$  ( $I_{Tb}$  at 545 nm) and the temperature-independent  ${}^5D_0 \rightarrow {}^7F_2$  ( $I_{Eu}$  at 612 nm) transitions, as defined in chapter 5.

The temperature dependence of the  $\Delta$  parameter is shown in figure 6.10 for the **AET** sample set. The figure presents the temperature dependence of the sensitivity for all proportions prepared. The best value ( $\sim 4.9\% \cdot K^{-1}$ ) is the largest one measured so far for lanthanide based molecular thermometers (1.5 times larger than the highest value previously reported using the same intensity ratio technique [185]).

Setting, as quality limit, a minimum sensitivity value of  $0.5\% \cdot K^{-1}$  in figure 6.10, leads to an optimal operation range of 150 K around the temperature of maximum sensitivity (120-190 K).

Furthermore, the absolute emission quantum yields of the **AET** nanoparticles, ranging from  $0.20 \pm 0.02$  (**AET-1.3**) to  $0.37 \pm 0.04$  (**AET-1.2**) (all results are presented in table 6.3), are sufficiently high so as to permit the use of commercial fibre optics for excitation and detection.

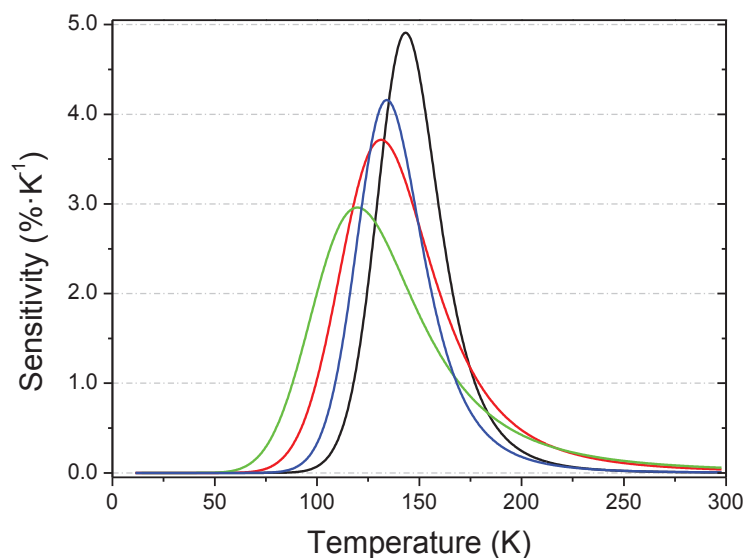


Figure 6.10: AET samples Sensitivities. The black, red, green and blue lines corresponds to **AET-1.1**, **AET-1.2**, **AET-1.3** and **AET-1.10**, respectively

Table 6.2: Absolute Quantum Yield of **AET** samples at room temperature for excitation wavelength of 358 nm (see section 3.2.3 for experimental details)

Sample	<b>AET-1.1</b>	<b>AET-1.2</b>	<b>AET-1.3</b>	<b>AET-2.1</b>
Quantum Yield	$0.27 \pm 0.03$	$0.37 \pm 0.04$	$0.20 \pm 0.02$	$0.24 \pm 0.02$

## Summary

In this chapter luminescent nanothermometers based on APTES/TEOS co-doped with Eu and Tb trivalent ions with remarkable properties are presented. The thermometers combine the possibility to fine-tune the emission color as a function of the temperature and  $\text{Eu}^{3+}/\text{Tb}^{3+}$  proportion, and measure temperature using a self-referenced algorithm allowing absolute measurements. The Ln-co-doped Si-NPs combine relative temperature sensitivities up to  $4.9\% \cdot \text{K}^{-1}$  in the temperature range 120-150K with high photostability for long-term use, resulting in a limit of detection of 0.5 K. The multifunctionality was also implemented combining magnetic and luminescent valences in the same NP platform, in a clear a step forward when compared with the  $\text{Ln}^{3+}$ -based thermometers presented in the literature (see section 2.1).

The NPs with mean diameter in the order of hundreds of micrometers present quantum yield up to 0.37 and demonstrate to be excited using conventional excitation sources, making their use possible in different experimental contexts, without major requirements.

Although the temperature range that obeys the criterium  $S_r > 0.5\% \cdot K^{-1}$  be relatively broad (120-190 K) it does not include the physiological temperature range (293-333 K) where most exciting practical applications appear. This intrinsic limitation was a starting point to the development of NP platforms with significant sensitivity in the physiological temperature range.

The most significant results presented in this chapter were reported in [33].



## Chapter 7

# Nanoparticles for Thermometry at the Physiological Temperature Range

The assortment of luminescent and non-luminescent nanothermometers that have been proposed in the last five years clearly point out the emergent interest of nanothermometry in numerable fields, such as electronic and optoelectronic machines and devices, micro- and nanofluidic systems, living cells and tissues, and nanostructures. Nanothermometry has indeed experienced a continuous and unprecedented growth over the past five years following, in most examples, the technological trends of sub-micron miniaturization, namely in the temperature mapping of microcircuits [150] and microfluids [19, 68, 174]. Moreover, there is a high demand for the development of intracellular thermometers [81, 104, 244, 270] capable of accurate temperature determination in living cells, namely for monitoring cellular activity (e.g. cell division, gene expression, enzyme reaction and changes in metabolic activity, etc. [179, 244, 270, 285]) as well as to investigate heat production and dissipation arising from most of these processes. However, despite actual promising progresses on microfluidic [174] and intracellular thermometry [179], precision control of fluid temperature by accounting for local temperature gradients and accurate temperature distributions within living cells have not yet been satisfactorily addressed. The major obstacle for progress has been the unavailability of a single molecular thermometer with the following requirements (that should be simultaneously satisfied):

- high temperature resolution ( $< 0.5K$ );
- ratiometric temperature output;

- high spatial resolution ( $< 3\mu m$ );
- functional independency of changes in pH, ionic strength and surrounding biomacromolecules;
- concentration-independent output.

Ratiometric (or self-referencing) intensity measurements are not compromised by the well know disadvantages of experiments based on the intensity of only one transition, such as the critical dependence on variations of the sensor concentration, small material inhomogeneities and optoelectronic drifts of the excitation source and detectors, and, thus, are much more reliable for precise temperature sensing.

Therefore, is unquestionable that an optimal luminescent nanothermometer should produce a ratiometric intensity response to temperature changes. Examples of ratiometric luminescent thermometers include organic dyes [14], polymers [46], the green fluorescent protein [62], quantum dots (QDs)[239],  $\text{Er}^{3+}$ -based nanocrystals [6],  $\text{Er}^{3+}/\text{Yb}^{3+}$ - and  $\text{Tm}^{3+}/\text{Yb}^{3+}$ -based [69, 200, 232, 238] UCNPs, a  $\text{Eu}^{3+}/\text{Tb}^{3+}$  mixed metal-organic framework [56], siloxane hybrid NPs co-doped with a  $\text{Eu}^{3+}$  complex and an organic dye [185], and siloxane hybrid magnetic NPs [33] and hybrid films [32] co-doped with  $\text{Eu}^{3+}$  and  $\text{Tb}^{3+}$  tris( $\beta$ -diketonate) chelates (see chapters 5 and 6). Among these luminescent ratiometric thermometers emphasis must be done to the handful of examples displaying spatial resolution lower than  $50\ \mu m$  in the physiological temperature range, 293-333 K (figure 2.11). Temperature sensing in spatial scales below  $10\ \mu m$  still remains a major challenge, demanding in most cases the development of new methodologies, including new materials and sensing schemes.

## 7.1 Strategies to attain the Physiological Temperature Range

To extend the operating temperature gamut of the siloxane-based hybrid magnetic nanothermometers to the physiological range, thus permitting the measurement of both the  $\text{Eu}^{3+}$  and  $\text{Tb}^{3+}$  emissions, we must change the host matrix and/or the  $\beta$ -diketonate chelate. This will modify the  $\text{Ln}^{3+}$ /ligands-host interactions with the concomitant increase of the energy of the first excited triplet state of the hybrid host (relatively to that of the

TEOS/APTES layer). This approach was followed in the case of  $\text{Eu}^{3+}/\text{Tb}^{3+}$  co-doped di-ureasil [32] thin films that permitted absolute temperature measurements at physiological temperatures with a relative sensitivity of  $0.7\% \cdot \text{K}^{-1}$  at 298-318K. For ratiometric nanothermometers, however, this is not attempted before.

The development of  $\text{Eu}^{3+}/\text{Tb}^{3+}$  luminescent nanothermometers operating in water suspensions at the physiological gamut is reported this chapter. The with an emission quantum yield between  $0.24 \pm 0.04$  and  $0.38 \pm 0.04$ , a relative sensitivity between 0.4 and  $0.9\% \cdot \text{K}^{-1}$  (maximum value, at 293 K) and a spatial resolution of  $65\mu\text{m}$  (to move out of the temperature uncertainly, stated as 0.5 K). None of the ratiometric luminescent and non-luminescent devices proposed so far (Table 2.2) can map, in a non-invasive way, the temperature in a microfluid at the physiological gamut with such high emission quantum yield, relative sensitivity and spatial resolution values. The synergy resulting from combining temperature mapping in microfluids with such figure of merit and superparamagnetism will provide a unique instrument to map temperature distributions in biological tissues during heat release, due to the application of an ac field to magnetic NPs (magnetic hyperthermia).

## 7.2 Morphological Characterization of the Luminescent Molecular Thermometers

The present luminescent molecular thermometers consist of  $\text{Ln}(\text{btfa})_3(\text{MeOH})(\text{bpeta})$  and  $\text{Ln}(\text{acac})_3 \cdot 3\text{H}_2\text{O}$   $\beta$ -diketonate chelates (where acac- stands for 2,4-pentanedionate or acetylacetonate, Ln=Eu and Tb, figure 3.7 in chapter 3) embedded into organic-inorganic hybrid nanoclusters (hydrodynamic size of 40-125 nm, figure 7.1) formed by a maghemite ( $\gamma - \text{Fe}_2\text{O}_3$ ) magnetic core (average size determined by TEM of  $11.8 \pm 2.3\text{nm}$ , figure 3.5) coated with an organosilica shell. Whereas the  $\text{Ln}(\text{btfa})_3(\text{MeOH})(\text{bpeta})$  chelates were embedded into a TEOS/TESP layer,  $\text{Eu}^{3+}/\text{Tb}^{3+}$ -containing  $\gamma - \text{Fe}_2\text{O}_3@$ TEOS/ TESP NPs, **PET-1.3**, (see chapter 3 for synthesis and labeling) the  $\text{Ln}(\text{acac})_3 \cdot 3\text{H}_2\text{O}$  complexes were incorporated into a TEOS/APTES shell,  $\text{Eu}^{3+}/\text{Tb}^{3+}$ -containing  $\gamma - \text{Fe}_2\text{O}_3@$ TEOS/APTES NPs **AET-1.4a** (see the section 3.1.5 for details about synthesis and labelling of the present nanothermometers, and table 7.2 for elemental analysis).

The EDS mappings show  $\text{Eu}^{3+}$  and  $\text{Tb}^{3+}$  distributions with contours and shapes similar to those of the NPs (figure 7.1), indicating that most of them contain both  $\text{Eu}^{3+}$  and  $\text{Tb}^{3+}$ .

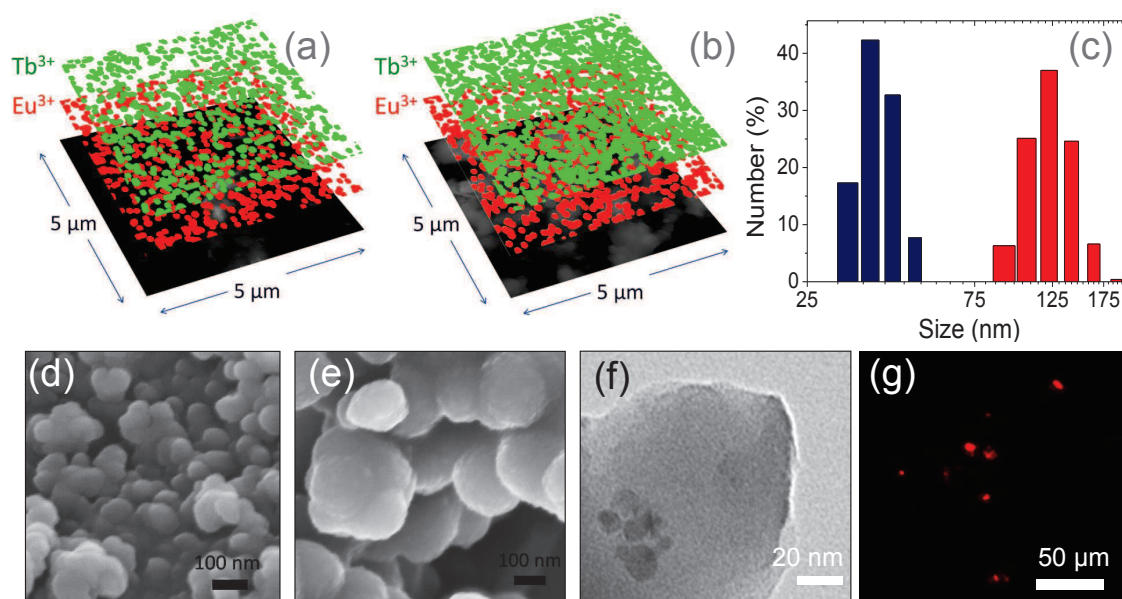


Figure 7.1: EDS mappings of the relative Eu and Tb content in SEM images of **PET-1.3** (a) and **AET-1.4a** (b); (c) DLS data showing the diameter distribution of **PET-1.3** (blue bars) and **AET-1.4a** (red bars); SEM images of **PET-1.3** (d) and **AET-1.4a**(e); TEM images of **AET-1.4a** (f) (g) Optical microscopy images of **PET-1.3** excited at 365 nm

The NPs are dispersible in water showing a monomodal size distribution centred at 40 nm (**PET-1.3**) and 125 nm (**AET-1.4A**), as seen in DLS measurements (figure 7.1). NPs with these characteristic sizes are also observed in SEM images (figure 7.1). Aggregation of the NPs that occur during the evaporation of the dispersions on the sample holder explain the aggregation seen in the SEM images (figure 7.1). TEM observations of **PET-1.3**, show sparse spherical silica NPS (figures 7.1 and figure 3.10). It is also observed that the magnetic  $\gamma - Fe_2O_3$  NPs are encapsulated in the core of the silica NPs (figure 7.1). The same can be said about **AET-1.4A** sample (figure 7.1). In both samples the size of the  $\gamma - Fe_2O_3$  NPs from TEM images is  $11.7 \pm 2.3$  nm.

The **PET-1.3** and **AET-1.4a** appear as red spots in optical microscopy with sizes of the order of 5  $\mu m$  (figures 7.1 and 7.2), with each spot corresponding to the emission either of a NP or a NP aggregate. The red colour of **PET-1.3** in figure 7.1 results for the dominance of the Eu<sup>3+</sup> emission at room-temperature independently of the excitation wavelength used (figures 7.3,7.2 and 7.8). For **AET-1.4a**, however, the emission at room-temperature is dominated by the Tb<sup>3+</sup> transitions (figures 7.7and 7.9).

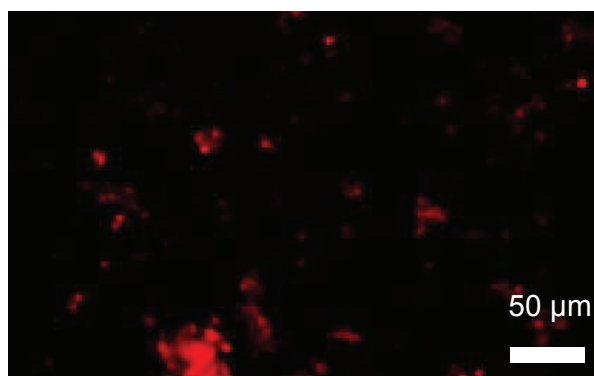


Figure 7.2: Optical microscopy image of **AET-1.4a** excited at 365 nm, acquired with a red filter, showing only the red emission assigned to Eu<sup>3+</sup> transitions.

Table 7.1: Eu, Tb, Fe and Si elemental analysis (% w/w). The Eu, Tb, Fe and Si content were obtained by inductively coupled plasma optical emission spectroscopy (ICP-OES) analysis on a Jobin Yvon Activa-M instrument with a glass concentric nebulizer. For the Eu and Tb analysis the samples were digested under microwaves with 2 mL of nitric acid (HNO<sub>3</sub>) and 0.75 mL of hydrogen peroxide (H<sub>2</sub>O<sub>2</sub>). The samples were collected in 25 mL flasks and the total volume adjusted using ultrapure water. The method is accurate within 10%.

Sample	Eu	Tb	Si	Fe
<b>PET-1.3</b>	1.3	4.1	10.2	0.1
<b>AET-1.4a</b>	0.6	2.4	22.9	0.3

In the next sections is presented the discussion of the photophysical properties of the nanothermometers and their use as thermometric parameter.

### 7.3 Operation Mechanism of PET-1.3.

The green  $\text{Tb}^{3+}$  luminescence of **PET-1.3** strongly decreases as the temperature increases, whereas the intensity of the red  $\text{Eu}^{3+}$  lines starts to increase at precisely the same temperature at which the  $\text{Tb}^{3+}$  emission starts to decrease (figure 7.3). This behaviour is similar to that already reported for  $\text{Ln}(\text{btfa})_3(\text{MeOH})(\text{bpeta})$  ( $\text{Ln}=\text{Eu}$  and  $\text{Tb}$ ) chelates embedded into a TEOS/APTES layer (see chapter 5 or reference [33]) and then the same concerted two-step process described is assumed to rationalize the intensity temperature dependence in **AET-1.1** to **AET-1.10**.

The TEOS/TESP hybrid host was rationally designed in order to present an excited triplet state with higher energy than that of the TEOS/APTES matrix permitting, therefore, the  $^5\text{D}_4$  depopulation (through thermally-driven  $^5\text{D}_4 \rightarrow \text{host}$  energy transfer) at an activation energy  $\Delta E$  higher ( $1195 \pm 15 \text{ cm}^{-1}$ , figures 7.10, 7.11 and 7.13) than that of the siloxane-based hybrid magnetic nanoclusters coated with a TEOS/APTES organosilica shell co-doped with  $\text{Eu}(\text{btfa})_3(\text{MeOH})(\text{bpeta})$  and  $\text{Tb}(\text{btfa})_3(\text{MeOH})(\text{bpeta})$  ( $687 \pm 14 \text{ cm}^{-1}$ )[33]. The energy difference between that triplet state and the  $^5\text{D}_0$  emitting level is too large to permit thermally-driven depopulation and the  $\text{Tb}^{3+}/\text{Tb}^{3+}$  relative intensity ratio of the **PET-1.3** nanothermometers guarantees the absolute measurement of temperature in the physiological gamut.

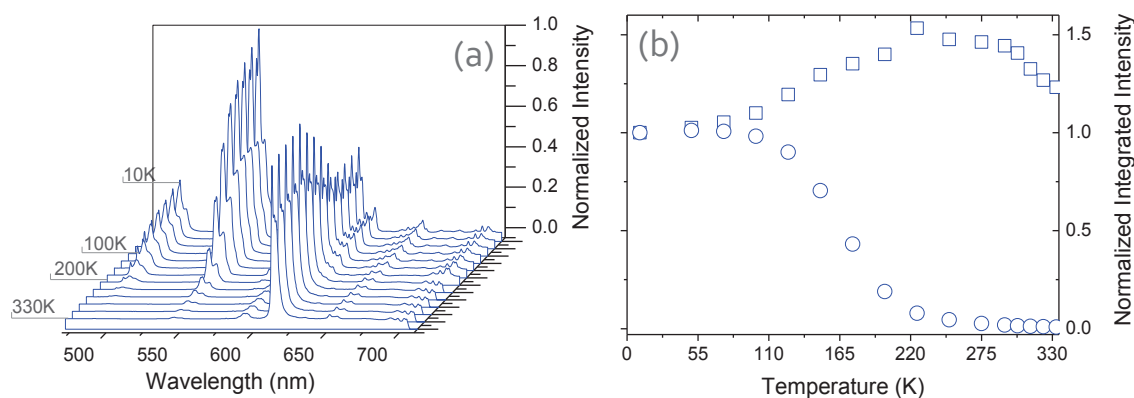


Figure 7.3: (a) Emission spectra of **PET-1.3** excited at 357nm. (b) Integrated areas of the  $^5\text{D}_4 \rightarrow ^7\text{F}_5$  transition of  $\text{Tb}^{3+}$  (circles) and  $^5\text{D}_0 \rightarrow ^7\text{F}_2$  transition of  $\text{Eu}^{3+}$  (squares) on the emission spectra of **PET-1.3**.

## 7.4 Operation Mechanism of AET-1.4a.

For **AET-1.4a**, however, the integrated intensities of the  ${}^5D_4 \rightarrow {}^7F_5$  ( $I_1$ ) and  ${}^5D_0 \rightarrow {}^7F_2$  ( $I_2$ ) transitions decrease in all the temperature range scanned (figure 7.4) pointing out a different mechanism to explain the thermometer operation. Two different regimes are clearly discernible: whereas for temperatures below 200 K ( $I_2$ ) presents a steeper slope compared to that of  $I_1$ , for temperatures within the physiological gamut, both intensities decay linearly. The switch between the two regimes occurs in the temperature range 175–200 K. Moreover, for temperatures above 175 K the natural logarithm of the  $I_1/I_2$  ratio changes linearly with the inverse of the temperature (figure 7.4).

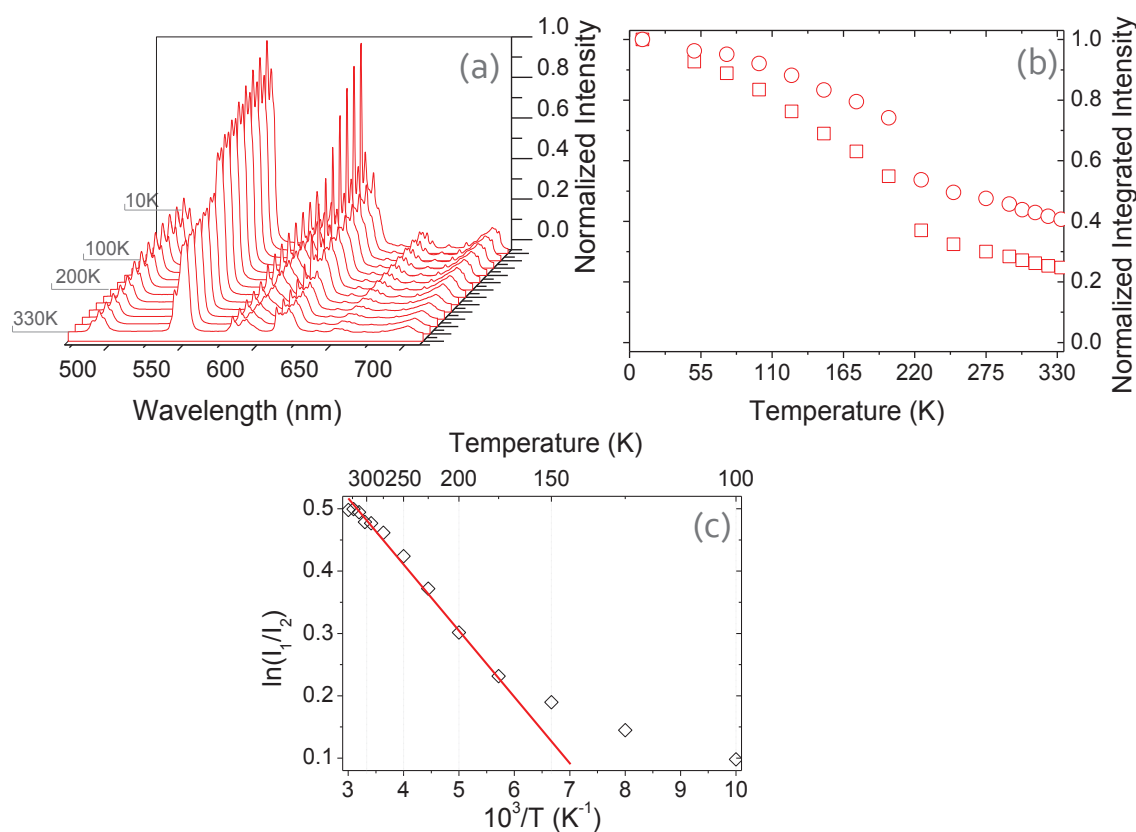


Figure 7.4: (a) Emission spectra of **AET-1.4a** (b) excited at 315nm. (b) Integrated areas of the  ${}^5D_4 \rightarrow {}^7F_5$  transition of  $Tb^{3+}$  (circles) and  ${}^5D_0 \rightarrow {}^7F_2$  transition of  $Eu^{3+}$  (squares) on the emission spectra of NP5-1.4. (c) Temperature dependence of the natural logarithm of the  $I_1/I_2$  intensity ratio for **AET-1.4a** (see text for details). The linear dependence above 175 K follows the equation  $\ln(I_1/I_2) = -105.2/T + 0.8$  ( $r^2 > 0.997$ ).

This dependence for  $I_1/I_2$  can be modelled considering that the intensity of a given transition is proportional to the population of a given excited state at absolute temperature  $T$ :

$$I \propto gAh\nu \exp\left(-\frac{\Delta E}{k_B T}\right) \quad (7.1)$$

where  $g$  is the degeneracy of the state,  $A$  is the spontaneous emission rate,  $h$  is the Planck constant,  $\nu$  is the frequency,  $k_B$  is the Boltzmann constant and  $\Delta E$  is the activation energy between the triplet host (or ligand) level and the  ${}^5D_0$  ( $17205.8 \pm 9.0 \text{ cm}^{-1}$ , figure 7.9 in the next section) and  ${}^5D_4$  ( $20336.6 \pm 10.1 \text{ cm}^{-1}$ ) emitting states. Taking the  $I_1/I_2$  ratio, it results:

$$\frac{I_1}{I_2} \propto \exp\left(-\frac{\Delta E_1 - \Delta E_2}{k_B T}\right) \implies \ln\left(\frac{I_1}{I_2}\right) \propto \frac{E_2 - E({}^5D_0) - E_2 + E({}^5D_4)}{k_B T} \times \frac{1}{T} \quad (7.2)$$

where  $E_1$  and  $E_2$  are the energies of the triplet host (or ligand) levels that quench the  $\text{Tb}^{3+}$  and  $\text{Eu}^{3+}$  emission, respectively. The slope of the linear fit to the experimental  $I_1/I_2$  ratio (figure 7.4) is  $-102.2 \pm 3.5 \text{ K}$  giving that  $E_1 - E_2 = 3276.8 \pm 14.4 \text{ cm}^{-1}$ . Attending to the energy level diagram of  $\text{Eu}^{3+}$ ,  $\text{Tb}^{3+}$ , APTES/TEOS hybrid matrix and acac ligand (figure 7.5), this difference is compatible with an energetic scheme in which above 175 K the  ${}^5D_4$  level is populated essentially through the triplet of the acac ligand ( $25300 \pm 1250 \text{ cm}^{-1}$ ) whereas the  ${}^5D_0$  one is populated through the triplet of the APTES/TEOS hybrid host ( $21273 \pm 3932 \text{ cm}^{-1}$ ). The acac - to -  ${}^5D_4$  and the host - to -  ${}^5D_0$  energy transfer are governed by the multipolar and exchange mechanisms, respectively [147].

Although the maximum sensitivity value for **PET-1.3** and **AET-1.4a** being bellow the physiological gamut, both thermometers present sensitivity higher than  $0.4\% \cdot K^{-1}$  (figure 7.6) in this temperature range, opening the possibility to use commercial detectors to follow the changes on the emission spectra for practical applications.

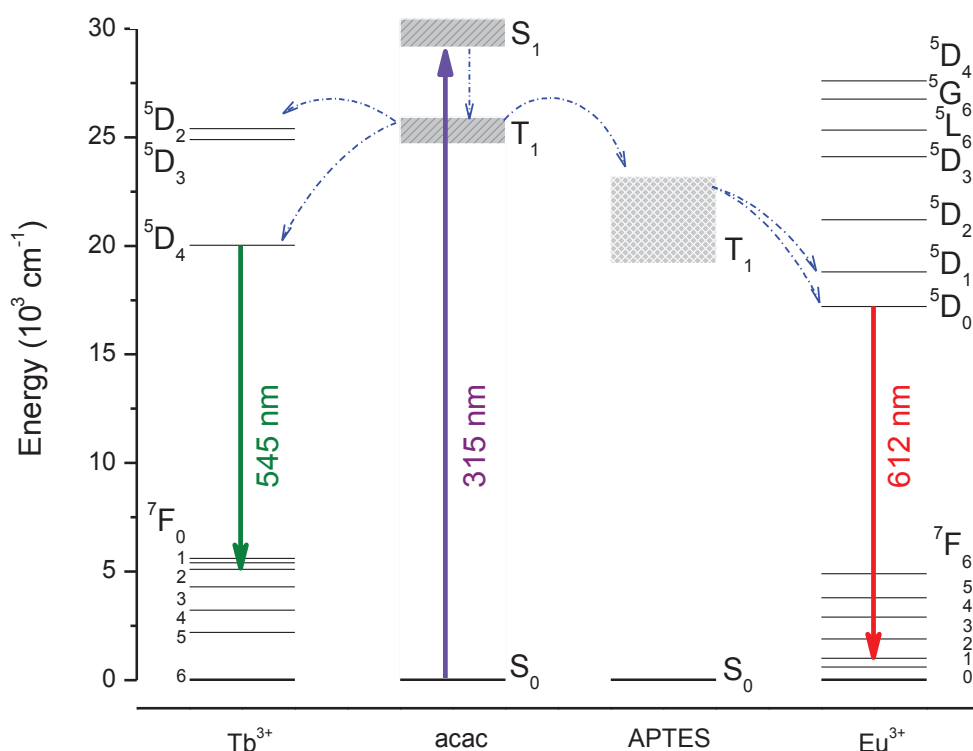


Figure 7.5: Partial energy level diagram of the **AET-1.4a** system. The dashed arrows represent the most probable inter- and intramolecular energy transfer processes above 175 K. Below that value the main energy transfer pathway for both ions involves the APTES triplet.

## 7.5 Photophysical Characterization of the Nanothermometers

In order to characterize the nanothermometers, the excitation spectra, high resolution emission spectra lifetime dependence on temperature were measured for both **PET-1.3** and **AET-1.4a**.

The broad bands in the excitation spectrum of  $\text{Tb}(\text{acac})_3 \cdot 3 \text{H}_2\text{O}$  and  $\text{Eu}(\text{btfa})_3(\text{MeOH})(\text{bpeta})$  are related to the excited states of the acac and btfa/bpeta ligands, respectively. In the spectra of **PET-1.3** and **AET-1.4a** the broad band ascribed to the excited states of the TEOS/APTES and TEOS/TESP shell are also discerned at  $\sim 270\text{nm}$  and  $\sim 280\text{nm}$  respectively. The high relative intensity of the ligands-related band with respect to that of

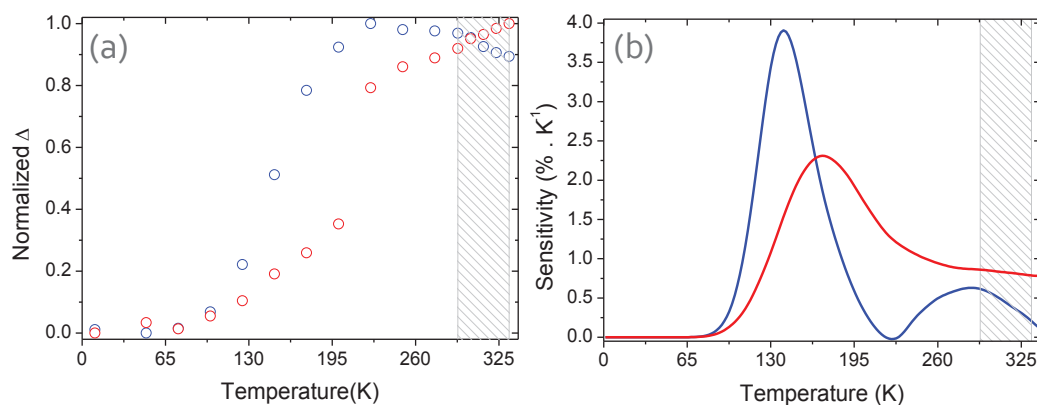


Figure 7.6: Normalized  $\Delta$  parameter (a) and the correspondent sensitivity (b) of **PET-1.3** (blue) and **AET-1.4a** (red) computed from the emission spectra of the NPs excited at 357 and 315 nm, respectively. The shadowed region corresponds to the physiological gamut.

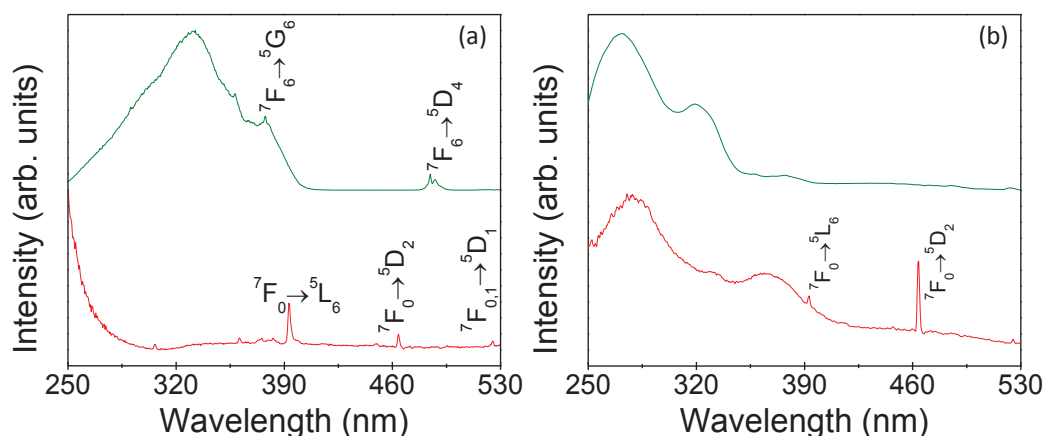


Figure 7.7: Excitation spectra (300 K) of (a) Tb(acac)<sub>3</sub> · 3H<sub>2</sub>O, monitored within the  ${}^5D_4 \rightarrow {}^7F_5$  (546.5 nm) transition (green line), Eu(acac)<sub>3</sub> · 3H<sub>2</sub>O, monitored within the  ${}^5D_0 \rightarrow {}^7F_2$  (613.5 nm) (red line) transition, (b) **AET-1.4a**, monitored within the  ${}^5D_4 \rightarrow {}^7F_5$  (Tb<sup>3+</sup>, 545.0 nm) (green line) transition, within the  ${}^5D_0 \rightarrow {}^7F_2$  (Eu<sup>3+</sup>, 611.1 nm) (red line) transition. The spectra were corrected for the spectral distribution of the lamp intensity using a photodiode reference detector.

the intra- $4f$  lines (quite absent for Tb<sup>3+</sup> in the spectrum of **PET-1.3** and **AET-1.4a**), indicates a more efficient ligands/host sensitization process when compared with direct intra- $4f$  excitation.

The presence of a single  ${}^5D_0 \rightarrow {}^7F_0$  (Eu<sup>3+</sup>) line, the local field splitting of the  $F_{1,2}$

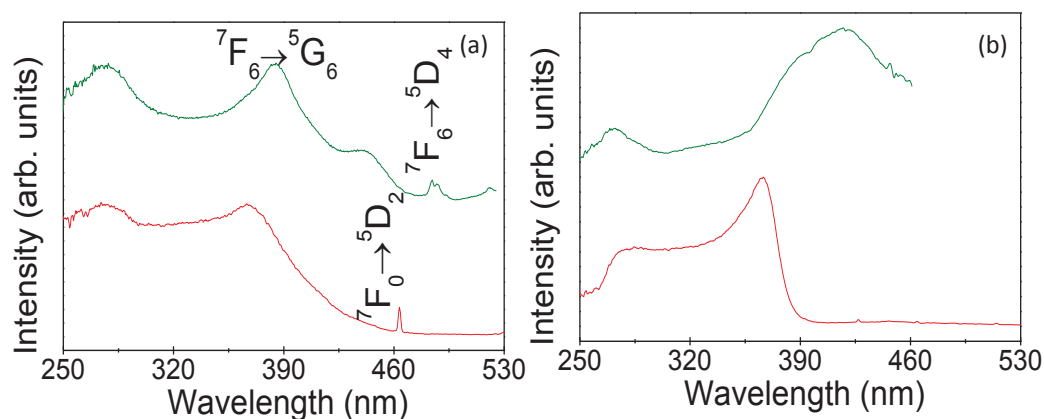


Figure 7.8: Excitation spectra (300 K) of (a)  $\text{Eu}(\text{btfa})_3(\text{MeOH})(\text{bpeta})$ , monitored within the  ${}^5D_0 \rightarrow {}^7F_2$  (612.0 nm) (red line) and  $\text{Tb}(\text{btfa})_3(\text{MeOH})(\text{bpeta})$ , monitored within the  ${}^5D_4 \rightarrow {}^7F_5$  (545.2 nm) (green line), and (b) **PET-1.3** monitored within the  ${}^5D_0 \rightarrow {}^7F_4$  (700.5 nm) (red line) transition  ${}^5D_4 \rightarrow {}^7F_6$  (490.5 nm) (green line) and transition. The spectra were corrected for the spectral distribution of the lamp intensity using a photodiode reference detector.

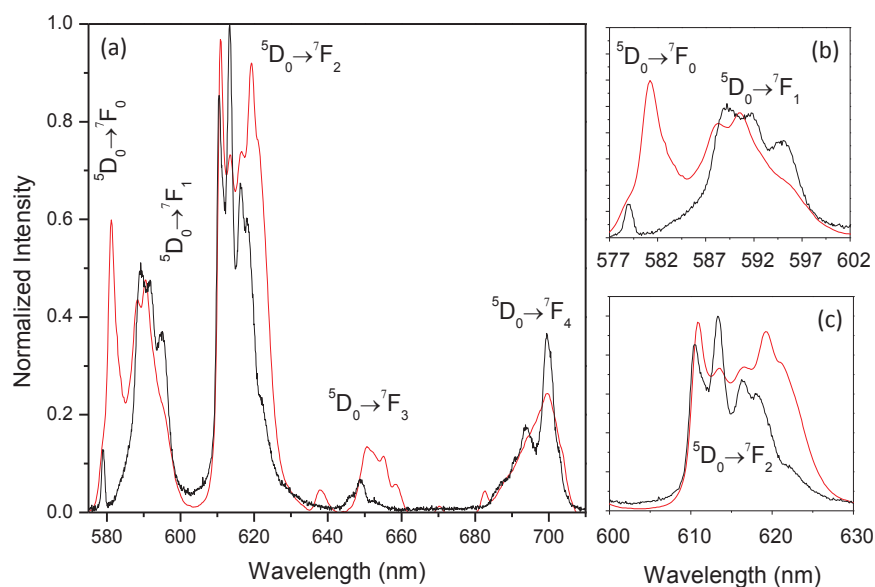


Figure 7.9: (a) Room-temperature emission spectra of  $\text{Eu}(\text{acac})_3 \cdot 3\text{H}_2\text{O}$  (black line), excited at 330.0 nm and **AET-1.4a** (red line), excited at 315.0 nm. (b) and (c) are magnifications of the  ${}^5D_0 \rightarrow {}^7F_{0-2}$  transitions.

levels in three and five Stark components, respectively, and the high relative intensity of the  ${}^5D_0 \rightarrow {}^7F_2$  transition indicate that the  $\text{Eu}^{3+}$  ions occupy a single low-symmetry local environment (without an inversion centre). This is unequivocally supported by the  ${}^5D_0$  and  ${}^5D_4$  decay curves which are well modelled by single exponential functions (figure 7.10).

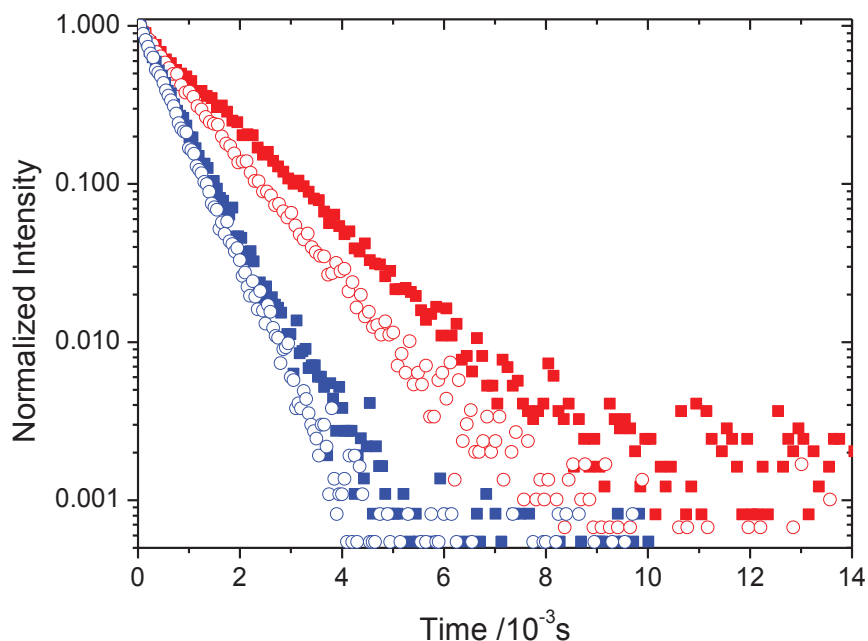


Figure 7.10:  ${}^5D_0$  and  ${}^5D_4$  decay curves for **PET-1.3** (blue symbols) and **AET-1.4a** (red symbols) excited at 357 and 315 nm, respectively. The squares corresponds to the  ${}^5D_0 \rightarrow {}^7F_2(\text{Eu}^{3+}, 613.5 \text{ nm})$  and the circles to the  ${}^5D_4 \rightarrow {}^7F_5(\text{Tb}^{3+}, 546.5 \text{ nm})$  transitions. All the decay curves present linear time dependence in the semi-logarithmic plot indicating that all the excited states lifetimes are well modelled by single exponential functions.

Comparison of the emission features of  $\text{Eu}(\text{btfa})_3(\text{MeOH})(\text{bpeta})$  and  $\text{Eu}(\text{acac})_3 \cdot 3 \text{H}_2\text{O}$  with those of **PET-1.3** and **AET-1.4a** shows that the energy, the full width at half maximum (fwhm) and the relative intensities of the  ${}^5D_0 \rightarrow {}^7F_{0-4}$  transitions are strongly altered, indicating an effective interaction between the  $\text{Eu}^{3+}$  ions and the TEOS/TESP and TEOS/APTES layer, respectively (figure 7.2). To quantify further the differences in the emission features between the nanocomposites and the  $\text{Eu}^{3+}$  complexes, the fwhm and the energy of the  ${}^5D_0 \rightarrow {}^7F_0$  transition were estimated by deconvoluting the emission spectra at 14 K, assuming a single Gaussian function, resulting in the outcome that, the energy of

Table 7.2: Absolute Quantum Yield of of **PET-1.3** and **AET-1.4a** at room temperature for excitation wavelength of 358 nm and 315 nm respectively (see section 3.2.3 for experimental details)

Sample	<b>PET-1.3</b>	<b>AET-1.4a</b>
Solid	$0.37 \pm 0.04$	$0.27 \pm 0.03$
Water suspension	$0.38 \pm 0.04$	$0.24 \pm 0.02$

the  ${}^5D_0 \rightarrow {}^7F_0$  transition for **PET-1.3** ( $17253.2 \pm 9.0 \text{ cm}^{-1}$ ) and **AET-1.4a** ( $17205.8 \pm 9.0 \text{ cm}^{-1}$ ) is red shifted in comparison with the energy estimated for  $\text{Eu}(\text{btfa})_3(\text{MeOH})(\text{bpeta})$  ( $17266.7 \pm 9.0 \text{ cm}^{-1}$ ), and  $\text{Eu}(\text{acac})_3 \cdot 3 \text{H}_2\text{O}$  ( $17272.1 \pm 9.0 \text{ cm}^{-1}$ ) respectively. The corresponding fwhm values are  $29.4 \pm 1.1 \text{ cm}^{-1}$ ,  $19.4 \pm 0.9 \text{ cm}^{-1}$ ,  $26.5 \pm 1.0 \text{ cm}^{-1}$  and  $29.2 \pm 1.2 \text{ cm}^{-1}$ , for  $\text{Eu}(\text{btfa})_3(\text{MeOH})(\text{bpeta})$ , **PET-1.3**,  $\text{Eu}(\text{acac})_3 \cdot 3 \text{H}_2\text{O}$  and **AET-1.4a**, respectively.

As reported for similar organic/inorganic hybrids incorporating analogous  $\beta$ -diketonate complexes [33, 148], the embedding of the complexes within the with TEOS/TESP NPs and with TEOS/APTES NPs induces the replacement of the labile MeOH and  $\text{H}_2\text{O}$  molecules, respectively, in the  $\text{Eu}^{3+}$  first coordination sphere, thus anchoring the complexes at the particle surface (*via* the silanol groups or the nitrogen atoms of APTES). This is supported by the increase in the  ${}^5D_0$  lifetime of  $0.443 \pm 0.002 \text{ ms}$  for  $\text{Eu}(\text{btfa})_3(\text{MeOH})(\text{bpeta})$  and  $0.057 \pm 0.001 \text{ ms}$  for  $\text{Eu}(\text{acac})_3 \cdot 3 \text{H}_2\text{O}$ , to  $0.557 \pm 0.005 \text{ ms}$  for **PET-1.3** and  $0.850 \pm 0.006 \text{ ms}$  for **AET-1.4a**, after the complexes embedding into the NPs (figure 7.9). This increase (already reported elsewhere [148]) is in good agreement with the replacement of the MeOH or  $\text{H}_2\text{O}$  molecules by silanol groups or nitrogen atoms of APTES/TESP. Further, the interaction between the  $\text{Eu}^{3+}$  ions and the particle surface is inferred by the measurement of the absolute emission quantum yields. The corresponding maximum absolute emission quantum yields ( $0.32 \pm 0.03$ ,  $0.01 \pm 0.01$ ,  $0.37 \pm 0.04$  and  $0.27 \pm 0.03$ , for  $\text{Eu}(\text{btfa})_3(\text{MeOH})(\text{bpeta})$ ,  $\text{Eu}(\text{acac})_3 \cdot 3 \text{H}_2\text{O}$ , **PET-1.3** and **AET-1.4a**, respectively) are listed in table 7.5.

The radiative deexcitation probability of the  $\text{Tb}^{3+} \ ^5\text{D}_4$  level may be approximately described in **PET-1.3** by the Mott-Seitz model, which expresses the temperature dependence of the experimental lifetime according equation 3.2. The activation energy obtained is  $1195 \pm 15 \text{ cm}^{-1}$ . The process of **AET-1.4a** follows a completely different dynamics, not explained by the Mott-Seitz model.

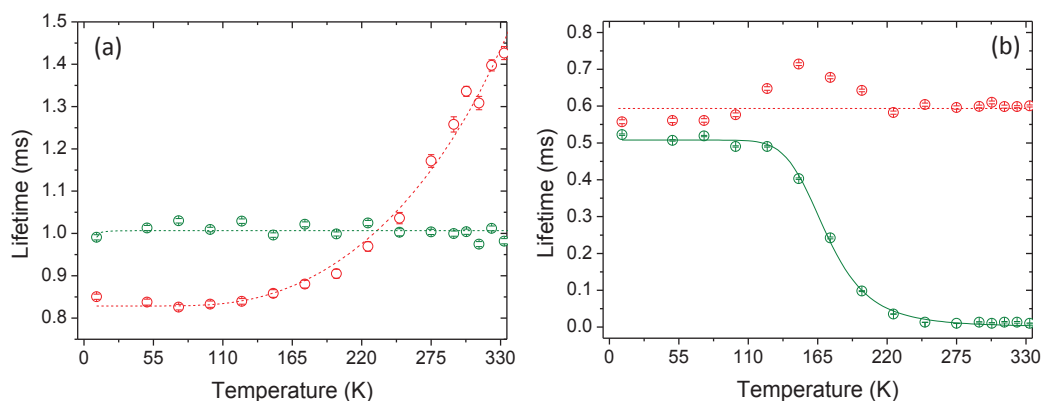


Figure 7.11: Lifetime dependence in the 10-330 K temperature range of **PET-1.3** (a) and **AET-1.4a** (b). The excitation wavelengths are 357 and 315 nm, respectively. The lifetimes were computed fitting the experimental decay curves, monitoring the  $^5\text{D}_0 \rightarrow ^7\text{F}_2$  ( $\text{Eu}^{3+}$ , 613.5 nm) (red circles) and the  $^5\text{D}_4 \rightarrow ^7\text{F}_5$  ( $\text{Tb}^{3+}$ , 546.5 nm) (green circles) transitions, to a single exponential. All the pointed lines are guides for the eyes.

## 7.6 Demonstration of Temperature mapping in Fluids.

Both **PET-1.3** and **AET-1.4a** are easily dispersible in water forming transparent and stable (at least during 1 day) suspensions under day light illumination (figure 7.12), making them ideal for temperature determination in transparent fluids using the temperature dependence of their emission properties. A demonstration of the use of these NPs in microfluidics (the field of fluidics that deals with the behavior, precise control and manipulation of fluids that are constrained to the sub-millimeter scale) was performed mapping the temperature of a 1 mm inner diameter glass tube, longitudinal length of 20 mm, filled with the **AET-1.4a** and **PET-1.3** water suspensions ( $1\text{mg/mL}$ ). A one-dimensional steady-state temperature gradient (up to  $0.03 \text{ degree} \cdot \mu\text{m}^{-1}$ ) was induced in the suspensions by an

electrical current flowing in a coil-shaped resistance (figure 7.12). The current was adjusted to produce the temperature gradient within the physiological gamut.

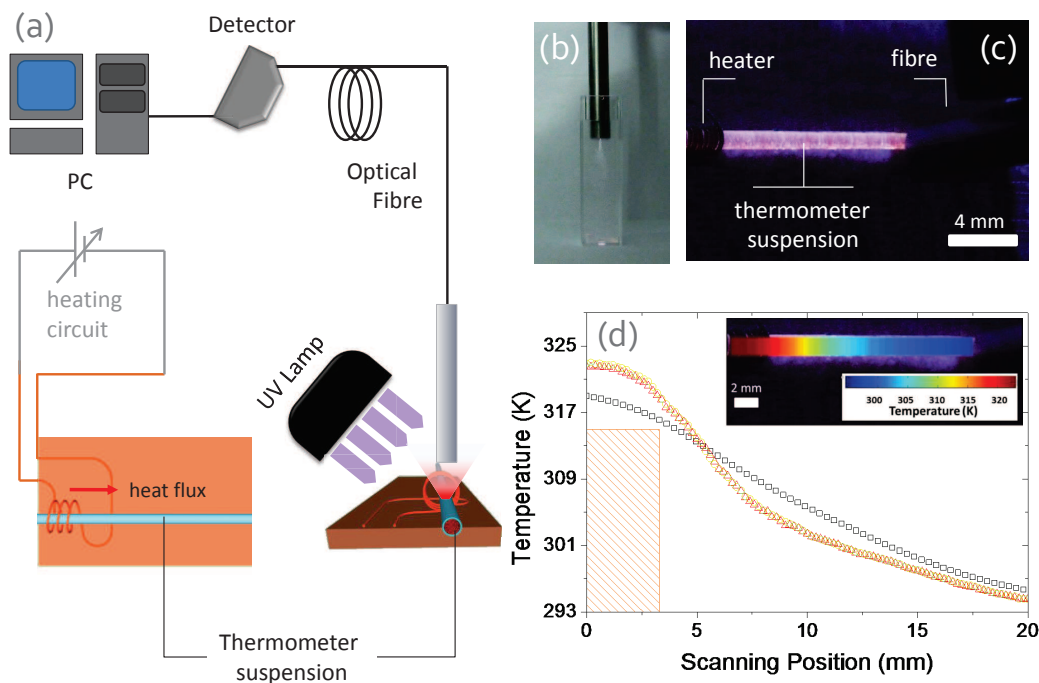


Figure 7.12: Temperature measurement in aqueous suspensions of NPs. (a) Experimental setup used for temperature mapping in nanofluids. (b) Photograph of the **AET-1.4a** suspension under UV irradiation (QR450-7-XSR optical fibre). The suspension displays a green-blue emission with Commission Internationale d'Éclairage (CIE) (x,y) colour coordinates of (0.26, 0.61). (c) Photograph of the **PET-1.3** suspension under UV irradiation (handheld lamp). The heater, the capillary tube and the optical fibre are also visualized. The suspension displays an orange-red emission with CIE (x,y) colour coordinates of (0.63, 0.37). (d) Comparison of the temperature profile obtained with the IR camera (black squares) and with the light emission of **AET-1.4a** (red triangles) and **PET-1.3** (blue circles). The shadowed area corresponds to the position of the heater. The pseudo-colour image of the **PET-1.3** suspension is represented as inset.

A map of the temperature, recorded with a state-of-the-art commercial IR camera (circuit mappings using the same camera demonstrated that the temperature algorithm makes a significant averaging integrating the information of several pixels -see mappings and discussion on the second circuit in chapter 5), was used as a control measurement. When illuminated with UV light (365 nm) the suspensions presented a red-orange emission (figure 7.12). The temperature measurements of the IR camera switching on/off the UV

light source results in a similar temperature profile within the camera uncertainty (0.1 degree). An optical fiber is used to collect the emission spectra which were converted into absolute temperatures. The conversion was based on the  ${}^5D_4 \rightarrow {}^7F_5$  ( $I_1$ ) and  ${}^5D_0 \rightarrow {}^7F_2$  ( $I_2$ ) integrated areas defining the thermometric parameter  $\Delta$ :

$$\Delta = I_2^2 - I_1^2$$

Although both transitions are temperature dependent in the physiological gamut, a local calibration curve can be generated for the particular experimental conditions used. In our case, the calibration curves were generated for water suspension **AET-1.4a** and **PET-1.3** excited at 365 nm (figure 7.13).

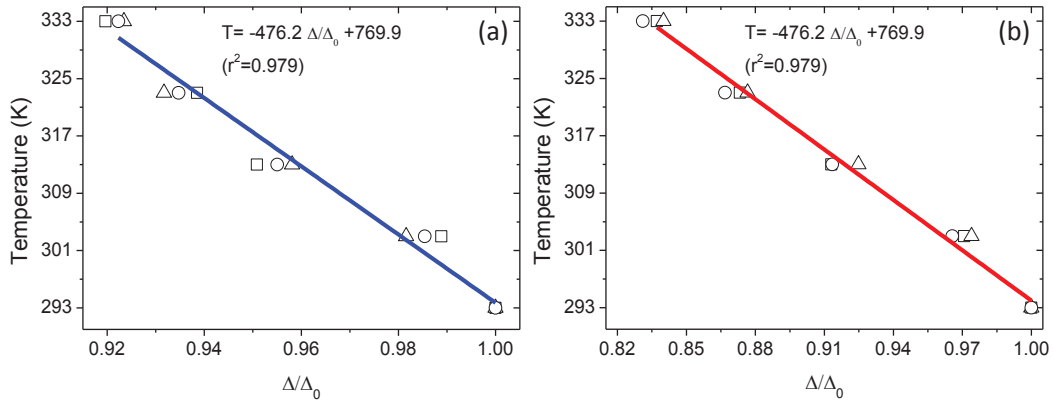


Figure 7.13: Calibration curves for (a) **PET-1.3** and (b) **AET-1.4a** in water suspensions (1.0 mg/mL). The temperature was cycled three times and the emission spectra (excited at 360 nm) recorded at equal time intervals when the temperature increases. For all spectra the computed  $\Delta$  parameter was divided by its value at room temperature ( $\Delta_0$ ). The results for all cycles are overlapped and the first degree polynomial fits presented in the figures are the local calibration curves. The open symbols corresponds to tree cycles of temperature increase.

The comparison between the two mappings is illustrated in figure 7.12. It is evident a high concordance between the temperature measurements of both thermometers in all the scanned range. Over the heater, the temperature obtained with the nanothermometers is up to 3.5 K higher than that measured by the IR camera. Along a distance of  $\sim 5\text{mm}$  both **AET-1.4a**, **PET-1.3** measurements are coincident and after this point the IR camera value rises up to 3.6 K above the nanothermometers reading. These results of the IR

camera point out to significant spatial averaging in the temperature algorithm. The **AET-1.4a**, **PET-1.3** thermometers and IR camera spatial resolutions are 65, 67 and 160  $\mu\text{m}$ , respectively, despite the 450  $\mu\text{m}$  of the optical fiber's inner diameter being  $\sim 1.5$  times larger than the camera pixel field of view (see discussion of the second circuit mapping in chapter 5). When compared with this camera, **AET-1.4a**, **PET-1.3** thermometers are suitable to sense higher temperature gradients within a temperature uncertainty of 0.4 K.

The temperature uncertainty was estimated using the following procedure: A temperature profile was acquired in the same apparatus described above in the absence of the heating source. When converted in absolute temperature, the emission spectra correspond to temperature fluctuations of 0.4 K, so this was assumed as the experimental temperature uncertainty on all temperature measurements.

## 7.7 Comparison with Literature Examples

Only few examples of luminescent ratiometric thermometers with spatial resolution below 100  $\mu\text{m}$  have been reported so far, and only one can operate in microfluids through laser-induced fluorescence (LIF) of Rhodamine-B or Sulforhodamine-101 dyes in ethanol/water solutions.[11] These thermometers exhibit sensitivities of  $1.5\% \cdot K^{-1}$  and  $2.7\% \cdot K^{-1}$ , respectively (under volumetric illumination from an Nd:YAG laser) and are able to measure one-dimensional steady-state temperature gradient in a fluid at the microscale. Averaging the image of seven parallel microfluidic channels over a spatial domain of 30 by 30 pixels, a spatial resolution of  $\sim 69\mu\text{m}$  (computed from published data) is obtained. The experimental uncertainty is lower than 0.55 K, which are still 2–3 times larger than those reported for macroscale [174] two-colour LIF.

Using a non ratiometric algorithm, Feng *et al.* [68] studied a gradient of temperature generated in a quartz tube filled with a luminescent pyrene-containing triarylboron molecule, dipyren-1-yl(2,4,6-triisopropylphenyl)borane (DPTB) in 2-methoxyethyl ether (MOE). Under 410 nm continuous excitation, the solution colour changes from green to blue when the temperature goes from 223 to 323 K [68]. Using CIE chromaticity diagram or the calibration curve (the shift of the emission maximum is the thermometric parameter) temperature profiles with spatial resolution of  $\sim 80\mu\text{m}$ , estimated from edge roughness of the DPTB-MOE images are obtained [68]. A recent report of Choudhury *et al.* [51] propose the use of the peak emission maximum shift with temperature to measure temperature

in microfluids. Using particles (*e.g.* carbon nanotubes) to perform nanoheating the authors measure the temperature following the emission of CdTe Quantum Dots. A microchannel was imaged and the respective temperature profile reconstructed with 0.2 degree resolution and 55  $\mu\text{m}$  spatial resolution, despite the low sensitivity value ( $0.05\% \cdot K^{-1}$ ).

The luminescent thermometers proposed so far that can operate in fluids are compared in figure. The best value of sensitivity of such thermometric systems in the physiological range is of the order of  $1 - 2\% \cdot K^{-1}$ . Also the cellular thermometers proposed by Vetrone *et al.*[238] and Maestro *et al.*[156] cover only partially the physiological gamut, despite the best spatial resolution. The **AET-1.4a** and **PET-1.3** are luminescent nathermometers working in water suspensions (thermometric nanofluids)that can cover the entire physiological gamut with spatial resolution bellow  $100\mu\text{m}$ . Particularly, the **AET-1.4a** is the presents nearly constant sensitivity over the entire physiological gamut.

## Summary

In summary, the luminescent molecular thermometer introduced here is a step forward in the molecular luminescent thermometers reported in chapters 5 and 6. It combines:

- the ability to fine-tune the emission colour as a function of the temperature,  $\text{Eu}^{3+}/\text{Tb}^{3+}$  proportion, organic-inorganic hybrid host and  $\beta$ -diketonate ligand;
- self-referencing that allows absolute measurements up to  $0.9\% \cdot K^{-1}$  in the physiological temperature range ( $3.8\% \cdot K^{-1}$  maximum temperature sensitivity at 132 K);
- high photostability for long-term use;
- flexibility to be used in water suspensions;
- a temperature uncertainly of 0.4 K and spatial resolution up to 64  $\mu\text{m}$ ;
- multifunctionality.

These features together are clearly a step forward in nanothermometers operating in fluids as compared to those proposed so far. This remarkable combination of properties can be used for combinatorial and array-based data acquisition as a function of temperature for applications in chemical and biological sciences. Microfluidics can be used to take

part of the short length scales and create simple linear temperature gradient across dozens of parallel microfluidic channels simultaneously. In this way, activation energies from catalytic reactions, melting point transitions from lipid membranes, and fluorescence quantum yield curves from semiconductor nanocrystal probes can be easily exploited. Moreover, the synergy arising from the combination of highly sensitive molecular thermometers for the physiological gamut with microfluidics methods will be useful to study protein crystallization, phase diagram measurements, chemical reaction optimization, or multivariable experiments [160].



# Chapter 8

## Conclusions and Future Work

The numerous reported results in the period 2005-2012 clearly point out to the emergent interest of nanothermometry in numerous fields, such as electronic and optoelectronic machines and devices, micro- and nanofluidic systems, living cells and tissues, nanostructures, and in many other conceivable applications, such as thermally-induced drug release and wherever exothermal chemical or enzymatic reactions occur at submicrometric scale.

Nanothermometry experienced a continuous and unprecedented growth over the period 2005-2012 following, in most examples, the technological trends of sub-micron miniaturization and it is foreseen that this trend will continue for the next coming years.

The work reported here is focused in the temperature determination at the sub-micrometric scales presenting an integrated approach beginning with the synthesis of metal-free silica NPs and reporting temperature determination using silica NPs and ureasil films co-doped with  $\text{Eu}^{3+}$  and  $\text{Tb}^{3+}$ .

Stable, cost-effective, brightly luminescent and metal-free APTES/TEOS NPs (molar percentage of APTES between 33 and 66%) were prepared using the Stöber method without any thermal treatment above 318 K. Contrarily to what has been reported before, it was demonstrated that annealing treatment is dispensable for preparing quite efficient metal-free tunable luminescent organosilica NPs exhibiting quantum yield up to  $0.15 \pm 0.02$ , the highest value reported so far for organosilica NPs without activator metals. The emission spectra and the emission quantum yield of the NPs are stable over time showing no aging effects after exposure to the ambient environment for more than 1 year. Synthesis routes based on the Stöber method without annealing can be therefore used as general approaches to fabricate a wide array of metal-free silica-based NPs with high potential for biolabeling.

Co-doping of the ureasil with lanthanides the **UET-1.3** film was prepared. The material is a versatile di-ureasil hybrid host incorporating  $\text{Eu}^{3+}$  and  $\text{Tb}^{3+}$  lanthanides that demonstrates to be processable as film or as bulk material. Its emission properties are temperature dependent and allow the absolute temperature determination applying an experimental parameter  $\Delta$  defined using the integrated intensities of both lanthanides. The  $\Delta$  dependence on temperature does not present significant hysteresis in the temperature ranges 10-300K or 300-330K. Moreover, repeating the procedure of film/ bulk material production the calibration curve remains unchanged within the experimental error. The sensitivity of the material is above  $0.5\% \cdot K^{-1}$  between 200 and 330 K reaching the maximum value of  $2.0\% \cdot K^{-1}$  at 280K. The processability of this material as film combined with the possibility of measuring temperature motivated a proof of concept of temperature mapping of integrated circuits recovered with an optical layer of **UET-1.3**. The experimental setup uses an optical fibre bundle for excitation and emission recovery that is shown not to limit the spatial resolution of the thermometric system. The finer spatial resolution was achieved for spatial scanning steps lower than half of the fibre inner diameter and corresponds to a value of  $1.4\mu\text{m}$ , the minimum distance between two adjacent points that can be detected by a remote sensing system with temperature LOD of 0.5 K.

The nanothermometer concept is used to produce APTES/TEOS co-doped with  $\text{Eu}^{3+}$  and  $\text{Tb}^{3+}$  with remarkable thermometric properties. These thermometers combine the possibility to fine-tune the emission color as a function of the temperature and  $\text{Eu}^{3+}/\text{Tb}^{3+}$  proportion, and measure temperature using a self-referenced algorithm allowing absolute measurements. The  $\text{Ln}^{3+}$ -co-doped Si-NPs combine relative temperature sensitivities up to  $4.9\% \cdot K^{-1}$  in the temperature range 120-150 K with high photostability for long-term use, presenting a limit of detection of 0.5 K. The multifunctionality was also implemented combining magnetic and luminescent valences in the same NP platform, in a clear step forward when compared with the  $\text{Ln}^{3+}$ -based thermometers presented in the literature. The NPs with mean diameter in the order of hundreds of nanometers present quantum yield up to  $0.37 \pm 0.04$  and demonstrate to be excited using conventional excitation sources, making their use possible in different experimental contexts, without major requirements. Although the temperature range that obeys the criterium  $S_r > 0.5\% \cdot K^{-1}$  is relatively broad (120-190 K) it does not include the physiological temperature range (300-350 K) where nowadays most exciting practical applications appear. This intrinsic limitation was a starting point to the development of nanoparticle platforms with significant sensitivity

in the physiological temperature range. The versatile design of the thermometer that allowed to produce luminescent nanothermometer based on co-doped silica shell can combine different silica host matrixes and ligands. The host matrix and ligand effect was studied looking ahead for the extent of NPs temperature range of operation to the physiological temperature range. The ligands demonstrate to play a central role in the definition of the temperature range of operation of the molecular thermometer. Using acac as  $\beta$ -diketonate ligand and maintaining the same APTES/TEOS host matrix or maintaining the same btfa(bpeta) ligand or changing the host matrix to a short pegylated silane (TESP) instead of APTES the emission properties are modified significantly. The new molecular thermometers allow the temperature mapping of fluids superating the mapping results of the IR camera. The spatial resolution achieved is  $64 \mu m$  and temperature uncertainty is 0.4 degree. The thermometers present sensitivity up to  $0.8\% \cdot K^{-1}$  in the physiological temperature range, demonstrating low hysteresis. These results supports the feasibility of temperature mapping in fluids, with prospective applications in microfluidics and moving fluids in general, with both spatial and temperature resolution in the order of magnitude of the state of the art detectors reported recently.

The driving forces of the future work will be the development of molecular thermometers for the physiological temperature range using luminescent probes adapted to specific applications, such as biological, electrical, etc. For instance, the temperature determination in *in vivo* samples require emission and excitation in the biological window of tissues, *i.e.* 700-1000 nm, with spatial resolution of  $\sim 1 \mu m$ . Highly integrated electronic require high spatial resolution mapping without limitations on the detection and emission wavelengths.

Another important line of research will be the combination of different sensing platforms in the same NP/film. The oxygen sensing appear as the natural step forward in this line, due to the similarity on the detection schemes and the physical principles beyond the oxygen sensing.

The rational design of the molecular thermometers allow the development of sensitive materials working both bellow and above the room temperature. Using the relative sensitivity is possible to compare different materials and techniques allowing a previous estimation of the temperature range of operation and the limit of detection of a temperature measurement. This strategy will undoubtedly lead to qualitatively new progresses in nanothermometry, with consequences in nanotechnology that cannot be yet foreseen.

Literally every week new developments are reported and the efforts to keep the ther-

ometers' database up-to-date is a very challenging task. In what the collaboration of Aveiro/Zaragoza (CiCECO/ICMA) is concern, recent experimental results includes new thermometers designed using the same fundamental principles described in this thesis that present significant improvement in the values of sensitivity in the physiological temperature range.

Using the ureasil matrix, co-doped with  $\text{Eu}^{3+}$  and  $\text{Tb}^{3+}$  and changing the  $\beta$ -diketonate complex to the trifluoroacetylacetonate ligand (tfac), the sensitivity in the physiological temperature range can reach the value of  $S_m = 20\% \cdot K^{-1}$  at  $T_m = 293K$  (figure 8.1). This preliminary result anticipates a temperature limit of detection up to 0.025 K using a detector with 0.5% detection threshold.

The gate to the nanothermometry world has only been slightly opened and there is still plenty of room at the bottom for developing this stimulating new field of research. A major challenge remains with the need to combine efforts from a large number of quite different disciplines such as coordination and supramolecular chemistry, thermodynamics, photophysics, nanotechnology, microelectronics, distinct microscopy techniques, materials design, assembly and integration, and biomedicine.

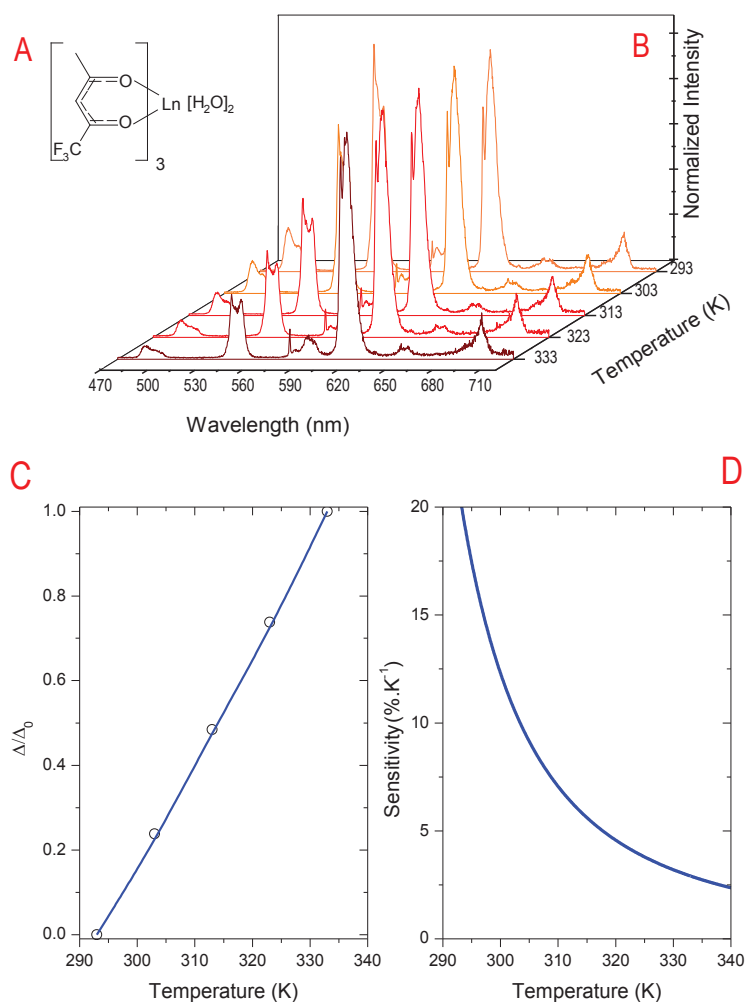


Figure 8.1: Summary of new results using a tfac ligand (structure in A) in the diureasil matrix. Its emission spectra, excited at 330 nm (B), presents a significant change in the temperature range 293-333 K. The relative sensitivity (D) computed from the evolution of the  $\Delta$  parameter (C) is very promising for temperature mapping applications with high accuracy.



# Bibliography

- [1] L. Aigouy, L. Lalouat, M. Mortier, P. Löw, and C. Bergaud. A scanning thermal probe microscope that operates in liquids. *Review of Scientific Instruments*, 82:036106, 2011.
- [2] L. Aigouy, E. Saïdi, L. Lalouat, J. Labéguerie-Egée, M. Mortier, P. Low, and C. Bergaud. Ac thermal imaging of a microwire with a fluorescent nanocrystal: Influence of the near field on the thermal contrast. *Journal of Applied Physics*, 106(7):074301–074301, 2009.
- [3] L. Aigouy, G. Tessier, M. Mortier, and B. Charlot. Scanning thermal imaging of microelectronic circuits with a fluorescent nanoprobe. *Applied Physics Letters*, 87:184105, 2005.
- [4] PM Ajayan, TW Ebbesen, T. Ichihashi, S. Iijima, K. Tanigaki, and H. Hiura. Opening carbon nanotubes with oxygen and implications for filling. *Nature*, 362(6420):522–525, 1993.
- [5] D. Albanesi, M. Martín, F. Trajtenberg, M.C. Mansilla, A. Haouz, P.M. Alzari, D. De Mendoza, and A. Buschiazzo. Structural plasticity and catalysis regulation of a thermosensor histidine kinase. *Proceedings of the National Academy of Sciences*, 106(38):16185–16190, 2009.
- [6] M.A.R.C. Alencar, G.S. Maciel, C.B. de Araújo, and A. Patra.  $er^{3+}$ -doped  $batio_3$  nanocrystals for thermometry: Influence of nanoenvironment on the sensitivity of a fluorescence based temperature sensor. *Applied Physics Letters*, 84(23):4753–4755, 2004.

- [7] SW Allison and GT Gillies. Remote thermometry with thermographic phosphors: Instrumentation and applications. *Review of Scientific Instruments*, 68:2615, 1997.
- [8] M. Asheghi and Y. Yang. *Micro-and Nano-Scale Diagnostic Techniques for Thermometry and Thermal Imaging of Microelectronic and Data Storage Devices*. Microscale Diagnostic Techniques, 2005.
- [9] M. Asheghi and Y. Yang. *Micro-and Nano-Scale Diagnostic Techniques for Thermometry and Thermal Imaging of Microelectronic and Data Storage Devices*, *Microscale Diagnostic Techniques*, volume 4. Springer Verlag, 2005.
- [10] R.G. Aswathy, Y. Yoshida, T. Maekawa, and D.S. Kumar. Near-infrared quantum dots for deep tissue imaging. *Analytical and Bioanalytical Chemistry*, 397(4):1417–1435, 2010.
- [11] V. Augusto, C. Baleizao, M.N. Berberan-Santos, and J.P.S. Farinha. Oxygen-proof fluorescence temperature sensing with pristine C<sub>70</sub> encapsulated in polymer nanoparticles. *Journal of Materials Chemistry*, 20(6):1192–1197, 2009.
- [12] E. Aznar, L. Mondragón, J.V. Ros-Lis, F. Sancenón, M.D. Marcos, R. Martínez-Máñez, J. Soto, E. Pérez-Payá, and P. Amorós. Finely tuned temperature-controlled cargo release using paraffin-capped mesoporous silica nanoparticles. *Angewandte Chemie*, 123(47):11368–11371, 2011.
- [13] L. Bai, PG Schunemann, K. Nagashio, RS Feigelson, NC Giles, et al. Luminescence and optical absorption study of p-type *cdgeas<sub>2</sub>*. *Journal of Physics: Condensed Matter*, 16:1279, 2004.
- [14] G.A. Baker, S.N. Baker, and T.M. McCleskey. Noncontact two-color luminescence thermometry based on intramolecular luminophore cyclization within an ionic liquid. *Chemical Communications*, (23):2932–2933, 2003.
- [15] C. Baleizão, S. Nagl, S.M. Borisov, M. Schäferling, O.S. Wolfbeis, and M.N. Berberan-Santos. An optical thermometer based on the delayed fluorescence of *c*-70. *Chemistry European Journal*, 13(13):3643–3651, 2007.
- [16] S. Banerjee and A. Datta. Photoluminescent silica nanotubes and nanodisks prepared by the reverse micelle sol- gel method. *Langmuir*, 26(2):1172–1176, 2009.

- [17] N. Barbosa III and A.J. Slifka. Spatially and temporally resolved thermal imaging of cyclically heated interconnects by use of scanning thermal microscopy. *Microscopy Research and Technique*, 71(8):579–584, 2008.
- [18] M. Bardosova, M.E. Pemble, I.M. Povey, and R.H. Tredgold. The langmuir-blodgett approach to making colloidal photonic crystals from silica spheres. *Advanced materials*, 22(29):3104–3124, 2010.
- [19] T. Barilero, T. Le Saux, C. Gosse, and L. Jullien. Fluorescent thermometers for dual-emission-wavelength measurements: Molecular engineering and application to thermal imaging in a microsystem. *Analytical Chemistry*, 81(19):7988–8000, 2009.
- [20] R. Beaulac, P.I. Archer, J. van Rijssel, A. Meijerink, and D.R. Gamelin. Exciton storage by  $\text{Mn}^{2+}$  in colloidal  $\text{Mn}^{2+}$ -doped cdse quantum dots. *Nano letters*, 8(9):2949–2953, 2008.
- [21] E. Bichoutskaia, A.M. Popov, Y.E. Lozovik, G.S. Ivanchenko, and N.G. Lebedev. Electromechanical nanothermometer. *Physics Letters A*, 366(4-5):480–486, 2007.
- [22] G. Binnig, H. Rohrer, C. Gerber, and E. Weibel. Tunneling through a controllable vacuum gap. *Applied Physics Letters*, 40(2):178–180, 1982.
- [23] S.M. Borisov, A.S. Vasylevska, C. Krause, and O.S. Wolfbeis. Composite luminescent material for dual sensing of oxygen and temperature. *Advanced Functional Materials*, 16(12):1536–1542, 2006.
- [24] S.M. Borisov and O.S. Wolfbeis. Temperature-sensitive europium (iii) probes and their use for simultaneous luminescent sensing of temperature and oxygen. *Analytical Chemistry*, 78(14):5094–5101, 2006.
- [25] ME Bourg, WE Van Der Veer, AG Guell, and RM Penner. Thermocouples from electrodeposited submicrometer wires prepared by electrochemical step edge decoration. *Chemistry of Materials*, 20(17):5464–5474, 2008.
- [26] A. Bousseksou, G. Molnár, L. Salmon, and W. Nicolazzi. Molecular spin crossover phenomenon: Recent achievements and prospects. *Chemical Society Reviews*, 40(6):3313–3335, 2011.

- [27] C. Bouzigues, T. Gacoin, and A. Alexandrou. Biological applications of rare-earth based nanoparticles. *ACS nano*, 2011.
- [28] T. Brankova, V. Bekiari, and P. Lianos. Photoluminescence from sol-gel organic/inorganic hybrid gels obtained through carboxylic acid solvolysis. *Chemistry of Materials*, 15(9):1855–1859, 2003.
- [29] T. Brintlinger, Y. Qi, K.H. Baloch, D. Goldhaber-Gordon, and J. Cumings. Electron thermal microscopy. *Nano letters*, 8(2):582–585, 2008.
- [30] C. D. S. Brites, P. P. Lima, N. J. O. Silva, A. Millán, V. S. Amaral, F. Palacio, and L. D. Carlos. Thermometry at the nanoscale. *Nanoscale*, in press, 2012.
- [31] C.D.S. Brites, P.P. Lima, N.J.O. Silva, A. Millán, V.S. Amaral, F. Palacio, and L.D. Carlos. Lanthanide-based luminescent molecular thermometers. *New Journal of Chemistry*, 2011.
- [32] C.D.S. Brites, P.P. Lima, N.J.O. Silva, A. Millán, V.S. Amaral, F. Palacio, and L.D. Carlos. Thermometry at the nanoscale using lanthanide-containing organic-inorganic hybrid materials. *Journal of Luminescence*, 2011.
- [33] C.D.S. Brites, P.P. Lima, N.J.O. Silva, A. Millán, V.S. Amaral, F. Palacio, and L.D. Carlos. A luminescent molecular thermometer for long-term absolute temperature measurements at the nanoscale. *Advanced Materials*, 22(40):4499–4504, 2010.
- [34] D.G. Cahill, W.K. Ford, K.E. Goodson, G.D. Mahan, A. Majumdar, H.J. Maris, R. Merlin, and S.R. Phillpot. Nanoscale thermal transport. *Journal of Applied Physics*, 93:793, 2003.
- [35] W. Cai, I.R. Gentle, G.Q. Lu, J.J. Zhu, and A. Yu. Mesoporous silica templated biolabels with releasable fluorophores for immunoassays. *Analytical Chemistry*, 80(14):5401–5406, 2008.
- [36] LD Carlos, V. de Zea Bermudez, R.A.S. Ferreira, L. Marques, and M. Assuncao. Sol-gel derived urea cross-linked organically modified silicates. 2. blue-light emission. *Chemistry of Materials*, 11(3):581–588, 1999.

- [37] L.D. Carlos, R.A.S. Ferreira, V.Z. Bermudez, and S.J.L. Ribeiro. Lanthanide-containing light-emitting organic–inorganic hybrids: A bet on the future. *Advanced Materials*, 21(5):509–534, 2009.
- [38] L.D. Carlos, R.A.S. Ferreira, V. de Zea Bermudez, B. Julián-López, and P. Escribano. Progress on lanthanide-based organic–inorganic hybrid phosphors. *Chemistry Society Reviews*, 40(2):536–549, 2011.
- [39] LD Carlos, R.A.S. Ferreira, RN Pereira, M. Assunção, and V. de Zea Bermudez. White-light emission of amine-functionalized organic-inorganic hybrids: Emitting centers and recombination mechanisms. *The Journal of Physical Chemistry B*, 108(39):14924–14932, 2004.
- [40] L.D. Carlos, R.A. Sá Ferreira, V. de Zea Bermudez, and S.J.L. Ribeiro. Full-color phosphors from amine-functionalized crosslinked hybrids lacking metal activator ions. *Advanced Functional Materials*, 11(2):111–115, 2001.
- [41] L.D. Carlos, RA Sá Ferreira, JP Rainho, and V. de Zea Bermudez. Fine-tuning of the chromaticity of the emission color of organic–inorganic hybrids co-doped with euiii, tbiii, and tmiii. *Advanced Functional Materials*, 12(11-12):819–823, 2002.
- [42] M.G. Cerruti, M. Sauthier, D. Leonard, D. Liu, G. Duscher, D.L. Feldheim, and S. Franzen. Gold and silica-coated gold nanoparticles as thermographic labels for *dna* detection. *Analytical Chemistry*, 78(10):3282–3288, 2006.
- [43] Y. Chan, J.P. Zimmer, M. Stroh, J.S. Steckel, R.K. Jain, and M.G. Bawendi. Incorporation of luminescent nanocrystals into monodisperse core–shell silica microspheres. *Advanced Materials*, 16(23-24):2092–2097, 2004.
- [44] N. Chandrasekharan and L.A. Kelly. A dual fluorescence temperature sensor based on perylene/excimer interconversion. *Journal of the American Chemical Society*, 123(40):9898–9899, 2001.
- [45] CF Chapman, Y. Liu, GJ Sonek, and BJ Tromberg. The use of exogenous fluorescent probes for temperature measurements in single living cells. *Photochemistry and Photobiology*, 62(3):416–425, 1995.

- [46] C.Y. Chen and C.T. Chen. A pnipam-based fluorescent nanothermometer with ratiometric readout. *Chemical Communications*, 2010.
- [47] Yongping Chen and Xingde Li. Near-infrared fluorescent nanocapsules with reversible response to thermal/ph modulation for optical imaging. *Biomacromolecules*, 12(12):4367–4372, 2011.
- [48] N. Chestnoy, TD Harris, R. Hull, and LE Brus. Luminescence and photophysics of cadmium sulfide semiconductor clusters: the nature of the emitting electronic state. *The Journal of Physical Chemistry*, 90(15):3393–3399, 1986.
- [49] PRN Childs, JR Greenwood, and CA Long. Review of temperature measurement. *Review of Scientific Instruments*, 71:2959, 2000.
- [50] L. Chow, D. Zhou, and F. Stevie. Fabrication of nanoscale temperature sensors and heaters, June 14 2005. US Patent 6,905,736.
- [51] S. Chowdhury, C. Maris, F.H.T. Allain, and F. Narberhaus. Molecular basis for temperature sensing by an rna thermometer. *The EMBO Journal*, 25(11):2487–2497, 2006.
- [52] J. Christofferson, K. Maize, Y. Ezzahri, J. Shabani, X. Wang, and A. Shakouri. Microscale and nanoscale thermal characterization techniques. *Journal of Electronic Packaging*, 130:041101, 2008.
- [53] J. Christofferson and A. Shakouri. Thermoreflectance based thermal microscope. *Review of Scientific Instruments*, 76:024903, 2005.
- [54] D. Chu, W.K. Wong, K.E. Goodson, and R.F.W. Pease. Transient temperature measurements of resist heating using nanothermocouples. *Journal of Vacuum Science & Technology B: Microelectronics and Nanometer Structures*, 21:2985, 2003.
- [55] B Cretin, S. Gomes, and P. S. Trannoy, N.and Vairac. *Scanning Thermal Microscopy in Microscale and Nanoscale Heat Transfer - Topics in Applied Physics*, volume 107. Springer-Verlag, 2007.
- [56] Y. Cui, H. Xu, Y. Yue, Z. Guo, J. Yu, Z. Chen, J. Gao, Y. Yang, G. Qian, and B. Chen. A luminescent mixed-lanthanide metal-organic framework thermometer. *Journal of the American Chemical Society*, 2012.

- [57] Z. Dai, WP King, and K. Park. A 100 nanometer scale resistive heater–thermometer on a silicon cantilever. *Nanotechnology*, 20:095301, 2009.
- [58] V. de Zea Bermudez, LD Carlos, and L. Alcácer. Sol-gel derived urea cross-linked organically modified silicates. 1. room temperature mid-infrared spectra. *Chemistry of Materials*, 11(3):569–580, 1999.
- [59] P.S. Dobson, J.M.R. Weaver, D.P. Burt, M.N. Holder, N.R. Wilson, P.R. Unwin, and J.V. Macpherson. Electron beam lithographically-defined scanning electrochemical-atomic force microscopy probes: Fabrication method and application to high resolution imaging on heterogeneously active surfaces. *Physical Chemistry Chemical Physics*, 8(33):3909–3914, 2006.
- [60] C.D.M. Donegá, S.A. Junior, and G.F. De Sá. Europium (iii) mixed complexes with  $\beta$ -diketones and o-phenanthroline-n-oxide as promising light-conversion molecular devices. *Chemical Communications*, (10):1199–1200, 1996.
- [61] N. Dong, M. Pedroni, F. Piccinelli, G. Conti, A. Sbarbati, J.R. Hernandez, L.M. Maestro, M.C. Iglesias de la Cruz, F. Sanz-Rodriguez, A. Juarranz, et al. Nir-to-nir two-photon excited  $\text{CaF}_2$ :  $\text{Tm}^{3+}$ ,  $\text{Yb}^{3+}$  nanoparticles: Multifunctional nanoprobles for highly penetrating fluorescence bio-imaging. *ACS Nano*, 2011.
- [62] J.S. Donner, S.A. Thompson, M.P. Kreuzer, G. Baffou, and R. Quidant. Mapping intracellular temperature using green fluorescent protein. *Nanoletters*, 12(4):2107–2111, 2012.
- [63] P.S. Dorozhkin, S.V. Tovstonog, D. Golberg, J. Zhan, Y. Ishikawa, M. Shiozawa, H. Nakanishi, K. Nakata, and Y. Bando. A liquid-ga-filled carbon nanotube: A miniaturized temperature sensor and electrical switch. *Small*, 1(11):1088–1093, 2005.
- [64] H.M. ElShimy, M. Nakajima, F. Arai, and T. Fukuda. Nano thermal sensors for sensing temperature in water environment. In *IEEE-NANO 2007 – 7th IEEE Conference on Nanotechnology, 2007.*, pages 1045–1049. IEEE, 2007.
- [65] M. Engeser, L. Fabbrizzi, M. Licchelli, and D. Sacchi. A fluorescent molecular thermometer based on the nickel (ii) high-spin/low-spin interconversion. *Chemical Communications*, (13):1191–1192, 1999.

- [66] F. Enrichi, E. Trave, and M. Bersani. Acid synthesis of luminescent amine-functionalized or erbium-doped silica spheres for biological applications. *Journal of Fluorescence*, 18(2):507–511, 2008.
- [67] P. Escribano, B. Julián-López, J. Planelles-Aragó, E. Cordoncillo, B. Viana, and C. Sanchez. Photonic and nanobiophotonic properties of luminescent lanthanide-doped hybrid organic–inorganic materials. *Journal of Materials Chemistry*.
- [68] J. Feng, K. Tian, D. Hu, S. Wang, S. Li, Y. Zeng, Y. Li, and G. Yang. A triarylboron-based fluorescent thermometer: Sensitive over a wide temperature range. *Angewandte Chemie International Edition*, 50(35):8072–8076, 2011.
- [69] L.H. Fischer, G.S. Harms, and O.S. Wolfbeis. Upconverting nanoparticles for nanoscale thermometry. *Angewandte Chemie International Edition*, 50(20):4546–4551, 2011.
- [70] DA Fletcher, KB Crozier, CF Quate, GS Kino, KE Goodson, D. Simanovskii, and DV Palanker. Near-field infrared imaging with a microfabricated solid immersion lens. *Applied Physics Letters*, 77:2109, 2000.
- [71] Q. Fu, G.V.R. Rao, L.K. Ista, Y. Wu, B.P. Andrzejewski, L.A. Sklar, T.L. Ward, and G.P. López. Control of molecular transport through stimuli-responsive ordered mesoporous materials. *Advanced Materials*, 15(15):1262–1266, 2003.
- [72] L. Gao, M.A. Peay, and T.G. Gray. Encapsulation of phosphine-terminated rhenium (iii) chalcogenide clusters in silica nanoparticles. *Chemistry of Materials*, 2010.
- [73] Y. Gao, Y. Bando, et al. Carbon nanothermometer containing gallium. *Nature*, 415(6872):599–599, 2002.
- [74] Y. Gao, Y. Bando, and D. Golberg. Melting and expansion behavior of indium in carbon nanotubes. *Applied Physics Letters*, 81:4133, 2002.
- [75] Y. Gao, Y. Bando, Z. Liu, D. Golberg, and H. Nakanishi. Temperature Measurement Using a Gallium-filled Carbon Nanotube Nanothermometer. *Applied Physics Letters*, 83:2913, 2003.

- [76] A.M. Giuliodori, F. Di Pietro, S. Marzi, B. Masquida, R. Wagner, P. Romby, C.O. Gualerzi, and C.L. Pon. The *cspa* mrna is a thermosensor that modulates translation of the cold-shock protein *cspa*. *Molecular Cell*, 37(1):21–33, 2010.
- [77] D. Golberg, Y. Bando, K. Kurashima, and T. Sato. Synthesis and characterization of ropes made of bn multiwalled nanotubes. *Scripta Materialia*, 44(8-9):1561–1566, 2001.
- [78] NW Gong, MY Lu, CY Wang, Y. Chen, and LJ Chen. Au (si)-filled  $\beta - ga_2o_3$  nanotubes as wide range high temperature nanothermometers. *Applied Physics Letters*, 92(7):073101–073101, 2008.
- [79] K.E. Goodson and M. Asheghi. Near-field optical thermometry. *Microscale Thermophysical Engineering*, 1(3):225–235, 1997.
- [80] C. Gosse, C. Bergaud, and P. Löw. Molecular probes for thermometry in microfluidic devices. *Thermal Nanosystems and Nanomaterials*, pages 301–341, 2009.
- [81] C. Gota, K. Okabe, T. Funatsu, Y. Harada, and S. Uchiyama. Hydrophilic Fluorescent Nanogel Thermometer for Intracellular Thermometry. *Journal of the American Chemical Society*, 131(8):2766–2767, 2009.
- [82] C. Gota, S. Uchiyama, and T. Ohwada. Accurate fluorescent polymeric thermometers containing an ionic component. *Analyst*, 132(2):121–126, 2006.
- [83] C. Gota, S. Uchiyama, T. Yoshihara, S. Tobita, and T. Ohwada. Temperature-dependent fluorescence lifetime of a fluorescent polymeric thermometer, poly (n-isopropylacrylamide), labeled by polarity and hydrogen bonding sensitive 4-sulfamoyl-7-aminobenzofurazan. *The Journal of Physical Chemistry B*, 112(10):2829–2836, 2008.
- [84] E.M. Graham, K. Iwai, S. Uchiyama, A.P. de Silva, S.W. Magennis, and A.C. Jones. Quantitative mapping of aqueous microfluidic temperature with sub-degree resolution using fluorescence lifetime imaging microscopy. *Lab Chip*, 10(10):1267–1273, 2010.

- [85] W.H. Green, K.P. Le, J. Grey, T.T. Au, and M.J. Sailor. White phosphors from a silicate-carboxylate sol-gel precursor that lack metal activator ions. *Science*, 276(5320):1826, 1997.
- [86] C.O. Gualerzi, A. Maria Giuliadori, and C.L. Pon. Transcriptional and post-transcriptional control of cold-shock genes. *Journal of Molecular Biology*, 331(3):527–539, 2003.
- [87] X. Guan, X. Liu, and Z. Su. Preparation and photophysical behaviors of fluorescent chitosan bearing fluorescein: Potential biomaterial as temperature/ph probes. *Journal of Applied Polymer Science*, 104(6):3960–3966, 2007.
- [88] X. Guo, F. Zhang, D.G. Evans, and X. Duan. Layered double hydroxide films: Synthesis, properties and applications. *Chemical Communications*, 46(29):5197–5210, 2010.
- [89] P. Gütllich and H.A. Goodwin. Spin crossover an overall perspective. *Spin Crossover in Transition Metal Compounds I*, pages 1–47, 2004.
- [90] W. Haeberle, M. Pantea, and JKH Hoerber. Nanometer-scale heat-conductivity measurements on biological samples. *Ultramicroscopy*, 106(8):678–686, 2006.
- [91] A. Hammiche, HM Pollock, M. Song, and DJ Hourston. Sub-surface imaging by scanning thermal microscopy. *Measurement Science and Technology*, 7:142, 1996.
- [92] A. Hammiche, M. Reading, HM Pollock, M. Song, and DJ Hourston. Localized thermal analysis using a miniaturized resistive probe. *Review of Scientific Instruments*, 67(12):4268–4274, 1996.
- [93] M. Hartmann. Minimal length scales for the existence of local temperature. *Contemporary Physics*, 47(2):89–102, 2006.
- [94] M. Hartmann, G. Mahler, and O. Hess. Existence of temperature on the nanoscale. *Physical Review Letters*, 93(8):80402, 2004.
- [95] X. He, J. Duan, K. Wang, W. Tan, X. Lin, and C. He. A novel fluorescent label based on organic dye-doped silica nanoparticles for hepg liver cancer cell recognition. *Journal of Nanoscience and Nanotechnology*, 4(6):585–589, 2004.

- [96] A.P. Herrera, M. Rodríguez, M. Torres-Lugo, and C. Rinaldi. Multifunctional magnetite nanoparticles coated with fluorescent thermo-responsive polymeric shells. *Journal of Materials Chemistry*, 18(8):855–858, 2008.
- [97] AL Heyes. On the design of phosphors for high-temperature thermometry. *Journal of Luminescence*, 129(12):2004–2009, 2009.
- [98] S. Höfner and F. Zerbetto. A rna-based nanodevice recording temperature over time. *Chemical Physics*, 369(2):91–95, 2010.
- [99] M. Honda, Y. Saito, N.I. Smith, K. Fujita, and S. Kawata. Nanoscale heating of laser irradiated single gold nanoparticles in liquid. *Optics Express*, 19(13):12375–12383, 2011.
- [100] MA Hopcroft, B. Kim, S. Chandorkar, R. Melamud, M. Agarwal, CM Jha, G. Bahl, J. Salvia, H. Mehta, HK Lee, et al. Using the temperature dependence of resonator quality factor as a thermometer. *Applied Physics Letters*, 91(1):013505, 2007.
- [101] A. Hoshino, K. Fujioka, T. Oku, M. Suga, Y.F. Sasaki, T. Ohta, M. Yasuhara, K. Suzuki, and K. Yamamoto. Physicochemical properties and cellular toxicity of nanocrystal quantum dots depend on their surface modification. *Nano Letters*, 4(11):2163–2169, 2004.
- [102] C.H. Hsia, A. Wuttig, and H. Yang. An accessible approach to preparing water-soluble  $\text{Mn}^{2+}$ -doped (cdsse) zns (core) shell nanocrystals for ratiometric temperature sensing. *ACS Nano*, 2011.
- [103] J. Hu and S. Liu. Responsive polymers for detection and sensing applications: Current status and future developments. *Macromolecules*, 2010.
- [104] H. Huang, S. Delikanli, H. Zeng, D.M. Ferkey, and A. Pralle. Remote control of ion channels and neurons through magnetic-field heating of nanoparticles. *Nature Nanotechnology*, 5(8):602–606, 2010.
- [105] T. Itoh, T. Shichi, T. Yui, H. Takahashi, Y. Inui, and K. Takagi. Reversible color changes in lamella hybrids of poly (diacetylenecarboxylates) incorporated in layered double hydroxide nanosheets. *The Journal of Physical Chemistry B*, 109(8):3199–3206, 2005.

- [106] K. Iwai, K. Hanasaki, and M. Yamamoto. Fluorescence label studies of thermo-responsive poly(n-isopropylacrylamide) hydrogels. *Journal of Luminescence*, 87:1289–1291, 2000.
- [107] K. Iwai, Y. Matsumura, S. Uchiyama, and A.P. de Silva. Development of fluorescent microgel thermometers based on thermo-responsive polymers and their modulation of sensitivity range. *Journal of Materials Chemistry*, 15(27-28):2796–2800, 2005.
- [108] A.M. Jakob and T.A. Schmedake. A novel approach to monodisperse, luminescent silica spheres. *Chemistry of Materials*, 18(14):3173–3175, 2006.
- [109] J.M. Jean and K.B. Hall. 2-aminopurine fluorescence quenching and lifetimes: Role of base stacking. *Proceedings of the National Academy of Sciences*, 98(1):37, 2001.
- [110] J.M. Jean and K.B. Hall. 2-aminopurine electronic structure and fluorescence properties in dna. *Biochemistry*, 41(44):13152–13161, 2002.
- [111] U. Jeong, Y. Wang, M. Ibisate, and Y. Xia. Some new developments in the synthesis, functionalization, and utilization of monodisperse colloidal spheres. *Advanced Functional Materials*, 15(12):1907–1921, 2005.
- [112] Y. Jin, S. Lohstreter, D.T. Pierce, J. Parisien, M. Wu, C. Hall Iii, and J.X. Zhao. Silica nanoparticles with continuously tunable sizes: synthesis and size effects on cellular contrast imaging. *Chemistry of Materials*, 20(13):4411–4419, 2008.
- [113] P. Jorge, M.A. Martins, T. Trindade, J.L. Santos, and F. Farahi. Optical fiber sensing using quantum dots. *Sensors*, 7(12):3489–3534, 2007.
- [114] W. Jung, Y.W. Kim, D. Yim, and J.Y. Yoo. Microscale surface thermometry using *su8/rhodamine - b* thin layer. *Sensors and Actuators A: Physical*, 2011.
- [115] J. Kai, M.C.F.C. Felinto, L.A.O. Nunes, O.L. Malta, and H.F. Brito. Intermolecular energy transfer and photostability of luminescence-tuneable multicolour pmma films doped with lanthanide- $\beta$ -diketonate complexes. *Journal of Materials Chemistry*, 21(11):3796–3802, 2011.
- [116] Y.S. Kang, S. Risbud, J.F. Rabolt, and P. Stroeve. Synthesis and characterization of nanometer-size  $\text{Fe}_3\text{O}_4$  and  $\gamma - \text{Fe}_2\text{O}_3$  particles. *Chemistry of Materials*, 8(9):2209–2211, 1996.

- [117] M. Karnebogen, D. Singer, M. Kallerhoff, and R.H. Ringert. Microcalorimetric investigations on isolated tumorous and non-tumorous tissue samples. *Thermochimica Acta*, 229:147–155, 1993.
- [118] S. Katagiri, K. Manseki, Y. Tsukahara, K. Mitsuo, and Y. Wada. Luminescent Polymer Film Containing Tetranuclear Eu(III) Complex as Temperature-Sensing Device. *Journal of Alloys and Compounds*, 453(1-2):L1–L3, 2008.
- [119] N. Kawamoto, M.S. Wang, X. Wei, D.M. Tang, Y. Murakami, D. Shindo, M. Mitome, and D. Golberg. Local temperature measurements on nanoscale materials using a movable nanothermocouple assembled in a transmission electron microscope. *Nanotechnology*, 22:485707, 2011.
- [120] AH Khalid and K. Kontis. 2d surface thermal imaging using rise-time analysis from laser-induced luminescence phosphor thermometry. *Measurement Science and Technology*, 20:025305, 2009.
- [121] G.E. Khalil, K. Lau, G.D. Phelan, B. Carlson, M. Gouterman, J.B. Callis, and L.R. Dalton. Europium  $\beta$ -diketonate Temperature Sensors: Effects of Ligands, Matrix, and Concentration. *Review of Scientific Instruments*, 75(1):192–206, 2004.
- [122] G. Kickelbick and Ebooks Corporation. *Hybrid materials: synthesis, characterization, and applications*. Wiley-vch Weinheim, Germany, 2007.
- [123] K.H. Kim, D.L. Nguyen, H. Lim, P.T. Nga, Y.H. Cho, et al. Shell layer dependence of photoblinking in cdse/znse/zns quantum dots. *Applied Physics Letters*, 98:012109, 2011.
- [124] S. Kim, K.C. Kim, and K.D. Kihm. Near-field thermometry sensor based on the thermal resonance of a microcantilever in aqueous medium. *Sensors*, 7(12):3156–3165, 2007.
- [125] B. Klinkert and F. Narberhaus. Microbial thermosensors. *Cellular and Molecular Life Sciences*, 66(16):2661–2676, 2009.
- [126] P. Kolodner and J.A. Tyson. Remote thermal imaging with 0.7- $\mu$ m spatial resolution using temperature-dependent fluorescent thin films. *Applied Physics Letters*, 42(1):117–119, 1983.

- [127] D. Kong, C. Zhang, Z. Xu, G. Li, Z. Hou, and J. Lin. Tunable photoluminescence in monodisperse silica spheres. *Journal of Colloid and Interface Science*, 352(2):278–284, 2010.
- [128] J. Kortmann, S. Sczodrok, J. Rinnenthal, H. Schwalbe, and F. Narberhaus. Translation on demand by a simple rna-based thermosensor. *Nucleic Acids Research*, 39(7):2855–2868, 2011.
- [129] M.E. Köse, B.F. Carroll, and K.S. Schanze. Preparation and spectroscopic properties of multiluminophore luminescent oxygen and temperature sensor films. *Langmuir*, 21(20):9121–9129, 2005.
- [130] M.E. Köse, A. Omar, A. Christopher, B.F. Carroll, and K.S. Schanze. Principal component analysis calibration method for dual-luminophore oxygen and temperature sensor films: Application to luminescence imaging. *Langmuir*, 21(20):9110–9120, 2005.
- [131] J. Lai, M. Chandrachood, A. Majumda, and JP Carrejo. Thermal detection of device failure by atomic force microscopy. *Electron Device Letters, IEEE*, 16(7):312–315, 1995.
- [132] Y. Lan, H. Wang, X. Chen, D. Wang, G. Chen, and Z. Ren. Nanothermometer using single crystal silver nanospheres. *Advanced Materials*, 21(47):4839–4844, 2009.
- [133] B. Lebeau and P. Innocenzi. Hybrid materials for optics and photonics. *Chemistry Society Reviews*, 40(2):886–906, 2011.
- [134] J. Lee, A.O. Govorov, and N.A. Kotov. Nanoparticle assemblies with molecular springs: A nanoscale thermometer. *Angewandte Chemie*, 117(45):7605–7608, 2005.
- [135] J. Lee and N.A. Kotov. Thermometer Design at the Nanoscale. *Nano Today*, 2(1):48–51, 2007.
- [136] S.Y. Lee, S. Lee, I.C. Youn, D.K. Yi, Y.T. Lim, B.H. Chung, J.F. Leary, I.C. Kwon, K. Kim, and K. Choi. A near-infrared fluorescence-based optical thermosensor. *Chemistry-A European Journal*, 15(25):6103–6106, 2009.

- [137] S. Lefèvre and S. Volz.  $3\omega$ -scanning thermal microscope. *Review of Scientific Instruments*, 76(3):033701–033701, 2005.
- [138] J. Li, X. Hong, Y. Liu, D. Li, Y.W. Wang, J.H. Li, Y.B. Bai, and T.J. Li. Highly photoluminescent *cdte*/poly (n-isopropylacrylamide) temperature-sensitive gels. *Advanced Materials*, 17(2):163–166, 2005.
- [139] S. Li, K. Zhang, J.M. Yang, L. Lin, and H. Yang. Single quantum dots as local temperature markers. *Nano letters*, 7(10):3102–3105, 2007.
- [140] Y. Li, Y. Bando, and D. Golberg. Single-crystalline *in<sub>2</sub>o<sub>3</sub>* nanotubes filled with in. *Advanced Materials*, 15(7-8):581–585, 2003.
- [141] Y. Li, Y. Bando, and D. Golberg. Indium-assisted growth of aligned ultra-long silica nanotubes. *Advanced Materials*, 16(1):37–40, 2004.
- [142] YB Li, Y. Bando, D. Golberg, and ZW Liu. Ga-filled single-crystalline mgo nanotube: Wide-temperature range nanothermometer. *Applied Physics Letters*, 83:999, 2003.
- [143] D.R. Lide. Crc handbook of physics and chemistry. *CRC Press, Boca Raton, USA*, 76:1995–1996, 2001.
- [144] P.P. Lima, F.A. Almeida Paz, R.A.S. Ferreira, V. de Zea Bermudez, and L.D. Carlos. Ligand-assisted rational design and supramolecular tectonics toward highly luminescent *eu<sup>3+</sup>*-containing organic-inorganic hybrids. *Chemistry of Materials*, 21(21):5099–5111, 2009.
- [145] PP Lima, RAS Ferreira, SA Júnior, OL Malta, and LD Carlos. Terbium (iii)-containing organic-inorganic hybrids synthesized through hydrochloric acid catalysis. *Journal of Photochemistry and Photobiology A: Chemistry*, 201(2-3):214–221, 2009.
- [146] P.P. Lima, S.S. Nobre, R.O. Freire, A. Severino, R.A.S. Ferreira, U. Pischel, O.L. Malta, and L.D. Carlos. Energy transfer mechanisms in organic-inorganic hybrids incorporating europium (iii): A quantitative assessment by light emission spectroscopy. *The Journal of Physical Chemistry C*, 111(47):17627–17634, 2007.

- [147] P.P. Lima, S.S. Nobre, R.O. Freire, A. Severino, R.A.S. Ferreira, U. Pischel, O.L. Malta, and L.D. Carlos. Energy transfer mechanisms in organic-inorganic hybrids incorporating europium (iii): a quantitative assessment by light emission spectroscopy. *The Journal of Physical Chemistry C*, 111(47):17627–17634, 2007.
- [148] P.P. Lima, R.A. Sá Ferreira, R.O. Freire, F.A. Almeida Paz, L. Fu, S. Alves Jr, L.D. Carlos, and O.L. Malta. Spectroscopic study of a uv-photostable organic-inorganic hybrids incorporating an  $eu^{3+}$   $\beta$ -diketonate complex. *ChemPhysChem*, 7(3):735–746, 2006.
- [149] Y. Lin, L. Zhang, W. Yao, H. Qian, D. Ding, W. Wu, and X. Jiang. Water-soluble chitosan-quantum dot hybrid nanospheres toward bioimaging and biolabeling. *ACS Applied Materials & Interfaces*, 2011.
- [150] W. Liu and B. Yang. Thermography techniques for integrated circuits and semiconductor devices. *Sensor Review*, 27(4):298–309, 2007.
- [151] Z. Liu, Y. Bando, M. Mitome, and J. Zhan. Unusual freezing and melting of gallium encapsulated in carbon nanotubes. *Physical Review Letters*, 93(9):95504, 2004.
- [152] B.B. Lowell and B.M. Spiegelman. Towards a molecular understanding of adaptive thermogenesis. *Nature*, 404(6778):652–660, 2000.
- [153] K. Luo, Z. Shi, J. Lai, and A. Majumdar. Nanofabrication of sensors on cantilever probe tips for scanning multiprobe microscopy. *Applied Physics Letters*, 68:325, 1996.
- [154] J.M. Lupton. A molecular thermometer based on long-lived emission from platinum octaethyl porphyrin. *Applied Physics Letters*, 81:2478, 2002.
- [155] L.M. Maestro, C. Jacinto, U.R. Silva, F. Vetrone, J.A. Capobianco, D. Jaque, and J.G. Solé. Cdte quantum dots as nanothermometers: Towards highly sensitive thermal imaging. *Small*, 2011.
- [156] LM Maestro, JE Ramírez-Hernández, N. Bogdan, JA Capobianco, F. Vetrone, J.G. Solé, and D. Jaque. Deep tissue bio-imaging using two-photon excited cdte fluorescent quantum dots working within the biological window. *Nanoscale*, 4(1):298–302, 2011.

- [157] L.M. Maestro, E.M. Rodríguez, F.S. Rodríguez, M.C.I. la Cruz, A. Juarranz, R. Nacache, F. Vetrone, D. Jaque, J.A. Capobianco, and J.G. Sole´. Cdse quantum dots for two-photon fluorescence thermal imaging. *Nano Letters*, 2010.
- [158] A. Majumdar. Scanning thermal microscopy. *Annual Review of Materials Science*, 29(1):505–585, 1999.
- [159] A. Majumdar, JP Carrejo, and J. Lai. Thermal imaging using the atomic force microscope. *Applied Physics Letters*, 62(20):2501–2503, 1993.
- [160] H. Mao, T. Yang, and P.S. Cremer. A microfluidic device with a linear temperature gradient for parallel and combinatorial measurements. *Journal of the American Chemical Society*, 124(16):4432–4435, 2002.
- [161] K.M. McCabe and M. Hernandez. Molecular thermometry. *Pediatric Research*, 67(5):469–475, 2010.
- [162] E.J. McLaurin, V.A. Vlaskin, and D.R. Gamelin. Water-soluble dual-emitting nanocrystals for ratiometric optical thermometry. *Journal of the American Chemical Society*, 2011.
- [163] I.L. Medintz, H.T. Uyeda, E.R. Goldman, and H. Mattoussi. Quantum dot bioconjugates for imaging, labelling and sensing. *Nature Materials*, 4(6):435–446, 2005.
- [164] BK Meyer, H. Alves, DM Hofmann, W. Kriegseis, D. Forster, F. Bertram, J. Christen, A. Hoffmann, M. Straßburg, M. Dworzak, et al. Bound exciton and donor–acceptor pair recombinations in zno. *Physica Status Solidi (B)*, 241(2):231–260, 2004.
- [165] R.B. Mikkelsen and D.F.H. Wallach. Temperature sensitivity of the erythrocyte membrane potential as determined by cyanine dye fluorescence. *Cell Biology International Reports*, 1(1):51–55, 1977.
- [166] G. Mills, H. Zhou, A. Midha, L. Donaldson, and JMR Weaver. Scanning thermal microscopy using batch fabricated thermocouple probes. *Applied Physics Letters*, 72:2900, 1998.
- [167] M. Mitsuishi, S. Kikuchi, T. Miyashita, and Y. Amao. Characterization of an ultra-thin polymer optode and its application to temperature sensors based on luminescent europium complexes. *Journal Materials Chemistry*, 13(12):2875–2879, 2003.

- [168] H.O. Müller, A. Hädicke, and W. Krech. On thermometer operation of ultrasmall tunnel junctions. *Physica Status Solidi (B)*, 188(2):667–677, 1995.
- [169] O. Nakabeppu, M. Chandrachood, Y. Wu, J. Lai, and A. Majumdar. Scanning thermal imaging microscopy using composite cantilever probes. *Applied Physics Letters*, 66(6):694–696, 1995.
- [170] M. Nakamura, S. Ozaki, M. Abe, T. Matsumoto, and K. Ishimura. One-pot synthesis and characterization of dual fluorescent thiol-organosilica nanoparticles as non-photoblinking quantum dots and their applications for biological imaging. *Journal of Materials Chemistry*, 2011.
- [171] T. Nakamura, Y. Yamada, H. Yamada, and K. Yano. A novel route to luminescent opals for controlling spontaneous emission. *Journal of Materials Chemistry*, 19(37):6699–6705, 2009.
- [172] F. Narberhaus. mrna-mediated detection of environmental conditions. *Archives of Microbiology*, 178(6):404–410, 2002.
- [173] F. Narberhaus, T. Waldminghaus, and S. Chowdhury. Rna thermometers. *FEMS Microbiology Reviews*, 30(1):3–16, 2006.
- [174] VK Natrajan and KT Christensen. Two-color laser-induced fluorescent thermometry for microfluidic systems. *Measurement Science and Technology*, 20:015401, 2009.
- [175] J. Neupert and R. Bock. Designing and using synthetic rna thermometers for temperature-controlled gene expression in bacteria. *Nature Protocols*, 4(9):1262–1273, 2009.
- [176] J. Neupert, D. Karcher, and R. Bock. Design of simple synthetic rna thermometers for temperature-controlled gene expression in escherichia coli. *Nucleic Acids Research*, 36(19):e124–e124, 2008.
- [177] S.S. Nobre, X. Cattoen, R.A.S. Ferreira, M.W.C. Man, and L.D. Carlos. Efficient spectrally dynamic blue-to-green emission of bipyridine-based bridged silsesquioxanes for solid-state lighting. *Physica Status Solidi (RRL)–Rapid Research Letters*, 4(3-4):55–57, 2010.

- [178] S.S. Nobre, P.P. Lima, L. Mafra, R.A.S. Ferreira, R.O. Freire, L. Fu, U. Pischel, V. de Zea Bermudez, O.L. Malta, and L.D. Carlos. Energy transfer and emission quantum yields of organic-inorganic hybrids lacking metal activator centers. *The Journal of Physical Chemistry C*, 111(8):3275–3284, 2007.
- [179] K. Okabe, N. Inada, C. Gota, Y. Harada, T. Funatsu, and S. Uchiyama. Intracellular temperature mapping with a fluorescent polymeric thermometer and fluorescence lifetime imaging microscopy. *Nature Communications*, 3:705, 2012.
- [180] Y. Okamura and T.L. Kohler. Fabrication of nanoscale thermoelectric devices, November 29 2005. US Patent 6,969,679.
- [181] Y. Ou, V. Jokubavicius, S. Kamiyama, C. Liu, R.W. Berg, M. Linnarsson, R. Yakimova, M. Syväjärvi, and H. Ou. Donor-acceptor-pair emission characterization in n-b doped fluorescent sic. *Optical Materials Express*, 1(8):1439–1446, 2011.
- [182] F Palacio, A Millán, N. J. O. Silva, L. D. Carlos, V. S. Amaral, P. P. Lima, and C.D. S. Brites. Luminescent molecular thermometer. *Spain Patent P200930367*, 2009.
- [183] A. Pavlov. Nanoscale measurements of the absolute temperature from the tunneling of the free electron gas. *Applied Physics Letters*, 85:2095, 2004.
- [184] H. Peng, M.I.J. Stich, J. Yu, L. Sun, L.H. Fischer, and O.S. Wolfbeis. Luminescent Europium (III) Nanoparticles for Sensing and Imaging of Temperature in the Physiological Range. *Advanced Materials*, 22(6):716–719, 2010.
- [185] H.S. Peng, S.H. Huang, and O.S. Wolfbeis. Ratiometric fluorescent nanoparticles for sensing temperature. *Journal of Nanoparticle Research*, pages 1–5, 2010.
- [186] Yuanzhe Piao, Andrew Burns, Jaeyun Kim, Ulrich Wiesner, and Taeghwan Hyeon. Designed fabrication of silica-based nanostructured particle systems for nanomedicine applications (adv. funct. mater. 23/2008). *Advanced Functional Materials*, 18(23):n/a–n/a, 2008.
- [187] C. Pietsch, R. Hoogenboom, and U.S. Schubert. Soluble polymeric dual sensor for temperature and ph value. *Angewandte Chemie*, 121(31):5763–5766, 2009.

- [188] C. Pietsch, R. Hoogenboom, and U.S. Schubert. Pmma based soluble polymeric temperature sensors based on ucst transition and solvatochromic dyes. *Polymer Chemistry*, 1(7):1005–1008, 2010.
- [189] C. Pietsch, A. Vollrath, R. Hoogenboom, and U.S. Schubert. A fluorescent thermometer based on a pyrene-labeled thermoresponsive polymer. *Sensors*, 10(9):7979–7990, 2010.
- [190] R.J. Pylkki, P.J. Moyer, and P.E. West. Scanning near-field optical microscopy and scanning thermal microscopy. *Japanese Journal of Applied Physics*, 33(part 1):3785–3790, 1994.
- [191] C. Quintero, G. Molnár, L. Salmon, A. Tokarev, C. Bergaud, and A. Bousseksou. Design of fluorescent spin-crossover nanoparticles for thermometry applications. In *Thermal Investigations of ICs and Systems (THERMINIC), 2010 16th International Workshop on*, pages 1–5. IEEE, 2010.
- [192] A. Rabhiou, J. Feist, A. Kempf, S. Skinner, and A. Heyes. Phosphorescent thermal history sensors. *Sensors and Actuators, A: Physical*, 169(1):18–26, 2011.
- [193] D. Ross, M. Gaitan, and L.E. Locascio. Temperature measurement in microfluidic systems using a temperature-dependent fluorescent dye. *Analytical Chemistry*, 73(17):4117–4123, 2001.
- [194] D.M. Roundhill. *Photochemistry and Photophysics of Metal Complexes*. Plenum Press New York, 1994.
- [195] PG Royall, VL Kett, CS Andrews, and DQM Craig. Identification of crystalline and amorphous regions in low molecular weight materials using microthermal analysis. *The Journal of Physical Chemistry B*, 105(29):7021–7026, 2001.
- [196] RA Sá-Ferreira, AL Ferreira, and LD Carlos. Modeling the emission red-shift in amorphous semiconductors and in organic-inorganic hybrids using extended multiple trapping. *The European Physical Journal B-Condensed Matter and Complex Systems*, 50(3):371–378, 2006.
- [197] S. Sadat, A. Tan, Y.J. Chua, and P. Reddy. Nanoscale thermometry using point contact thermocouples. *Nanoletters*, 10(7):2613–2617, 2010.

- [198] S. Sadeghi. Plasmonic meta-resonance nanosensors: Ultra-sensitive tunable optical sensors based on nanoparticle molecules. *IEEE Transactions on Nanotechnology*, (99):1–1, 2011.
- [199] E. Saïdi, N. Babinet, L. Lalouat, J. Lesueur, L. Aigouy, S. Volz, J. Labéguerie-Eg ea, and M. Mortier. Tuning temperature and size of hot spots and hot-spot arrays. *Small*, 7(2):259–264, 2011.
- [200] E. Saïdi, B. Samson, L. Aigouy, S. Volz, P. L ow, C. Bergaud, and M. Mortier. Scanning thermal imaging by near-field fluorescence spectroscopy. *Nanotechnology*, 20:115703, 2009.
- [201] V. Salgueiri no-Maceira, M.A. Correa-Duarte, M. Spasova, L.M. Liz-Marz an, and M. Farle. Composite silica spheres with magnetic and luminescent functionalities. *Advanced Functional Materials*, 16(4):509–514, 2006.
- [202] L. Salmon, G. Moln ar, D. Zitouni, C. Quintero, C. Bergaud, J.C. Micheau, and A. Bousseksou. A novel approach for fluorescent thermometry and thermal imaging purposes using spin crossover nanoparticles. *Journal Material Chemistry*, 20(26):5499–5503, 2010.
- [203] R. Samy, T. Glawdel, and C.L. Ren. Method for microfluidic whole-chip temperature measurement using thin-film poly (dimethylsiloxane)/rhodamine b. *Analytical Chemistry*, 80(2):369–375, 2008.
- [204] C. Sanchez, P. Belleville, M. Popall, and L. Nicole. Applications of advanced hybrid organic–inorganic nanomaterials: from laboratory to market. *Chemistry Society Reviews*, 40(2):696–753, 2011.
- [205] C. Sanchez, B. Juli an, P. Belleville, and M. Popall. Applications of hybrid organic–inorganic nanocomposites. *Journal of Materials Chemistry*, 15(35-36):3559–3592, 2005.
- [206] R.A. Sayer, S. Kim, A.D. Franklin, S. Mohammadi, and T.S. Fisher. Shot noise thermometry for thermal characterization of templated carbon nanotubes. *Components and Packaging Technologies, IEEE Transactions on*, 33(1):178–183, 2010.

- [207] HG Schild. Poly (n-isopropylacrylamide): Experiment, theory and application. *Progress in Polymer Science*, 17(2):163–249, 1992.
- [208] A. Schlossbauer, S. Warncke, P.M.E. Gramlich, J. Kecht, A. Manetto, T. Carell, and T. Bein. A programmable dna-based molecular valve for colloidal mesoporous silica. *Angewandte Chemie International Edition*, 49(28):4734–4737, 2010.
- [209] DR Schmidt, CS Yung, and AN Cleland. Nanoscale radio-frequency thermometry. *Applied Physics Letters*, 83:1002, 2003.
- [210] P. Shah and M.A. Gilchrist. Is thermosensing property of rna thermometers unique? *PloS One*, 5(7):e11308, 2010.
- [211] E. Shapira, D. Marchak, A. Tsukernik, and Y. Selzer. Segmented metal nanowires as nanoscale thermocouples. *Nanotechnology*, 19:125501, 2008.
- [212] L. Shi, O. Kwon, A.C. Miner, and A. Majumdar. Design and batch fabrication of probes for sub-100 nm scanning thermal microscopy. *Journal of Microelectromechanical Systems*, 10(3):370–378, 2001.
- [213] Y. Shiraishi, R. Miyamoto, and T. Hirai. A hemicyanine-conjugated copolymer as a highly sensitive fluorescent thermometer. *Langmuir*, 24(8):4273–4279, 2008.
- [214] T. Shiraki, A. Dawn, Y. Tsuchiya, and S. Shinkai. Thermo-and solvent-responsive polymer complex created from supramolecular complexation between a helix-forming polysaccharide and a cationic polythiophene. *Journal of the American Chemical Society*, 2010.
- [215] S.K. Singh, K. Kumar, and SB Rai.  $er^{3+} / yb^{3+}$  codoped  $gd_2o_3$  nano-phosphor for optical thermometry. *Sensors and Actuators A: Physical*, 149(1):16–20, 2009.
- [216] SK Singh, K. Kumar, and SB Rai. Multifunctional  $Er^{3+}/Yb^{3+}$  Codoped  $Gd_2O_3$  Nanocrystalline Phosphor Synthesized Through Optimized Combustion Route. *Applied Physics B: Lasers and Optics*, 94:165–173, 2009.
- [217] R.B. Soriano, E. Kpatcha, A.M. Jakob, J.W. Merkert, C.M. Carlin, and T.A. Schmedake. Long-lifetime emission in luminescent colloidal silica. *Applied Physics Letters*, 91:091909, 2007.

- [218] L. Spietz, KW Lehnert, I. Siddiqi, and RJ Schoelkopf. Primary electronic thermometry using the shot-noise of a tunnel junction. *Science*, 300(5627):1929–1932, 2003.
- [219] L. Spietz, RJ Schoelkopf, and P. Pari. Shot noise thermometry down to 10 mk. *Applied Physics Letters*, 89:183123, 2006.
- [220] M.I.J. Stich, L.H. Fischer, and O.S. Wolfbeis. Multiple fluorescent chemical sensing and imaging. *Chem. Soc. Rev.*, 39(8):3102–3114, 2010.
- [221] W. Stober, A. Fink, and E. Bohn. Controlled growth of monodisperse silica spheres in the micron size range\* 1. *Journal of Colloid and Interface Science*, 26(1):62–69, 1968.
- [222] M. Stopka, L. Hadjiiski, E. Oesterschulze, and R. Kassing. Surface investigations by scanning thermal microscopy. *Journal of Vacuum Science & Technology B: Microelectronics and Nanometer Structures*, 13(6):2153–2156, 1995.
- [223] H. Sugiyama and I. Saito. Theoretical studies of gg-specific photocleavage of dna via electron transfer: Significant lowering of ionization potential and 5'-localization of homo of stacked gg bases in b-form dna. *Journal of the American Chemical Society*, 118(30):7063–7068, 1996.
- [224] L.N. Sun, J. Yu, H. Peng, J.Z. Zhang, L.Y. Shi, and O.S. Wolfbeis. Temperature-sensitive luminescent nanoparticles and films based on a terbium (iii) complex probe. *The Journal of Physical Chemistry C*, 114(29):12642–12648, 2010.
- [225] M. Suzuki, V. Tseeb, K. Oyama, and S. Ishiwata. Microscopic detection of thermogenesis in a single hela cell. *Biophysical Journal*, 92(6):L46–L48, 2007.
- [226] P. Tallury, K. Payton, and S. Santra. Silica-based multimodal/multifunctional nanoparticles for bioimaging and biosensing applications. *Nanomedicine*, 3(4):579–592, 2008.
- [227] C.L. Tan and Q.M. Wang. Photophysical studies of novel lanthanide (eu<sup>3+</sup> and tb<sup>3+</sup>) luminescent hydrogels. *Inorganic Chemistry Communications*, 2011.

- [228] L. Tang, J.K. Jin, A. Qin, W.Z. Yuan, Y. Mao, J. Mei, J.Z. Sun, and B.Z. Tang. A fluorescent thermometer operating in aggregation-induced emission mechanism: probing thermal transitions of pnipam in water. *Chemical Communications*, (33):4974–4976, 2009.
- [229] R. Tashiro and H. Sugiyama. A nanothermometer based on the different  $\pi$  stackings of b-and z-dna. *Angewandte Chemie International Edition*, 42(48):6018–6020, 2003.
- [230] G. Tessier, M. Bardoux, C. Boué, C. Filloy, and D. Fournier. Back side thermal imaging of integrated circuits at high spatial resolution. *Applied Physics Letters*, 90(17):171112–171112, 2007.
- [231] D. Teyssieux, L. Thiery, and B. Cretin. Near-infrared thermography using a charge-coupled device camera: Application to microsystems. *Review of Scientific Instruments*, 78:034902, 2007.
- [232] V.K. Tikhomirov, K. Driesen, V.D. Rodriguez, P. Gredin, M. Mortier, and V.V. Moshchalkov. Optical nanoheater based on the  $yb^{3+}$ - $er^{3+}$  co-doped nanoparticles. *Optics Express*, 17(14):11794–11798, Jul 2009.
- [233] A.T. Tilke, L. Pescini, H. Lorenz, and R.H. Blick. Fabrication and transport characterization of a primary thermometer formed by coulomb islands in a suspended silicon nanowire. *Applied Physics Letters*, 82:3773, 2003.
- [234] S. Uchiyama, N. Kawai, A.P. de Silva, and K. Iwai. Fluorescent polymeric and logic gate with temperature and ph as inputs. *Journal of the American Chemical Society*, 126(10):3032–3033, 2004.
- [235] S. Uchiyama, A. Prasanna de Silva, and K. Iwai. Luminescent molecular thermometers. *Journal of Chemical Education*, 83(5):720, 2006.
- [236] L. Vaccaro, G. Vaccaro, S. Agnello, G. Buscarino, and M. Cannas. Wide range excitation of visible luminescence in nanosilica. *Solid State Communications*, 150(45-46):2278–2280, 2010.
- [237] W.G. Van Sark, P.L.T.M. Frederix, A.A. Bol, H.C. Gerritsen, and A. Meijerink. Blueing, bleaching, and blinking of single cdse/zns quantum dots. *ChemPhysChem*, 3(10):871–879, 2002.

- [238] F. Vetrone, R. Naccache, A. Zamarrón, A. Juarranz de la Fuente, F. Sanz-Rodríguez, L. Martinez Maestro, E. Martín Rodríguez, D. Jaque, J. García Solé, and J.A. Capobianco. Temperature sensing using fluorescent nanothermometers. *ACS nano*, 4(6):3254–3258, 2010.
- [239] V.A. Vlaskin, N. Janssen, J. Van Rijssel, R. Beaulac, and D.R. Gamelin. Tunable dual emission in doped semiconductor nanocrystals. *Nano Letters*, 2010.
- [240] A. Vyalikh, A.U.B. Wolter, S. Hampel, D. Haase, M. Ritschel, A. Leonhardt, H.J. Grafe, A. Taylor, K. Krämer, B. Büchner, et al. A carbon-wrapped nanoscaled thermometer for temperature control in biological environments. *Nanomedicine*, 3(3):321–327, 2008.
- [241] T. Waldminghaus, J. Kortmann, S. Gesing, and F. Narberhaus. Generation of synthetic rna-based thermosensors. *Biological Chemistry*, 389(10):1319, 2008.
- [242] G.W. Walker, V.C. Sundar, C.M. Rudzinski, A.W. Wun, M.G. Bawendi, and D.G. Nocera. Quantum-dot optical temperature probes. *Applied Physics Letters*, 83:3555, 2003.
- [243] X. Wan and S. Liu. Fluorescent water-soluble responsive polymers site-specifically labeled with fret dyes possessing ph-and thermo-modulated multicolor fluorescence emissions as dual ratiometric probes. *Journal of Materials Chemistry*, 2011.
- [244] C. Wang, R. Xu, W. Tian, X. Jiang, Z. Cui, M. Wang, H. Sun, K. Fang, and N. Gu. Determining intracellular temperature at single-cell level by a novel thermocouple method. *Cell Research*, 2011.
- [245] C.Y. Wang and L.J. Chen. Nanothermometers for transmission electron microscopy–fabrication and characterization. *European Journal of Inorganic Chemistry*, 2010(27):4298–4303, 2010.
- [246] C.Y. Wang, N.W. Gong, and L.J. Chen. High-sensitivity solid-state *pb* (core)/*zno* (shell) nanothermometers fabricated by a facile galvanic displacement method. *Advanced Materials*, 20(24):4789–4792, 2008.

- [247] D. Wang, R. Miyamoto, Y. Shiraishi, and T. Hirai. Bodipy-conjugated thermoresponsive copolymer as a fluorescent thermometer based on polymer microviscosity. *Langmuir*, 25(22):13176–13182, 2009.
- [248] F. Wang, W.B. Tan, Y. Zhang, X. Fan, and M. Wang. Luminescent nanomaterials for biological labelling. *Nanotechnology*, 17:R1, 2006.
- [249] J. Wang and L. Huang. Thermometry based on phonon confinement effect in nanoparticles. *Applied Physics Letters*, 98:113102, 2011.
- [250] L. Wang, M.C. Estévez, Meghan O’Donoghue, , and W. Tan. Fluorophore-free luminescent organosilica nanoparticles. *Langmuir*, 24(5):1635–1639, 2008.
- [251] L. Wang, W. Zhao, and W. Tan. Bioconjugated silica nanoparticles: Development and applications. *Nano Research*, 1(2):99–115, 2008.
- [252] S. Wang, S. Westcott, and W. Chen. Nanoparticle luminescence thermometry. *The Journal of Physical Chemistry B*, 106(43):11203–11209, 2002.
- [253] X. Wang, X. Kong, Y. Yu, Y. Sun, and H. Zhang. Effect of annealing on upconversion luminescence of  $zno: er^{3+}$  nanocrystals and high thermal sensitivity. *The Journal of Physical Chemistry C*, 111(41):15119–15124, 2007.
- [254] X. Wang, X. Song, C. He, C.J. Yang, G. Chen, and X. Chen. Preparation of reversible colorimetric temperature nanosensor and their application in quantitative two-dimensional thermo-imaging. *Analytical Chemistry*, 2011.
- [255] M.H.W. Weber and M.A. Marahiel. Bacterial cold shock responses. *Science Progress*, 86, 1(2):9–75, 2003.
- [256] D. Wei and A. Ivaska. Applications of ionic liquids in electrochemical sensors. *Analytica Chimica Acta*, 607(2):126–135, 2008.
- [257] S. I. Weissman and D. Lipkin. The electromagnetic mechanism of the beta phosphorescence of fluorescein in acid solution. *Journal of the American Chemical Society*, 64(8):1916–1918, 1942.

- [258] G. Wielgoszewski, P. Sulecki, T. Gotszalk, P. Janus, P. Grabiec, M. Hecker, Y. Ritz, and E. Zschech. Scanning thermal microscopy: A nanoprobe technique for studying the thermal properties of nanocomponents. *Physica Status Solidi (B)*, 248(2):370–374, 2011.
- [259] G. Wielgoszewski, P. Sulecki, P. Janus, P. Grabiec, E. Zschech, and T. Gotszalk. A high-resolution measurement system for novel scanning thermal microscopy resistive nanoprobes. *Measurement Science and Technology*, 22:094023, 2011.
- [260] C.C. Williams and HK Wickramasinghe. Scanning thermal profiler. *Microelectronic Engineering*, 5(1-4):509–513, 1986.
- [261] OS Wolfbeis. Sensor paints. *Advanced Materials*, 20(19):3759–3763, 2008.
- [262] F.H.C. Wong, D.S. Banks, A. Abu-Arish, and C. Fradin. A molecular thermometer based on fluorescent protein blinking. *Journal of the American Chemical Society*, 129(34):10302–10303, 2007.
- [263] M.S. Wrighton, D.S. Ginley, and D.L. Morse. Technique for the determination of absolute emission quantum yields of powdered samples. *The Journal of Physical Chemistry*, 78(22):2229–2233, 1974.
- [264] T. Wu, G. Zou, J. Hu, and S. Liu. Fabrication of photoswitchable and thermotunable multicolor fluorescent hybrid silica nanoparticles coated with dye-labeled poly (n-isopropylacrylamide) brushes. *Chemistry of Materials*, 21(16):3788–3798, 2009.
- [265] W. Wu, J. Shen, P. Banerjee, and S. Zhou. Core-shell hybrid nanogels for integration of optical temperature-sensing, targeted tumor cell imaging, and combined chemophothermal treatment. *Biomaterials*, 31(29):7555–7566, 2010.
- [266] W. Wu, J. Shen, P. Banerjee, and S. Zhou. A multifunctional nanoplatfrom based on responsive fluorescent plasmonic *zno–au@peg* hybrid nanogels. *Advanced Functional Materials*, 2011.
- [267] Y. Wu and P. Yang. Germanium/carbon core–sheath nanostructures. *Applied Physics Letters*, 77:43, 2000.

- [268] D. Yan, J. Lu, J. Ma, M. Wei, D.G. Evans, and X. Duan. Reversibly thermochromic, fluorescent ultrathin films with a supramolecular architecture. *Angewandte Chemie International Edition*, 50(3):720–723, 2011.
- [269] Q. Yan, J. Yuan, Y. Kang, Z. Cai, L. Zhou, and Y. Yin. Dual-sensing porphyrin-containing copolymer nanosensor as full-spectrum colorimeter and ultra-sensitive thermometer. *Chemical Communications*, 46(16):2781–2783, 2010.
- [270] J.M. Yang, H. Yang, and L. Lin. Quantum dot nano thermometers reveal heterogeneous local thermogenesis in living cells. *ACS Nano*, 2011.
- [271] O. Yarimaga, S. Lee, D.Y. Ham, J.M. Choi, S.G. Kwon, M. Im, S. Kim, J.M. Kim, and Y.K. Choi. Thermofluorescent conjugated polymer sensors for nano-and microscale temperature monitoring. *Macromolecular Chemistry and Physics*, 2011.
- [272] F. Ye, C. Wu, Y. Jin, Y.H. Chan, X. Zhang, and D.T. Chiu. Ratiometric temperature sensing with semiconducting polymer dots. *Journal of the American Chemical Society*, 2011.
- [273] J. Yu, L. Sun, H. Peng, and M.I.J. Stich. Luminescent terbium and europium probes for lifetime based sensing of temperature between 0 and 70°C. *Journal Materials Chemistry*, 20(33):6975–6981, 2010.
- [274] Y.J. Yu, M.Y. Han, S. Berciaud, A.B. Georgescu, T.F. Heinz, L.E. Brus, K.S. Kim, and P. Kim. High-resolution spatial mapping of the temperature distribution of a joule self-heated graphene nanoribbon. *Applied Physics Letters*, 99(18):183105–183105, 2011.
- [275] V. Zeeb, M. Suzuki, and S. Ishiwata. A novel method of thermal activation and temperature measurement in the microscopic region around single living cells. *Journal of Neuroscience Methods*, 139(1):69–77, 2004.
- [276] Q. Zhan, J. Qian, H. Liang, G. Somesfalean, D. Wang, S. He, Z. Zhang, and S. Andersson-Engels. Using 915-nm laser excited  $\text{tm}^{3+}/\text{er}^{3+}/\text{ho}^{3+}$  doped  $\text{NaYbF}_4$  upconversion nanoparticles for in vitro and deeper in vivo bioimaging without overheating irradiation. *ACS nano*, 2011.

- [277] A. Zhanbotin, R.B. Soriano, A.K. Ikonen, T.N. Nurakhmetov, and T.A. Schmedake. Luminescent Mesoporous Colloidal Silica: A Nanoporous Substrate for Photosensitization of Lanthanide Ions. *Materials Letters*, 2010.
- [278] X. Zhang, H. Choi, A. Datta, and X. Li. Design, fabrication and characterization of metal embedded thin film thermocouples with various film thicknesses and junction sizes. *Journal of Micromechanics and Microengineering*, 16:900, 2006.
- [279] Y. Zhang, E.E. Castillo, R.J. Mehta, G. Ramanath, and T. Borca-Tasciuc. A non-contact thermal microprobe for local thermal conductivity measurement. *Review of Scientific Instruments*, 82(2):024902–024902, 2011.
- [280] Y. Zhang, PS Dobson, and JMR Weaver. Batch fabricated dual cantilever resistive probe for scanning thermal microscopy. *Microelectronic Engineering*, 2011.
- [281] Y. Zhang, C.L. Hapenciuc, E.E. Castillo, T. Borca-Tasciuc, R.J. Mehta, C. Karthik, and G. Ramanath. A microprobe technique for simultaneously measuring thermal conductivity and seebeck coefficient of thin films. *Applied Physics Letters*, 96(6):062107–062107, 2010.
- [282] Y. Zhong, K.S. Wong, W. Zhang, and DC Look. Radiative recombination and ultralong exciton photoluminescence lifetime in gan freestanding film via two-photon excitation. *Applied Physics Letters*, 89:022108, 2006.
- [283] H. Zhou, A. Midha, G. Mills, S. Thoms, SK Murad, and JMR Weaver. Generic scanned-probe microscope sensors by combined micromachining and electron-beam lithography. *Journal of Vacuum Science & Technology B: Microelectronics and Nanometer Structures*, 16(1):54, 1998.
- [284] J. Zhou, Z. Liu, and F. Li. Upconversion nanophosphors for small-animal imaging. *Chemical Society Reviews*, 2011.
- [285] O. Zohar, M. Ikeda, H. Shinagawa, H. Inoue, H. Nakamura, D. Elbaum, D.L. Alkon, and T. Yoshioka. Thermal imaging of receptor-activated heat production in single cells. *Biophysical Journal*, 74(1):82–89, 1998.



# Appendix A

## List of Acronyms

- [C<sub>4</sub>mpy][Tf<sub>2</sub>N]- 1-butyl-1-methylpyrrolidinium bis(trifluoromethylsulfonyl)imide  
3 HF-AM - 2-[4-(3-hydroxy-4-oxo-4H-chromen-2-yl)phenoxy]ethylacrylamide  
AFM - atomic force microscope  
APTES - 3-aminopropyltriethoxysilane  
BBS - 4,4'-bis(2-benzoxazolyl)stilbene  
bpeta - 1,2-bis(4-pyridyl)ethane  
BTD - 2-bis(trimethoxysilyl)decane  
btfa - 4,4,4-trifluoro-1-phenyl-1,3-butanedionate  
ca - citric acid  
CNT - carbon nanotube  
cyclam - 1,4,8,11-tetraazacyclotetradecane  
DBD-AA - N-[2-[(7-N,N-dimethylaminosulfonyl)-2,1,3-benzoxadiazol-4-yl](methyl)amino]ethyl-N-methylacrylamide  
dbma - dibenzoylmethanide  
DEGMA - di(ethylene glycol) methyl ether methacrylate  
DNA - deoxyribonucleic acid  
DPTB - pyrene-containing triarylboron molecule  
dipyren-1-yl(2,4,6-triisopropylphenyl)borane  
DT - tris(dinaphthoylethane)-bis-(trioctylphosphine oxide)  
FDA - Food and Drug Administration  
FEM - finite elements method  
FIR - fluorescence intensity ratio

FRET - fluorescence resonant energy transfer  
 fwhm - full-width-at-half-maximum  
 GFP - green fluorescent protein  
 HS - high spin  
 HEK 293 - human embryonic kidney  
 IL - ionic liquid  
 IR - infrared  
 LAURDAN - 6-dodecyl-2-dimethylamino-naphthalene  
 LDHs - layer double hydroxides  
 LED - light emitting diode  
 $\text{Ln}^{3+}$  - trivalent lanthanide  
 LS - low spin  
 MEMS - micro-electromechanical system  
 MeOH - methanol  
 MOE -2-methoxyethyl ether  
 mRNA - messenger ribonucleic acid  
 MWCNT - multiwalled carbon nanotube  
 NBD - 7-nitro-2,1,3-benzoxadiazole  
 NIPMAM - N-isopropylmethacrylamide  
 NIR - near infrared  
 NMR - nuclear magnetic resonance  
 NNPAM - N-n-propylacrylamide  
 NP - nanoparticle  
 NSOM - near-field scanning optical microscopy  
 OASN - N-octyl-4-(3-aminopropyltrimethoxysilane)-1,8-naphthalimide  
 P(VDC-co-AN) - poly(vinylidene chloride-co-acrylonitrile)  
 PDA - polydiacetylene  
 PDMS - poly(dimethylsiloxane)  
 Pdot - polymer dot  
 PEG - poly(ethyleneglycol)  
 PEO -polyethylene Oxide  
 PMMA - poly(methyl methacrylate)  
 PNIPAM-co-BODIPY - poly(N-isopropylacrylamide) incorporating boron-dipyrromethene

- PNIPAM - poly(N-isopropylacrylamide)  
PNIPAM:FMA - poly(N-isopropylacrylamide) incorporating fluorescent modified acrylamide  
PNIPAM-co-HC - poly(N-isopropylacrylamide) incorporating hemicyanine  
PPO - poly(p-phenylene oxide)  
PS - polystyrene  
PtBMA - poly(tert-butyl meth-acrylate)  
PTBS - poly-(tert-butyl styrene)  
PtOEP -2,3,7,8,12,13,17,18-octaethyl 21H,23H - porphyrin platinum(II)  
PtTFPP -5,10,15,20-tetrakis(pentafluorophenyl)porphyrin platinum(II)  
PVA - poly(vinyl alcohol)  
PyMMA - polymerizable pyrene dye methacrylate monomer  
QD - quantum dot  
rf - radio-frequency  
Rh-110 - rhodamine-110  
RhB - rhodamine B  
RNA - ribonucleic acid  
Ruphen - tris-(1,10-phenanthroline)ruthenium(II)  
 $S_m$  - maximum relative sensitivity  
Si-NP - silica nanoparticle  
SThM - scanning thermal microscopy  
STM - scanning tunneling microscope  
SWCNT - single-walled carbon nanotube  
TEM - transmission electron microscopy  
TEOS - tetraethyl orthosilicate  
 $T_m$  - temperature of maximum relative sensitivity is maximum  
tta<sup>-</sup> - thenoyltrifluoroacetate  
UC - up-conversion  
UCNP - up-converting nanoparticle  
UV - ultraviolet